Novel Spectral Imaging Instrumentation for Environmental Sensing in Extreme Environments

Mary Barbara Stuart

A thesis submitted in accordance with the requirements for award of the degree of Doctor of Philosophy

Department of Electronic and Electrical Engineering

University of Sheffield

February 2022

Abstract

Spectral imaging techniques provide a valuable means of improving our understanding of the world around us. Environmental monitoring approaches that utilise these techniques are, therefore, essential to our understanding of the effects of climate change. Hyperspectral imaging applications are of particular benefit to a broad range of environmental monitoring scenarios, providing rich datasets that combine both spectral and spatial information, enabling intricate features and variations to be visualised. However, to date, most commercially available hyperspectral instrumentation remains bulky and expensive, significantly limiting their user-base and accessibility. These factors substantially limit the use of these instruments resulting in much of our information coming from a few well-resourced research teams across a limited number of more easily accessed field locations. These limitations, have a compounded effect on the quality and robustness of hyperspectral data outputs, particularly within more extreme settings, as the comparatively small sample of more accessible locations is not necessarily representative of the much larger whole.

This thesis presents on the development and testing of three novel low-cost hyperspectral imaging instruments designed specifically for environmental monitoring applications, providing valuable, low-cost alternatives to currently available commercial systems. Specifically, the three instruments presented within this thesis are: a low-cost laboratory-based hyperspectral imager, a semi-portable instrument capable of accurate data capture within a laboratory setting; the Hyperspectral Smartphone, an ultra-low-cost smartphone-based fully portable hyperspectral imager; and a low-cost high-resolution hyperspectral imager capable of resolving mm-scale spatial targets. All instruments were rigorously tested to analyse and evaluate their performances. Each instrument was shown to perform well across a range of environmental monitoring applications demonstrating that expensive commercial instrumentation is not required to achieve accurate and robust hyperspectral imaging. These low-cost instruments could promote the widespread dissemination of accessible hyperspectral imaging equipment, facilitating the democratisation of hyperspectral measurement modalities across environmental monitoring applications and beyond.

Author's Declaration

I declare that the work in this thesis was carried out in accordance with the requirements of the University's Regulations and Code of Practice for Research Degree Programmes and that it has not been submitted for any other academic award. Except where indicated by specific reference in the text, the work is the candidate's own work. Work done in collaboration with, or with the assistance of, others, is indicated as such. Any views expressed in the thesis are those of the author.

Mary B. Stuart

Acknowledgements

I would like to thank my supervisors, Dr Jon Willmott and Dr Andrew McGonigle for providing me with the opportunity to undertake a PhD at the University of Sheffield and for their support, encouragement and advice over the last three and a half years. I am extremely grateful for my friends and colleagues within the Sensor Systems Group: Dr Matthew Hobbs, Dr Yufeng Lai, Matthew Davies, Callum Fisk, Emilios Leonidas, Benedict Davies, Michael Holliday, Matthew Grainger, Lizzy Allen, Jonathan Walsh, Dr Chengxi Zhu (Todd), Dr Nick Boone, Dr Leigh Stanger, Dr Andy Heeley, Dr Richard Hodgkinson, and Dr Tom Rockett. Thank you for providing a great place to work, and for introducing me to the Wednesday Lunch! Outside of the research group, I would like to thank my friends and colleagues in Geography, in particular Dr Tom Wilkes, and Dr Tom Pering for their support and advice over the years.

Thank you to the Moors for the Future Partnership for their advice, and provision of environmental monitoring datasets, and the Beadamoss team for their provision of Sphagnum samples for the peatland health project discussed within this thesis. Additionally, I would like to acknowledge the Department of Electronic and Electrical Engineering, and EPSRC without whom this research would not have been possible.

Finally, I would like to thank my friends and family, in particular, my parents Bruce and Sarah, brother Alasdair, and husband Alistair for their continued support and encouragement.

Publications

Published:

Stuart, M.B.; McGonigle, A.J.S.; Willmott, J.R. Hyperspectral Imaging in Environmental Monitoring: A Review of Recent Developments and Technological Advances in Compact Field Deployable Systems. *Sensors* **2019**, *19*, 3071. https://doi.org/10.3390/s19143071

Stuart, M.B.; Stanger, L.R.; Hobbs, M.J.; Pering, T.D.; Thio, D.; McGonigle, A.J.S.; Willmott, J.R. Low-Cost Hyperspectral Imaging System: Design and Testing for Laboratory-Based Environmental Applications. *Sensors* **2020**, *20*, 3293. https://doi.org/10.3390/s20113293

Stuart, M.B.; McGonigle, A.J.S.; Davies, M.; Hobbs, M.J.; Boone, N.A.; Stanger, L.R.; Zhu, C.; Pering, T.D.; Willmott, J.R. Low-Cost Hyperspectral Imaging with A Smartphone. *J. Imaging* **2021**, 7, 136. https://doi.org/10.3390/jimaging7080136

Davies, M.; **Stuart, M.B.**; Hobbs, M.; McGonigle, A.; Willmott, J.R. Image Correction and In-Situ Spectral Calibration for Low-Cost Smartphone Hyperspectral Imaging. *Remote Sensing,* **2022**, 14, 1152. https://doi.org/10.3390/rs14051152

Stuart, M.B.; Davies, M.; Hobbs, M.J.; Pering, T.D.; McGonigle, A.J.S.; Willmott, J.R. High-Resolution Hyperspectral Imaging Using Low-Cost Components: Application within Environmental Monitoring Scenarios. *Sensors*, **2022**, 22, 4652. https://doi.org/10.3390/s22124652

Submitted:

Stuart, M.B.; Davies, M.; Hobbs, M.J.; McGonigle, A.J.S.; Willmott, J.R. Peatland plant spectral response as a proxy for peat health, analysis using low-cost hyperspectral imaging techniques. *Remote Sensing*, Manuscript ID: remotesensing-1807953

Contents

List of Figures

List of Tables

List of Common Acronyms

CCD	Charged Coupled Device
CMOS	Complementary Metal-Oxide Semiconductor
DVD	Digital Video Disk
FOV	Field of View
FWHM	Full Width at Half Maximum
GCP	Ground Control Point
HFOV	Horizontal Field of View
IFOV	Instantaneous Field of View
InGaAs	Indium Gallium Arsenide
LED	Light Emitting Diode
MIR	Mid Infrared
MTF	Modulation Transfer Function
NIR	Near Infrared
PCB	Printed Circuit Board
RC	Resistor-Capacitor
SNR	Signal to Noise Ratio
TFOV	Total Field of View
UAV	Unmanned Aerial Vehicle
UV	Ultraviolet
VFOV	Vertical Field of View
WES	White Aesthetic Score Index

Chapter 1

Introduction

This chapter provides a brief overview of optical spectroscopy, advances in sensor development including single point spectrometers, multispectral, and hyperspectral set-ups, and highlights current developments in low-cost, compact sensor systems. Following this, I outline the aims and objectives of my thesis.

1.1. An Introduction to Optical Spectroscopy

Optical spectroscopy is an invaluable tool that has become a critical analysis method for a broad range of measurement and monitoring applications. It provides valuable insights into the processes and products that drive our world as well as providing critical early warnings of large-scale environmental changes. It is a measurement modality that has, and continues to, receive significant attention across multiple disciplines, from point-of-care analyses, to industrial and environmental monitoring. Whilst many disciplines employ the techniques discussed in this chapter, environmental monitoring applications in particular benefit significantly from the implementation of spectral sensing techniques. Optical spectroscopy has seen widespread use across environmental monitoring applications, enriching our knowledge and understanding of many environmental settings and conditions, however, as will be discussed in this thesis, at present many gaps remain. As our knowledge has evolved, so to have our measurement and monitoring methods from basic spectral sensing, to complex contiguous hyperspectral images. This chapter will introduce the origins of our modern-day methods, providing an insight into the complex and exciting potential of spectral sensing technologies both now and in the future.

1.1.1. A Brief History of Spectral Sensing

Spectroscopy is defined as the study of the interaction between matter and electromagnetic radiation as a function of wavelength [1]–[3]**.** The history of spectroscopy and spectral sensing dates back to the 17th Century when hypotheses on the nature and composition of light first began to come to prominence. Isaac Newton first described his, “new theory of light and colours” [4], in which he theorised that light in its natural state was made up of individual-coloured spectra rather than white light as theories of the time suggested. This theory was the result of measurements undertaken with a prism, wherein he directed a beam of sunlight through a collimating lens, and glass prism and observed the output of the individual spectral colours. The device Newton designed for his spectral experiments can now be recognised as a rudimentary spectroscope [5], [6].

Newton is recognised as the first to demonstrate that light is made up of a series of coloured spectra and as such, scientists have been studying the spectrum of light since this discovery. In 1802 William Hyde Wollaston observed dark lines present across the solar spectrum, theorising that these dark regions represented the natural boundaries present between the different colour regions. In 1814 these dark lines were rediscovered by Joseph Van Fraunhofer who went on to systematically document the precise wavelengths at which these lines were present. Today these features within the solar spectrum are known as Fraunhofer lines. In completing these observations and analysis both Wollaston and Fraunhofer had provided the foundations for spectroscopic analysis [5], [6].

Fraunhofer provided further improvements to the field of spectroscopy by replacing the prism in spectral instruments of the time with a diffraction grating, changing the method of wavelength

dispersion. Due to the precision afforded by this new technique, where the wavelengths were separated by a series of equally spaced slits, resulting in the wavelength dependent angular dispersion of the incident light, it significantly improved the spectral resolution of the instrument and, in turn, allowed for wavelengths to be quantified. As these wavelengths were now quantifiable, observations could be compared between different laboratories and different instruments, providing a significant advance within the field. With these improvements Fraunhofer had established the first practical spectrometer [1], [5].

Further advances took place within the 1860s when German physicists Robert Bunsen and Gustav Kirchhoff developed a spectroscope to systematically study the spectrum. During their studies they discovered that Fraunhofer lines corresponded to emission spectral lines observed in laboratory light sources, going on to produce a detailed examination of the spectral response of chemical compounds. By observing a variety of samples with their instrument they were able to determine characteristic features present within the spectrum of each sample. They went on to identify two new elements, rubidium and caesium, and in doing so, they definitively established the link between chemical elements and their unique spectral patterns, providing the foundations for modern spectral analysis techniques [1], [5].

1.1.1.1. Modern Spectrometers

From these beginnings spectroscopy has gone on to become a valuable tool with a wide range of specific applications. Modern optical spectrometers continue to utilise techniques similar to those found in early designs, with dispersion provided either through refraction (through a prism) or diffraction (with a diffraction grating), although improving technologies and manufacturing techniques have resulted in the latter becoming the more common of the two options more recently.

In a spectrometer the diffraction grating is situated between lenses or mirrors that control the geometry of light rays both incident upon and exiting the grating. Light is collimated before the diffraction grating then refocused onto a detector after diffraction. The entrance slit controls both the light throughput of the spectrometer but also, perhaps more importantly, affects the spectral resolution of the system. Generally, the smaller the slit, the greater the spectral resolution achievable with the instrument. However, this results in a trade-off between spectrometer sensitivity and spectral resolution, with the lower sensitivity associated with instruments with high spectral resolution resulting in significant target illumination requirements.

There are several different optical configurations found within modern spectrometer designs, these include; the Fastie-Ebert, Littrow, and Czerny-Turner configurations. In a Fastie-Ebert configuration one large mirror is used. A section of this mirror first collimates the incident light onto the diffraction grating, whilst a different section of the mirror focuses the light exiting the diffraction grating onto the sensor array. This configuration has been used extensively, however, it is limited by its ability to maintain image quality off-axis due to system aberrations [7]. Conversely, both the Littrow and the Czerny-Turner configurations utilise two separate mirrors. The Littrow configuration utilises one mirror for collimating and focusing, and a separate flat mirror to direct the rays onto the sensor, whereas the Czerny-Turner configuration utilises two separate mirrors for collimating and focusing the rays. In a Littrow configuration the geometry of the components is arranged such that light is diffracted back towards the incident direction, however, in a Czerny-Turner configuration the geometry of the system is flexible, enabling the inclusion of a wide variety of optical components. The differences between each of these configurations is highlighted in Figure 1.1. The crossed Czerny-Turner configuration has increased in popularity in recent years as the folded optical layout is well suited to the creation of compact, miniature systems. Despite these variations in configuration each spectrometer measures

variations in spectral characteristics over a given range, for example across visible wavelengths (400 - 700 nm), ultraviolet wavelengths (100 - 400 nm), or the infrared (700 nm – 1 µm). Indeed, spectral sensing is versatile with a wide range of feasible applications across different regions of the electromagnetic spectrum.

Spectrometers have enabled a wealth of data collection, allowing for precise spectral responses to be obtained from a variety of target features. This has provided significant benefits to an array of applications from point-of-care analysis [8], [9], to environmental monitoring [10], [11]. Furthermore, as technologies have continued to advance miniaturised technologies, including those incorporated with smartphone technologies have emerged [8], creating an opportunity for compact, portable spectral sensing applications. However, despite these significant advances spectrometers remain limited by their spatial resolution, where they typically only provide spectral data for a single point location on the target object. Whilst this technique has been demonstrated to provide valuable datasets, it lacks the spatial resolution required for larger or more complex targets, making it difficult to gain a complete understanding of the target or the precise location of specific spectral features across the object of interest. Spectral imaging, therefore, provides a viable alternative.

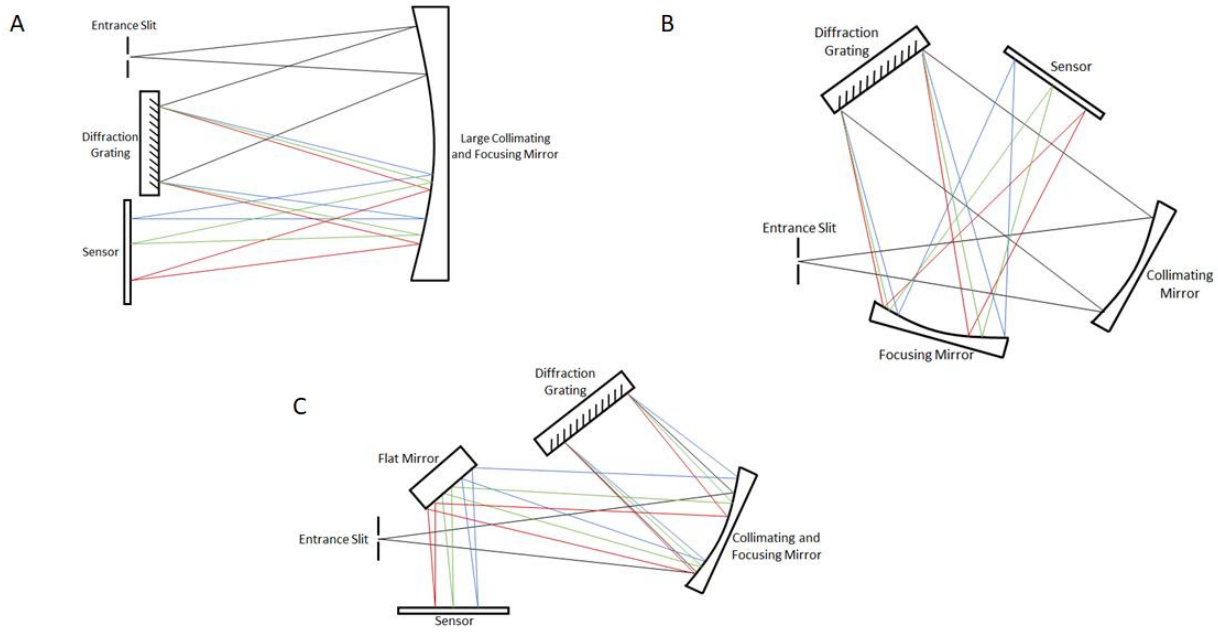

Figure 1.1 Schematic diagram of example spectrometer configurations. A - Fastie-Ebert, B - Czerny-Turner, C – Littrow. Note, black lines indicate white light. Blue, green, and red lines represent example wavelength rays after the light has been split into its component spectra after diffraction. Incident light enters the system at the entrance slit in each configuration. Not to scale.

1.1.1.2. Spectral Imaging

Spectral imaging combines the fields of spectroscopy and imaging, permitting the capture of datasets that contain both spatial and spectral information [3], [12]. Whilst imaging provides an intensity for every pixel within an image, and a spectrometer provides a single spectrum, a spectral image provides a spectrum for each pixel within the scene [3]. Furthermore, spectral imaging is not limited to the visible spectrum, therefore, enabling the capture of multiple wavebands across different regions of the electromagnetic spectrum. Its origins can be traced back to the 19th Century where astronomer Pierre Janssen used a double-slit monochromator to view the solar corona, adjusting the relative

position of the slit with respect to prism dispersion to view the scene at different wavelengths [12]. Later, Charles Fabry and Alfred Perot developed their interferometric filter allowing astronomers to view a full scene over a narrow spectral band and tune the filter wavelength, giving them the opportunity to build three-dimensional datasets of the target scene [12], [13]. The Fabry-Perot interferometer represented an important advance within the field of spectral imaging, providing an opportunity to obtain information the was previously very difficult to acquire [12].

There are several different methods for data capture using spectral imagers. Data can either be captured through a spatial scan, where the spectral information is captured line-by-line (push broom) or pixel-by-pixel (whiskbroom), or as a snapshot where the whole scene is captured simultaneously either one wavelength at a time (framing) or as a single exposure (windowing/snapshot). Furthermore, there are two main types of spectral imaging; Multispectral imaging, where the sensor captures datasets from a few, spaced spectral bands, and Hyperspectral imaging where wavelengths are captured contiguously. Whilst multispectral imaging can provide spectral data from several preselected wavebands (usually in the order of ten nanometres), hyperspectral imaging provides a more complete dataset, collecting a continuous spectral response across the spectral range of the sensor. Whilst spectral imaging with multispectral sensors has been achieved since the late 1960s [14], recent advances in the spectral and spatial resolution of sensors has opened-the-door to more detailed scene analysis with hyperspectral imaging [15], [16]. As a result, over the past three decades, hyperspectral imaging has emerged as an effective tool for a variety of applications ranging from remote sensing of the Earth's surface [15], [17], [18], to art conservation and archaeology [19]–[21]. Whilst hyperspectral data capture can be achieved without the inclusion of image data, choosing to include this feature can be of considerable benefit to a broad range of applications. Focusing on hyperspectral imaging, helps to provide additional context to the spectral datasets, making it easier to determine key areas of spectral change. This is of significant importance across more challenging environments with intricate or more complex targets because it allows the operator to pin-point the exact location of spectral variations across the target scene. This increases the accessibility of these datasets, making them more user-friendly and, in turn, enables more detailed target analysis.

1.2. Hyperspectral Imaging

Hyperspectral images are characterized by both their spatial and spectral resolution [22], [23], e.g., with two spatial dimensions (Sx and Sy) and one spectral dimension (Sλ). The spatial resolution measures the geometric relationship between the image pixels, while the spectral resolution determines the variations in illumination within the image pixels as a function of wavelength [18]. These data are represented in the form of a three-dimensional hyperspectral data cube [15], [18], where each "slice" of this data cube along Sλ, represents a specific band from the electromagnetic spectrum [18].

Initially developed for remote sensing applications [19], [24], hyperspectral imaging sensors typically acquire images across hundreds of narrow spectral bands within the visible, Near Infrared (NIR), and Mid Infrared (MIR) segments of the electromagnetic spectrum [18], [11]. This enables the construction of an almost continuous reflectance spectrum for each pixel in a scene which, in turn, allows for the in-depth spectral examination of scene features that would be rather less perceptible with the coarser bandwidths of multispectral scanners [14], [16], [17], [25]. This recent development in sensor technologies has led to the uptake of hyperspectral imaging methods across a wide variety of disciplines, opening new possibilities for measuring and monitoring multiple aspects of our environment.

In recent years, there has been a considerable uptake of field deployable hyperspectral imaging within the discipline of environmental monitoring [26], [27]. This is an exciting, and potentially revolutionary, development that could result in substantial future alterations to existing monitoring methods and sensing modalities, involving capture of higher quality data [28]. However, despite this uptake, there remains a considerable lack of low-cost, field deployable technologies across more extreme environments, resulting in a significant gap in the existing literature. The considerable lack of affordable hyperspectral imaging instrumentation suitable for field deployment in these environments presents a significant problem for the continued advancement of environmental monitoring, leading to a lack of data to inform our understanding of underlying processes in these environments. This research, therefore, aims to provide a significant improvement to current sensing technologies in these environments by introducing accessible low-cost, miniaturised alternatives to the currently existing monitoring methods.

1.3. Objectives

The overarching goal of this thesis was to develop a variety of low-cost, portable hyperspectral imaging sensors capable of providing valuable datasets from and undertaking field-based analyses in a variety of more extreme environmental settings. As highlighted above, these environments in particular are lacking in accessible hyperspectral imaging technologies, resulting in existing sensors being available only in more easily accessed locations and/or to select, well-resourced, research teams. This results in the majority of our knowledge of these, often volatile, environments coming from a small percentage of these locations, significantly limiting our knowledge of these dynamic and highly important environments. By providing a variety of accessible and robust hyperspectral sensors it will significantly enhance the opportunities for hyperspectral data collection in these locations, leading to a better understanding of these locations and improving the accessibility of this research field.

1.3.1. Objective 1

The first objective of this thesis was to design and construct a low-cost, miniaturised hyperspectral imager from commercially available components and demonstrate its capabilities in a variety of environmental monitoring applications. This device had to be capable of scientific grade data capture, therefore, making it a valuable addition to the field.

1.3.2. Objective 2

Building on the findings from Objective 1, the second objective of this thesis was to develop a low-cost, portable hyperspectral imager. For this objective the aim was to determine what could be achieved for the lowest possible cost to provide a springboard for future innovation.

1.3.3. Objective 3

The third objective of this thesis was to develop the low-cost portable hyperspectral imager design into a robust, scientific grade device, capable of in-field data collection. This device was developed to be an accessible sensor that could cope with the demands associated with undertaking fieldwork in a range of environmental conditions.

1.3.4. Objective 4

Building on the findings from Objective three, the fourth objective of this thesis was to develop a semi-portable, high-resolution hyperspectral sensor that was capable of mm-scale hyperspectral data capture at a fraction of the cost of commercially available systems. This instrument was intended to complement and build on the instruments of Objectives one and three by providing a very high-resolution set-up capable of on-site analyses.

1.3.5. Objective 5

The fifth objective of this thesis was to demonstrate the performance of these portable hyperspectral set-ups within appropriate environmental applications. The devices were tested within a variety of environmental applications and their performance analysed. This work was intended to demonstrate the proficiency of these low-cost portable set-ups as well as to enhance the current datasets available for these locations and applications.

1.4. Thesis Structure

Below is an overview of the layout of this thesis highlighting the discussion and achievement of the objectives outlined above. Furthermore, the work discussed in this thesis has resulted in a number of publications, therefore, where these pieces fit into the present body of work is also outlined below.

Chapter 2 comprises an overview of pertinent theory related to spectral instrumentation and hyperspectral imaging before going on to provide a review of existing literature related to the use of hyperspectral imaging techniques within environmental monitoring applications. Specifically, this chapter discusses spectrometers and optical materials, and the principles of hyperspectral imaging, before highlighting current applications of both UAV and ground-based sensors across a variety of environmental monitoring disciplines. This review has been published in Stuart et al., [29] which highlighted the current state-of-the-art in the field.

Chapter 3 addresses objective 1. It presents the design and testing of a semi-portable low-cost hyperspectral imaging system that is capable of laboratory-based hyperspectral data collection. This chapter is associated with the work published in Stuart et al., [30] which detailed the development of this instrument and its application to laboratory-based environmental monitoring scenarios.

Chapter 4 addresses objectives 2 and 3. It presents the development of a smartphone-based portable hyperspectral imaging instrument. Building on the narrative of Chapter 3, this chapter first discusses the development of a very low-cost portable design capable of demonstrating the potential within this field of research. Subsequently, this chapter demonstrates the design and testing of a valuable low-cost field portable hyperspectral imager which is published within Stuart et al., [31]. Further improvements to the image correction and spectral calibration processes, published in Davies et al., [32] are also discussed.

Chapter 5 addresses objective 4. It presents the development of a low-cost, semi-portable hyperspectral imager capable of high-resolution image capture, allowing for mm-scale targets to be easily resolved. This instrument further bridges the gap to the realisation of the democratisation of hyperspectral imaging techniques, combining the benefits and skills gained from the development of the instrumentation discussed in Chapters 3 and 4, to enable the best quality image capture possible with a low-cost, semi-portable instrument. Its efficacy is demonstrated in its application to the field of mineralogy where it is used to determine mm-scale spectral differences across a range of complex samples. This work has been published within Stuart et al., [33].

Chapter 6 addresses objective 5. It presents the application of the Hyperspectral Smartphone (Chapter 4) and the Low-Cost High-Resolution instrument (Chapter 5) to a real-world systematic study where they are utilised within the field of peatland health monitoring, and is associated with the work to be published in Stuart et al., [34]. The instruments are utilised to monitor variations in spectral response related to the onset of drought stress within Sphagnum moss samples. Both instruments are shown to perform well, detecting variations in spectral response up to three weeks before the onset of distinct visual changes, demonstrating that expensive, commercial instrumentation is not necessarily required for accurate and robust hyperspectral data capture.

Chapter 7 summarises the work presented in this thesis and presents future avenues and alternative applications of the instrumentation developed and discussed within the previous chapters. Specifically, it presents a discussion that brings together the instrumentation presented within this body of work, before detailing future work and potential extended applications for the low-cost instrumentation highlighted in this thesis.

1.5. References

[1] J. C. Brand, *Lines of light: The sources of dispersive spectroscopy, 1800-1930*. Routledge, 2017.

[2] D. W. Ball, *Field guide to spectroscopy*. Bellingham, Washington: SPIE Press, 2006.

[3] Y. Garini, I. T. Young, and G. McNamara, "Spectral imaging: Principles and applications," *Cytom. Part A*, vol. 69, no. 8, pp. 735–747, 2006.

[4] I. Newton, *The optical papers of Isaac Newton: Volume 1, The Optical Lectures 1670-1672*. Cambridge: Cambridge University Press, 1984.

[5] K. Hentschel, "Prisms, Spectroscopes, Spectrographs, and Gratings," in *A Companion to the History of Science*, B. Lightman, Ed. Wiley Blackwell, 2016, pp. 543–556.

[6] D. W. Ball, *The Basics of Spectroscopy*. SPIE Press, 2001.

[7] J. Lerner and A. Thevenon, *The optics of spectroscopy*. 1988.

[8] A. J. S. McGonigle *et al.*, "Smartphone spectrometers," *Sensors (Switzerland)*, vol. 18, no. 1, pp. 1–15, 2018.

[9] C. Zhang, G. Cheng, P. Edwards, M. Da Zhou, S. Zheng, and Z. Liu, "G-Fresnel smartphone spectrometer," *Lab Chip*, vol. 16, no. 2, pp. 246–250, 2016.

[10] T. C. Wilkes, T. D. Pering, A. J. S. McGonigle, G. Tamburello, and J. R. Willmott, "A low-cost smartphone sensor-based UV camera for volcanic SO2emission measurements," *Remote Sens.*, vol. 9, no. 1, pp. 1–11, 2017.

[11] A. J. Das, A. Wahi, I. Kothari, and R. Raskar, "Ultra-portable, wireless smartphone spectrometer for rapid, non-destructive testing of fruit ripeness," *Sci. Rep.*, vol. 6, no. April, pp. 1–8, 2016.

[12] N. Hagen and M. W. Kudenov, "Review of snapshot spectral imaging technologies," *Opt. Eng.*, vol. 52, no. 9, p. 090901, 2013.

[13] C. Fabry and A. Perot, "On a new form of interferometer," *Astrophys. J.*, vol. 13, p. 265, 1901.

[14] D. Landgrebe, "Information extraction principles and methods for multispectral and hyperspectral image data," *Inf. Process. Remote Sens.*, pp. 3–38, 2000.

[15] P. GHAMISI *et al.*, "Advances in Hyperspectral Image and Signal Processing," *IEEE Geosci. Remote Sens. Mag.*, vol. 5, no. 4, pp. 37–78, 2017.

[16] E. Honkavaara *et al.*, "Processing and assessment of spectrometric, stereoscopic imagery collected using a lightweight UAV spectral camera for precision agriculture," *Remote Sens.*, vol. 5, no. 10, pp. 5006–5039, 2013.

[17] M. Govender, K. Chetty, and H. Bulcock, "A review of hyperspectral remote sensing and its application in vegetation and water resource studies," vol. 33, no. 2, pp. 145–152, 2006.

[18] M. J. Khan *et al.*, “Modern Trends in Hyperspectral Image Analysis: A Review,” vol. 6, 2018.

[19] C. Fischer and I. Kakoulli, “Multispectral and hyperspectral imaging technologies in conservation: current research and potential applications,” *Stud. Conserv.*, vol. 51, no. sup1, pp. 3–16, 2006.

[20] R. Padoan, T. Steemers, M. Klein, and B. Aalderink, “Quantitative Hyperspectral Imaging of Historical Documents: Technique and Application,” *ART Proc.*, no. May, pp. 25–30, 2008.

[21] H. Liang, “Advances in multispectral and hyperspectral imaging for archaeology and art conservation,” *Appl. Phys. A Mater. Sci. Process.*, vol. 106, no. 2, pp. 309–323, 2012.

[22] J. Luo, F. Cai, X. Yao, J. Li, Q. Huang, and S. He, “Experimental Demonstration of an Anti-Shake Hyperspectral Imager of High Spatial Resolution and Low Cost,” *IEEE Sens. J.*, vol. 20, no. 14, pp. 8082–8090, 2020.

[23] L. Liu, L. Xu, and J. Peng, “3D Reconstruction from UAV-Based Hyperspectral Images,” *Appl. Comput. Vis. (WACV), 2015 IEEE Winter Conf.*, vol. XLII, pp. 318–325, 2015.

[24] T. Adão *et al.*, “Hyperspectral imaging: A review on UAV-based sensors, data processing and applications for agriculture and forestry,” *Remote Sens.*, vol. 9, no. 11, 2017.

[25] C. C. Wilcox, M. Montes, M. Yetzbacher, J. Edelberg, and J. Schlupf, “An ultra-compact hyperspectral imaging system for use with an unmanned aerial vehicle with smartphone-sensor technology,” *Proc. SPIE - Int. Soc. Opt. Eng.*, vol. 10639, no. May, 2018.

[26] C. Baccani *et al.*, “Optical design of a hyperspectral drone advanced camera for soil monitoring using an electro-optical liquid crystal technology,” *Opt. Des. Eng. VII*, no. June 2018, p. 20, 2018.

[27] R. Näsi *et al.*, “Remote sensing of bark beetle damage in urban forests at individual tree level using a novel hyperspectral camera from UAV and aircraft,” *Urban For. Urban Green.*, vol. 30, no. December 2017, pp. 72–83, 2018.

[28] R. Garzonio, B. di Mauro, R. Colombo, and S. Cogliati, “Surface reflectance and sun-induced fluorescence spectroscopy measurements using a small hyperspectral UAS,” *Remote Sens.*, vol. 9, no. 5, pp. 1–24, 2017.

[29] M. B. Stuart, A. J. S. McGonigle, and J. R. Willmott, “Hyperspectral imaging in environmental monitoring: A review of recent developments and technological advances in compact field deployable systems,” *Sensors (Switzerland)*, vol. 19, no. 14, 2019.

[30] M. B. Stuart *et al.*, “Low-cost hyperspectral imaging system: Design and testing for laboratory-based environmental applications,” *Sensors (Switzerland)*, vol. 20, no. 11, pp. 1–13, 2020.

[31] M. B. Stuart *et al.*, “Low-cost hyperspectral imaging with a smartphone,” *J. Imaging*, vol. 7, no. 8, pp. 1–13, 2021.

[32] M. Davies, M. B. Stuart, M. Hobbs, A. McGonigle, and J. R. Willmott, “Image correction and in-situ spectral calibration for low-cost, smartphone hyperspectral imaging,” *Remote Sens.*, vol. 14, p. 1152, 2022.

[33] M. B. Stuart, M. M. J. Davies, M. J. Hobbs, T. D. Pering, A. J. S. McGonigle, and J. R. Willmott, “High-Resolution Hyperspectral Imaging Using Low-Cost Components: Application Within Environmental Monitoring Scenarios,” *Sensors*, 2022.

[34] M. B. Stuart, M. Davies, M. J. Hobbs, A. J. S. McGonigle, and J. R. Willmott, “Peatland Plant Spectral Response as a Proxy for Peat Health, Analysis Using Low-Cost Hyperspectral Imaging Techniques,” *Remote Sens.* In Press.

Chapter 2

Hyperspectral Imaging in Environmental Monitoring, Theory and Current Applications

This chapter provides a more detailed examination of spectral instrument design and hyperspectral imaging. It aims to provide a background of the theory upon which much of the subsequent chapters are based, before going on to provide a review of the existing literature, which is associated with the work presented in Stuart et al., [1]. It reviews the various categories of hyperspectral imaging systems available to date with a focus on current progress within the design of low-cost systems, particularly within the field of environmental monitoring. Specifically, this chapter focuses on spectral imaging components and optical materials, an introduction to radiometry, principles of hyperspectral imaging, and current applications within environmental monitoring. Later chapters will present the development and application of new low-cost, small-scale alternatives, broadening the applicability of low-cost hyperspectral imaging far beyond its current extent, allowing novel data collection to be achieved in a variety of more challenging environmental settings.

2.1. Introduction

As highlighted in Chapter 1, spectral sensing technologies are an integral component of environmental monitoring research, providing comprehensive datasets that cannot otherwise be observed. It is clear that hyperspectral sensing is becoming increasingly beneficial due to the detailed spectral and spatial datasets these instruments can provide, opening new avenues for more in-depth research across multiple environmental settings and application areas. However, the vast majority of currently available hyperspectral sensing systems, that are capable of direct field deployment, remain largely inaccessible due to the substantial costs associated with their initial purchase and their often bulky design limiting their overall usability. These limitations are beginning to be overcome through advances in low-cost miniaturised technologies, allowing research teams to develop their own bespoke systems, providing user friendly designs, at a fraction of the cost of the currently available commercial systems. However, despite this potential a substantial range of more challenging environmental settings continue to be widely neglected. The provision of accessible, user friendly hyperspectral sensors for these more extreme environments is of significant Importance, not only due to the increased potential for comprehensive data collection but also the far reaching benefits of accessible technologies which can benefit more than just the immediate academic community which will be discussed in detail in later chapters. Each of these instruments is subject to underlying theory and concepts that influence the performance and the specific abilities of each component and the set-up as a whole, therefore, this chapter will first discuss the relevant theory relating to spectral instrument design and hyperspectral imaging, before focusing on the existing literature pertaining to current accessibility of low-cost hyperspectral sensors across a range of environmental monitoring fields with the aim of highlighting the significant gaps present in the existing literature at this time.

2.2. Spectrometers and Hyperspectral Imaging

Hyperspectral imaging enables the capture of three-dimensional datasets using two-dimensional hardware. Due to the complexities involved in building such datasets, hyperspectral imagers contain a variety of components to enable the capture of both spatial and spectral information. The method of spatial data collection is dependent on the hyperspectral imaging technique used. Spatial information can be captured either sequentially e.g. pixel-by-pixel or line-by-line, enabling a two-dimensional spatial dataset to be built out of the captured data; or as a single frame using a two-dimensional sensor array to provide the x and y dimensions. Spectral information can also be captured using a variety of methods, e.g. using tuneable filters, or spectrometer components, with the latter being typically more commonplace, particularly in more compact designs. A spectrometer, on its own, provides a detailed contiguous spectral dataset for a single point location of a target scene. When combined with the additional optics and spatial scanning components required for hyperspectral imaging, a spectrometer forms an integral component of a hyperspectral imaging system, providing the spectral dimension to the spatial image. Therefore, in order to fully understand the concept of hyperspectral imaging we must first discuss spectrometers and their associated components in more detail. The following sections will discuss the theory and fundamental knowledge associated with spectrometers and spectral imaging, before returning to hyperspectral imaging in Section 2.4. where the principles of hyperspectral imaging and the various image capture techniques available are discussed in more detail.

2.2.1 Spectral Imaging: Components and Optical Materials

Spectrometers come in a range of different configurations, as highlighted in Chapter 1, however, the individual components and optical materials present within each set-up are reasonably standardised and, as such, are subject to conventional basic criteria. For example, the chosen optical material must be capable of a smooth polish, and be mechanically and chemically stable [2]. A homogeneous refractive index is also required to ensure light rays can pass evenly through the material [2]. Furthermore, the material should not possess artefacts that may result in the distortion of the optical throughput and must be capable of transmitting or reflecting wavelengths consistently across the region of its intended use. Meeting these criteria will enable the development of a robust spectral imaging set-up, however, the exact abilities of any particular instrument are highly reliant on the specific configuration of the components and the conditions of its intended use. As such, each component within a spectral imaging system plays a key role in defining the capabilities of the instrument.

2.2.1.1. The Entrance Slit, Collimating and Focusing Components

Working in order of interaction, light rays entering a spectrometer will first interact with the entrance slit. The quantity of light a spectrometer can capture is generally dependent on the f number of the spectrometer aperture, and the spatial distribution of the optical power at the output plane of any focusing optics positioned prior to the entrance slit. In a well-designed system, the focal point formed by any focusing optics will be circularly symmetrical and should be equal to the f number of the spectrometer aperture. This allows the optimum quantity of light to enter the spectrometer without the influence of unwanted stray reflections. Furthermore, unless the width of the focal point is smaller than or equal to the width of the spectrometer slit, a portion of the optical power incident on this surface will be blocked from entering the spectrometer. Inaccuracies within the focusing and alignment of these components can, therefore, lead to increased measurement period requirements because, if only limited optical power is available to the spectrometer sensor, longer exposure times are required to ensure the accurate detection of the spectral response. The entrance slit, therefore, controls the light throughput of the spectrometer but is also a critical component that effects the spectral resolution of the instrument. A spectrometer with a narrower entrance slit will be capable of

a higher spectral resolution, however, this creates a trade-off between spectral resolution and light throughput. This is of particular relevance when the spectrometer is being utilised within a spectral range where the quantum efficiency of the sensor is low, for example, a silicon photodiode utilised within ultraviolet wavelengths. Furthermore, the capture of datasets from targets with a highly diffuse reflection pattern can also be restricted in higher resolution systems as the reduced levels of directly reflected light limit the light available to the sensor. This results in more diffuse targets having significant illumination requirements in order to achieve valuable data outputs.

Once incident light has passed through the entrance slit, a series of lenses or mirrors then refract the light rays within the instrument. The selection of lens or mirror components depends on the particulars of the chosen system; lenses allow for more linear formats, whereas mirrors are typically utilised in crossed or folded formats (Figure 2.1.), allowing for more compact designs. These components control the geometry of the rays by either collimating or focusing them at specific points within the instrument. Collimators are used to align the incident rays entering through the slit, prior to their interaction with the diffraction grating, whereas focusing components are generally used to focus the rays exiting the diffraction grating on to the sensor. Some spectrometer configurations utilise further components to alter the light ray geometries to the specifics of their configuration, such as the flat mirror component used within the Littrow design, or combine components, such as the single collimating and focusing mirror utilised in Fastie-Ebert configurations. Each design has its benefits, however, the specific component selection and configuration depends on the details of the instruments intended use.

2.2.1.2. Diffraction and the Diffraction Grating

The diffraction grating is a crucial component within a spectral imaging instrument because it is responsible for the wavelength dependent angular dispersion of the incident light rays. Whilst some instruments use prisms to refract the incident light rays, diffraction gratings are typically more common place in modern spectral instrument designs due to their greater dispersion potential. Diffraction is a process that involves the interaction of light waves with edges and features e.g. an aperture or the lines of a diffraction grating, that are close in scale to the wavelength. It can be described using Huygen's principle of light wave propagation. According to Huygen's principle each point on a wave front can be a source of wavelets. These wavelets reinforce or interfere with each other to form the new wave front, which is a line tangent of the wavelets [2]. In a diffraction grating the series of precisely ruled lines on a clear or reflecting base act as an obstacle. Light can both pass directly through the grating and also be diffracted into its component colours. When light passes through a diffraction grating the diffraction effect causes the wave front to curve backwards causing the rays to split. The exact dispersion of the light is reliant on the spacing between the lines of the grating. At certain angles the diffracted wavelets reinforce and maxima are produced [2];

$$\sin\theta = \frac{n\lambda}{d} \pm \sin I \tag{2.1}$$

Where λ is the wavelength, d is the spacing of the grating lines, *I* is the angle of incidence and *n* is an integer (order of the maxima). The positive sign is used for a transmission grating, and the negative sign for a reflective grating. Decreasing the spacing between the lines of the diffraction grating increases the spacing between these maxima by increasing the angle of diffraction. The diffraction grating equation, giving the angle of diffraction for the nth order beam is stated as,

$$d\sin\theta = n\lambda \tag{2.2}$$

$Sin\theta$ is proportional to the wavelength**.** The decision to use a transmission or reflective diffraction grating is highly dependent on the intended configuration of the instrument, however, both

approaches are used extensively across a broad range of instruments and applications. Transmission gratings are typically designed by etching a series of narrow, parallel grooves onto a transparent substrate. Reflective gratings are coated with a highly reflective covering within the required wavelength range e.g. a silver or gold coating can be used for infrared regions, parallel grooves are then etched across the surface, similar to transmission gratings [3]. The diffraction grating is an important component of a spectral instrument because it determines the angular dispersion of the wavelengths across the sensor and is, therefore, integral to the spectral resolution of the sensor.

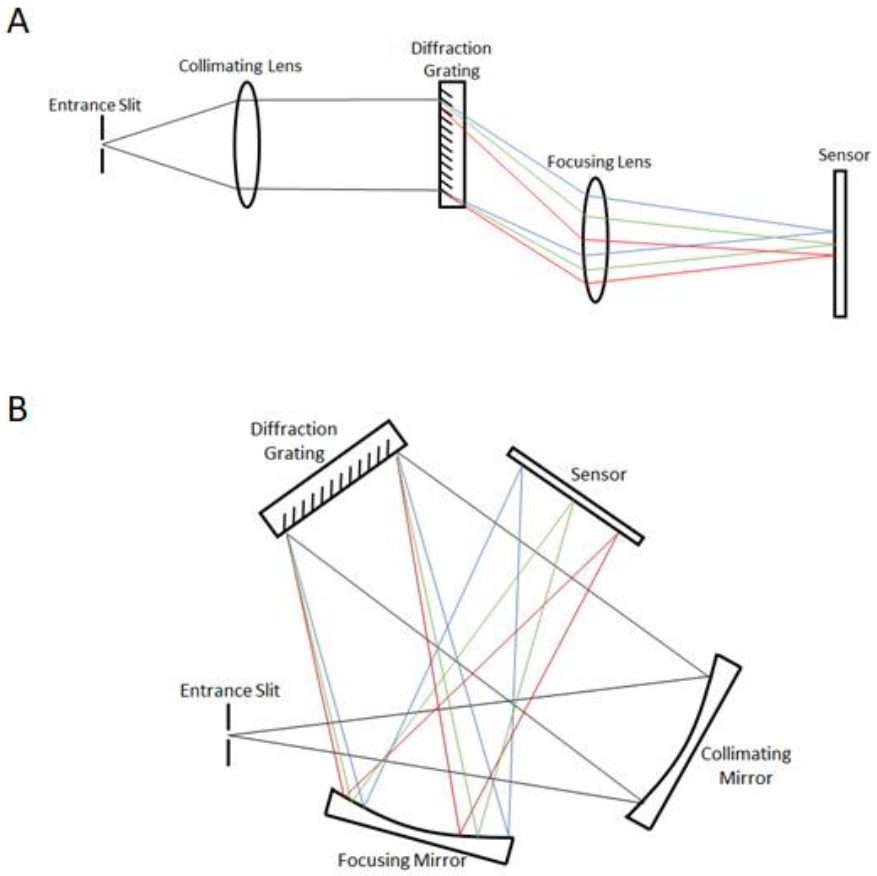

Figure 2.1 Example spectral formats, A demonstrates a basic linear format utilising lenses and a transmission diffraction grating. B demonstrates a crossed format utilising mirrors and a reflective diffraction grating.

2.2.1.3. The Sensor Array

Whilst each component in an optical system plays a key role in determining the overall performance of the instrument, the sensor array has been shown to typically have the largest impact on performance [4], [5]. The sensor array is the final stage in a spectral imaging system. Light exiting the diffraction grating is focused onto the sensor by a focusing mirror or lens. The light incident on the surface of the sensor is then converted into an array of electrical signals, that provide the spectral information for a specific location, or pixel, within the target scene. A lens is required to provide a one-to-one mapping between a spatial location of an object and its corresponding spatial coordinate on the image sensor array. These output signals can then be combined to provide a spectral image of the chosen target containing both spectral and spatial information.

A variety of different sensor materials are used in spectral optics depending on the wavelength range of the instrument. Silicon-based sensors, such as Charged Coupled Devices (CCDs) and Complimentary

Metal-Oxide Semiconductors (CMOS) are typically utilised for applications focusing on the visible spectrum, however, the physical properties of silicon mean that these sensors are also capable of detecting wavelengths in ultraviolet and the near infrared regions [6]. However, these sensors are not typically used for applications focusing predominantly on infrared wavelengths due to silicon's band gap. In these regions sensors such as Indium Gallium Arsenide (InGaAs) sensors are more commonly used as their sensitivity is better suited to these longer wavelength applications.

For visible and ultraviolet applications, CCD sensors have traditionally been the dominant sensor design, however, improvements in technologies and manufacturing techniques have allowed CMOS sensors to overtake CCDs as the sensor of choice for a broad range of applications [4], [6], [7], and they are now commonly used in commercial colour imagers such as, smartphones and digital cameras [7]. Originally, CMOS sensors were affected by higher noise levels, limiting their ability to produce high quality outputs. This made them less appealing than the more expensive CCD sensors which had been quickly optimised for imaging applications [6]. Since their initial development, technological improvements combined with an increasing demand for high sensitivity imaging, has led to significant improvements in CMOS sensor design allowing them to become comparable, and often superior, to CCD sensor options.

InGaAs sensors are typically used for applications that require high sensitivity over the range of 900 – 1700 nm. Across this region silicon-based sensors cannot be used as the material lacks sensitivity within this region of the spectrum. This is due to silicon's band gap which limits its use to the near infrared and shorter wavelengths. A band gap is an energy region within which no electronic states can exist. It represents the minimum energy required to excite an electron to move from its bound state, within the valence band, to its free state, within the conduction band. Shorter wavelengths, such as those within the visible region of the spectrum contain higher energy photons than the longer wavelengths of the infrared. Focusing on silicon, this means that visible wavelengths contain enough energy to excite its electrons to move to the conduction band, allowing the electrons to participate in conduction and, therefore, these wavelengths can be absorbed. However, the longer wavelengths of the mid infrared do not contain enough energy to excite the electrons, meaning they remain within their bound state in the valence band. In this case conduction does not take place and, therefore, the silicon allows the infrared light to pass through it without interaction.

Whilst silicon's band gap means that it lacks the sensitivity for applications over ca. 1100 nm, InGaAs sensors have a lower/smaller band gap, making them the ideal choice for infrared applications. The majority of InGaAs sensors are utilised within the shortwave infrared, with some sensors being capable of reaching ca. 2500 nm with changes in their material composition. Although these sensors have a greater sensitivity within infrared wavelengths, their lower band gap also results in a higher dark current, increasing the noise and, therefore, limiting the quality of data the sensor is capable of producing. These limitations can be minimised with the introduction of cooling methods that help to increase the signal to noise by reducing the dark current, however, this adds to the general complexity and size of the instrument which can be crucial factors for a number of applications.

2.2.1.4. Colour Filter Arrays and Their Inclusion in Spectral Sensing Instrumentation

Colour filter arrays are commonplace in many off-the-shelf optical technologies and are widely implemented in a number of lower cost, consumer market components, such as smartphones. As smartphones and other consumer market technologies provide a valuable, user friendly starting point for the creation of affordable spectral imaging instrumentation, these filters, and their influence on spectral outputs, must be considered as these low-cost, consumer market based hyperspectral and

multispectral sensors increase in popularity. The potential available within the field of smartphone-based hyperspectral imaging is discussed further in Section 2.6.

To achieve colour image outputs from CMOS and CCD sensors, colour filter arrays are applied to the sensor pixels. The specifics of the colour filter array vary depending on the proposed application of the instrument, however, a common choice is the Red-Green-Green-Blue Bayer filter array (Figure 2.2.). For this pattern, each pixel produces a signal that corresponds to one of the colours within the filter. To produce a full colour image a demosaicing algorithm is implemented, wherein the pixel values relating to the colour channel outputs (Red, Green, and Blue) are used to simulate a full colour image. Whilst this is beneficial for the traditional use of these sensors as standard colour cameras, it can prove problematic in the creation of spectral sensing and imaging devices that utilise these consumer components.

The inclusion of a Bayer filter, of course, has an impact on the spectral output of any imaged target and, therefore, must be accounted for in post-processing, or removed [8], in order to obtain true, quantitative datasets from spectral sensors containing this feature. Cross-talk between the colour pixels can also occur which can further compromise the credibility of the colour outputs [4]. Furthermore, the application of this filter limits the wavelength sensitivity of the sensor by attenuating incident UV and NIR radiation, whilst this is suitable for applications based centrally within visible wavelengths it can be a limiting factor for targets with key spectral features present near these boundaries. To remove these limitations many sensors do not include a colour filter array, instead using the monochrome sensor. This is beneficial in that it allows for the full range of wavelength sensitivity to be utilised and removes the potential for colour distortions in the output images, making it easier to obtain a spectral response that is true to the imaged target. Furthermore, the resolution of these sensors is typically higher because there are no limitations imposed by the presence of a colour filter array. However, it should be noted that these sensors can also be affected by cross-talk which can lead to limitations in image accuracy [6].

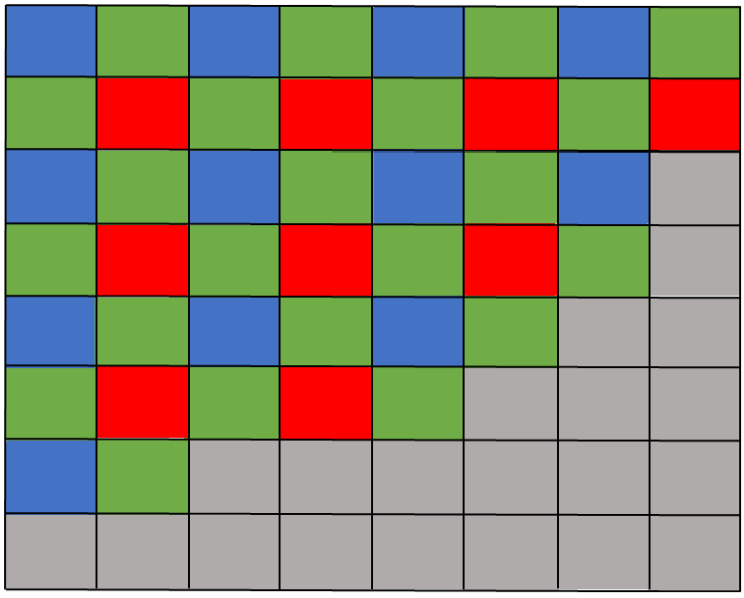

Figure 2.2 Example Bayer colour filter array layout on top of a sensor array. Grey squares show the underlying sensor array.

2.3. An Introduction to Radiometry

Radiometry is the science of measuring and quantifying optical radiation at any wavelength across the electromagnetic spectrum [2], [9], and, as such, it is critical to the detection of accurate quantifiable hyperspectral datasets. Although radiometry can be applied over the entirety of the electromagnetic spectrum, in practice the term is usually limited to measurements within the optical region, focusing on infrared, visible, and ultraviolet light. Radiometry, therefore, represents an important part of the design process for most optical instrumentation [10]. The basic unit of power used in radiometric measurements is the watt. In spectral sensing applications radiometry often focuses on radiative transfer which is used to describe the way that targets, or 'bodies', radiate power and energy to and from each other, this radiation is often described in terms of power per unit area. Additionally, blackbody furnaces provide an excellent means by which to calibrate colour and relate these calibrations to the watt using radiation thermometer transfer standards, therefore, they are commonly utilised in radiometric calibrations.

Emissivity is a term that is often used when discussing radiometry, it is a radiative relative material property that describes how effectively a target object or material can emit thermal radiation as a consequence of its temperature. A target's emissivity value is between 0 and 1 and provides the ratio of radiation an object emits compared to that of a perfect emitter (or perfect body) at the same temperature. A perfect body, known as a blackbody, is one that totally absorbs all radiation incident upon it [10], [11]. A blackbody has an emissivity of 1 [2], [10], [11]. Perfect blackbodies, are hypothetical, however, heated blackbodies**,** such as the blackbody furnaces mentioned above, provide a close approximation and are subject to known laws. These sources are, therefore, utilised extensively as standard sources for the calibration and testing of radiometric instrumentation [2].

2.3.1. Planck's Law

Planck's law, derived by Max Planck in 1900, describes the spectral energy distribution of radiation emitted by a blackbody at a given temperature. It describes the spectral radiant emittance of a perfect blackbody as a function of its temperature and the wavelength of emitted radiation [2]. However, this assumes a perfect blackbody, as these perfect bodies do not exist the emissivity value of a target is used to apply Planck's law to the real-world;

$$B_{(\lambda,T)} = \frac{2hc^2}{\lambda^5}\frac{1}{e^{\frac{hc}{\lambda kT}}-1} \tag{2.3}$$

Where $B_{(\lambda,T)}$ is spectral radiance with respect to wavelength and temperature, h is the Planck constant, c is the speed of light in m/s, λ is the wavelength in m, k is the Boltzmann constant, and T is the blackbody temperature in Kelvin.

2.3.2. Radiant Power, Radiance, and Irradiance

Radiometric calibrations are essential to accurate quantitative optical data collection. By calibrating instruments against known standards it provides an opportunity to gain a better understanding of the true capabilities of the instrument and enables the accurate comparison of samples from different sources. For example, for datasets acquired from satellite and airborne sensors, radiometric calibrations allow for direct comparisons to be made between scenes imaged on different days and/or by different sensors. Without completing this calibration an accurate direct comparison would not be possible due to variations in a range of factors during data capture; from changes in atmospheric and illumination conditions, to differences within the dark currents of each sensor. By calibrating these instruments against a known reference it enables a wealth of data collection and comparison.

Radiometric calibrations focus on the optical radiation emitted from or reflected by a target, and that received by the imaging sensor. Radiant power (ϕ_e), also known as radiant flux, refers to the radiant energy reflected, emitted, transmitted, or received by an object per unit time passing through a given surface and can be defined as follows;

$$\Phi_e = \frac{\partial Q_e}{\partial t} \tag{2.4}$$

Where ∂ is the partial derivative; Q_e is the radiant energy reflected, emitted, transmitted or received; and t is time.

Radiance refers to the radiant power emitted, reflected, transmitted, or received by a given surface per unit solid angle, per unit area. Figure 2.3. provides an example of radiance where the radiance can be defined as the amount of radiant power emitted from location 'A' within the angular space defined by the cone with its vertex centred at 'A', representing the solid angle. The radiance (R) of an emitting area can be calculated using;

$$R = \frac{\Phi_e}{(A \times \Omega)} \tag{2.5}$$

Where ϕ_e is the radiant power emitted from the given area (A), and Ω is the solid angle. Radiance is typically used as a means to understand and describe sources e.g. the light emitted by a bulb or reflected by a target object. To gain a better understanding of detectors irradiance is generally used. Irradiance refers to the radiant power received by a surface per unit area and is measured in watts per square metre. Irradiance (E_e) is defined as;

$$E_e = \frac{\partial \Phi_e}{\partial A} \tag{2.6}$$

Where ∂ is the partial derivative, ϕ_e is the radiant power received, and A is the area. The total power detected by an optical detector is the integral of the irradiance from all directions over the area of the sensor. In Figure 2.3. if it is assumed that the total optical power passing through location 'B' is evenly distributed, the irradiance can be determined by dividing the radiant power on this surface by the area of 'B'.

Etendue is a property of light within an optical system that is used to characterise how stretched or 'spread out' the light is in area and angle, allowing the optical throughput of the instrument to be calculated, and, therefore, represents an important calculation within instrumental designs. For the instruments discussed later within this thesis the important calculation is the relationship between the field stop (the optical aperture that limits the FOV of the instrument), and the aperture stop (the aperture that limits the amount of light that can pass through an optical system). This calculation is shown in the following equation;

$$\frac{(A^2 \times B^2)}{L^2} \tag{2.7}$$

Where A is the aperture stop, B is the field stop, and L is the distance between the aperture and field stops. Calculating the optical throughput of a sensor is important as it improves our understanding of the instrument's capabilities and provides information on the effectiveness of the optical configuration. By better understanding these factors it provides a quantitative means of comparing different instruments.

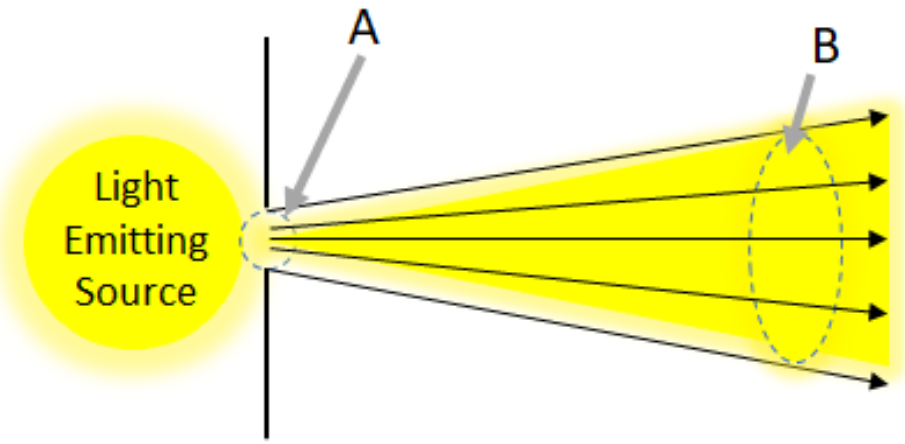

Figure 2.3 Schematic diagram demonstrating a basic radiance and irradiance example. Location A represents an area where radiant power is being emitted. Location B represents a surface where radiant power is received.

By completing a radiometric calibration for an instrument, it allows the radiant power represented by each pixel in an image scene to be calculated. This provides valuable information regarding the capabilities of a given instrument, allowing for targets obtained from varying sources to be compared effectively. Furthermore, when focusing on reflection-based imaging techniques, if the radiant power of both the target object and the emitting illumination source are both defined, the optical throughput, related to etendue, can be calculated allowing for the properties of the light rays within the optical system to be characterised.

A radiometric calibration of the optical power per unit area detected by an instrument can be performed by measuring the radiant power reflected by a standard reference target, such as a spectrally flat panel. This calibration is completed using a radiometer to determine the voltage received by the sensor. For spectral instruments, measurements of the illuminated reference target should be completed with and without the presence of a relevant band pass filter. The band pass filter location should be based at a wavelength that corresponds to a region of high signal within the spectral range of the instrument to avoid complications related to the noise associated with areas of low signal. Measuring the voltage with the filter in place allows for the calculation to be determined for a specific point within the spectrum, providing a more precise measurement, whereas the unfiltered measurement allows the data to be extrapolated to estimate a value over the wavelength range of the instrument. Once these voltages have been measured, Ohm's Law is used to determine the photocurrent;

$$I = \frac{V}{R} \tag{2.8}$$

Where *I* is the current in amps, *V* is the voltage in volts and *R* is the resistance of the conductor in units of Ohms.

To calculate the power; the photocurrent, responsivity of the photodetector and transmission factor must be known. The power is then calculated by dividing the photocurrent by the responsivity, before subtracting the transmission factor. The power per unit area is then defined by dividing the power by the extent of the measurement field on the mesurand, and then multiplying this value by the difference between the filtered and unfiltered measurements. If the size of the pixels present within the spectral imaging instrument are known, the power per unit area can be used to determine the power represented by each pixel.

2.3.3. Light Interactions

The light characterised by an optical system is dependent on the spectral range of the instrument, but also on how the light interacts with the target. The interactions of light with matter are complex and depend on the optical properties of the medium [12]. There are four main ways that light can interact with a target; reflection, transmission, absorption, and emission. For most targets a combination of these interactions is observed rather than one specific response. In spectroscopy and spectral sensing, we focus on the reflection and absorption of light across a target surface in order to obtain information about its spectral response.

Reflection is caused by the change in direction of the wave vector of a light wave by a surface [13]. It is a function of the distribution of the incident radiance, the reflective properties of the target surface, and the incident and viewing directions [12]. Three types of reflection are possible (Figure 2.4): specular reflection occurs when the incident light interacts with a flat surface resulting in a single angle of reflection producing a 'mirror-like' reflection; Retro-reflection, where a portion of the reflected light is directed back at its source, with minimal scattering. This type of reflection is created using specific retro-reflective sheeting which typically contains tiny glass beads that refract the incident light before it is reflected by a mirrored surface behind the beads; and diffuse reflection which occurs when the incident light contacts a rough surface, causing the incident ray to be scattered, producing multiple angles of reflection. Diffuse reflection can also result in Lambertian reflection which occurs when the incident light hits a perfectly diffusing surface. A Lambertian surface is similar to a Lambertian emitter; a Lambertian emitter is a source of radiation that has the same radiance when viewed from any angle [12]. Similarly, when light interacts with a Lambertian surface, multiple reflection angles are created but the luminance/radiance remains constant regardless of the angle of view. This is expressed in Lambert's cosine law which states that the intensity observed from an ideal diffusely reflecting surface is directly proportional to the cosine of the angle ϑ between the direction of the incident light and the surface normal [2];

$$I_\theta = I_0 \cos(\theta) \tag{2.9}$$

Where I_ϑ is the illuminance at an angle ϑ from the normal and I_0 is the illuminance in the direction of the normal. It should be noted that, similarly to perfect blackbodies, Lambertian surfaces are theoretical, however, targets such as Spectralon panels provide suitable approximations, producing highly diffuse reflection that can be utilised as a calibration target. With spectral sensing techniques we can quantify the volume of light reflected at each wavelength within the instrument's range to determine the chemical make-up of the target surface.

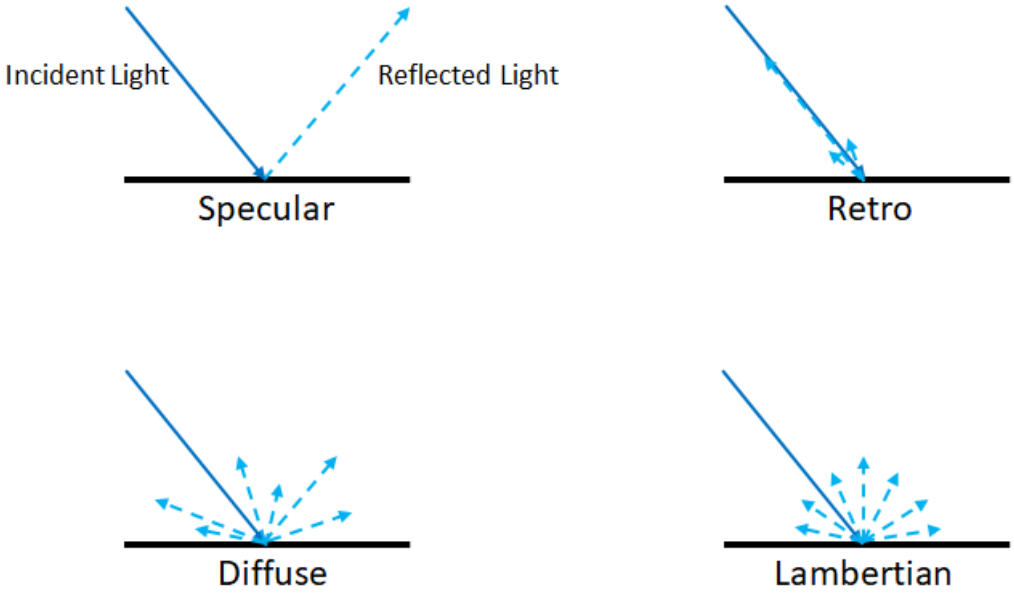

Figure 2.4 Reflection patterns. Note the differences in the number and angle of the reflection paths.

Light is absorbed by the target surface if the energy of the light is equal to or near the energy states of the surface material involved [13]. In spectroscopy absorbance is the measure of the quantity of light absorbed by the sample. Identifying key absorption features in a target scene's spectral response enables, for example, the detection and quantification of certain pigments present across a target, providing essential information on the status of the chosen target. This allows for potential issues to be identified prior to their identification by more traditional means, as such, reflectance and absorbance spectroscopy are used extensively across a wide range of application areas, from monitoring health and quality in fresh produce, to cancer detection in point-of-care analyses.

2.3.4. Optical Aberration

Aberrations are a property of optical systems that cause variations in the focus of light over a region of space. This results in distortions and blurring within output images, with the nature of the distortion depending on the type of aberration. For monochromatic light there are five types of aberration, these are; spherical aberration, coma, astigmatism, curvature of field, and distortion [3]. Additionally, there is chromatic aberration, which occurs when wavelengths are focused at different distances within an optical system [3]. In this section each of these aberration types will be discussed in turn to better understand their influence and how best to resolve these issues within optical systems.

2.3.4.1. Spherical Aberration

Spherical aberrations occur as a consequence of light interactions with the spherical surfaces present within an optical system, such as lenses or mirrors. They are not affected by the angle of imaging and can, therefore, affect both paraxial and off-axis targets [3]. These aberrations cause incident light rays to intersect the optical axis at varying distances from the lens. These intersections can cause positive aberrations, where rays intersect the optical axis at a location closer to the lens; and negative aberrations, where rays intersect at a location further from the lens. These aberrations result in spherical regions of defocusing, or blur, within the output image.

To address these affects a combination of concave and convex lenses can be used. These lenses will produce spherical aberrations of opposite signs and should, therefore, cancel each other out when combined. Furthermore, if the optical system cannot accommodate for the inclusion of multiple lens

components a plano-convex lens, with the convex face facing the incident rays, can help to reduce these aberrations in simpler configurations [3].

2.3.4.2. Coma

Coma is an off-axis aberration that is non-symmetrical around the optical axis and increases rapidly with aperture [2], [3]. This type of aberration causes off-axis targets to appear distorted due to the formation of comatic circles making the target object appear to have a tail, similar to that of a comet. Similar to spherical aberrations, coma may occur in both positive and negative quantities with negative coma occurring when rays incident upon the lens further away from the paraxial region focus closer to the axis than rays incident closer to the paraxial region, and positive coma when the opposite occurs. This results from a change in magnification with off-axis height. This can be better understood within the concept of principal planes. The principal planes of a lens (the hypothetical planes through which all refraction can be considered to happen) can only truly be considered planes within the paraxial region of the lens, therefore, rays incident upon the lens at greater distances from the paraxial region interact with a more curved surface, affecting the focal length of these particular rays. The focusing of a specific ray is, therefore, dependent on the extent of its off-axis incident angle.

Coma can be removed from an optical system by satisfying the Abbe Sine Condition [3];

$$nh \sin\theta + n'h' \sin\theta' = 0 \tag{2.10}$$

Where *h* and *h'* represent object and image size respectively, and angles ϑ and ϑ' are the angles of the rays in the optical media *n* and *n'* respectively. Coma results from a change in magnification with height as discussed above, therefore, to remove the coma aberrations within an optical system the magnification must be consistent everywhere. Using the Abbe Sine Condition this would mean that coma would be prevented when;

$$\frac{\sin\theta}{\sin\theta'} = constant \tag{2.11}$$

2.3.4.3. Astigmatism and Curvature of Field

When rays propagating in two perpendicular planes have different focus points, the form of aberration is known as astigmatism [2]. Astigmatism increases with the off-axis distance of the target and with the aperture size of the refracting surface. These aberrations result in blur occurring in output images at different distances due to the varying focal points of the rays. For example, if a cross is used as the target object, the vertical and horizontal lines would be in focus at two different distances [3]. Altering lens shape and spacing can help to minimise these aberrations by bringing the focal points back to a single standard location.

Curvature of field is similar to astigmatism except that it is symmetrical around the optical axis [2], [3]. Curvature of field causes targets to become impossible to bring into complete focus despite being located within the optical axis of the instrument. This results in circular regions of the target appearing in focus whilst other regions of the same target appear blurred. To correct for this, it can be beneficial to include an aperture stop to reduce and remove edge light rays, limiting the quantity of non-paraxial rays, however, this can also significantly limit the light collecting abilities of the system creating longer exposure and imaging requirements.

2.3.4.4. Distortion

Unlike the forms of aberration discussed above, which result in blurring within the output image, distortion simply causes scene information to be misplaced geometrically, resulting in a crisp image where the intended target is distorted in size and/or shape [3]. Figure 2.5., shows examples of image distortion for a grid of squares. Magnification that increases with distance will result in pincushion

distortion where the squares appear to bow inwards, whereas, magnification that decreases with distance will result in barrel distortion, causing the squares to appear to expand in a size. In both scenarios, as shown in Figure 2.5., the image quality remains sharp but the object shape is distorted. These aberrations can be corrected with alterations to the lens system e.g. the inclusion of an aperture stop positioned at the lens. It can also be corrected algorithmically, however, this results in significant additional processing time requirements.

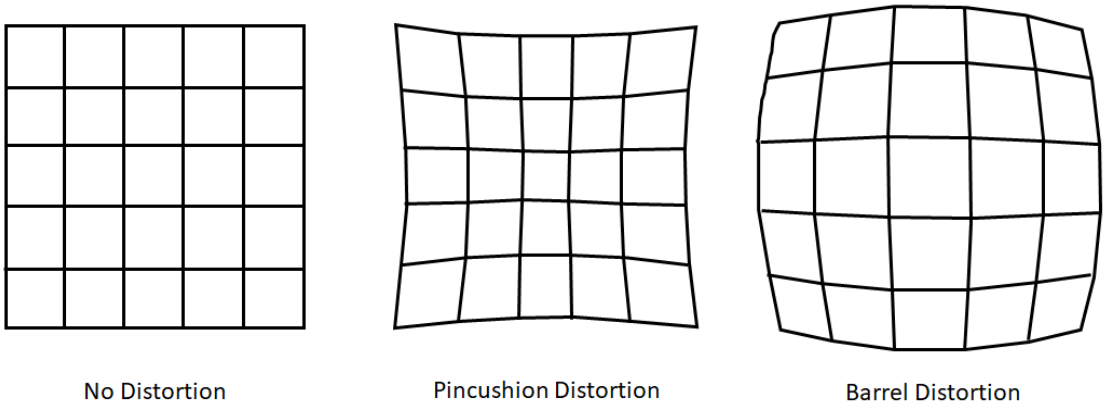

Figure 2.5 The different types of distortion possible within optical systems. Note the clarity of the image despite the geometric distortions.

2.3.4.5. Chromatic Aberration

Chromatic aberration differs from the monochromatic aberrations discussed above as it takes into account variations in a material's refractive index with wavelength [2], [3], and is simply a failure of a lens system to focus all wavelengths at the same focal point. There are two types of chromatic aberration; longitudinal, and lateral [3]. Longitudinal aberrations occur when images formed by different wavelengths are not coincident, creating aberrations throughout the output image. This results in blurring and the creation of rainbow-like edges in areas of contrast within a target scene. Lateral aberrations occur when different wavelengths are focused at different positions because the magnification of the lens also varies with wavelength. Lateral aberrations, therefore, do not occur within the centre of an image, instead increasing in intensity towards the edges of the image. Chromatic aberrations are typically corrected for in an optical system with the inclusion of an achromatic doublet, consisting of a convex and concave lens of different glass types, and dispersion, cemented together. This results in a compound lens that reduces the amount of chromatic aberration over a certain wavelength range, providing more accuracy to the optical system.

2.3.5. Ray Tracing

Ray tracing is a method of simulating the physical behaviour of light within an optical system and is an important step within the development of an instrument. Rays of light that contribute to the production of an image within an optical system usually do not exist perfectly along the optical axis and, therefore, their interaction with optical components cannot be accurately determined from assumptions related to paraxial rays. To ensure an optical system is capable of producing accurate images with minimal aberrations the interaction of light rays with the components of the optical system must be analysed with the aim of reducing the volume of rays that deviate substantially from the ideal path [3]. Ray tracing, therefore, entails the tracing of the geometry of individual rays through an optical system using the laws of reflection and refraction. Whilst these techniques used to be completed by hand requiring complex and highly accurate sketches of the optical system, many of

these calculations are now completed using specially designed computer software, such as Zemax. By completing ray trace models on an optical system it enables the user to determine the influence of aberrations on the current optical configuration. The computer software can easily calculate geometries for both meridional rays (those that pass through the optical axis), and non-paraxial rays (that do not pass through the optical axis). Non-paraxial rays are typically more complex to calculate due to the need for three-dimensional geometry within their calculations, however, the determination of a range of aberrations is reliant on the analysis of these non-paraxial rays. Ray tracing is, therefore, of substantial importance, particularly for more complex optical system design, as it enables the optimisation of component configurations prior to their assembly.

2.4. Principles of Hyperspectral Imaging

Hyperspectral imaging techniques utilise light interactions to inform and build three-dimensional datasets of a target object or scene, allowing the specific spectral response of each scene element to be quantified. It is a valuable analytical technique that has been implemented across a wide range of application areas and environments. Building on the abilities of point spectrometers and multispectral imagers, hyperspectral imaging enables the collection of contiguous spectral datasets for each pixel within a spatial image scene, providing a wealth of data that can be used to inform further investigation or analysis. Chapter 1 highlighted the significant uptake of hyperspectral imaging techniques across environmental monitoring applications. The following sections will discuss the principles of hyperspectral imaging focusing on the different types of hyperspectral sensors, data processing requirements and considerations, and technological developments before highlighting existing applications across environmental monitoring fields.

2.4.1. Types of Hyperspectral Sensor

There are a number of different approaches to hyperspectral imaging and, as such, a variety of sensor types are available (Figure 2.6.) [14]. Typically, sensors are characterised by the arrangement and/or the number of spectral bands involved in the instrumental architecture [14], [15], as well as the applied image capture method. Push broom sensors have been traditionally used for large airborne imaging applications and have recently been successfully miniaturised for use within UAV (unmanned aerial vehicle) systems [14], [16], [17]. This push broom measurement approach is favoured due to its high spatial and spectral resolution [18], however, this image acquisition method, whereby a line of spectral information per exposure is recorded [14], [19], can cause difficulties in post-processing [14]. Similarly, whiskbroom sensors, which image a single pixel or spatial location at a time [20], [21], using a rotating mirror to sweep a scan line perpendicular to the direction of the sensor platform's movement [20] - [22], are affected by the same issues [20]. Furthermore, whiskbroom sensors provide inherently slower frame rates than push broom units, resulting in lengthier data acquisition periods where all other things are equal [20], [23]. Another disadvantage is that the rotation of the optics can result in spatial distortions in the image outputs [24]. However, recent work reported by Uto et al. [22], has demonstrated the pioneering of low-cost whiskbroom image formation suitable for UAV deployment.

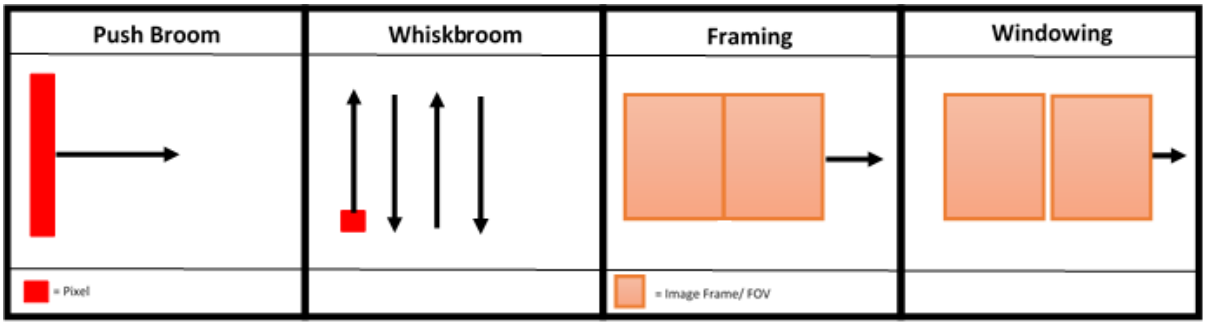

Figure 2.6. Image capturing techniques for each sensor type. Note the different methods of image formation; from the pixel-based capture of Push Broom and Whiskbroom scanners, to the two-dimensional comprehensive image capture of Framing and Windowing instruments. This highlights the potential issues related to image distortion resulting from the rotation of the optics in the pixel-based instruments, as mentioned above.

Alternatively, framing instruments (Figure 2.6.) can capture scenes through two-dimensional images with additional optics that focus on either an individual wavelength or wavelength bands using tuneable filters, such as framing band pass filters translated across the spectrum [24]. The design of such sensors is significantly simpler than those of push broom and whiskbroom sensors [20], [25], however, the use of spectral filtering substantially reduces the intensity of light captured at the sensor, limiting signal to noise [24]. Windowing/snapshot instruments also employ a two-dimensional Field of View (FOV) that moves across a scene in a continuous fashion [26]. However, instruments that utilise this image capture approach acquire a distinct exposure each time the FOV moves forward, with no integration between exposures [26].

The literature highlights that although there can be significant variation caused by slit width, lens focal length, and integration time [14], push broom sensors, at present, offer a better combination of spatial and spectral resolution. Push broom sensors are typically more stable than whiskbroom sensors due to the line-by-line image acquisition process, therefore, confining potential data misalignments to between lines rather than between individual pixels [18]. Furthermore, they often have a significantly greater spectral resolution, for example Jaud et al. [25], reports a spectral resolution of 1.85 nm for their push broom device. Framing and windowing/snapshot devices are often limited due to the filtering of spectral bands, resulting in spectral resolutions of > 5 nm being more common for these devices [14], [26]. High spatial resolution is also easier to achieve with current push broom devices as miniaturisation allows for them to be deployed on more manoeuvrable, light-weight devices, for example, a number of studies highlight successful image acquisitions with spatial resolutions of less than 10 cm [25], with Lucieer et al. [16], and Malenovský et al. [17], achieving a spatial resolution of 4 cm with UAV-based deployments. Framing and windowing/snapshot devices are currently limited due to their typically larger size, making push broom sensors significantly more compatible to light-weight, miniaturised sensing applications at present.

Although several of these sensor designs (Figure 2.7.) have been successfully miniaturised, making them suitable for light-weight aerial remote sensing, they do not currently contain any internal georeferencing data and, therefore, require the addition of external (e.g., GPS receiver) devices to record this information if it is required [14], [27]. Whilst this does not particularly effect traditional remote sensing and ground-based imaging methods, it can become problematic when designing effective UAV integrated payloads [14], [20]. Each of these sensor designs has its advantages, depending on the parameters of the proposed application, however, the push broom design has been the most popular, particularly within the field of light-weight UAV image acquisition [18]. Whilst these sensor implementations can involve distortions within the acquired data, they currently outperform full-frame image capturing approaches as the latter systems currently require a compromise between spatial coverage, spatial resolution and spectral resolution [14], [25]. However, as interest and demand within this area continues to grow [18], [28], significant advances in compact sensor designs, including the incorporation of linear variable filters, can be anticipated in the future.

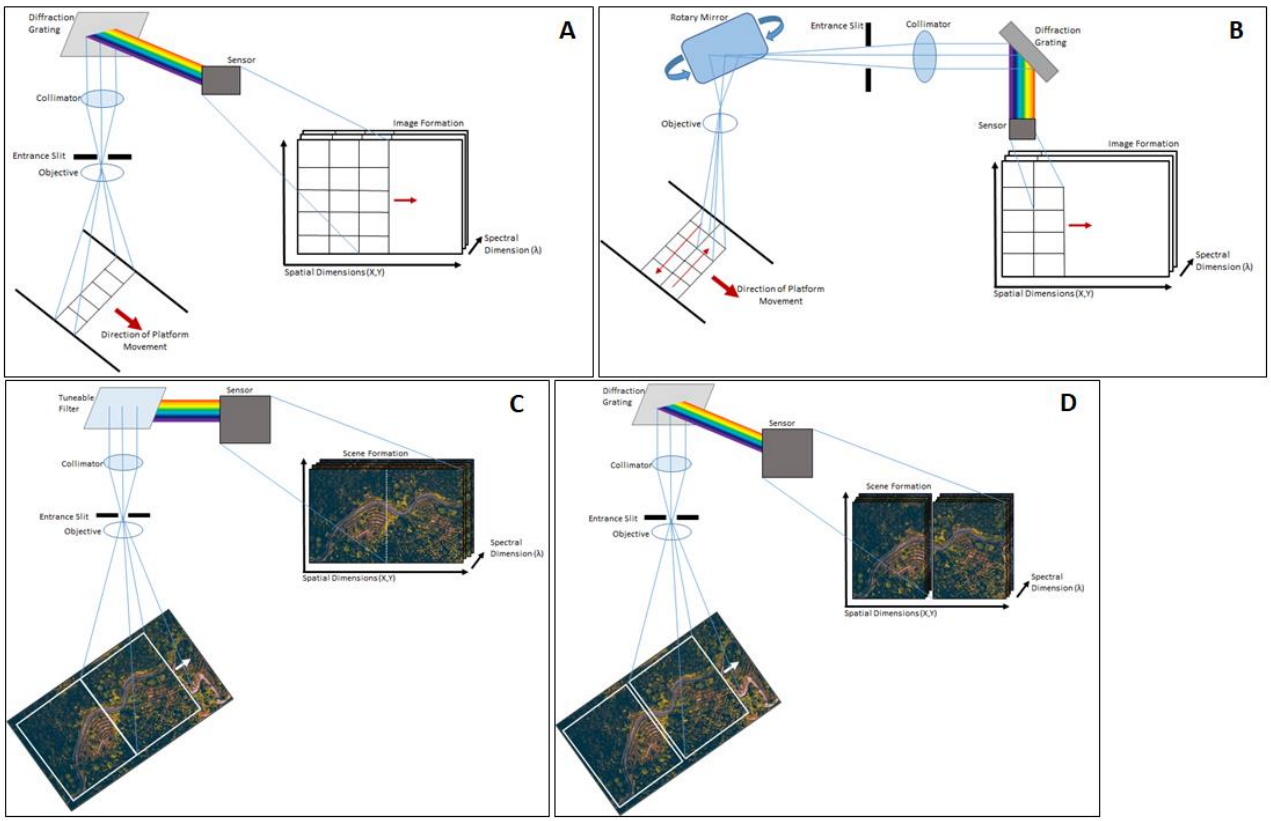

Figure 2.7. Example schematic designs for each sensor type. (a) Push Broom, (b) Whiskbroom, (c) Framing, (d) Windowing/Snapshot. Not to scale.

2.4.2. Hyperspectral Data Processing Requirements and Considerations

The calibration of hyperspectral instrumentation is important for the collection of accurate, high quality datasets. A raw dataset provides spectral information for the chosen spatial scene, however, in this format, these datasets are subject to a variety of distortions and biases that must be corrected for in order to obtain the true output data for the chosen scene. These distortions and biases are accounted for at varying stages e.g. during instrument calibration or output image post-processing.

2.4.2.1. Instrument Calibration

The importance of radiometric calibration has been discussed in Section 2.3., however, in order to produce accurate spectral datasets a hyperspectral instrument must also be spectrally calibrated prior to the capture of a target scene. This is achieved by uniformly illuminating the entrance slit of the spectrometer with a source that contains a distinct array of narrow band spectral lines across a range of wavelengths within the spectral capabilities of the instrument (Figure 2.8). In a perfect system, these spectral lines align linearly with the spatial coordinates of the sensor array, however, in reality, these lines are often subject to curvature caused by spatial-spectral distortions [29]. An example of these distortions is shown in Figure 2.9. A variety of illumination sources are commonly used for spectral calibration measurements. These include; monochromators, lasers, and gas lamps that emit at a number of specific spectral lines e.g. Mercury vapour is known to produce defined peaks at 436 nm and 546 nm. Another means of calibration is to precisely measure the characteristics of each component of the instrument individually, using this information to inform and build a model, however, this approach is generally avoided due to its complexity and impracticality [29].

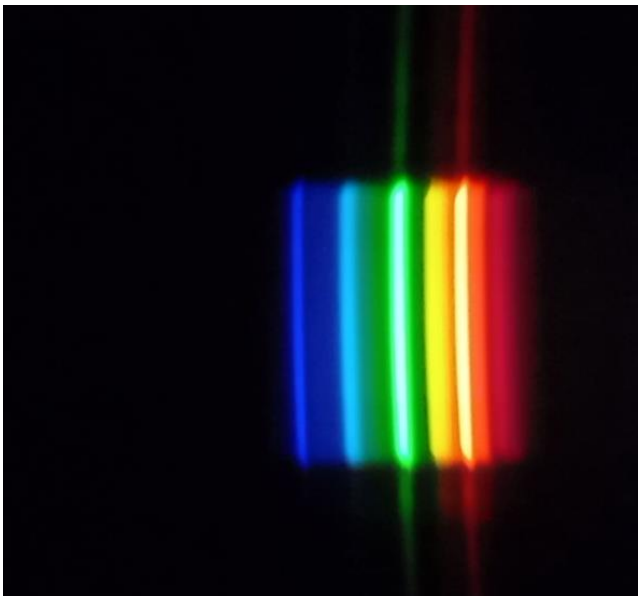

Figure 2.8 Example calibration frame of a gas lamp demonstrating distinct spectral lines combined with subtler spectral responses across the visible spectrum.

Figure 2.9. Distorted spectral lines. Note, the curve of the spectral peaks. This can create complications within the calibration process due to the shifting linear location of the spectral peaks.

2.4.2.2. Post-Processing Image Correction

Dark and light corrections are completed, typically after data capture, to remove sensor and illumination biases from the resulting datasets. These corrections are an important component of the data collection process as they allow for the true spectrum of the target object to be obtained, making accurate quantitative measurements possible. To correct for sensor bias caused by the dark current characteristics of the sensor array, a measurement should be obtained during the data collection period where all light is blocked from entering the set-up. This provides a 'dark image' that can be used to remove the sensor's input from the target's response (Equation 2.13). Additionally, to remove the illumination bias from the spectral response of a non-emitting target a light (or white) reference is completed. This is typically completed using a spectrally flat white calibration tile, that is illuminated in the same manner as the intended target. The spectral response acquired from this measurement can be used to remove the illumination bias from the scene (Equation 2.13). This measurement should also be completed at the time of data collection. This is especially important when working under natural lighting conditions due to the potential variations in illumination caused by variations in cloud cover and meteorological conditions more generally. The equation below provides an example of the removal of sensor and illumination biases from a given target,

$$\frac{S_{target}-S_{dark}}{S_{light}-S_{dark}} = \frac{R_{target}}{R_{light}} = R_{target} \tag{2.12}$$

Where *S* represents the signal measured during data capture and *R* represents the reflected response. The subscripts *target, dark,* and *light* refer to the target object, dark reference, and light reference respectively.

2.4.3. Technological Developments and Associated Complexities

Currently, hyperspectral imaging is generally performed by satellite or aircraft platforms [19], [25], [30], with recent advances in airborne and spaceborne technologies providing end users with rich spectral, spatial, and temporal information [31], [32]. As such, hyperspectral imaging has been well established in the remote sensing community, with large-scale uptake across many different domains [14], [33]. Furthermore, the recent development of CubeSat miniature satellites, such as HyperCube [34], shows significant potential for future development of light-weight, low-cost spaceborne image acquisition [35]–[37]. However, whilst these sensors enable the analysis of extensive areas of the Earth's surface, providing large-scale datasets with long time series [25], they are often constrained by factors outside the users' control, such as cloud coverage and spatial resolution [18], [25], [31]. Furthermore, manned aerial surveys operated on an on-demand basis can be rather expensive and

somewhat reliant on favourable meteorological conditions [38]. As a result, these drawbacks significantly limit the suitability of these measurement types for many smaller scale, local applications.

Jaud et al. [25], highlights this sizable gap between the small-scale, fine resolution outputs of field surveys and the comparatively coarse resolution provided by satellite and aerial sensors. However, the development of UAV platforms over the last decade has enabled the development of an intermediary protocol, in the form of UAV integrated hyperspectral sensing [19], [28], [38], [39]. These UAV-based platforms provide greater flexibility than traditional sensing methods, permitting the user to vary parameters such as survey size and flight altitude [25], [40], in a manner tailored to the proposed application. Additionally, due to their typically small size and low weight they can be easily, and readily, stored and deployed [39], [41]. A number of UAV integrated hyperspectral sensors have been tested in recent years within a variety of different fields; Habib et al. [19], present a low-cost UAV integrated hyperspectral scanner applied to the field of precision agriculture. Their multirotor system proved successful, providing detailed imagery of the survey area, however, difficulties arose during the georectification process, with the accurate generation of georeferenced products proving difficult to establish [19]. Similarly, Jaud et al. [25], experienced complications during the line-by-line georectification and referencing required of their push broom, multi-rotor UAV sensor acquisitions, with the push broom image formation process leading to a major source of complexity during the geometrical correction step [25].

2.4.3.1. Georectification Difficulties

Due to the light-weight nature of multi-rotor UAV systems they generate substantial high frequency vibrations and can perform faster trajectory changes than larger platforms, therefore, these systems require fast, accurate proprioceptive sensors to enable accurate logging of altitude and position [25], [42]. Mozgeris et al. [43], directly compared the results obtained from a UAV-based hyperspectral imaging camera and a similar sensor based within a manned, fixed wing, ultra-light aircraft in the context of precision agriculture monitoring at a site in Lithuania. They determined that the manned aircraft sensor outperformed the UAV-based device in terms of the quality of output data as a function of cost. A key factor in this was the higher relative accuracy of georeferencing in the case of the manned deployment, which the higher spatial resolution coverage of the UAV sensor was not sufficient to counteract [43]. Conversely, Freitas et al. [18], present a direct georectification method applied on their fixed wing UAV-based sensor, which substantially improved the accuracy of target georeferencing. Whilst they still experienced difficulties due to the nature of push broom image acquisition, the results obtained suggest that reliable acquisition of accurately georeferenced data using a UAV-based sensor is now possible. As such a variety of different georectification solutions, demonstrating varying levels of success, have been presented in the literature.

A significant challenge facing the collection of high quality, georeferenced hyperspectral datasets, particularly from UAV-based deployments, is a lack of fast processing workflows that are capable of retrieving geometrically accurate datasets [44]. Many existing solutions require the collection of multiple Ground Control Point (GCP) locations [45], [46], and/or the manual identification of scene features [42]. These approaches are limited in that they are typically computer- and time-intensive and can often have outputs with limited accuracies. Angel et al., [44], have designed a fully automated approach capable of producing accurate georectified hyperspectral datasets for UAV-based push broom scanners. Initial results show promise, however, further work is required to ensure their approach can be applied across different terrains and under a range of atmospheric conditions.

A number of studies have circumvented these georectification issues simply by implementing ground-based data acquisition protocols [47], however, the obtained images can still be affected by other

factors, such as, variable meteorological conditions [28]. Indeed, this issue can affect both ground-based and aerial hyperspectral imaging [23], [47]. Variations in illumination, in particular, during the study period can have a significant effect on the captured data, introducing apparent changes in captured spectra unrelated to changes in the scene surface covering [19], [23], [28], [47]. However, the effect of these variations can be minimised by recording trends in illumination in parallel with the image capture [28], which can be used to calibrate the hyperspectral image data acquired during these periods [18], [23], [27].

The demand for smaller and lighter hyperspectral imaging sensors continues to grow, with the application of UAV integrated sensors being one of the most rapidly developing areas of remote sensing technology [28], [40]. The desire to reduce the physical size of these sensor systems whilst maintaining the data quality available from larger units is an aspiration in both aerial and ground-based sensing configurations [40], [47]. With the advent of widely available 3D printing services [48], [49], and the continued development of sensors for both scientific and commercial purposes [38], the opportunities to pioneer units specifically tailored to desired application areas have never been greater. Whilst at present, push broom and whiskbroom sensors are subject to limitations in temporal resolution, associated with the georectification process, there are considerable ongoing improvements in accurate direct and indirect georectification methods [18], [25]. In general, the continued development of more compact, light-weight devices creates the opportunity for imaging surveys with high spatial and spectral resolutions, delivering added flexibility in the acquisition parameters [25], [38], [47].

2.5. Applications within Environmental Monitoring

As highlighted in the sections above there is considerable potential for, and progress towards, compact, field portable hyperspectral imaging sensors for a variety of environmental monitoring applications. With the additional benefits of integrating low-cost, high quality consumer market components, there is now a significant opportunity to make hyperspectral imaging more common within environmental monitoring. There has, therefore, been a wide variety of devices developed for sensing applications across these conditions. Due to the significant variations between these settings the devices required can differ substantially in terms of size, weight, and robustness, to name a few factors. This section will discuss developments across these contrasting environments, concentrating on some key examples, to illustrate the current state-of-the art in the field. Within this section the term “low-cost” is used to refer to hyperspectral devices assembled, often ‘in house’, from mass produced components allowing for the overall build costs to be significantly lower than that of commercial, scientific grade instruments.

2.5.1. UAV-Based Applications

2.5.1.1. Agricultural and Natural Vegetation Monitoring

As discussed above, the development of light-weight, and low-cost, UAV compatible sensors is a rapidly expanding area of research resulting in significant developments across a wide range of environmental monitoring applications. Whilst there are potential issues relating to the georectification process [19], [25], [50], the benefits related to improvements in spatial resolution and reduced fieldwork costs are substantial. The monitoring of vegetation across both natural and agricultural environments is a particular area of environmental monitoring that has benefitted from the advances in miniaturisation and cost reduction of hyperspectral technologies [51], [52], allowing for precise, in-depth monitoring and data collection to be accomplished even in the most inaccessible locations. The light-weight sensors that have been developed to date show significant potential in their application for close-range environmental monitoring [51], with the introduction of devices for

monitoring vegetation health receiving particular attention [52]–[55]. The continued monitoring of these environments with hyperspectral technologies is of considerable importance. Due to the spectral resolution of these devices it is possible to observe areas of vegetation stress, such as water stress or potential pest outbreaks, before they become visible to the naked eye. This is done through the examination of pigments, such as Chlorophyll, that will vary in quantity depending on the health of the vegetation, subsequently effecting its spectral response. In the initial stages of vegetation stress these changes can be subtle and, therefore, best recognised with hyperspectral imaging. This, in turn, allows for any potential issues to be resolved or minimised before significant damage can be done.

Traditional monitoring methods for both agricultural and natural vegetation typically require time consuming direct measurements or the use of spaceborne sensors [56], [57], with limitations in spatial resolution in respect of the latter [58], [59]. The introduction of UAV-based hyperspectral sensors creates the opportunity to acquire accurate, close-range data that do not require the complex processing typical of satellite and high-altitude airborne systems. Indeed, these UAV deployments aim to deliver data in an intermediary format, which provides both the satellite-based benefits of spatial coverage as well as the spatial resolution afforded from ground-based deployments [60]–[62]. In particular, Garzonio et al. [60] present a multi-rotor UAV equipped with a cost-effective hyperspectral sensor capable of detecting wavelengths within the visible and NIR (350–1000 nm) for a variety of vegetation monitoring applications. Due to the multi-rotor design, the device presented was capable of both transect and fixed target measurements, allowing it to be utilised for a variety of scenarios. Furthermore, it provided a systematic and rapid method of high quality data collection, suitable for relatively inaccessible locations, such as dense vegetation forests and forest canopies, allowing large, high-resolution datasets to be collected with relative ease [60]. However, despite overcoming issues related to in-flight mechanical vibration of the sensor, the spectral resolution and signal to noise ratio of the device were not optimal to capture all of the desired measurements, with particular problems related to the capture of sun-induced fluorescence data [60].

Similarly, Näsi et al. [51] deployed such technology for monitoring insect damage across urban forests. Their low-cost sensor enabled analysis at an individual tree level, providing a new level of specificity in forest health management practices [51], [54]. Whilst such detailed spatial resolution has been achieved by a few studies in the past, such as Minařík and Langhammer [63], and Dash et al. [64], they pertain, solely, to multispectral approaches. This hyperspectral unit [51] performed well, however, difficulties were encountered related to temporal illumination changes during the data acquisition [51]. As highlighted above, this is a potential issue that is generic to hyperspectral imaging from most airborne, and ground-based, devices [18], [28], and is, therefore, not a result of the low-cost of this device, but simply a factor that requires attention during extended data acquisitions. A method that provides the simultaneous monitoring of illumination change and data acquisition, and/or reference panel measurements would help to minimise these issues in future work [28], [65]. Despite these minor setbacks, the development of these new, easy to use technologies could have significant benefits for monitoring of both urban and rural forest health, with these low-cost units enabling far wider sensor proliferation than possible hitherto, with the more expensive previously applied instrumentation. This in turn could lead to significant benefits in terms of avoidance of future pest outbreaks and the potential resulting forest losses [51], [66].

A number of other studies have utilised similar UAV-based techniques for the monitoring of agricultural vegetation [67], [68], and soil quality [69], [70], producing accurate, high spatial resolution results, further emphasising the wide ranging usability of these designs. However, there remain limitations related to the weight and power supply of these devices, with heavier payloads having a negative effect on the potential duration of aerial surveys [60]. Whilst this is limiting the practical

utilisation of these devices at present, as technologies continue to be miniaturised and UAVs themselves advance, survey flight times will become proportionately longer in the future [40].

2.5.1.2. Extreme Environment Monitoring

A particular benefit of the continued development of these devices is that they allow non-destructive data acquisition, which is of considerable importance for highly sensitive and/or protected environments, which are often a key focus of environmental monitoring research and operations. Moreover, they also enable the acquisition of high spatial resolution data from locations where ground-based field surveys would prove impractical or hazardous. Key examples here include glacial and ice sheet regions, which have been host to considerable UAV-based monitoring, for example Crocker et al. [71], Hugenholtz et al. [72], Rippin et al. [73], and Ryan et al. [74]. However, work in this domain to date has been largely restricted to multispectral and/or photogrammetry-based data acquisitions, with hyperspectral monitoring being mostly confined to spaceborne observations [75]. The addition of field portable hyperspectral sensing to glacial settings will provide a significant improvement to current datasets, such as the identification of supraglacial debris composition in otherwise difficult to access locations [76]. Application of UAV-based hyperspectral image capture in the cryosphere is likely to be a highly promising future area of research.

Furthermore, low-cost, field portable hyperspectral technologies would also be of substantial benefit to a range of more temperate environments as application areas within these regions are also often subject to limited accessibility and/or represent fragile ecosystems and habitats, making them complex data collection targets. The monitoring of peatland habitats is of significant importance due to their prominence in climate warming mitigation strategies [77]–[79]**.** At present much of the monitoring within these settings is conducted through invasive ground surveys that require the collection of a range of samples or through the collection of aerial datasets with comparatively poor spatial resolution. Due to the importance and vulnerability of many peatland habitats, improvements to current data collection techniques are vital.

Additionally, less easily accessed locations such as cave systems contain considerable potential for in-situ hyperspectral monitoring applications, however, due to the challenges of accessibility and the subsequent limitation on the weight and size of instrumentation, few of these environments have been analysed to their full potential [80]–[82]. The development of light weight, portable hyperspectral imagers for these settings, therefore, provides a gateway to a wealth of knowledge hitherto undiscovered.

2.5.1.3. Pollution and Particulate Monitoring

Inland water quality and pollution monitoring with hyperspectral sensors, has only recently involved a move away from purely spaceborne imaging methods [83], [84]. This change has been largely driven by the limitations of satellite-based remote sensing as the spatial resolution provided by most such sensors is somewhat limited, without substantial pixel mixing [83]–[85]. Hyperspectral sensors used to monitor these environments provide high-resolution optical data that allows for the simultaneous detection and monitoring of air and water quality. This provides an extensive and accurate means of pinpointing potential pollution outbreaks and/or monitoring the quality of freshwater sources across relatively large areas. Although the majority of recently developed sensors within these fields remain aircraft based [83], [86]–[89], with the advantage of coverage of larger survey areas than typically possible with UAVs, a number of pioneering optical sensors for pollution and particulate monitoring are beginning to emerge. These new devices are providing significant improvements to current monitoring techniques with the introduction of UAV-based [90], [91], and lower cost portable [92], approaches. The promising success rates of these new devices are providing significant improvements

to our understanding of particulate pollutants [93], whilst also highlighting the substantial scope for further development and integration of UAV-based hyperspectral sensor systems to this field.

2.5.2. Hand-Held and Ground-Based Device Applications

Whilst the majority of hyperspectral sensing measurements have been achieved from airborne platforms, there have also been significant developments in hand-held and ground-based hyperspectral sensing in recent years [58], [59]. These devices are typically relatively light-weight and field portable, (Figure 2.10.) making them of significant benefit to a variety of small-scale fieldwork-based studies. However, as this hardware is not subjected to the stringent payload requirements of UAV compatible devices, there are relaxed tolerances with regards to weight, bulk, and power supply. A variety of miniaturised hand-held sensors have been developed for several applications, with a degree of device commercialisation implicit in this activity [94], [95]. In particular, Shan et al. [96] have developed a field portable hyperspectral imager capable of detecting micro-plastic contamination in soils for particle sizes between 0.5–5 mm. Whilst previous research has already successfully detected micro-plastic contamination using hyperspectral imaging [97], that study focused on micro-plastic detection within sea water filtrates, which required the manual separation of micro-plastics from the substrate prior to image acquisition due to difficulties related to plastic identification through water [96]. In contrast, the device developed by Shan et al. [96] enables in-situ measurements with minimal disruption to the study area. Given the increasing importance of this area, this technology is likely to be of ever-increasing utility here in the future.

Furthermore, Chennu et al. [98] discuss the development of a diver-operated underwater device for the monitoring of shallow marine ecosystems, such as coral reefs. This device is the first of its kind and represents a significant, cost-effective improvement in hyperspectral data acquisition for these environments, avoiding the effects of complex optical paths through the atmosphere and the water column [98], associated with observations taken above the water surface. Whilst the spatial resolution of this sensor was lower than that of comparable digital camera imagers, it could sufficiently identify the spectral reflectance features of corals at the organism level. The user friendly nature of this device allowed it to be operated with no prerequisite skills, however, its present design is too large for integration with unmanned platforms, highlighting a significant avenue for future research.

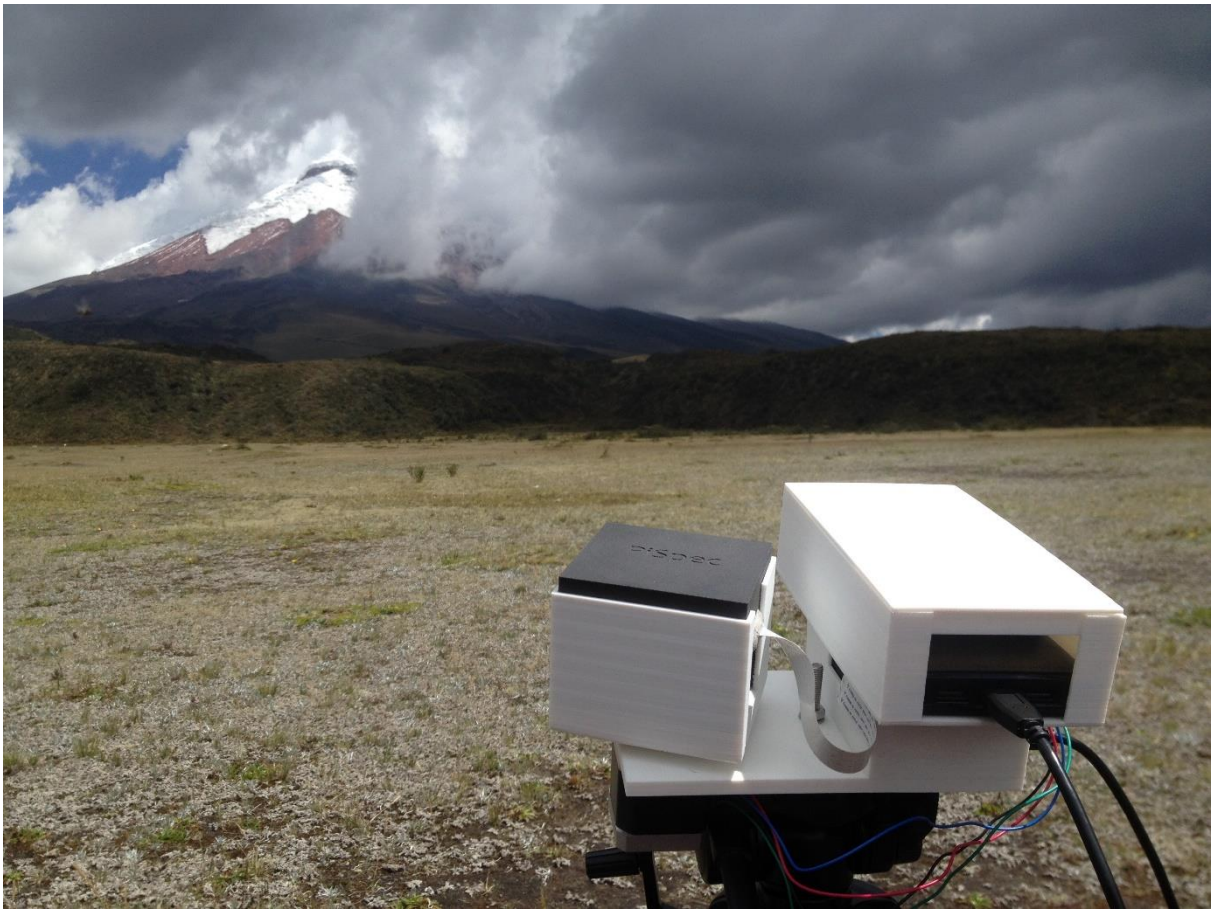

Figure 2.10 Compact UV hyperspectral imager measuring Sulphur Dioxide release from Cotopaxi volcano, Ecuador. Image provided by Andrew McGonigle (unpublished).

The examples above highlight the versatility of these devices, with miniaturised hyperspectral sensors replacing conventional non-imaging spectroscopy in a number of application areas [51], [58]. Furthermore, this proliferation appears set to continue as the speed of image capture, and the processing power of these units, increase year on year, just as the unit costs are reduced on an annual basis [58]. However, the development of more robust low-cost, field portable sensors for deployment in more extreme settings remains somewhat limited. The development of future low-cost hyperspectral sensors for these environments would build on the implementation of low-cost spectral technologies in hostile environments [8], [49], [99], [100], which have been based in configurations suitable for short-term deployments. Indeed, Wilkes et al. [99] estimate that more sustained deployments would require significant improvements to the outer casings of the device for ruggedisation and weatherproofing and robust product testing. This is a difficult hurdle to overcome due to the highly dynamic and often volatile nature of these environments, making year-round field-based monitoring challenging, even with state-of-the-art designs [75], [101]. Future work could, therefore, involve improvement of robust low-cost hyperspectral imagers to allow them to successfully compete with their scientific grade equivalents for prolonged data collection in these more extreme environments. In this respect, UAV-based units have the advantage that deployments are by nature discrete and time limited, rather than continuous, as discussed above.

2.6. Discussion

The development of these devices, and their application to a panoply of environmental monitoring areas, represent a series of significant technical and scientific advances. These units provide accurate,

high-resolution datasets, which help to bridge the gap between sparse and discontinuous field observations and continuous but coarse resolution spaceborne technologies [51], [60], [75], as well as enabling real-time analysis and decision making in environmental monitoring contexts [59], making them a beneficial addition to existing field monitoring techniques. Furthermore, miniaturised, low-cost systems can be operated on a local scale by small organisations and/or companies, considerably reducing the time required to organise specific remote sensing campaigns [51], relative to manned airborne surveys, reducing the need for expensive and time consuming direct measurement methods and enabling affordable and rapid environmental monitoring [51]. This is particularly advantageous in less well-resourced countries, where there are acute needs in terms of crop monitoring, for example. However, there remain a number of limitations on these devices at present [50]. For UAV-based applications, these limitations are largely related to the currently rather large weight, bulk, and power supply requirements of the deployed sensors, highlighting the need for future miniaturisation in such devices [60]. Although this hurdle is beginning to be overcome [53], often with the application of off-the-shelf consumer electronics components [58], [62], there still typically remains a trade-off between sensor size and data quality in these next generation units [50], [95], [96]. Similar limitations also affect ground-based and hand-held devices, although in these contexts the restrictions are not as profound. The foremost challenge faced by the majority of these devices is their successful deployment for long-term data collection. However, with potential future developments in ruggedisation of the hardware, which will allow such units to become competitive with commercial scientific grade devices for long-term field deployments, the application of ground-based hyperspectral imaging appears set to proliferate rapidly in the coming years (Figure 2.11.).

With the technological move towards more compact, miniaturised devices for optical sensing [102], [103], the implementation of low-cost consumer electronics in environmental monitoring is on the rise [102], [103]. The application of smartphone-based spectroscopy has been of particular interest for a variety of disciplines [40], [49], [104], and is a technological step towards the realisation of smartphone-based hyperspectral imaging. Compared to basic mobile devices, smartphones are equipped with a number of features that expedite sensing applications [102], enabling performance of advanced scientific measurements [105], [106]. This is particularly driven by the low-cost of these units, relative to commercial scientific grade cameras [103], [107]–[109], resulting in these units being developed into a variety of lab-in-a-phone technologies [49], [99], [109], [110]. Initial developments in this field have seen the creation of devices that work within the set-up of an existing smartphone, with considerable potential for future device development. However, current work has faced issues in connection with the unit operating systems, wherein raw data files (required for quantitative sensing applications) can be difficult to access and/or are effected by auto-scaling, e.g., Smith et al. [111], and the presence of Bayer filters within the majority of smartphone camera sensor designs, limiting most smartphone sensing to the visible portion of the electromagnetic spectrum within the three defined spectral bands corresponding to the cameras RGB pixels [100]. However, as smartphone-based spectrometers improve in performance, producing results similar to those of commercial scientific devices [49], the “compromise” in using these cheaper units, is becoming less of a relative downside. An in-depth review of these initial developments in smartphone spectroscopy can be found in McGonigle et al. [100].

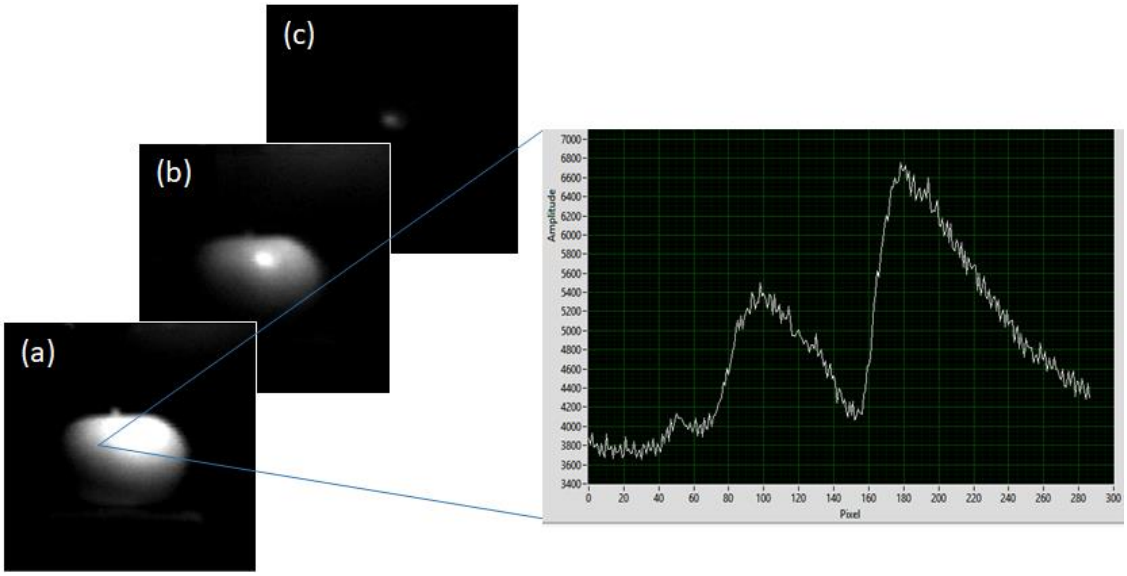

Figure 2.11 Example dataset captured using a low-cost hyperspectral device; 128 × 128 hyperspectral image displaying spectral reflectance from 340–850 nm of a green apple and tungsten filament lamp. Image tiles display reflectance peaks across the Red (a), Green (b), and Blue (c) portions of the electromagnetic spectrum. Note the corresponding peaks in reflectance captured in the spectral response graph.

As smartphone spectroscopy continues to develop, there is now the beginning of applying these units for hyperspectral imaging. In particular, Wilcox et al. [40], present an ultra-compact hyperspectral imaging system, for use within a UAV set-up, that has been developed to incorporate smartphone technologies. Similarly, Rissaren et al. [112], and Näsilä et al. [113], report initial developments in smartphone compatible hyperspectral imaging. Critically, this demonstrates that the ever-increasing processor performance from state-of-the-art smartphone handsets is sufficient to manage the significantly larger data volumes associated with hyperspectral imaging in contrast to mere spectral data capture [14], [40]. Just as smartphone spectroscopy has now been proven in a number of application areas [104], [109], [111], allowing for increased data collection at costs up to an order of magnitude lower than from conventional devices [99], it is likely that hyperspectral imaging with smartphones will be increasingly applied in the coming years.

In considering field portable hyperspectral imaging instrumentation for the majority of environmental monitoring settings, three design considerations are particularly pertinent:

• Compact light-weight design—Allowing for easy portability to a variety of field sites of varying accessibility. This criterion has particular benefits in relation to set-up times, enabling for rapid deployment of technical devices as well as significantly reducing the personnel requirements of field visits. As discussed above, this design feature is also of significant importance for sensors designed for UAV integration.

• Low-cost—Whilst this is not an essential requirement for successful environmental monitoring using field-based hyperspectral imaging, the production of low-cost sensors will increase the accessibility of this measurement modality, beyond the relatively limited field deployments achieved hitherto with the rather expensive previously available instrumentation. This is particularly the case for smartphone-based platforms, given the ubiquity of these units, and their suitability for implementation as nodes within internet of things type architectures.

• Flexibility—In order to achieve the best results, deployed devices need to be easily configurable by researchers, allowing for adaptations to be made relating to the proposed device application. This

criterion is most easily met by devices assembled ‘in house’ as it allows researchers to develop and assemble components in the best arrangement for the proposed application, resulting in a device specifically designed for its task. This is typically more favourable than generic, commercial devices, which can be rather difficult to align to specific applications. Furthermore, a device developed ‘in house’ can also provide significant reductions in set-up times as the researchers will generally be familiar with the device design.

Indeed, given the above it is evident that more and more research groups are opting to develop their own devices instead of relying on commercially available more expensive equipment, pointing to the proliferation and democratisation of hyperspectral imaging across the environmental sciences. Although, at present, many of these technologies are restricted by the current limitations of miniaturisation, and the associated trade-offs that miniaturisation can bring in terms of the sensor performance, initial results from smartphone-based hyperspectral imaging suggest that significant improvements in cost-effective, high spatial resolution data acquisition can be expected in the near future. This increase in performance, coupled to further reductions in instrumental cost, are likely to lead to increased utility and proliferation of these units in the coming decades, therefore.

However, an important additional consideration are the potential costs of required components external to the sensor design. This is of particular importance for sensors designed with the low-cost criterion in mind as the savings made during sensor assembly can quickly be lost through other device requirements. For example, when considering UAV integrated hyperspectral sensors, it is imperative that low-cost designs also adhere to the compact light-weight criterion in order to prevent the incursion of extensive costs related to the acquisition of UAVs with higher payload weight limits. As failure to consider this factor can lead to significant additional build costs, it is, therefore, of considerable importance to understand the payload specifications and limitations of the proposed UAV system in tandem with implementing the sensor design and development process. A number of articles discuss the variations, and subsequent categorisation, of different UAV systems, highlighting the, often substantial, differences in terms of payload weight, fuel requirements, and survey length [61], [114]–[116]. In general, multi-rotor UAVs are more suited to operation within more confined/inaccessible field sites due to their ability to take off/land vertically, whereas fixed wing UAVs are typically suited to longer endurance applications and provide more stable data collection [113], however, the final decision as to which design of UAV is selected is established by the specific parameters of the proposed application and, therefore, varies substantially between projects. Nevertheless, these characteristics are of considerable importance to the successful deployment of a UAV integrated sensor and can significantly impact the overall cost to deliver the measurement. Furthermore, costs and payload weights can be minimised further with the thorough selection of required ancillary sensors, such as RGB cameras and GPS units, e.g., both Näsi et al. [54], and Honkavaara et al. [67], reduced the overall costs of their set-ups with the inclusion of additional small consumer cameras instead of more expensive top-of-the-range models.

It is clear that in order to design a successful low-cost compact hyperspectral imaging instrument a complex list of design variables must be considered and potentially juggled to enable best delivery against the monitoring objectives. Within this there are two key exciting new frontiers, which these low-cost units now expedite: firstly, their potential for deployment and monitoring in less well-resourced countries and research areas, allowing for valuable research data to be acquired without the associated costs. Secondly there is the potential for future, long-term deployments in more extreme environments, for example with applicability in pioneering cost-effective early warning/monitoring systems for more volatile settings. Although the effectiveness of these units is limited by currently available technologies, the increasing interest and development in this sector looks

set to produce vast improvements to low-cost and miniaturised hyperspectral data collection, and thus provides the opportunity to improve datasets across a wealth of environmental monitoring domains.

2.7. Chapter Summary

This chapter has provided an overview of pertinent theory and an in-depth review of current miniaturised and low-cost field deployable hyperspectral technologies and their subsequent integration into the environmental monitoring field. Whilst the miniaturisation and deployment of these devices is ongoing, it is evident that this is a burgeoning area of research with the potential to revolutionise environmental monitoring in a wide variety of fields. At present, these devices largely complement existing monitoring techniques, however, as technologies continue to improve, it is likely that they will be increasingly applied in stand-alone monitoring capacities. As the literature highlights, there is a clear need to further expand the applications for these devices, in particular allowing them to be successfully utilised even in more extreme and challenging environments, as well as further capitalising on the reduced cost of consumer available technology in this domain. With the latest low-cost devices now producing scientific grade results, it appears as though hyperspectral imaging with smartphones in particular is now set to become a promising new frontier in empirical environmental science, significantly broadening the reach of hyperspectral image capture. This chapter has highlighted the potential for what could become a steep rising curve of community uptake, broadening applicability far beyond those application domains covered to date. The coming chapters will discuss the design and testing of a variety of new low-cost, miniaturised hyperspectral imagers that are capable of robust, scientific grade data capture and, as such, help to reduce the current gap within the literature, providing a means of enriching our existing knowledge of a wide range of environmental settings. Please note, the terms “portable” and semi-portable” are used throughout this work to describe the various instruments discussed within this thesis. The term “semi-portable” is used to describe currently laboratory-based instrumentation with the aim of highlighting their increased manoeuvrability over traditional laboratory-based hyperspectral imagers which are typically large, static and immovable once established. In comparison, the semi-portable instrumentation discussed within this thesis are designed to be smaller and capable of adaptation/manoeuvrability to increase their potential applications. Additionally, these instruments have the potential to be converted to fully portable instruments in future. The term “portable” is used to describe instrumentation that can be used in a broad range of laboratory and field-based locations and can be easily operated and transported by a single individual.

2.8. References

[1] M. B. Stuart, A. J. S. McGonigle, and J. R. Willmott, “Hyperspectral imaging in environmental monitoring: A review of recent developments and technological advances in compact field deployable systems,” *Sensors (Switzerland)*, vol. 19, no. 14, 2019.

[2] W. J. Smith, *Modern Optical Engineering: The Design of Optical Systems*, 4th ed. McGraw-Hill Education, 2008.

[3] F. Pedrotti and L. Pedrotti, *Introduction to optics*, Second Edi. Englewood Cliffs, NJ: Prentice-Hall Inc., 1993.

[4] A. El Gamal and H. Eltoukhy, “CMOS image sensors,” *IEEE Circuits Devices Mag.*, vol. 21, no. 3, pp. 6–20, 2005.

[5] J. E. Farrell, F. Xiao, P. B. Catrysse, and B. A. Wandell, “A simulation tool for evaluating digital camera image quality,” *Image Qual. Syst. Perform.*, vol. 5294, no. December 2003, pp. 124–131, 2003.

[6] L. C. P. Gouveia and B. Choubey, “Advances on CMOS image sensors,” *Sens. Rev.*, vol. 36, no. 3, pp. 231–239, 2016.

[7] K. Kurita *et al.*, “Proximity Gettering Design of Hydrocarbon – Molecular – Ion – Implanted Silicon Wafers Using Dark Current Spectroscopy for CMOS,” vol. 19, p. 2073, 2019.

[8] T. C. Wilkes *et al.*, “Ultraviolet imaging with low cost smartphone sensors: Development and application of a raspberry pi-based UV camera,” *Sensors (Switzerland)*, vol. 16, no. 10, 2016.

[9] G. E. Stillman, “Optoelectronics,” in *Reference Data for Engineers*, 9th Editio., W. M. Middleton and M. E. Van Valkenburg, Eds. 2002, pp. 21-1-21–31.

[10] W. L. Wolfe, *Introduction to Radiometry*. SPIE Press, 1998.

[11] B. G. Grant, *Field Guide to Radiometry*. Bellingham, Washington: SPIE Press, 2011.

[12] B. C. Johnson, H. Yoon, J. P. Rice, and A. C. Parr, *Principles of optical radiometry and measurement uncertainty*, vol. 47, no. December 2014. 2014.

[13] D. W. Ball, *The Basics of Spectroscopy*. SPIE Press, 2001.

[14] H. Aasen, E. Honkavaara, A. Lucieer, and P. J. Zarco-Tejada, “Quantitative remote sensing at ultra-high resolution with UAV spectroscopy: A review of sensor technology, measurement procedures, and data correctionworkflows,” *Remote Sens.*, vol. 10, no. 7, pp. 1–42, 2018.

[15] A. F. H. Goetz, “Three decades of hyperspectral remote sensing of the Earth: A personal view,” *Remote Sens. Environ.*, vol. 113, no. SUPPL. 1, pp. S5–S16, 2009.

[16] A. Lucieer, Z. Malenovky, T. Veness, and L. Wallace, “HyperUAS—Imaging Spectroscopy from a MultirotorUnmanned Aircraft System,” *J. F. Robot.*, vol. 33, no. 1, pp. 1–17, 2014.

[17] Z. Malenovský, A. Lucieer, D. H. King, J. D. Turnbull, and S. A. Robinson, “Unmanned aircraft system advances health mapping of fragile polar vegetation,” *Methods Ecol. Evol.*, vol. 8, no. 12, pp. 1842–1857, 2017.

[18] S. Freitas, H. Silva, J. Almeida, and E. Silva, “Hyperspectral Imaging for Real-Time Unmanned Aerial Vehicle Maritime Target Detection,” *J. Intell. Robot. Syst. Theory Appl.*, vol. 90, no. 3–4, pp. 551–570, 2018.

[19] A. Habib, T. Zhou, A. Masjedi, Z. Zhang, J. Evan Flatt, and M. Crawford, “Boresight Calibration of GNSS/INS-Assisted Push-Broom Hyperspectral Scanners on UAV Platforms,” *IEEE J. Sel. Top. Appl. Earth Obs. Remote Sens.*, vol. 11, no. 5, pp. 1734–1749, 2018.

[20] J. E. Fowler, “COMPRESSIVE PUSHBROOM AND WHISKBROOM SENSING FOR HYPERSPECTRAL REMOTE-SENSING IMAGING,” *IEEE*, pp. 684–688, 2014.

[21] T. Uto, K.; Seki, H.; Saito, G.; Kosugi, Y.; Komatsu, “Development of a Low-Cost Hyperspectral Whiskbroom Imager Using an Optical Fiber Bundle, a Swing Mirror, and Compact Spectrometers,” *IEEE J. Sel. Top. Appl. Earth Obs. Remote Sens.*, vol. 9, pp. 3909–3925, 2016.

[22] J. P. Kerekes and J. . Schott, “Hyperspectral imaging systems.,” in *Hyperspectral Data Exploitation: Theory and Applications*, 2007, pp. 19–46.

[23] K. Uto, H. Seki, G. Saito, and Y. Kosugi, “Development of lightweight hyperspectral imaging system for UAV observation,” *IEEE*, 2014.

[24] R. M. Willett, M. F. Duarte, M. A. Davenport, and R. G. Baraniuk, “Sparsity and structure in hyperspectral imaging : Sensing, reconstruction, and target detection,” *IEEE Signal Process. Mag.*, vol. 31, no. 1, pp. 116–126, 2014.

[25] M. Jaud *et al.*, “Direct georeferencing of a pushbroom, lightweight hyperspectral system for mini-UAV applications,” *Remote Sens.*, vol. 10, no. 2, pp. 1–15, 2018.

[26] G. D. Boreman, “Classification of imaging spectrometers for remote sensing applications,” *Opt. Eng.*, vol. 44, no. 1, p. 013602, 2005.

[27] M. J. Khan *et al.*, “Modern Trends in Hyperspectral Image Analysis: A Review,” vol. 6, 2018.

[28] E. Honkavaara *et al.*, “Processing and assessment of spectrometric, stereoscopic imagery collected using a lightweight UAV spectral camera for precision agriculture,” *Remote Sens.*, vol. 5, no. 10, pp. 5006–5039, 2013.

[29] M. T. Eismann, “Imaging Spectrometer Calibration,” *Hyperspectral Remote Sens.*, pp. 417–450, 2012.

[30] M. Clark, “Mapping land cover with hyperspectral and multispectral satellites using machine learning and Spectral Mixture Analysis,” *IEEE*, 2016.

[31] M. Govender, K. Chetty, and H. Bulcock, “A review of hyperspectral remote sensing and its application in vegetation and water resource studies,” vol. 33, no. 2, pp. 145–152, 2006.

[32] P. GHAMISI *et al.*, “Advances in Hyperspectral Image and Signal Processing,” *IEEE Geosci. Remote Sens. Mag.*, vol. 5, no. 4, pp. 37–78, 2017.

[33] C. Fischer and I. Kakoulli, “Multispectral and hyperspectral imaging technologies in conservation: current research and potential applications,” *Stud. Conserv.*, vol. 51, no. sup1, pp. 3–16, 2006.

[34] R. Glumb, M. Lapsley, D. Lee, P. Mantica, and J. P. Dery, “TRL6 testing of a hyperspectral infrared CubeSat instrument.,” 2017.

[35] D. Selva and D. Krejci, “A survey and assessment of the capabilities of Cubesats for Earth observation,” *Acta Astronaut.*, vol. 74, pp. 50–68, 2012.

[36] R. Wright, P. Lucey, S. Crites, K. Horton, M. Wood, and H. Garbeil, “BBM/EM design of the thermal hyperspectral imager: An instrument for remote sensing of earth’s surface, atmosphere and ocean, from a microsatellite platform,” *Acta Astronaut.*, vol. 87, pp. 182–192,

2013.

[37] A. Poghosyan and A. Golkar, “CubeSat evolution: Analyzing CubeSat capabilities for conducting science missions,” *Prog. Aerosp. Sci.*, vol. 88, no. September 2016, pp. 59–83, 2017.

[38] T. Adão *et al.*, “Hyperspectral imaging: A review on UAV-based sensors, data processing and applications for agriculture and forestry,” *Remote Sens.*, vol. 9, no. 11, 2017.

[39] A. Habib, W. Xiong, F. He, H. L. Yang, and M. Crawford, “Improving orthorectification of UAV-based pushbroom scanner imagery using derived orthophotos from frame cameras,” *IEEE J. Sel. Top. Appl. Earth Obs. Remote Sens.*, vol. 10, pp. 262–276, 2017.

[40] C. C. Wilcox, M. Montes, M. Yetzbacher, J. Edelberg, and J. Schlupf, “An ultra-compact hyperspectral imaging system for use with an unmanned aerial vehicle with smartphone-sensor technology,” *Proc. SPIE - Int. Soc. Opt. Eng.*, vol. 10639, no. May, 2018.

[41] S. R. Herwitz *et al.*, “Imaging from an unmanned aerial vehicle: Agricultural surveillance and decision support,” *Comput. Electron. Agric.*, vol. 44, no. 1, pp. 49–61, 2004.

[42] R. Hruska, J. Mitchell, M. Anderson, and N. F. Glenn, “Radiometric and geometric analysis of hyperspectral imagery acquired from an unmanned aerial vehicle,” *Remote Sens.*, vol. 4, no. 9, pp. 2736–2752, 2012.

[43] G. Mozgeris, D. Jonikavičius, D. Jovarauskas, R. Zinkevičius, S. Petkevičius, and D. Steponavičius, “Imaging from manned ultra-light and unmanned aerial vehicles for estimating properties of spring wheat,” *Precis. Agric.*, vol. 19, no. 5, pp. 1–19, 2018.

[44] Y. Angel, D. Turner, S. Parkes, Y. Malbeteau, A. Lucieer, and M. F. McCabe, “Automated georectification and mosaicking of UAV-based hyperspectral imagery from push-Broom sensors,” *Remote Sens.*, vol. 12, no. 1, pp. 1–25, 2020.

[45] P. J. Zarco-Tejada, R. Diaz-Varela, V. Angileri, and P. Loudjani, “Tree height quantification using very high resolution imagery acquired from an unmanned aerial vehicle (UAV) and automatic 3D photo-reconstruction methods,” *Eur. J. Agron.*, vol. 55, pp. 89–99, 2014.

[46] J. Suomalainen *et al.*, “A lightweight hyperspectral mapping system and photogrammetric processing chain for unmanned aerial vehicles,” *Remote Sens.*, vol. 6, no. 11, pp. 11013–11030, 2014.

[47] P. Hödl, R. Booysen, M. Khodadadzadeh, and R. G. Id, “Integration of Terrestrial and Drone-Borne Hyperspectral and Photogrammetric Sensing Methods for Exploration Mapping and Mining Monitoring,” 2018.

[48] C. Zhang, N. C. Anzalone, R. P. Faria, and J. M. Pearce, “Open-Source 3D-Printable Optics Equipment,” *PLoS One*, vol. 8, no. 3, 2013.

[49] T. C. Wilkes, A. J. S. McGonigle, J. R. Willmott, T. D. Pering, and J. M. Cook, “Low-cost 3D printed 1 nm resolution smartphone sensor-based spectrometer: instrument design and application in ultraviolet spectroscopy,” *Opt. Lett.*, vol. 42, no. 21, p. 4323, 2017.

[50] R. Reulke and A. Eckardt, “Low cost hyperspectral systems for atmospheric and surface studies,” *Imaging Spectrom. XXII Appl. Sensors, Process.*, no. September 2018, p. 23, 2018.

[51] R. Näsi *et al.*, “Remote sensing of bark beetle damage in urban forests at individual tree level using a novel hyperspectral camera from UAV and aircraft,” *Urban For. Urban Green.*, vol. 30, no. December 2017, pp. 72–83, 2018.

[52] C. Senf, R. Seidl, and P. Hostert, “Remote sensing of forest insect disturbances: Current state

and future directions," *Int. J. Appl. Earth Obs. Geoinf.*, vol. 60, no. April, pp. 49–60, 2017.

[53] H. Aasen, A. Burkart, A. Bolten, and G. Bareth, "Generating 3D hyperspectral information with lightweight UAV snapshot cameras for vegetation monitoring: From camera calibration to quality assurance," *ISPRS J. Photogramm. Remote Sens.*, vol. 108, pp. 245–259, 2015.

[54] R. Näsi *et al.*, "Using UAV-based photogrammetry and hyperspectral imaging for mapping bark beetle damage at tree-level," *Remote Sens.*, vol. 7, no. 11, pp. 15467–15493, 2015.

[55] E. A. S. Moriya, N. N. Imai, A. M. G. Tommaselli, and G. T. Miyoshi, "Mapping mosaic virus in sugarcane based on hyperspectral images.," *IEEE J. Sel. Top. Appl. Earth Obs. Remote Sens.*, vol. 10, pp. 740–748, 2017.

[56] M. Havašová, T. Bucha, J. Ferenčík, and R. Jakuš, "Applicability of a vegetation indices-based method to map bark beetle outbreaks in the High Tatra Mountains," *Ann. For. Res.*, vol. 58, no. 2, pp. 295–310, 2015.

[57] J. A. Long and R. L. Lawrence, "Mapping percent tree mortality due to mountain pine beetle damage," *For. Sci.*, vol. 62, no. 4, pp. 392–402, 2016.

[58] E. A. Gooding, E. R. Deutsch, J. Huehnerhoff, and A. R. Hajian, "Fast, cheap and in control: spectral imaging with handheld devices," vol. 10210, no. June 2017, p. 102100E, 2017.

[59] J. Huehnerhoff, J. A. Lozo, E. R. Deutsch, and A. R. Hajian, "High resolution handheld Raman and reflectance hyperspectral imaging for remote sensing and threat detection," *Next-Generation Spectrosc. Technol. XI*, no. May 2018, p. 21, 2018.

[60] R. Garzonio, B. di Mauro, R. Colombo, and S. Cogliati, "Surface reflectance and sun-induced fluorescence spectroscopy measurements using a small hyperspectral UAS," *Remote Sens.*, vol. 9, no. 5, pp. 1–24, 2017.

[61] I. Colomina and P. Molina, "Unmanned aerial systems for photogrammetry and remote sensing: A review," *ISPRS J. Photogramm. Remote Sens.*, vol. 92, pp. 79–97, 2014.

[62] K. Uto, H. Seki, G. Saito, Y. Kosugi, and T. Komatsu, "Development of hyperspectral imaging system using optical fiber bundle and swing mirror," *Work. Hyperspectral Image Signal Process. Evol. Remote Sens.*, vol. 2015-June, pp. 1–4, 2017.

[63] R. Minařík and J. Langhammer, "Use of a multispectral UAV photogrammetry for detection and tracking of forest disturbance dynamics," *Int. Arch. Photogramm. Remote Sens. Spat. Inf. Sci. - ISPRS Arch.*, vol. 41, no. July, pp. 711–718, 2016.

[64] J. P. Dash, M. S. Watt, G. D. Pearse, M. Heaphy, and H. S. Dungey, "Assessing very high resolution UAV imagery for monitoring forest health during a simulated disease outbreak," *ISPRS J. Photogramm. Remote Sens.*, vol. 131, pp. 1–14, 2017.

[65] A. Wendel and J. Underwood, "Illumination compensation in ground based hyperspectral imaging," *ISPRS J. Photogramm. Remote Sens.*, vol. 129, pp. 162–178, 2017.

[66] J. R. K. Lehmann, F. Nieberding, T. Prinz, and C. Knoth, "Analysis of unmanned aerial system-based CIR images in forestry-a new perspective to monitor pest infestation levels," *Forests*, vol. 6, no. 3, pp. 594–612, 2015.

[67] E. Honkavaara *et al.*, "HYPERSPECTRAL REFLECTANCE SIGNATURES and POINT CLOUDS for PRECISION AGRICULTURE by LIGHT WEIGHT UAV IMAGING SYSTEM," *ISPRS Ann. Photogramm. Remote Sens. Spat. Inf. Sci.*, vol. 1, no. September, pp. 353–358, 2012.

[68] G. Bareth *et al.*, "Low-weight and UAV-based Hyperspectral Full-frame Cameras for Monitoring

Crops: Spectral Comparison with Portable Spectroradiometer Measurements.," *Photogrammetrie-Fernerkundung-Geoinformation*, vol. 1, pp. 69–79, 2015.

[69] G. Rossi *et al.*, "Optical design of a hyperspectral drone advanced camera for soil monitoring using an electro-optical liquid crystal technology," *Opt. Des. Eng. VII*, no. June 2018, p. 20, 2018.

[70] S. Jakob, R. Zimmermann, and R. Gloaguen, "The Need for Accurate Geometric and Radiometric Corrections of Drone-Borne Hyperspectral Data for Mineral Exploration: MEPHySTo-A Toolbox for Pre-Processing Drone-Borne Hyperspectral Data," *Remote Sens.*, vol. 9, no. 1, 2017.

[71] R. I. Crocker, J. A. Maslanik, J. J. Adler, S. E. Palo, U. C. Herzfeld, and W. J. Emery, "A sensor package for ice surface observations using small unmanned aircraft systems.," *IEEE Trans. Geosci. Remote Sens.*, vol. 50, pp. 1033–1047, 2012.

[72] C. H. Hugenholtz *et al.*, "Geomorphological mapping with a small unmanned aircraft system (sUAS): Feature detection and accuracy assessment of a photogrammetrically-derived digital terrain model," *Geomorphology*, vol. 194, pp. 16–24, 2013.

[73] D. M. Rippin, A. Pomfret, and N. King, "High resolution mapping of supra-glacial drainage pathways reveals link between micro-channel drainage density, surface roughness and surface reflectance," *Earth Surf. Process. Landforms*, vol. 40, no. 10, pp. 1279–1290, 2015.

[74] J. C. Ryan *et al.*, "UAV photogrammetry and structure from motion to assess calving dynamics at Store Glacier, a large outlet draining the Greenland ice sheet," *Cryosphere*, vol. 9, no. 1, pp. 1–11, 2015.

[75] A. Bhardwaj, L. Sam, Akanksha, F. J. Martín-Torres, and R. Kumar, "UAVs as remote sensing platform in glaciology: Present applications and future prospects," *Remote Sens. Environ.*, vol. 175, pp. 196–204, 2016.

[76] B. Di Mauro *et al.*, "Impact of impurities and cryoconite on the optical properties of the Morteratsch Glacier (Swiss Alps)," *Cryosphere*, vol. 11, no. 6, pp. 2393–2409, 2017.

[77] D. Carless, D. J. Luscombe, N. Gatis, K. Anderson, and R. E. Brazier, "Mapping landscape-scale peatland degradation using airborne lidar and multispectral data," *Landsc. Ecol.*, vol. 34, no. 6, pp. 1329–1345, 2019.

[78] E. Grand-Clement *et al.*, "Evaluating ecosystem goods and services after restoration of marginal upland peatlands in South-West England," *J. Appl. Ecol.*, vol. 50, no. 2, pp. 324–334, 2013.

[79] UK Government, "England Peat Action Plan," no. May, 2021.

[80] D. Giordan, D. Godone, M. Baldo, M. Piras, N. Grasso, and R. Zerbetto, "Survey solutions for 3d acquisition and representation of artificial and natural caves," *Appl. Sci.*, vol. 11, no. 14, 2021.

[81] E. Castillo, V. Bayarri, E. Castillo, and S. Ripoll, "Improved application of hyperspectral analysis to rock Art," *Appl. Sci.*, 2021.

[82] E. Garcia-Anton *et al.*, "Mineral-variations study of Canelobre cave phosphate stalactites by Raman and luminescence methods," *Spectrosc. Lett.*, vol. 44, no. 7–8, pp. 539–542, 2011.

[83] H. Pu, D. Liu, J. Qu, and D. Sun, "Applications of Imaging Spectrometry in Inland Water Quality Monitoring — a Review of Recent Developments," 2017.

[84] Rosa Elvira Correa Pabón, "Reflectance and imaging spectroscopy applied to detection of petroleum hydrocarbon pollution in bare soils," *Sci. Total Environ.*, vol. 649, pp. 1224–1236, 2019.

[85] A. Gholizadeh, M. Saberioon, E. Ben-Dor, and L. Borůvka, “Monitoring of selected soil contaminants using proximal and remote sensing techniques: Background, state-of-the-art and future perspectives,” *Crit. Rev. Environ. Sci. Technol.*, vol. 48, no. 3, pp. 243–278, 2018.

[86] L. G. Olmanson, P. L. Brezonik, and M. E. Bauer, “Airborne hyperspectral remote sensing to assess spatial distribution of water quality characteristics in large rivers: The Mississippi River and its tributaries in Minnesota,” *Remote Sens. Environ.*, vol. 130, pp. 254–265, 2013.

[87] R. E. C. Pabón and C. . de Souza Filho, “Spectroscopic characterization of red latosols contaminated by petroleum-hydrocarbon and empirical model to estimate pollutant content and type,” *Remote Sens. Environ.*, vol. 175, pp. 323–336, 2016.

[88] R. D. P. M. Scafutto, C. R. de Souza Filho, and B. Rivard, “Characterization of mineral substrates impregnated with crude oils using proximal infrared hyperspectral imaging,” *Remote Sens. Environ.*, vol. 179, pp. 116–130, 2016.

[89] R. D. P. M. Scafutto, C. R. de Souza Filho, and W. J. de Oliveira, “Hyperspectral remote sensing detection of petroleum hydrocarbons in mixtures with mineral substrates: Implications for onshore exploration and monitoring,” *ISPRS J. Photogramm. Remote Sens.*, vol. 128, pp. 146–157, 2017.

[90] G. Memisoglu, B. Gulbahar, J. Zubia, and J. Villatoro, “Theoretical modeling of viscosity monitoring with vibrating resonance energy transfer for point-of-care and environmental monitoring applications,” *Micromachines*, vol. 10, no. 1, 2018.

[91] M. Alvarado, F. Gonzalez, A. Fletcher, and A. Doshi, “Towards the development of a low cost airborne sensing system to monitor dust particles after blasting at open-pit mine sites,” *Sensors (Switzerland)*, vol. 15, no. 8, pp. 19703–19723, 2015.

[92] C. L. Ng, F. M. Kai, M. H. Tee, N. Tan, and H. F. Hemond, “A prototype sensor for in situ sensing of fine particulate matter and volatile organic compounds,” *Sensors (Switzerland)*, vol. 18, no. 1, pp. 1–9, 2018.

[93] J. P. Reid *et al.*, “The viscosity of atmospherically relevant organic particles,” *Nat. Commun.*, vol. 9, no. 1, pp. 1–14, 2018.

[94] L. Ziph-Schatzberg *et al.*, “Compact, high performance hyperspectral systems design and applications,” no. June 2015, p. 94820W, 2015.

[95] R. Holasek *et al.*, “The selectable hyperspectral airborne remote sensing kit (SHARK) as an enabler for precision agriculture,” vol. 1021304, no. May 2017, p. 1021304, 2017.

[96] J. shan, J. Zhao, L. Liu, Y. Zhang, X. Wang, and F. Wu, “A novel way to rapidly monitor microplastics in soil by hyperspectral imaging technology and chemometrics,” *Environ. Pollut.*, vol. 238, pp. 121–129, 2018.

[97] T. M. Karlsson, H. Grahn, B. van Bavel, and P. Geladi, “Hyperspectral imaging and data analysis for detecting and determining plastic contamination in seawater filtrates,” *J. Near Infrared Spectrosc.*, vol. 24, pp. 141–149, 2016.

[98] A. Chennu, P. Färber, G. De’ath, D. De Beer, and K. E. Fabricius, “A diver-operated hyperspectral imaging and topographic surveying system for automated mapping of benthic habitats,” *Sci. Rep.*, vol. 7, no. 1, pp. 1–12, 2017.

[99] T. C. Wilkes, T. D. Pering, A. J. S. McGonigle, G. Tamburello, and J. R. Willmott, “A low-cost smartphone sensor-based UV camera for volcanic SO2emission measurements,” *Remote Sens.*, vol. 9, no. 1, pp. 1–10, 2017.

[100] A. J. S. McGonigle *et al.*, “Smartphone spectrometers,” *Sensors (Switzerland)*, vol. 18, no. 1, pp. 1–15, 2018.

[101] A. Bhardwaj, P. K. Joshi, L. Sam, and Snehmani, “Remote sensing of alpine glaciers in visible and infrared wavelengths: a survey of advances and prospects,” *Geocarto Int.*, vol. 31, no. 5, pp. 557–574, 2016.

[102] C. Zhang, G. Cheng, P. Edwards, M. Da Zhou, S. Zheng, and Z. Liu, “G-Fresnel smartphone spectrometer,” *Lab Chip*, vol. 16, no. 2, pp. 246–250, 2016.

[103] F. Sigernes, M. Syrjäsuo, R. Storvold, J. Fortuna, M. E. Grøtte, and T. A. Johansen, “Do it yourself hyperspectral imager for handheld to airborne operations,” *Opt. Express*, vol. 26, no. 5, p. 6021, 2018.

[104] M. A. Hossain, J. Canning, K. Cook, and A. Jamalipour, “Optical fiber smartphone spectrometer,” *Opt. Lett.*, vol. 41, no. 10, p. 2237, 2016.

[105] N. D. Lane, E. Miluzzo, H. Lu, D. Peebles, T. Choudhury, and A. T. Campbell, “A survey of mobile phone sensing,” *ieee communications magazine*, pp. 140–150, 2010.

[106] J. C. Contreras-Naranjo, Q. Wei, and A. Ozcan, “Mobile Phone-Based Microscopy, Sensing, and Diagnostics,” *IEEE J. Sel. Top. Quantum Electron.*, vol. 22, no. 3, pp. 1–14, 2016.

[107] H. Zhu, U. Sikora, and A. Ozcan, “Quantum dot enabled detection of Escherichia coli using a cell-phone,” *Analyst*, vol. 137, pp. 2541–2544, 2012.

[108] S. Dutta, A. Choudhury, and P. Nath, “Evanescent wave coupled spectroscopic sensing using smartphone,” *IEEE Photonics Technol. Lett.*, vol. 26, no. 6, pp. 568–570, 2014.

[109] M. Arafat Hossain, J. Canning, S. Ast, K. Cook, P. J. Rutledge, and A. Jamalipour, “Combined ‘dual’ absorption and fluorescence smartphone spectrometers,” *Opt. Lett.*, vol. 40, no. 8, p. 1737, 2015.

[110] A. Ozcan, “Mobile phones democratize and cultivate next-generation imaging, diagnostics and measurement tools,” *Lab Chip*, vol. 14, no. 17, pp. 3187–3194, 2014.

[111] Z. J. Smith *et al.*, “Cell-phone-based platform for biomedical device development and education applications,” *PLoS One*, vol. 6, no. 3, 2011.

[112] C. Holmlund *et al.*, “MEMS FPI-based smartphone hyperspectral imager,” *Next-Generation Spectrosc. Technol. IX*, vol. 9855, no. May 2016, p. 985507, 2016.

[113] A. Näsilä *et al.*, “Hand-held MEMS hyperspectral imager for VNIR mobile applications,” no. February 2018, p. 25, 2018.

[114] B. Vergouw, H. Nagel, G. Bondt, and B. Custers, “Drone technology: Types, payloads, applications, frequency spectrum issues and future developments.,” in *The Future of Drone Use, Information Technology and Law*, 2016, pp. 21–45.

[115] A. M. Cunliffe, K. Anderson, L. DeBell, and J. P. Duffy, “A UK Civil Aviation Authority (CAA)-approved operations manual for safe deployment of lightweight drones in research,” *Int. J. Remote Sens.*, vol. 38, no. 8–10, pp. 2737–2744, 2017.

[116] R. Clarke, “Understanding the drone epidemic,” *Comput. Law Secur. Rev.*, vol. 30, no. 3, pp. 230–246, 2014.

Chapter 3

Development of a Low-Cost, Miniaturised Hyperspectral Imager and its Application to Laboratory-Based Environmental Monitoring Scenarios

This chapter is associated with the work presented in Stuart et al., [1]. It presents the development of a low-cost laboratory-based hyperspectral imager constructed using commercially available components. This chapter demonstrates that it is possible to develop a low-cost hyperspectral imager using low-cost, accessible components, that is capable of scientific grade analyses, highlighting the potential for further developments within this field. Imager calibration and metrology are presented alongside a demonstration of the imager's abilities in a variety of laboratory-based environmental applications.

3.1. Introduction

The continued development of hyperspectral imaging technologies represents a significant area of study with the potential to revolutionise data acquisition methods across a vast range of research domains. Whilst, traditionally, hyperspectral imaging sensors are based within spaceborne and aircraft set-ups [2], [3], the recent surge in miniaturised, low-cost components, discussed within Chapter 2, provides an opportunity to expand the scope of hyperspectral technologies to a variety of field-based and portable applications [4]–[8]. These developments not only begin to improve on the often substantial costs associated with traditional hyperspectral data collection methods, but they also significantly improve the accessibility of hyperspectral sensing technologies [4], [5], [9]. These new imager designs provide accurate, high spatial resolution datasets that are not constrained by factors, such as variable meteorological conditions, limited temporal resolution, and expensive set-up costs, which readily affect traditional monitoring methods [7], [10], [11]. Furthermore, as these technologies continue to improve and develop, a substantial increase in the availability of hyperspectral datasets across a wide variety of environments can be expected.

Hyperspectral imaging has also been proven to be a powerful tool for laboratory-based applications, yet the majority of imagers currently used in these settings remain bulky and expensive, subsequently limiting their user-base and accessibility [9]. Furthermore, their large size results in many of these instruments being comparatively rigid devices because their design prevents them from being capable of adjustment to better fit a particular measurement application, again significantly limiting their usability and data collection potential. However, as the recent development of low-cost components and electronics has enhanced field-based applications, it can also inspire advancement within a laboratory setting. This chapter details the design and construction of a laboratory-based hyperspectral imager that was developed using low-cost, commercially available components. This instrument represents a significant reduction in hyperspectral system development costs, whilst maintaining the ability to capture accurate and robust datasets across a range of application areas. Existing hyperspectral cameras on sale today can cost greater than £30,000 (e.g., the Specim FX17e),

with some commercial systems costing as much as £150,000 (e.g., the Specim FX50). In comparison, the low-cost hyperspectral imager costs less than £6,000 to develop with the main costs associated with the development systems. The instrument weighs approximately 3.1 kg, including a 3 kg optical breadboard and has dimensions (Length x Width x Height) of 35 cm x 20 cm x 13 cm. The instrument design discussed within this chapter, therefore, aims to demonstrate the successful application of this low-cost, semi-portable instrument, whilst highlighting the abundant potential present within the field of low-cost miniaturised hyperspectral imaging. Specifically, this chapter discusses the initial development and performance testing of this instrument within a laboratory setting, providing a metrology-based calibration for the instrument before applying it to a variety of environmental applications to demonstrate its potential as a valuable laboratory measurement tool with the potential to provide significant improvements to the accessibility of robust hyperspectral imaging.

3.2. Development of the Laboratory-Based Hyperspectral Imager

3.2.1. Component Selection and Instrument Design

The development of a laboratory-based hyperspectral imaging system capable of scientific grade data collection whilst maintaining a low, accessible, price point provides a unique opportunity to demonstrate that high quality datasets can be achieved utilising components acquired from consumer markets. To design such an instrument, the individual components that comprise the hyperspectral imaging instrument were specifically selected to best fit the intended application requirements. As such, the main objectives to be met with this design were: it had to remain low-cost, making it an accessible device that could be more easily utilised than currently available commercial set-ups, it must be sufficiently compact to allow it to be portable within a laboratory setting giving it a greater range of application potential, and it must be capable of detecting a wavelength range suitable for a selection of environmental monitoring-based applications. To allow the instrument to be capable of low-cost, light-weight spectral sensing a miniature spectrometer was sought as a critical component of the overall design. These compact components drive the development of low-cost spectral sensing instrumentation with wavelengths ranging from ultraviolet through to infrared, making them ideal for compact, low-cost spectral instrument design. Furthermore, these miniature spectrometers are available within commercial markets, providing a range of sensors and wavelength regions to choose from. This wealth of choice enables the development of a versatile instrument that can be converted to a variety of different wavelength regions to better suit a range of applications. For the purposes of this particular design and application, the imager is capable of detecting wavelengths predominantly within the visible region of the electromagnetic spectrum, however, the abundance of miniature and micro spectrometer components within commercial markets mean that the instrument could be converted to cover different wavelength ranges with relative ease.

The developed instrument, shown in Figure 3.1., consists of the following components; the C12880MA Hamamatsu miniature spectrometer, New Scale Technologies DK-M3-RS-U-2M-20-L rotary mirrors, and a Thorlabs Plano-convex lens (LA1401-A). The miniature spectrometer has a wavelength range and spectral resolution of 340 – 850 nm and 15 nm respectively. It should be noted that the plano-convex lens used within this set-up has an anti-reflective coating for the wavelength range of 350 nm to 700 nm. This coating benefits the set-up by minimising surface reflections and, therefore, improving transmission within this range. Whilst this range is narrower than that of the spectrometer and, therefore, limits the spectral range of the instrument this did not limit the intended application of this device within the contexts of this chapter because the wavelengths of interest were present within the visible spectrum and, therefore, were not significantly affected by this limitation. These components provide a suitable wavelength range, and spectral resolution ensuring the instrument is capable of producing robust output datasets whilst maintaining a low price point. Beam steering is provided by

the New Scale Technologies rotary mirror system and focusing provided by the Plano-convex lens. This represents a very basic optical system, consisting of a single lens, however, similar to the selection of the miniature spectrometer above, the inclusion of more complex optics would add significant costs to the instrument design. In its current format, the laboratory-based hyperspectral imager can produce robust and accurate hyperspectral outputs, demonstrating that expensive components are not necessarily required for quality hyperspectral imaging. Component justification and price break-down can be found in Table 3.1.

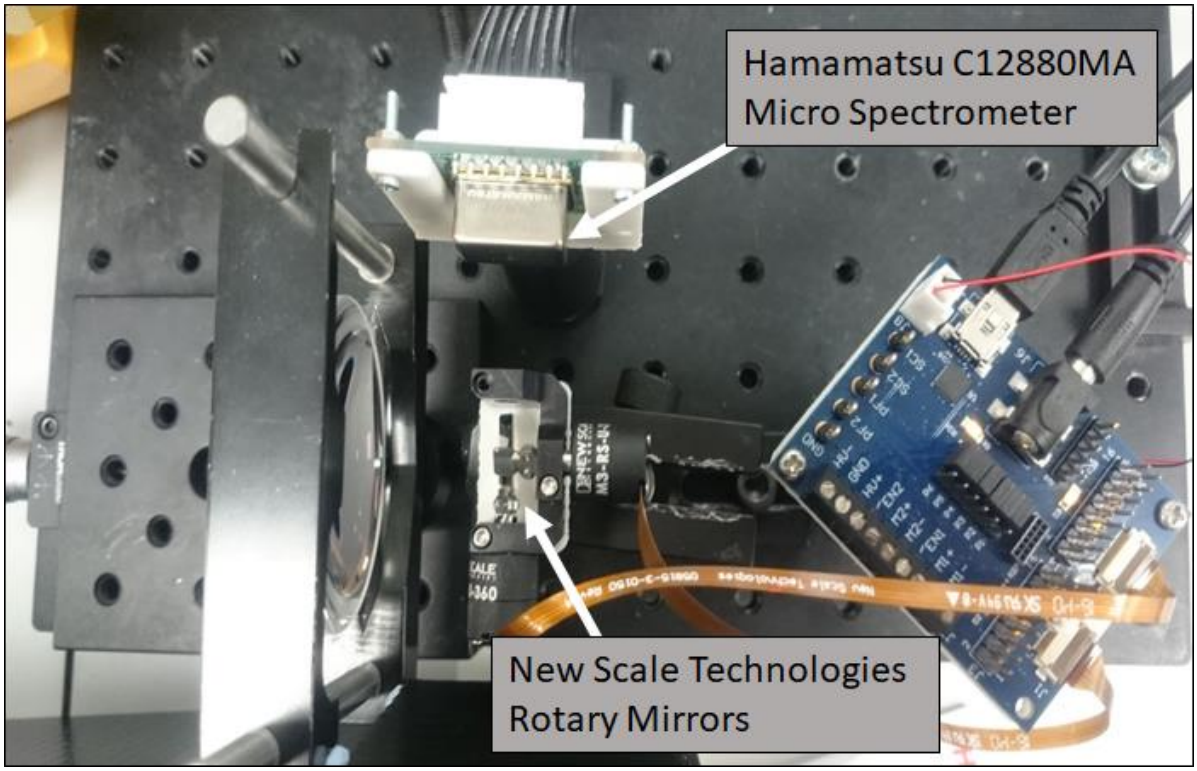

Figure 3.1 Components of the hyperspectral set-up.

Each of the components included within this design are commercially available and represent typical components present within consumer markets. Furthermore, the miniature spectrometer and the rotary mirror system are user friendly and can be easily programmed to suit a variety of applications. This allows the instrument to be readily accessible and increases its ease of replication by a broad range of research groups and organisations, including those that are less well-resourced. To assemble the instrument the separate components were aligned with a suitable image distance, creating a compact design. The required object distance was then calculated using the lens equation;

$$\frac{1}{f} = \frac{1}{u} + \frac{1}{v} \tag{3.1.}$$

Where *f* represents the focal length, *u* the image distance, and *v* the object distance. Given an image distance of 68.11 mm and a lens focal length of 60 mm the object distance for this set-up was calculated to be ca. 50 cm. Figure 3.2. shows a schematic diagram of the instrumental set-up.

Ray trace modelling was performed in Zemax software to estimate the theoretical instantaneous field of view (IFOV) of the single pixel upon the target. This was calculated to be approximately 2.50 mm × 4.90 mm for a 95% energy enclosure, and includes the diffraction limit of the spectrometer. The model is shown within Appendix 8.1. This also accounts for the use of a singlet lens where chromatic and spherical aberrations are uncontrolled within this wide aperture, low f/number system. The maximum

angle of the mirror system is ±20◦ providing a total field of view (TFOV) of 36.4 cm for an image; however, the ability of the optics to form a focused image limits the TFOV below this maximum value. No additional coupling optics were used before the spectrometer.

A bi-directional raster scanning pattern was implemented to capture each pixel in a scene, with beam steering provided by the rotary mirror system. The mirror system comprises a short mirror of dimensions 3 mm × 5 mm × 0.4 mm, and a long mirror of dimensions 11 mm × 5 mm × 0.4 mm. Image resolution is user defined and, therefore, configurable to the requirements of the proposed application. Exposure time per pixel can also be configured by the operator to best fit the illumination of the target. Whilst increases to the exposure time per pixel and the resolution of a scene will help to provide clearer imagery, there remains an engineering compromise with the overall scan time required.

Table 3.1. Cost break-down and individual component justification for the Laboratory-Based Hyperspectral Imager.

Component	Cost	Justification
Hamamatsu C12880MA Miniature Spectrometer	£4,000	A miniature spectrometer was specifically sought for this application because they provide compact, low-cost, and reliable data capture. Additionally, Hamamatsu provides a range of these devices covering different spectral regions, increasing the ease of component replacements for different applications. A spectrometer with a wavelength range predominantly within the visible spectrum was selected for this research to best fit the applications of this early project.
New Scale Technologies DK-M3-RS-U-2M-20-L Rotary Mirrors	£1,945	These mirrors were selected because they provided a user friendly means of precise point-to-point beam steering. Their miniature size is also beneficial to the overall instrument design. Their ease of operation was highly beneficial in the contexts of this early stage research.
Thorlabs Plano-Convex Lens LA1401-A	£35	This lens was selected to provide simple target focusing at minimal cost. A plano-convex lens was selected to reduce potential aberrations without the inclusion of a more complex (and costly) lens system. The lens' anti-reflective coating increases transmission across its spectral range (350 nm – 700 nm). This was deemed beneficial for this particular set-up because it was intended for use across visible wavelengths.
Total Cost	**£5,980**	

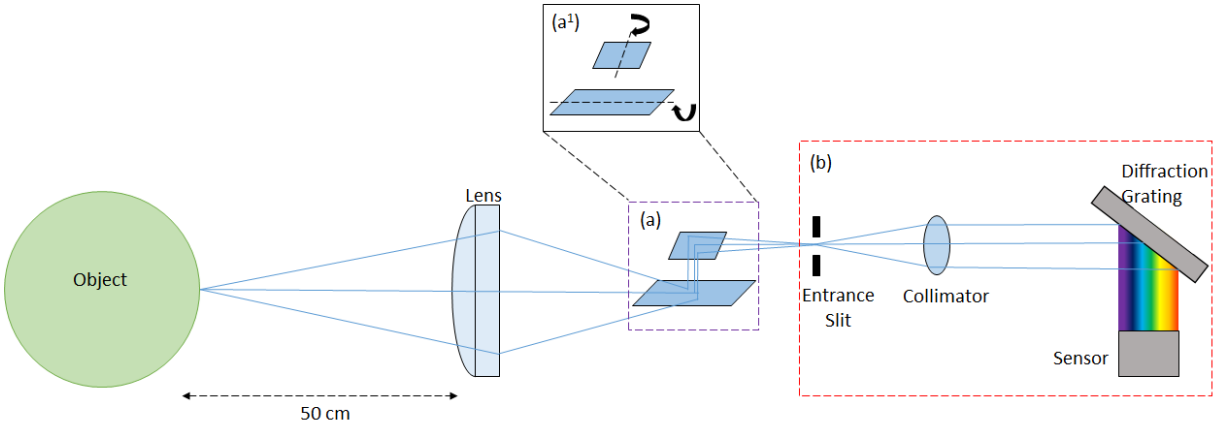

Figure 3.2 Schematic diagram of the low-cost hyperspectral imager: (a) and (b) comprise the rotary mirror system and the miniature spectrometer respectively, illustrating the main components of each device. Inset (a^1) displays the rotational axis for each mirror. Note, beam steering of the field of view (FOV) is provided by the mirrors. The image distance is ca. 65.6 mm. This is distributed as follows: ca. 30 mm lens to mirrors, ca. 3.6 mm between mirrors, and ca. 32 mm mirrors to spectrometer. Not to scale.

3.2.2. Instrument Control

To obtain hyperspectral datasets from these components the rotary mirrors and the miniature spectrometer had to first be programmed separately, then combined to allow them to work in tandem to produce a hyperspectral image. This programming was completed within LabVIEW software. Whilst the software incorporated within the rotary mirrors development kit contained a header file suitable for use within LabVIEW, the miniature spectrometer required the creation of a header file to allow the appropriate libraries and functions to be accessed by the LabVIEW compiler.

Due to the range of tasks required of the miniature spectrometer during its operation several subroutines, known as sub VIs in LabVIEW, were created to condense the extensive programme into a number of smaller, easier to use blocks. The rotary mirrors required a much less complex programme to move the mirrors through a predetermined set of coordinates to produce a bi-directional raster scan of the chosen scene, therefore, a single sub VI was required for the mirror programme. Table 3.2. details these sub VIs and explains the function of each. These sub VIs were then combined to provide a working piece of software that enabled the collection, assembly, and analysis of the hyperspectral data cube and individual spectral response graphs. The final LabVIEW programme converts the collected one-dimensional data array into the three-dimensional data cube format. Operator inputs through a computer terminal can determine the acquisition parameters, such as the required dimensions of the scene and the exposure time required for each pixel. The spectral response can be visualised in real-time as the scene is captured, detailing the response from individual pixels. After the scene capture is complete, the operator can use the data cube to scroll through the data to observe the response captured across different wavelengths. The spectral response from a specific area or pixel can also be visualised in a separate graph to allow for more detailed analysis. This software can be found within Appendix 8.2.

Table 3.2 Individual Sub VIs that make up the laboratory-based hyperspectral imager software.

Sub VI	Task
Mirror-coords	This Sub VI controlled the rotary mirror system and programmatically defined the mirror coordinates according to the operator-defined acquisition parameters to produce a bi-directional raster scan of the target scene.
Initialise	This Sub VI was part of the miniature spectrometer software. It initiated the connection with the spectrometer and the library. It also enables the operator to select the capture mode and the exposure time (us) required.
Capture	This Sub VI was responsible for the capture of data from the spectrometer. Short wait periods (ms) were included here to ensure that the physical optics remained synchronised with the image capture process. In this Sub VI the data captured was displayed in an array and on a waveform graph providing the operator with a real-time view of the data acquisition. Data storage was also controlled here by connecting to a file outside of the Sub VI.
Uninitialise	This Sub VI terminates the connection to the spectrometer and the library when prompted, allowing the device to be disconnected from the computer terminal after the data capture period is complete.

3.2.3. Bias Correction

To remove the spectral influence of illumination and sensor sources, as discussed in Chapter 2, the following analysis was implemented within the LabVIEW programme:

$$Ratio = \frac{S_{target} - S_{dark}}{S_{white} - S_{dark}} = \frac{R_{target}}{R_{white}} \approx R_{target} \quad (3.2.)$$

Note, this equation is identical to Equation 2.12 of Chapter 2. To provide a value for R_{white}, a reference 'orb' was three-dimensionally printed and coated with Edmund Optics white reflectance coating (Stock #83–890). This coating was applied using an airbrush to ensure uniform coverage across the object and is specified to provide >97% reflectivity from 350–850 nm. The 'orb', a ca. 60-mm-diameter sphere, was used in place of a target object to obtain the white reflectance value. These bias corrections were completed using further LabVIEW programming to produce accurate spectral outputs for the chosen targets. This code can be found in Appendix 8.3. Additionally, the digital equivalent of a long-pass filter was then applied to the spectral data within LabVIEW as a smoothing factor to minimise the influence of excess noise. A long-pass filter provides a valuable means of reducing noise within a dataset by allowing for the removal of values above or below a certain cut off, subsequently smoothing the dataset. In this work, this filter was specifically used as a means of reducing the influence of the blue peak of the LED illumination source within the dataset. This is shown in Equation 3.3.

$$f_{smooth}(\lambda_i) = f_{smooth}(\lambda_{i-1}) + \frac{f(\lambda_i) - f(\lambda_{i-1})}{A} \quad (3.3.)$$

Where $f_{smooth}(\lambda_i)$ is the smoothed value of discrete wavelength λ_i, $f(\lambda_i)$ is the raw wavelength, A is the smoothing factor and $f_{smooth}(\lambda_{i-1})$ is the wavelength value immediately preceding $f(\lambda_i)$. This correction was applied to all datasets discussed in this chapter. The imager is capable of capturing a variety of scenes, making it practical for a versatile range of applications, and it allows for real-time monitoring and decision making, which is of significant benefit to a variety of measurement and monitoring applications.

To assess the optical power reflected from the surface of the target objects and, ultimately, the power represented by each pixel of the image, a radiometric measurement of the power reflected from the surface of the white reference "orb" was measured. This was measured using the silicon photodiode-based radiometer as described in Zhu et al., [12]. For this measurement, the RG850 long-pass filter was removed to allow light corresponding to the wavelength range of the imager to be measured. It was replaced in the sight path with a narrow bandpass filter from Thorlabs (Stock #FB550–10), centred on 550 nm with a full width half maximum of 10 nm. The photocurrent was measured with the radiometer sighted upon the orb with and without the narrow bandpass filter in place. From these data and the spectral properties of the radiometer and filter, the reflected optical power collected by the radiometer was calculated to be 13.8 nW. Given that the FOV of the radiometer represented a circular area of approximately 14 mm in diameter upon the target, and assuming diffuse reflections, the reflected power per unit area was calculated to be approximately 89.6 $\mu W/m^2$. Therefore, given that each pixel of the hyperspectral imager represents an area of 12.25×10^{-6} m^2, the total power collected per pixel of the imager is approximately 1.10 nW for the white reference "orb". This calibration enables samples from different sources to be accurately compared, significantly increasing the imager's usability. Furthermore, as these measurements are traceable to the watt, it provides a degree of precision that would not otherwise be available. Traceability was by means of a certified, calibrated radiation thermometer (AMETEK Land Cyclops C100) that was used in tandem with an approximate blackbody furnace (AMETEK Land R1500P) to calibrate the aforementioned radiometer that, in turn, was used to calibrate our hyperspectral imaging system. The origin of the traceability was the United Kingdom National Measurement Institute (NPL, Teddington, UK).

3.2.3.1. Development of a Low-Cost Integrating Sphere Analogue

During the initial testing phase of the hyperspectral imager, discussed in Section 3.3. below, it became clear that directional scatter across a target object can often result in the manifestation of bright spots and shadowing across an acquired image. To prevent this, during later measurements, the object to be imaged was placed within a low-cost integrating sphere analogue (Figure 3.3.). Integrating spheres have been used extensively across a range of hyperspectral imaging applications [13]–[15]. The inclusion of such a device can improve the illumination of the target object by ensuring the even distribution of incident light rays across the objects surface, minimising the influence of illumination variation caused by bright spots and/or shadows across the target caused by factors such as, directional illumination, or variations across the target's surface. Much like the optical components discussed within Chapter 2, integrating spheres must also be selected for the wavelength range of the chosen application because they too will have a specific wavelength range, where a Lambertian-like reflectance distribution can be achieved. A number of ports, or objectives, are present within the sphere allowing for illumination sources and/or sensors to be positioned. It is important to arrange a set-up in such a way that prevents the direct illumination of the sensor from an illumination source. This can be done in a number of ways, from specifically configuring the position of the objectives to ensure a direct line-of-sight is not possible, to the inclusion of baffles within the sphere to block the illumination sources from the sensor.

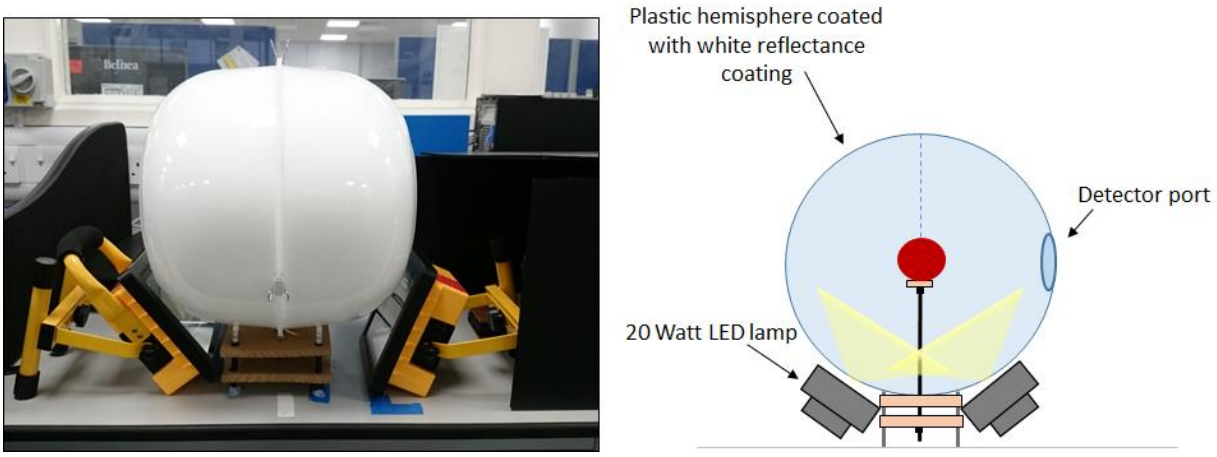

Figure 3.3 Low-cost integrating sphere analogue set-up for image capture. Schematic not to scale.

The low-cost integrating sphere analogue used within this research comprises two plastic hemispheres, ca. 30 cm in diameter, coated with the same Edmund Optics white reflectance coating as applied to the 'orb'. A detector port is present for the hyperspectral imager, and two lighting ports allow for object illumination provided by two 20 W light emitting diode (LED) lamps angled to prevent the direct illumination of the sensor. The inclusion of the integrating sphere analogue provides uniform illumination across the object surface, minimising the shadow and directional scattering resulting from a three-dimensional surface. The object is diffusely illuminated by the sphere, which ensures that any variations observed are a result of variations within the object and not resultant from favourable lighting e.g., bright spots and/or shadows. The hyperspectral imager is covered during image acquisition to prevent the interference of ambient stray light during image capture. In its current format (Figure 3.4.), the low-cost hyperspectral imager is suitable for laboratory-based, bench-top image acquisition. It is capable of a variety of image capture applications, making it a valuable laboratory measurement tool.

To better define the characteristics of the integrating sphere analogue to understand its potential impacts on the spectral reflectance of target objects, the spectral response of the inner surface of the sphere was measured with a Thorlabs CCD spectrometer (CCS200). During this measurement the sphere was uniformly illuminated with natural light. Illumination bias was then subtracted from the spectral response in order to visualise the true response of the integrating sphere analogue. Figure 3.5. shows the resulting spectral response graph for the visible spectrum. This figure highlights the relatively even spectral response provided by the sphere demonstrating it to be a valuable diffuse reflector. With a maximum variation in reflectance intensity across this spectral range of ca. 5% and a lack of distinct spectral features and/or significant variations it provides a diffuse spectral response that can be easily removed from the true spectral response of a target object. From this information it can, therefore, be inferred that the integrating sphere analogue has minimal influence/impact on the spectral response of target objects placed within the sphere.

Figure 3.4 The current set-up of the hyperspectral imager: (A) displays the true set-up during image capture, with the hyperspectral imager covered by a dark box, while (B) displays the alignment between the sphere and the hyperspectral imager with the dark box removed.

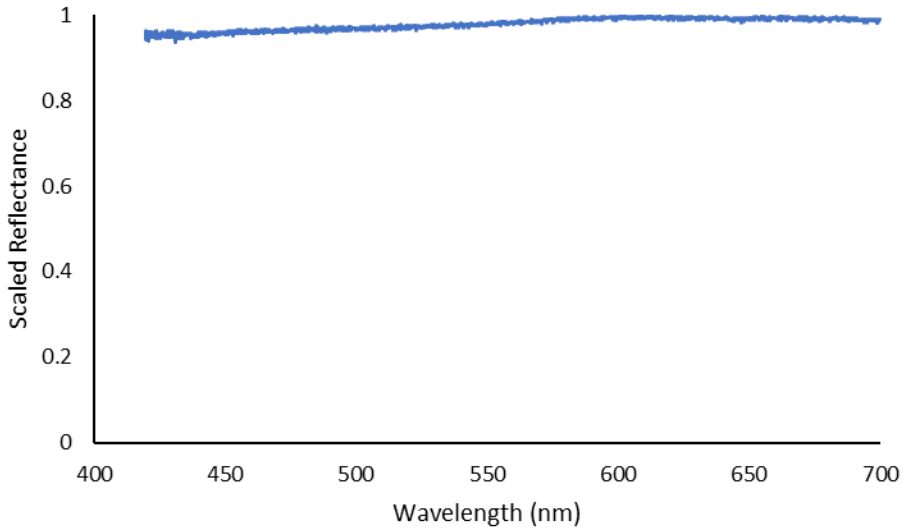

Figure 3.5 Spectral response of the integrating sphere analogue demonstrating a linear spectral response across the visible spectrum.

3.3. Initial Testing

3.3.1. Spatial Measurements

The initial testing of this instrument focused on determining its basic spatial and spectral data capture abilities. Preliminary measurements focused on emitting and back-illuminated targets, where the illumination source was present within the imaging path. These measurements were completed to gain a better understanding of the spatial abilities of the instrument and to determine how well a range of non-complex targets could be resolved in the output data. A number of well defined targets were used, including an illuminated button LED, and a diffusely back-illuminated cylindrical target with a tapered tip. Their resulting spatial datasets were analysed for any potential distortions or variations, providing an opportunity to fine-tune the instrument and a starting point for better understanding the capabilities of the set-up. The circular aperture of the button LED was well defined within the dataset as shown in Figure 3.6. however, there was obvious interference around the edges of the aperture. Similarly, the cylindrical target can be clearly identified, but the edges of the object are less well defined (Figure 3.6.). This interference and lack of distinction around the edges of target features results from the limited resolution of the instrumentation but is also a factor of the slit method of image capture causing a degree of blur across boundaries within imaged outputs.

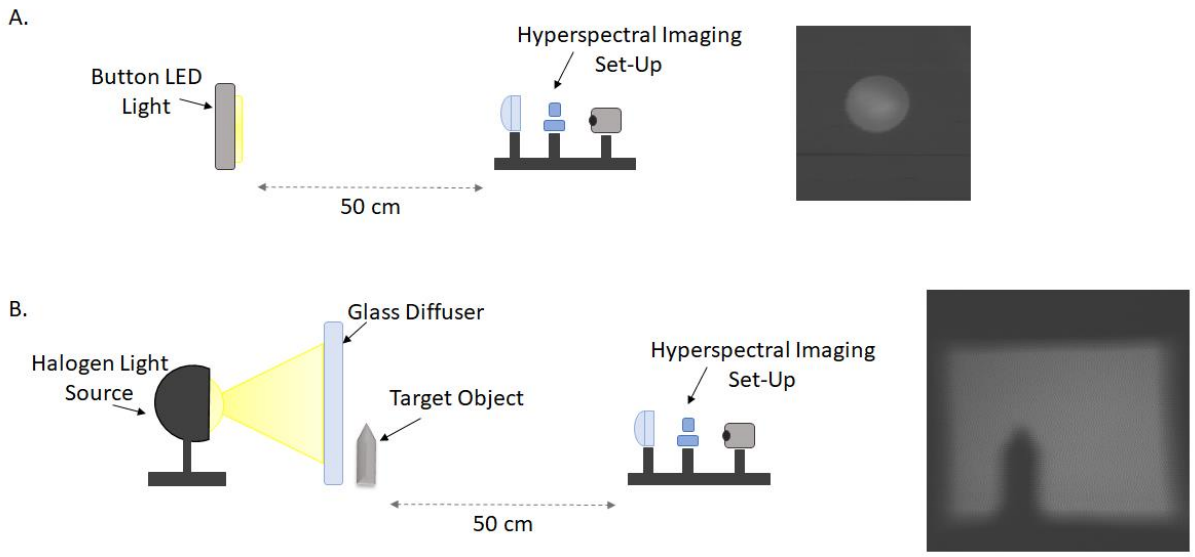

Figure 3.6 Example spatial target tests. A, shows the schematic layout and an output image of the button LED target. B, shows the schematic layout and an example image of the cylindrical tapered target. These demonstrate the spatial abilities of the low-cost laboratory-based hyperspectral imager. Schematic diagrams not to scale.

Further measurements of spatial resolution were conducted using a large modulation transfer function (MTF) plate consisting of a range of equally spaced alternating solid and clear bars. By completing these measurements, it provides a quantifiable visual representation of the spatial abilities of this instrument as well as providing information as to how the system is affected by aberrations. Determining the frequency of bars the instrument was capable of resolving allowed the spatial frequency limits of the set-up to be determined, providing a better understanding of the overall spatial abilities of the instrument, and providing a quantifiable means of comparing this system to the spatial abilities of other instruments. Although the spatial resolution of the set-up was known to be unable to resolve the line spacing on a commercial resolution testing target (e.g. Thorlabs R3L3S1N), which was to be expected given the basic optical system employed, it was capable of resolving a number of larger line spacing targets as shown in Figure 3.7. It is clear in this figure that when the band frequency is increased, the instrument is less able to resolve the banding resulting in increased blurring. However, this demonstrates that the set-up is proficient at achieving a suitable resolution given its components and price point.

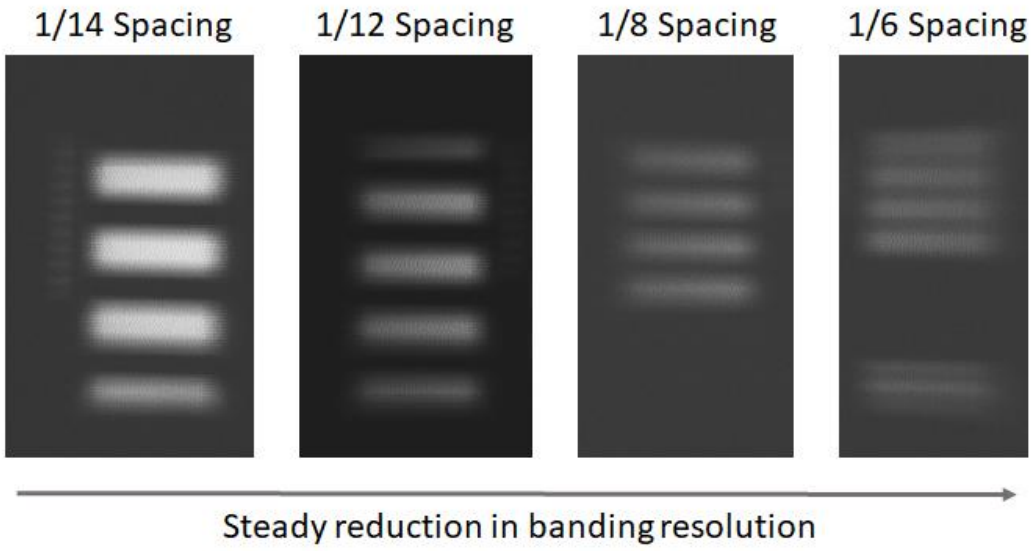

Figure 3.7 Imager spatial resolution abilities demonstrated using a large MTF plate.

3.3.2. Spectral Measurements

Preliminary spectral measurements focused on a range of targets that portrayed variable spectral responses that could be initially verified through visual analysis to ensure that the spectral outputs produced by this instrument were reliable. To demonstrate the imager's ability to accurately replicate its intended target, a simple colour target was displayed on a phone screen, providing a simple emitting target. Figure 3.8. displays this target, consisting of solid red, green, blue, and white blocks, alongside the instrument's replication of the spectral and spatial data. This figure clearly shows that the instrument is capable of accurately replicating the spectral outputs of this target. Each colour block is accurately depicted within the spectral data, alongside the white block which is clearly visible at each of the selected wavelengths, as expected. Additionally, a reconstructed colour image, utilising the output spectral data for reference further demonstrates the accuracy of this replication, emphasising the quality of data capture possible with this instrument.

Furthermore, an apple was utilised as a more complex reflecting target to determine how well an object, and its features, could be resolved by the instrument when the illuminating source was not within the imaging path, resulting in lower light levels. The use of an apple as a target also demonstrated the instrument's abilities at detecting the different pigments present across the apple's surface. Variations in these pigments can be used to better understand the health of the fruit and is an area of industry where hyperspectral imaging techniques are highly beneficial. Furthermore, apples are well characterised spectrally within the existing literature [16]–[18]**,** and, therefore, provide good, non-trivial pseudo standards. For this initial test, wavelengths within red, green, and blue regions were directly compared. Given the green/red colour of the target, these wavelengths were expected to produce a brighter response than present within blue regions. More detailed analyses of fruit targets and the application of the laboratory-based hyperspectral imager to this field is covered in greater detail in Section 3.4.1. Figure 3.9. shows that the instrument is capable of detecting the target object and can spatially resolve features on the surface as well as demonstrating clear spectral variations across the visible spectrum, highlighting its potential as a robust scientific grade hyperspectral imager.

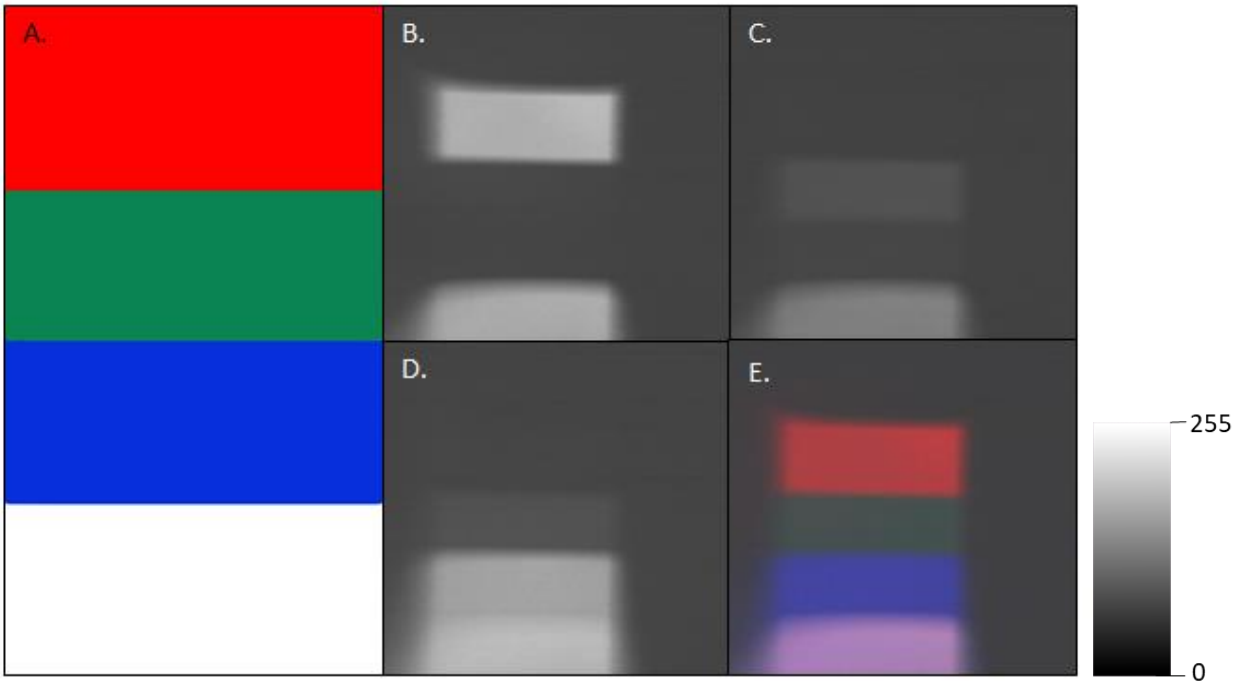

Figure 3.8 Hyperspectral images of a smartphone screen captured by the laboratory-based hyperspectral imager. A, shows the image as displayed on the phone screen, B, C, and D show the spectral responses from the red, green, and blue portions of the spectrum respectively. E shows a reconstruction of the colour image using the hyperspectral data, note, the similarities between the output and the original image. Scale shows pixel intensity.

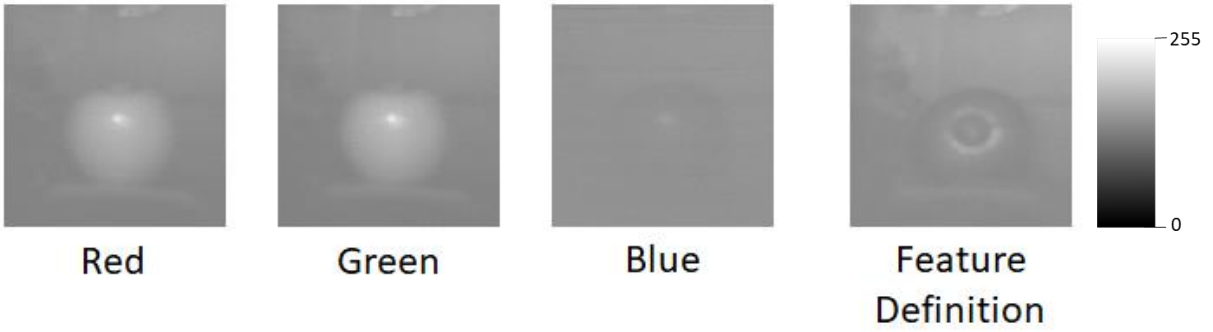

Figure 3.9 Hyperspectral datasets obtained of an apple target. Note the variations in spectral response across red, green, and blue channels as well as the feature definition which demonstrates the imager's ability to define differences across the top of the apple. This figure also demonstrates the influence of directional illumination sources, with the presence of bright spots and shading across the target, that was observed prior to the implementation of the integrating sphere. Scale shows pixel intensity.

3.4. Environmental Applications

After the completion of initial tests, in order to demonstrate the imager's capabilities within more 'real-world' scenarios, it was tested within a variety of laboratory-based applications. The applications discussed below were selected as they represent areas of research where hyperspectral datasets were shown to be beneficial; however, the current literature suggests that they are lacking in low-cost, accessible hyperspectral imagers at this time. By demonstrating the imager's capabilities in these domains, the aim is to introduce robust low-cost hyperspectral systems for ongoing development in these settings. For these applications the target object was placed within the low-cost integrating

sphere analogue introduced in Section 3.2.3.1. to reduce the effects of bright spots and shading across the chosen targets.

3.4.1. Fruit Quality Identification

Hyperspectral imaging was shown to be an effective, non-destructive means of quality assessment for a variety of food categories [19]–[22], providing an accurate early detection method for product deterioration [23], which may not be so easily recognised with traditional analysis methods [24]–[26]. Whilst qualitative assessments in this field are typically completed using features present within the near infrared portion of the electromagnetic spectrum [24], [27], [28], research shows that absorption features present within the visible spectrum can also be used as a low-cost alternative means of quality control [16], [24], [29], [30]. Similar experiments were completed by, for example Hossain et al. [29] and Das et al. [17] to test a variety of smartphone spectrometers [31]; however, to the best of my knowledge, this represents the first test of a low-cost hyperspectral imager in this capacity.

Two key areas within this field were focused on: changes in spectral reflectance as the fruit ages, and the development and identification of fruit bruising. The fruits were imaged over the course of five days in order to detect any pigment variations or bruise development in the affected fruits. During image acquisition, each fruit was placed within the integrating sphere and illuminated as described in Section 3.2.3.1. A 128 × 128 pixel scan with an exposure time of 15 ms per pixel was then acquired. These parameters were selected because they represented a suitable balance between image quality and acquisition speed, allowing for the collection of images with appropriate spatial resolution to define target object features with minimal time restraints. When image capture was not taking place, the fruits were stored under ambient light within the laboratory. From the observed data, the pixels that make up the target object were then averaged to produce one comparable response from each fruit measured, allowing for comparisons to be drawn between different fruits and/or different days over the measurement period. Figure 3.10. displays the reflectance spectrum of a healthy apple over the course of the five-day measurement period.

Whilst the fruit ages, an increase in reflectance is expected to occur as a result of the breakdown and transformation of fruit pigments during the ripening process [18], [32]. This gradual increase in reflectance over time is clearly displayed in the spectra collected using our low-cost hyperspectral imager, correlating well with the results of previous research. Furthermore, the absorption features of the fruit pigments are also clearly visible within this data, notably, the stagnation at ca. 550 nm which can be attributed to anthocyanin absorption, a shoulder at ca. 650 nm related to chlorophyll b absorption, and the distinct loss in reflectance at ca. 675 nm highlighting the presence of chlorophyll a [16], [29]. Whilst the peaks and troughs present within the blue spectrum in this figure may be associated with variations in carotenoids within the fruit [16], the features are not distinct enough in this dataset to pinpoint. It is, therefore, believed that these fluctuations are anomalies resulting from noise located in this section of the dataset related to the limited signal of LED light sources across this spectral region.

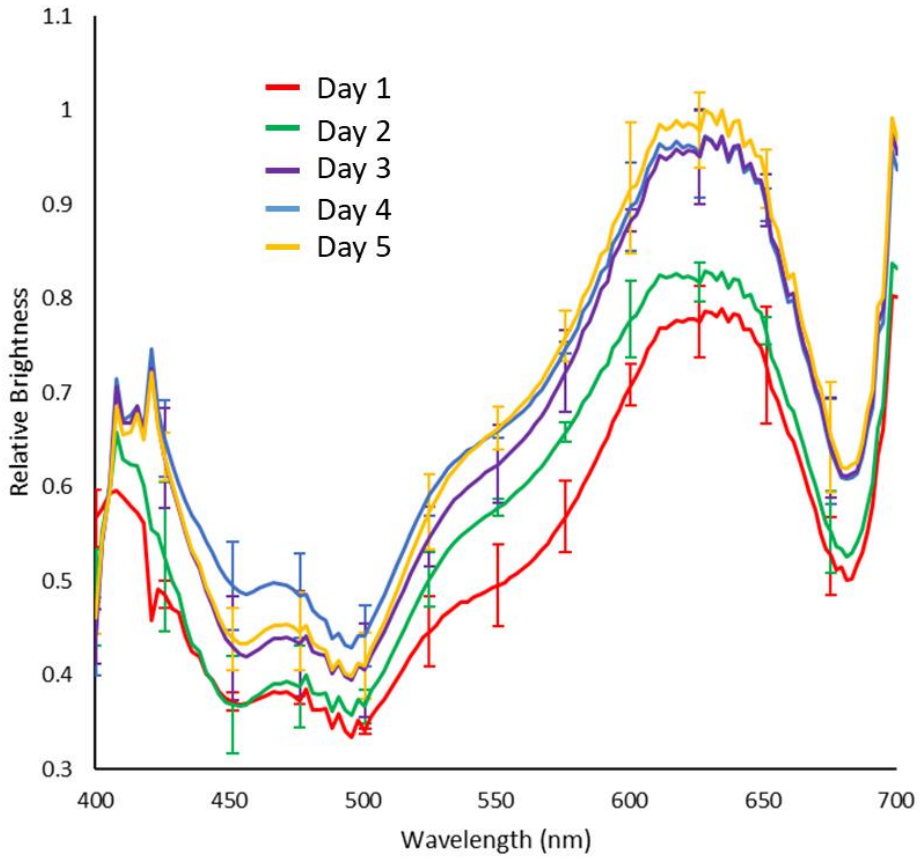

Figure 3.10 Spectral reflectance of a healthy apple measured over a five-day period, highlighting the changes in pigments that occur during the ripening process. Note the absorption features present at ca. 550 nm, ca. 650 nm, and ca. 675 nm. Error bars show the standard deviation.

The incorporation of hyperspectral analysis to fruit quality control was shown to provide significant improvements in the accurate identification of poor-quality, damaged produce [22], [33], [34]. These improvements are further illustrated in the data collected by this research. It is established that, particularly during the early stages, bruise identification can be extremely difficult due to the near invisibility of initial symptoms [26], [35]. Figure 3.11. highlights the varying degrees of bruise detection across the different wavelengths. Bruising is much more obvious at wavelengths across the red–green spectrum due to the increased reflectivity of the healthy tissues at these wavelengths, which emphasises the decreased reflectance of the damaged tissue. Conversely, bruising remains almost invisible in the blue portion of the spectrum due to the generally lower reflectance of fruit tissues at these wavelengths, making the apple appear more homogeneous. Furthermore, the detection of bruising on fruits with darker pigmentations can remain unobvious for extended time periods using standard colour image techniques, increasing the likelihood of deterioration of additional produce within a batch. However, with the use of hyperspectral datasets, which can pinpoint individual wavelength responses, these bruises can be identified much more efficiently [22], [36]. With the introduction of low-cost hyperspectral measurement methods, this level of high-quality produce analysis can become more readily available, providing a substantial advantage to the industry through the introduction of affordable hyperspectral sensors.

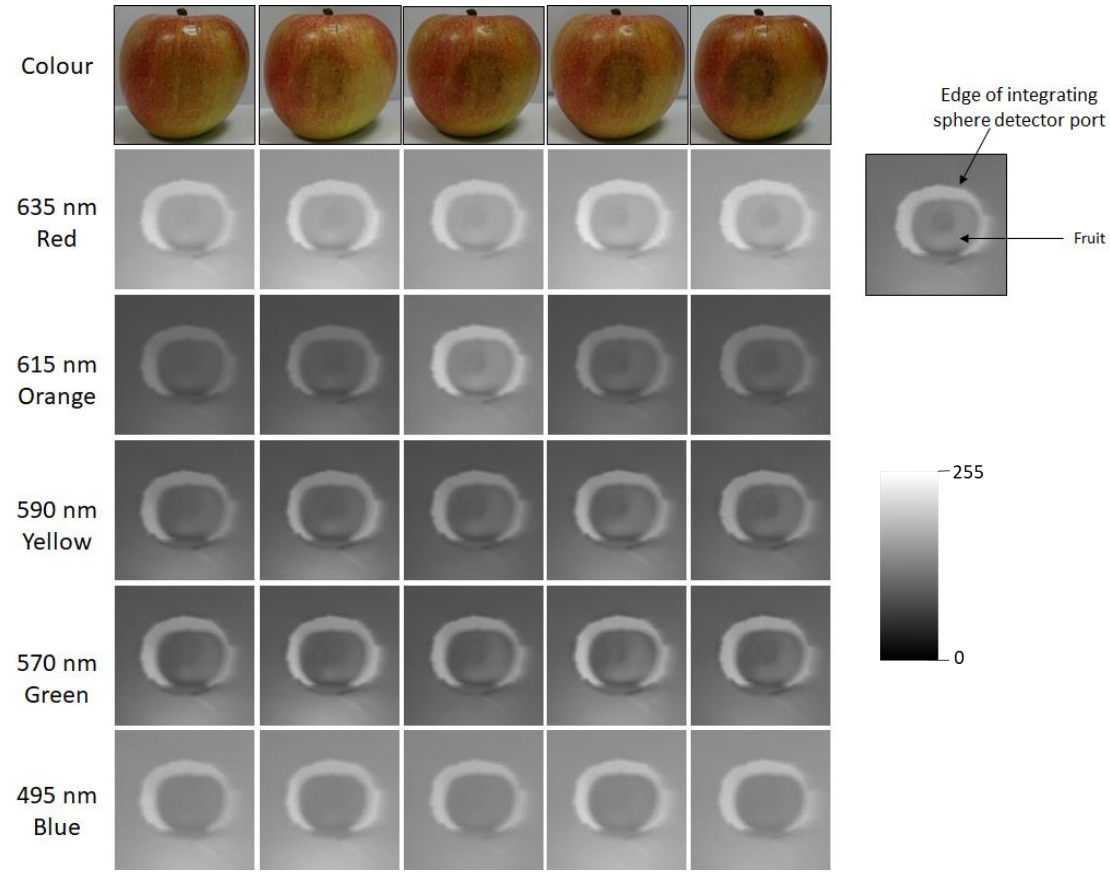

Figure 3.11 Bruise development over the measurement period: comparison between colour and hyperspectral datasets captured with a 128 × 128 pixel scene at 15 ms exposure per pixel. Note the varying levels of detection at different wavelengths. Note, these data are subject to potential temperature instability of the integrating sphere. Scale shows pixel intensity.

Figure 3.12. shows the spectral response data gathered from two fruits. One represents a healthy sample with no defects, the other has impact bruising across its surface. The difference between the spectral responses of these two fruits is clear within the figure, with the bruised fruit showing a general reduction in reflectance across all wavelengths with significant losses present across the ranges of 525 nm – 575 nm and 600nm – 650 nm. The data was further tested to determine whether a statistical difference in spectral response was present. An Anderson-Darling normality test showed a non-normal distribution, therefore, a Mann-Whitney U test was completed, producing a p value of 4.88×10^{-13}. Given that $p < 0.05$ the difference between these spectral response curves can be inferred to be statistically significant.

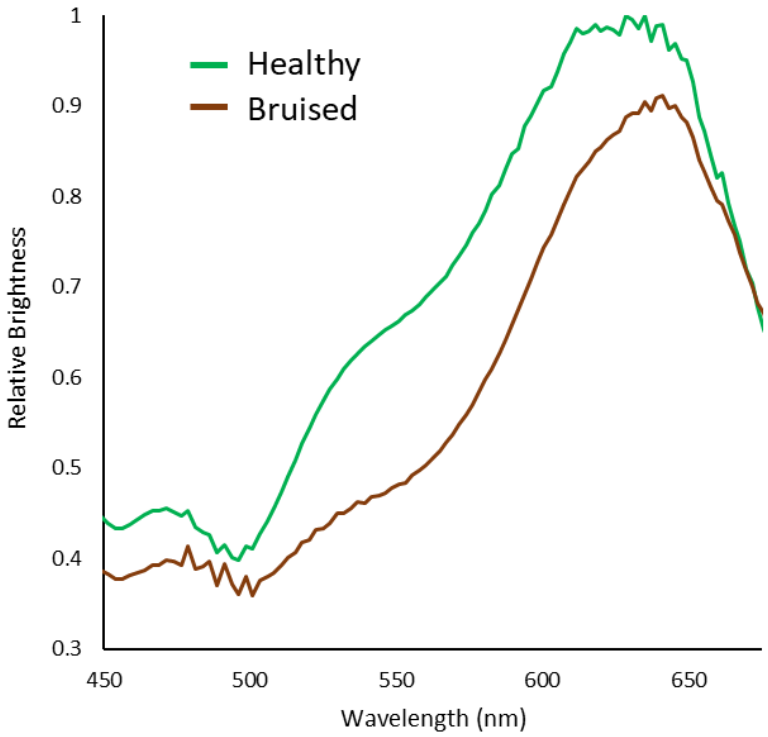

Figure 3.12 Difference in spectral response between bruised and healthy fruit tissues. Note the distinct losses present between 525nm - 575nm and 600nm – 650 nm.

3.4.2. Volcanic Rock Mineralogy

The characterisation of the surface spectral reflectance of volcanic rocks is an important area of research that is seeing a recent increase in popularity [37]. Traditionally, characterisation of these materials is completed through satellite-based remote sensing; however, this is limited by the comparatively low spatial resolution of hyperspectral satellite data, which results in significant spectral mixing [4], [37]. Laboratory-based measurements, therefore, represent a suitable alternative. Previous studies, e.g., Abrams et al. [38], Li et al. [39], Aufaristama et al. [40], and Amici et al. [41], completed spectral analyses on a variety of volcanic rocks providing substantial information about their variable spectral responses. The low-cost hyperspectral imager's abilities in this discipline were, therefore, tested with an outlook to producing a version that can be used in a field setting in future.

A variety of volcanic rocks of differing crystal size were imaged using the hyperspectral imager. A 128 × 128 pixel scan was taken of each rock with an additional 256 × 256 pixel scan which provided a more detailed view of different rock features. These images were acquired with an exposure time of 25 ms. This longer exposure was required due to the more limited reflectance of these objects. Within the rocks sampled, several contained varying crystals, such as flow banding, to determine whether the low-cost imager would be capable of differentiating these variable features. Figure 3.13. displays an example image recorded of an ash tuff with obsidian flow banding. The hyperspectral data demonstrate that this imager is capable of distinguishing between the different rock features present within the sample. Image clarity could be improved with the upgrade of the current lens system as discussed above. An improved optical system, such as a custom design featuring multiple lenses, would be capable of mitigating aberrations, achieving greater image clarity. However, the inclusion of such a system would result in a significant increase in incurred costs and, therefore, does not fit with the aims

of this low-cost design. In its current format, it is clear that the imager is capable of identifying different rock features within a sample, highlighting its potential for growth and development in this field.

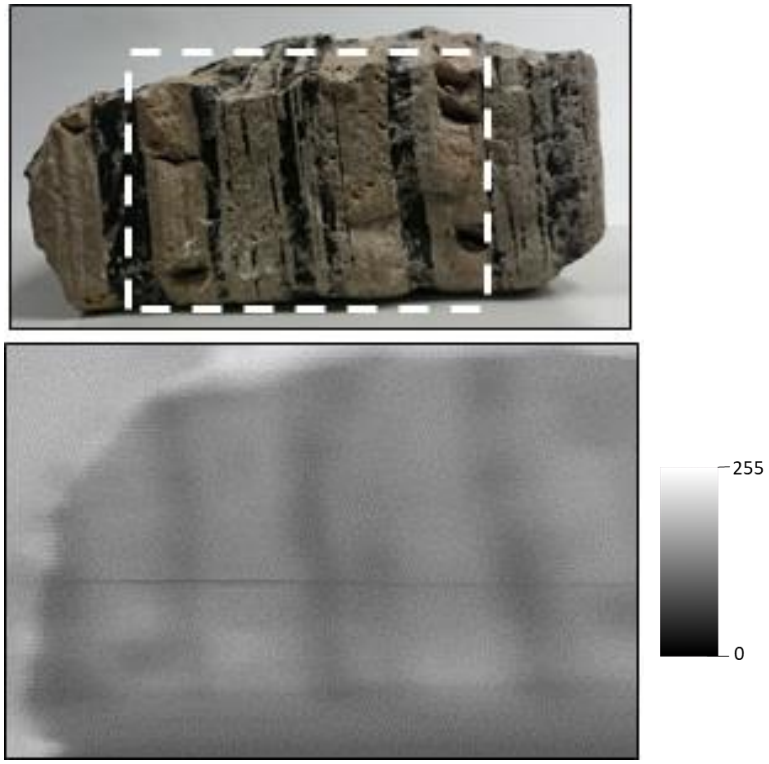

Figure 3.13 Example image captured using the low-cost hyperspectral imager displaying the presence of flow banding. Hyperspectral image taken from 613 nm of a 256 × 256 pixel scan.

Whilst volcanic rocks, such as basalt, obsidian, and andesite, typically display low reflectance values within the visible spectrum, with minor variations resulting from oxidization and/or vegetation growth [38], [39], [41], minerals, such as sulphur display much more distinctive reflectance curves [42], [43]. Figure 3.14**.** shows the reflectance curve obtained from a sulphur rock imaged using the low-cost hyperspectral imager. This figure clearly displays the expected increase in reflectance from ca. 500 nm that is observed with the sulphur mineral, where variations in this curve are believed to relate to the obvious variations across the surface of the rock sample used. Furthermore, Figure 3.15. displays some of the hyperspectral data collected during image acquisition of the sulphur rock. This figure demonstrates the brightest responses present in the yellow and green regions of the spectrum, correlating well with the observed spectral reflectance curve.

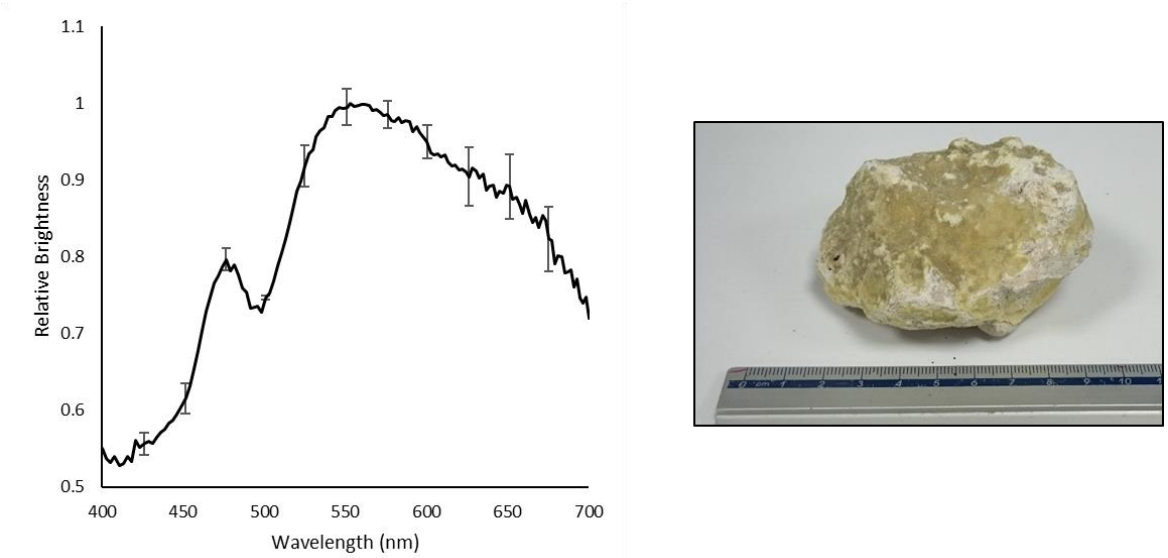

Figure 3.14 Observed spectral reflectance for the sulphur sample (right); note the significant increase in reflectance observed from ca. 500 nm in the spectral data (left). Error bars show the standard deviation.

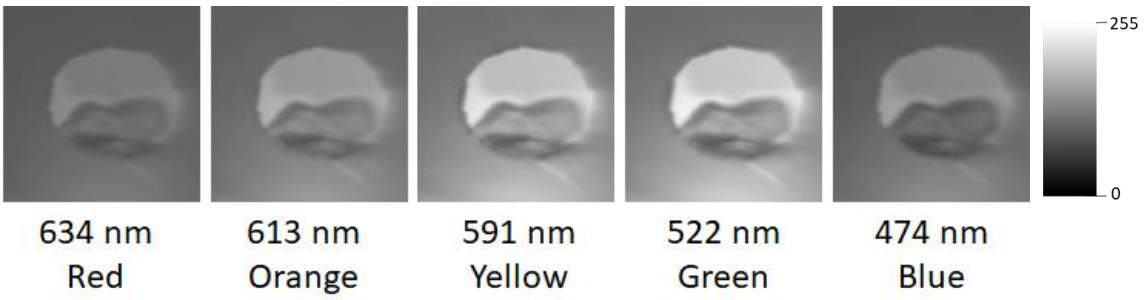

Figure 3.15 Variations in reflectance across the hyperspectral data for the sulphur target. Images taken from a 128 × 128 pixel scan. Scale shows pixel intensity.

The ability to differentiate between the spectral reflectance and identify crystal variations in volcanic rocks is of significant benefit to the research community, helping to improve our knowledge of these changeable environments, as well as providing planetary analogues for ongoing solar system exploration missions [41], [44]–[46]. The results derived from this imager highlight its proficiency within this field. Future work will look to better develop a low-cost hyperspectral set-up in order to allow it to be accurately implemented in a variety of field environments as a low-cost portable imager.

3.4.3. Tooth Shade Determination

The field of dentistry is another area of research where the application of low-cost hyperspectral imaging technologies could prove to be extremely beneficial. Tooth aesthetics play an important role in the appearance of the mouth, and factors such as tooth form, shape, and colour, together with the shape of the dental arches, contribute to this [47]. Accurate tooth colour matching is, therefore, an important consideration when achieving good-quality dentistry. Matching the colour of synthetic tooth replacements to existing teeth can be a challenge, especially for single-unit replacements. Belser et al. [48], proposed a White Aesthetic Score index (WES) to address this issue in single-tooth implants. This index also takes into account other important factors, such as tooth form, volume, outline, surface texture, and translucency. The WES index, whilst originally devised for use in implantology, lends itself nicely to all aesthetically driven restorations, and it encapsulates well the different factors that need

to be considered regarding aesthetic dental restorations. There are different commercially available systems to help the dentist with regard to colour matching; these include visual shade guide systems such as the samples used below (Figure 3.16.), comprising multiple handled tabs of differing hue, value, and chroma, as well as automatic shade determination devices such as colourimeters, digital imaging devices, and spectrophotometers.

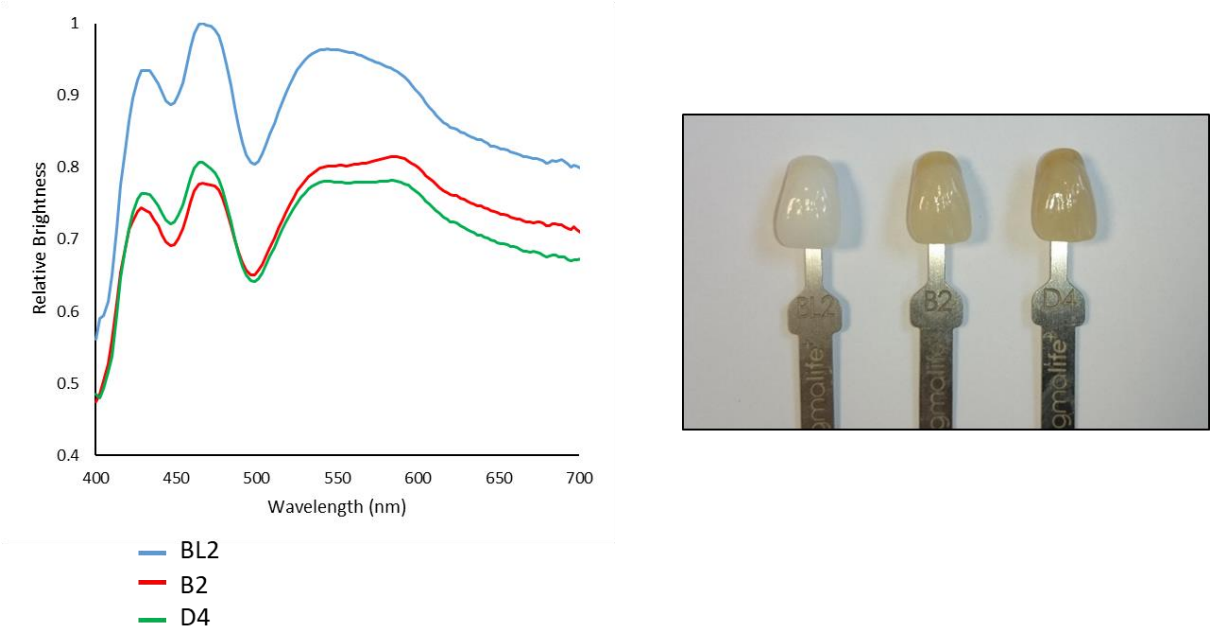

Figure 3.16 Spectral response across the visible spectrum for three dental shade tabs of varying shades.

Visual determination was shown to be very subjective, and is affected by factors such as the quality of background illumination, degree of hydration of the tooth surface, and eye fatigue. [49], [50]. Automatic shade determination technology, therefore, advanced considerably in the last 20–30 years and, while not wholly accurate, it was shown to have good reproducibility and reliability [51]–[53]. Spectrophotometry was shown to be the most precise and accurate method of visual determination; whilst inconsistent, it is not necessarily less precise than colourimetric methods [52], [54]. Hyperspectral imaging has the potential to provide a means of more reliable shade determination. It was, therefore, decided to test the low-cost imager's capabilities in this field.

Three dental tabs of different shades (BL2, B2, and D4) were imaged using the hyperspectral imager set-up described above. These images were captured at 256 × 256 pixels due to the small size of the target objects, with an exposure time of 15 ms per pixel. Figure 3.16. displays the spectral reflectance responses gathered for each shade. In this figure, the varying shades of the tabs are clearly demonstrated; BL2, the tab with the lightest shading, can be seen to produce the highest level of reflectance across all wavelengths measured, with B2 providing a slightly brighter reflectance than D4, as would be expected given the relative shading of these tabs. Furthermore, the spectral response of both B2 and D4 also displays a slight increase in reflectance at ca. 590 nm, whereas BL2 displays a slight drop in reflectance in this region. This more pronounced response from B2 and D4 at this location correlates well with their more yellow colouring compared to BL2. Finally, the spectral responses present in the blue portion of the spectrum could be a result of fluorescing in this region due to its proximity to the ultraviolet spectrum. These results demonstrate the hyperspectral imager's proficiency in tooth shade determination, as it can capably identify the different shades presented to it. This suggests that the imager has significant ongoing potential in this field of study.

3.5. Chapter Summary

This chapter has presented a laboratory-based hyperspectral imager developed from low-cost, commercially available components. This demonstrates that high quality hyperspectral imagers can be successfully constructed from low-cost, accessible components, emphasising the potential available within this field. Imager calibration was provided, enabling the accurate comparison of different samples with traceability to the watt, and the imager's proficiency within several environmental applications was demonstrated, highlighting it to be a valuable, low-cost laboratory measurement tool capable of both quantitative and qualitative hyperspectral measurements. Its current format allows it to complete bench-top measurements; later chapters will use this instrumental design as a foundation for further innovation, with an outlook to the incorporation of low-cost hyperspectral imaging instrumentation in future field deployments. This imager represents an initial development in accessible hyperspectral technologies, providing a basis for future improvements and a steppingstone towards the development of more portable systems. The continued development of these low-cost devices is of significant importance to a variety of laboratory- and field-based applications. Their ability to provide accurate hyperspectral measurements at a fraction of the cost of current systems allows for increased opportunities to gain a better understanding of the processes and products that influence a variety of environmental settings.

3.6. References

[1] M. B. Stuart *et al.*, "Low-cost hyperspectral imaging system: Design and testing for laboratory-based environmental applications," *Sensors (Switzerland)*, vol. 20, no. 11, pp. 1–13, 2020.

[2] A. Habib, T. Zhou, A. Masjedi, Z. Zhang, J. Evan Flatt, and M. Crawford, "Boresight Calibration of GNSS/INS-Assisted Push-Broom Hyperspectral Scanners on UAV Platforms," *IEEE J. Sel. Top. Appl. Earth Obs. Remote Sens.*, vol. 11, no. 5, pp. 1734–1749, 2018.

[3] M. Jaud *et al.*, "Direct georeferencing of a pushbroom, lightweight hyperspectral system for mini-UAV applications," *Remote Sens.*, vol. 10, no. 2, pp. 1–15, 2018.

[4] M. B. Stuart, A. J. S. McGonigle, and J. R. Willmott, "Hyperspectral imaging in environmental monitoring: A review of recent developments and technological advances in compact field deployable systems," *Sensors (Switzerland)*, vol. 19, no. 14, 2019.

[5] F. Sigernes, M. Syrjäsuo, R. Storvold, J. Fortuna, M. E. Grøtte, and T. A. Johansen, "Do it yourself hyperspectral imager for handheld to airborne operations," *Opt. Express*, vol. 26, no. 5, p. 6021, 2018.

[6] H. Aasen, A. Burkart, A. Bolten, and G. Bareth, "Generating 3D hyperspectral information with lightweight UAV snapshot cameras for vegetation monitoring: From camera calibration to quality assurance," *ISPRS J. Photogramm. Remote Sens.*, vol. 108, pp. 245–259, 2015.

[7] E. Honkavaara *et al.*, "Processing and assessment of spectrometric, stereoscopic imagery collected using a lightweight UAV spectral camera for precision agriculture," *Remote Sens.*, vol. 5, no. 10, pp. 5006–5039, 2013.

[8] T. Adão *et al.*, "Hyperspectral imaging: A review on UAV-based sensors, data processing and applications for agriculture and forestry," *Remote Sens.*, vol. 9, no. 11, 2017.

[9] G. Rateni, P. Dario, and F. Cavallo, "Smartphone-based food diagnostic technologies: A review," *Sensors (Switzerland)*, vol. 17, no. 6, 2017.

[10] Y. Vanbrabant, L. Tits, S. Delalieux, K. Pauly, W. Verjans, and B. Somers, "Multitemporal chlorophyll mapping in pome fruit orchards from remotely piloted aircraft systems," *Remote Sens.*, vol. 11, no. 12, 2019.

[11] R. Garzonio, B. di Mauro, R. Colombo, and S. Cogliati, "Surface reflectance and sun-induced fluorescence spectroscopy measurements using a small hyperspectral UAS," *Remote Sens.*, vol. 9, no. 5, pp. 1–24, 2017.

[12] C. Zhu, M. J. Hobbs, R. C. Masters, C. Rodenburg, and J. R. Willmott, "An accurate device for apparent emissivity characterization in controlled atmospheric conditions up to 1423 K," *IEEE Trans. Instrum. Meas.*, vol. 69, no. 7, pp. 4210–4221, 2020.

[13] T. M. Karlsson, H. Grahn, B. van Bavel, and P. Geladi, "Hyperspectral imaging and data analysis for detecting and determining plastic contamination in seawater filtrates," *J. Near Infrared Spectrosc.*, vol. 24, pp. 141–149, 2016.

[14] A. Dal Farra, S. Kaspari, J. Beach, T. D. Bucheli, M. Schaepman, and M. Schwikowski, "Spectral signatures of submicron scale light-absorbing impurities in snow and ice using hyperspectral microscopy," *J. Glaciol.*, vol. 64, no. 245, pp. 377–386, 2018.

[15] A. Wendel and J. Underwood, "Illumination compensation in ground based hyperspectral imaging," *ISPRS J. Photogramm. Remote Sens.*, vol. 129, pp. 162–178, 2017.

[16] M. N. Merzlyak, A. E. Solovchenko, and A. A. Gitelson, “Reflectance spectral features and non-destructive estimation of chlorophyll, carotenoid and anthocyanin content in apple fruit,” *Postharvest Biol. Technol.*, vol. 27, no. 2, pp. 197–211, 2003.

[17] A. J. Das, A. Wahi, I. Kothari, and R. Raskar, “Ultra-portable, wireless smartphone spectrometer for rapid, non-destructive testing of fruit ripeness,” *Sci. Rep.*, vol. 6, no. April, pp. 1–8, 2016.

[18] A. Solovchenko, O. Chivkunova, A. Gitelson, and M. Merzlyak, “Non-Destructive Estimation Pigment Content, Ripening, Quality and Damage in Apple Fruit with Spectral Reflectance in the Visible Range,” *Fresh Prod.*, vol. 4, no. 1, pp. 91–102, 2010.

[19] J. H. Cheng and D. W. Sun, “Rapid and non-invasive detection of fish microbial spoilage by visible and near infrared hyperspectral imaging and multivariate analysis,” *LWT - Food Sci. Technol.*, vol. 62, no. 2, pp. 1060–1068, 2015.

[20] H. Pu, D. Liu, L. Wang, and D.-W. Sun, “Soluble Solids Content and pH Prediction and Maturity Discrimination of Lychee Fruits Using Visible and Near Infrared Hyperspectral Imaging,” *Food Anal. Methods*, vol. 9, no. 1, pp. 235–244, 2016.

[21] S. Jarolmasjed, L. R. Khot, and S. Sankaran, “Hyperspectral imaging and spectrometry-derived spectral features for bitter pit detection in storage apples,” *Sensors (Switzerland)*, vol. 18, no. 5, 2018.

[22] T. Wang, J. Chen, Y. Fan, Z. Qiu, and Y. He, “SeeFruits: Design and evaluation of a cloud-based ultra-portable NIRS system for sweet cherry quality detection,” *Comput. Electron. Agric.*, vol. 152, no. July, pp. 302–313, 2018.

[23] J. Li, W. Luo, Z. Wang, and S. Fan, “Early detection of decay on apples using hyperspectral reflectance imaging combining both principal component analysis and improved watershed segmentation method,” *Postharvest Biol. Technol.*, vol. 149, no. November 2018, pp. 235–246, 2019.

[24] T. Ma, X. Li, T. Inagaki, H. Yang, and S. Tsuchikawa, “Noncontact evaluation of soluble solids content in apples by near-infrared hyperspectral imaging,” *J. Food Eng.*, vol. 224, pp. 53–61, 2018.

[25] W. Che *et al.*, “Pixel based bruise region extraction of apple using Vis-NIR hyperspectral imaging,” *Comput. Electron. Agric.*, vol. 146, no. February, pp. 12–21, 2018.

[26] J. Xing, C. Bravo, P. T. Jancsók, H. Ramon, and J. De Baerdemaeker, “Detecting bruises on ‘Golden Delicious’ apples using hyperspectral imaging with multiple wavebands,” *Biosyst. Eng.*, vol. 90, no. 1, pp. 27–36, 2005.

[27] L. M. Dale *et al.*, “Hyperspectral imaging applications in agriculture and agro-food product quality and safety control: A review,” *Appl. Spectrosc. Rev.*, vol. 48, no. 2, pp. 142–159, 2013.

[28] A. Hussain, H. Pu, and D. W. Sun, “Innovative nondestructive imaging techniques for ripening and maturity of fruits – A review of recent applications,” *Trends Food Sci. Technol.*, vol. 72, no. December 2017, pp. 144–152, 2018.

[29] M. A. Hossain, J. Canning, K. Cook, and A. Jamalipour, “Optical fiber smartphone spectrometer,” *Opt. Lett.*, vol. 41, no. 10, p. 2237, 2016.

[30] R. Beghi, A. Spinardi, L. Bodria, I. Mignani, and R. Guidetti, “Apples Nutraceutic Properties Evaluation Through a Visible and Near-Infrared Portable System,” *Food Bioprocess Technol.*, vol. 6, no. 9, pp. 2547–2554, 2013.

[31] A. J. S. McGonigle *et al.*, “Smartphone spectrometers,” *Sensors (Switzerland)*, vol. 18, no. 1, pp.

1–15, 2018.

[32] O. B. Chivkunova, A. E. Solovchenko, S. G. Sokolova, M. N. Merzlyak, I. V. Reshetnikova, and A. A. Gitelson, “Reflectance Spectral Features and Detection of Superficial Scald – induced Browning in Storing Apple Fruit,” *J. Russ. Phytopathol. Soc.*, vol. 2, no. June, pp. 73–77, 2001.

[33] S. Gutiérrez, A. Wendel, and J. Underwood, “Spectral filter design based on in-field hyperspectral imaging and machine learning for mango ripeness estimation,” *Comput. Electron. Agric.*, vol. 164, no. July, p. 104890, 2019.

[34] I. Tahmasbian *et al.*, “Using laboratory-based hyperspectral imaging method to determine carbon functional group distributions in decomposing forest litterfall,” *Catena*, vol. 167, no. August 2017, pp. 18–27, 2018.

[35] N. Wang and G. El Masry, “Bruise detection of apples using hyperspectral imaging,” in *Hyperspectral Imaging for Food Quality Analysis and Control*, 2010, pp. 295–320.

[36] M. S. Kim, Y. R. Chen, and P. M. Mehl, “Hyperspectral reflectance and fluorescence imaging system for food quality and safety,” *Trans. Am. Soc. Agric. Eng.*, vol. 44, no. 3, pp. 721–729, 2001.

[37] M. Aufaristama, A. Hoskuldsson, M. O. Ulfarsson, I. Jonsdottir, and T. Thordarson, “The 2014-2015 lava flow field at Holuhraun, Iceland: Using airborne hyperspectral remote sensing for discriminating the lava surface,” *Remote Sens.*, vol. 11, no. 5, 2019.

[38] M. Abrams, E. Abbott, and A. Kahle, “Combined use of visible, reflected infrared, and thermal infrared images for mapping Hawaiian lava flows,” *J. Geophys. Res.*, vol. 96, no. B1, pp. 475–484, 1991.

[39] L. Li, C. Solana, F. Canters, J. C. W. Chan, and M. Kervyn, “Impact of environmental factors on the spectral characteristics of lava surfaces: Field spectrometry of basaltic lava flows on tenerife, Canary Islands, Spain,” *Remote Sens.*, vol. 7, no. 12, pp. 16986–17012, 2015.

[40] M. Aufaristama, Höskuldsson, I. Jónsdóttir, and R. Ólafsdóttir, “Mapping and Assessing Surface Morphology of Holocene Lava Field in Krafla (NE Iceland) Using Hyperspectral Remote Sensing,” *IOP Conf. Ser. Earth Environ. Sci.*, vol. 29, no. 1, 2016.

[41] S. Amici, A. Piscini, and M. Neri, “Reflectance Spectra Measurements of Mt. Etna: A Comparison with Multispectral/Hyperspectral Satellite,” *Adv. Remote Sens.*, vol. 03, no. 04, pp. 235–245, 2014.

[42] T. H. Burbine, T. J. McCoy, and E. . Cloutis, “Reflectance spectra of Aubrites, Sulfides, and E Asteroids: Possible implications for Mercury,” in *Mercury: Space Environment, Surface, and Interior*, 2001.

[43] R. N. Clark, “Spectroscopy of rocks and minerals, and principle of spectroscopy,” in *Manual of Remote Sensing*, 1999, pp. 3–58.

[44] F. Capaccioni *et al.*, “Mars-IRMA: In-situ infrared microscope analysis of Martian soil and rock samples,” *Adv. Sp. Res.*, vol. 28, no. 8, pp. 1219–1224, 2001.

[45] M. Sgavetti *et al.*, “Two geologic systems providing terrestrial analogues for the exploration of sulfate deposits on Mars: Initial spectral characterization,” *Planet. Space Sci.*, vol. 57, no. 5–6, pp. 614–627, 2009.

[46] S. Amici, A. Piscini, M. F. Buongiorno, and D. Pieri, “Geological classification of Volcano Teide by hyperspectral and multispectral satellite data,” *Int. J. Remote Sens.*, vol. 34, no. 9–10, pp. 3356–3375, May 2013.

[47] P. K. Vallittu, A. S. J. Vallittu, and V. P. Lassila, “Dental aesthetics - A survey of attitudes in different groups of patients,” *J. Dent.*, vol. 24, no. 5, pp. 335–338, 1996.

[48] U. C. Belser, L. Grütter, F. Vailati, M. M. Bornstein, H.-P. Weber, and D. Buser, “Outcome Evaluation of Early Placed Maxillary Anterior Single-Tooth Implants Using Objective Esthetic Criteria: A Cross-Sectional, Retrospective Study in 45 Patients With a 2- to 4-Year Follow-Up Using Pink and White Esthetic Scores,” *J. Periodontol.*, vol. 80, no. 1, pp. 140–151, Jan. 2009.

[49] A. Watts and M. Addy, “Watts, A., & Addy, M. (2001). Tooth discolouration and staining: Tooth discolouration and staining: a review of the literature. British Dental Journal, 190(6), 309–316. doi:10.1038/sj.bdj.4800959 url to share this paper: sci-hub.tw/10.1038/sj.bdj.4800959,” *Br. Dent. J.*, vol. 190, no. 6, pp. 309–316, 2001.

[50] A. Hill, “How we see colour,” in *Colour Physics for Industry*, 1987, pp. 211–281.

[51] S. Okubo, A. Kanawati, M. Richards, and S. Childress, “Evaluation of visual and instrument shade matching,” *J. Prosthet. Dent*, vol. 80, pp. 642–648, 1998.

[52] H. Chen *et al.*, “A systematic review of visual and instrumental measurements for tooth shade matching.,” *Quintessence Int.*, vol. 43, no. 8, pp. 649–659, Sep. 2012.

[53] K. Lehmann, A. Devigus, S. Wentaschek, C. Igiel, H. Scheller, and R. Paravina, “Comparison of visual shade matching and electronic color measurement device.,” *Int. J. Esthet. Den*, vol. 12, pp. 396–404, 2017.

[54] J. Raghunathan, A. Ramesh, K. Prabhu, and R. Gayathri, “A systematic review of efficacy of shade matching in prosthodontics,” *Int. J. Recent Sci. Res.*, vol. 7, pp. 9949–9954, 2016.

Chapter 4

Hyperspectral Smartphone: Development of a Smartphone-Based Portable Hyperspectral Imager

This chapter is associated with the work presented in Stuart et al., [1] and Davies et al., [2]. It builds on the narrative of the previous chapter as we progress from a laboratory-based instrument to a more field-ready design. This chapter discusses the development of the Hyperspectral Smartphone from a very low-cost teaching and demonstration aid, to a valuable low-cost, field portable hyperspectral imager capable of hand-held hyperspectral data collection. Device metrology is presented alongside several environmental application scenarios as well as a direct comparison of the Hyperspectral Smartphone and the Laboratory-based Hyperspectral Imager from Chapter 3.

4.1. Introduction

Portability and ease of deployment in a range of environmental settings are factors that greatly influence the data collection potential of an instrument. If an instrument is bulky and, therefore, difficult to manoeuvre its suitability is limited significantly to only the most accessible of locations. This has a cumulative effect, often resulting in a lack of high quality datasets from more remote locations, limiting our knowledge of these environmental settings and, therefore, limiting our understanding of these important locations. This has become more apparent in recent years as the climate crisis continues to progress, systematically highlighting the limitations of our current understanding as increasing numbers of environmental settings are affected by and begin to adapt to the changing climate. This is a particular issue for a variety of more extreme environmental settings, due to the substantial impact that these changes will have on these already dynamic settings, with subsequent changes having potentially far reaching implications far beyond the immediate academic community. It is, therefore, key that we work to better understand these settings not just for the benefit of academic research but for local communities and the general public. The development of more portable, low-cost instruments is, therefore, of paramount importance.

The rapid progression of smartphone technologies in recent years has led to a significant uptake in smartphone-based components in the design of optical sensing technologies. The inclusion of these consumer market components provides a significant advantage to device developers due to the substantial reduction in costs provided by the off-the-shelf nature of these components [3], [4]. Furthermore, the increased processing power and the high-resolution camera systems often associated with these low-cost devices provides substantial opportunities to develop state-of-the-art optical sensing technologies at a fraction of the cost of currently available systems without compromising on the data quality captured. To date, smartphone technologies have been utilised in a variety of devices such as smartphone spectrometers [5]–[7] and multispectral sensors [8]–[10]. These devices have been implemented in a wide variety of settings, from point-of-care analysis to environmental monitoring applications. As such, smartphones represent one of the most promising platforms for the development of cost-effective portable measurement technologies.

More recently, there has been a drive toward developing smartphone-based hyperspectral imaging to provide a level of data resolution not possible with single pixel and multispectral designs. A number of studies have produced low-cost hyperspectral imagers either comprised of smartphone components or capable of communication with a smartphone for data viewing processes, e.g., [11]–[14]. Furthermore, studies such as those of He and Wang [15] and Park et al. [16] have developed smartphone-based hyperspectral imagers through the virtual transformation of the RGB data acquired by the built-in camera sensor. Whilst the examples above demonstrate that accessibility is beginning to improve, affordable, field deployable hyperspectral sensors remain in short supply across a wide range of application areas [17], with the increasing focus on our changing climate highlighting the growing need for low-cost, field deployable hyperspectral sensors across environmental monitoring applications. By developing a range of low-cost, portable hyperspectral sensors, we increase the potential for valuable data collection across a wider range of key environmental areas. This, in turn, allows us to improve our understanding of the processes that effect these highly important, dynamic environments.

To date, very low-cost spectrometers have been designed for incorporation with smartphone devices. These devices have largely been designed as teaching aids, providing easily accessible, educational set-ups, for example, Public Lab [18], presents a simple papercraft spectrometer, where a cardboard housing and a simple diffraction grating utilising a digital video disc (DVD) fragment are used to capture a spectral dataset from a smartphone camera. Whilst this simple design does allow for spectral datasets to be observed, its basic components limit its potential uses, for example, the use of a DVD fragment as a diffraction grating substitute can introduce potential data quality issues, resulting from scattered light interference as well as transmittance shifts leading to the intensity variations of imaged objects at each wavelength of interest [19]–[21]. Despite these limitations, this basic design highlights the potential available for low-cost, accessible, smartphone-based data collection. This chapter, aims to demonstrate the opportunities available for low-cost smartphone-based sensing units through the construction of a low-cost unit capable of accurate, field-based data collection. Building on the work of Chapter 3, using the knowledge obtained from the development of the low-cost laboratory-based hyperspectral imager to progress from a laboratory system to a universally accessible, fully portable design. This chapter creates a narrative that develops from a very low-cost demonstrative hyperspectral imager that utilises the Public Lab spectrometer design, to a robust field deployable instrument capable of accurate hand-held hyperspectral image capture. It goes on to introduce a low-cost, field deployable system where a standard smartphone can be utilised as a hyperspectral imager through the addition of a 3-D printed attachment. This device is capable of data capture across the visible spectrum (400 –700 nm) and represents a valuable, easily implemented design, which, to the best of my knowledge, is the first fully incorporated smartphone-based hyperspectral imaging system of its kind. Instrumental improvements and further testing are discussed resulting in a fully portable, hand-held low-cost hyperspectral imaging instrument that is capable of robust and accurate data capture in a range of environmental conditions.

4.2. Initial Design – A Very Low-Cost Test Instrument

To first test the hypothesis and determine the feasibility of this method of smartphone-based hyperspectral data capture a basic cardboard prototype based on the Public Lab spectrometer design was developed. Whilst the Public Lab instrument is designed to capture a single point spectral dataset, the cardboard prototype designed here was adapted for hyperspectral data capture. This set-up, shown in Figure 4.1., consists of a cardboard housing and a DVD fragment that acts as a rudimentary diffraction grating. The cardboard housing is attached in front of the rear facing smartphone camera ensuring alignment between the camera optics, the diffraction grating, and the entrance slit. The

entrance slit, in this design, acts as a spatial filter, restricting the FOV of the smartphone camera optics, whilst the DVD diffraction grating is situated immediately in front of the smartphone camera lens and provides the angular dispersion of the incident light rays. It should be noted that the wavelength dispersion provided by this very low-cost set-up is not reliable and it is subsequently affected by sizeable spatial-spectral distortions. It is, therefore, incapable of robust hyperspectral measurements, however, despite these limitations this set-up is sufficient to demonstrate the concept of this data capture methodology. The simplicity of this design allows it to be constructed and utilised by any individual with access to a smartphone, providing a valuable teaching and demonstration aid.

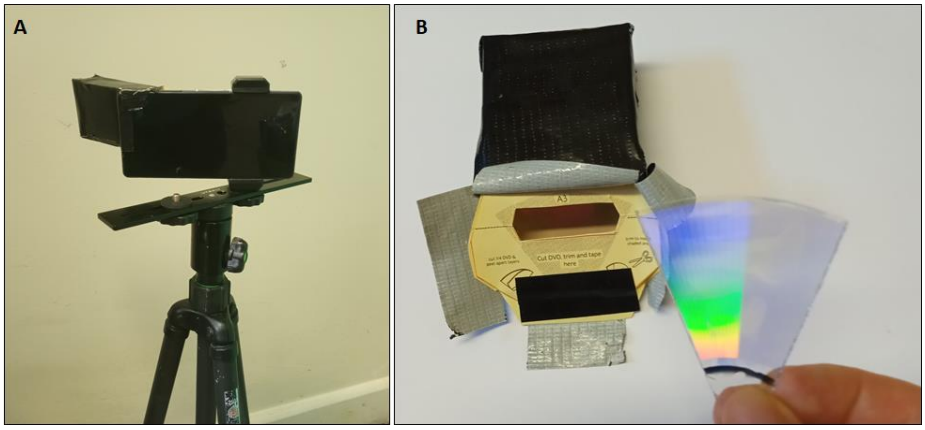

Figure 4.1 The initial prototype design. A shows the attachment connected to a smartphone and mounted to a tripod. B shows the paper craft attachment and an example DVD fragment diffraction grating which is attached to the housing on the reverse of the exposed panel.

The greatest limitation associated with this basic design is the DVD fragment diffraction grating. The use of the grooved polycarbonate substrate of a DVD as a transmission diffraction grating, compared to a commercial diffraction grating has the following drawbacks. Firstly, the finish of the DVD surfaces, both the grooved surface and the flat surface will not typically be as smooth as that of a commercial diffraction grating. This can result in imperfections which, in turn, can lead to randomly scattered light. Furthermore, the average grating period of a commercial DVD is approximately 710 ± 19 nm, which equates to a groove spacing tolerance of ± 2.68% [19]. This non-periodic error may generate focused stray light on the sensor. Both randomly scattered light and focused stray light reduce the spectrum contrast, therefore, reducing the performance of the set-up. Finally, the spectral transmittance of polycarbonate shifts approximately 8% from 400 nm to 700 nm [20]. This transmittance shift is much higher than the spectral transmittance variation of glass B270 which has a shift of less than 1% from 400 nm to 700 nm [21]. This unwanted transmittance shift will lead to intensity variations of imaged objects at each wavelength of interest which requires further calibration for quantitative measurements. Nevertheless, despite these limitations this very low-cost design is a valuable step towards reliable smartphone-based hyperspectral imaging, highlighting the potential within this application area and providing a foundation for further innovation.

To enable the acquisition of hyperspectral datasets the smartphone was repositioned manually to obtain spatial resolution across the horizontal axis. Image capture was completed using the video function of the smartphone camera. Once recording, the device was tracked left to right across a scene. To ensure a semi-consistent rate of movement, the device was tracked at 1 mm/second intervals across the target. These measurements were completed by eye using a ruler positioned at the bottom of the scene, and a stopwatch. Although this is subject to human error, this method provided a suitable means of scene translation based on the abilities of this initial design. Furthermore, to minimise the influence of image distortion resulting from operator shake, the device was mounted to a tripod with

a basic translation stage allowing for more stable movement in the horizontal plane. Once capture was complete individual frames were extracted from the video file. Further data processing such as bias corrections and the extraction of spectral datasets were also implemented, however, these are discussed in greater detail in Section 4.3.1. in the context of the scientific grade Hyperspectral Smartphone where their discussion is of greater relevance.

4.2.1. Proof of Concept Testing

Whilst previous research has demonstrated that smartphones are capable of detecting and accurately producing spectral datasets from spectrometer designs [5]–[7], further information was required to determine whether this could be progressed towards the production of a spectral image. To test its capabilities, it was decided to recreate the environmental applications utilised within Chapter 3. These particular experiments were replicated because they can be simply implemented and produce rapid results, allowing the potential of this methodology to be quickly determined. Hyperspectral datasets were acquired with the very low-cost set-up of an obsidian flow banded ash tuff rock and a red-green Braeburn apple, to determine how well distinct spatial and spectral variations could be resolved by this method of hyperspectral data capture. Figure 4.2. shows the results obtained from these measurements. Whilst these datasets are clearly severely affected by noise, demonstrating the instruments incompatibility with robust data capture applications, the individual targets can both be identified within the output images. Furthermore, it is clear that spectral variations are also observable in these targets as highlighted in the red, green, and blue channels of the apple dataset. These results clearly demonstrate the potential available in this area of research. If rudimentary, but recognisable, hyperspectral datasets can be obtained from a basic set-up costing ca. £10 to develop, the potential data capture capable of a more robust instrumental design is substantial.

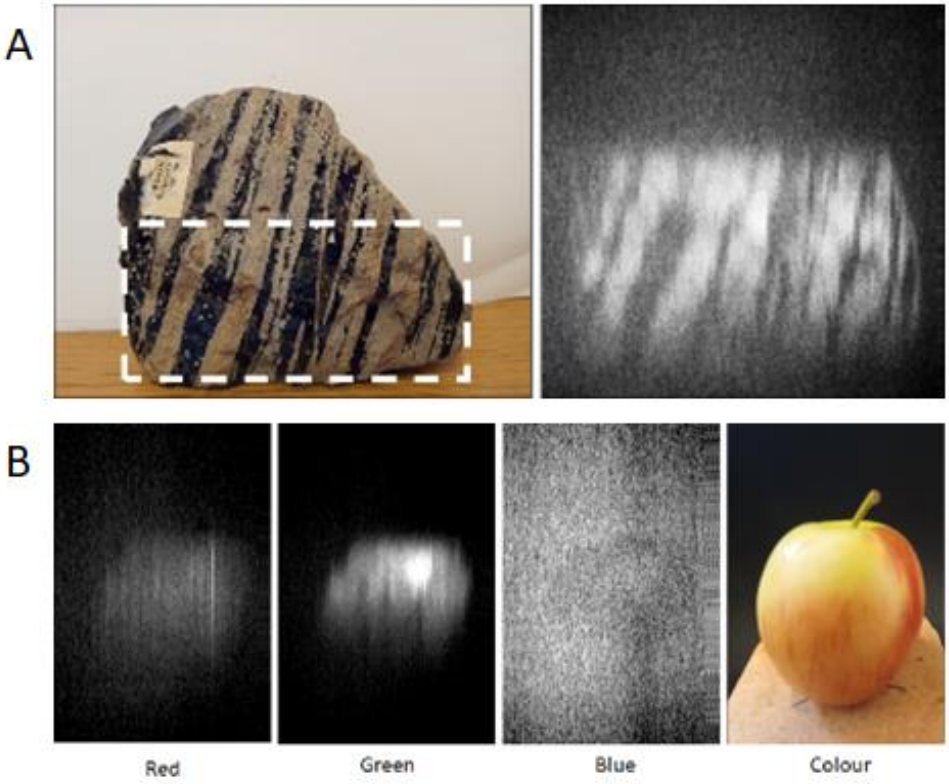

Figure 4.2 Spatial and spectral datasets acquired using the prototype design. A shows an obsidian flow banded ash tuff, B shows a red-green Braeburn apple. Note that despite the noise present within the images the target objects remain recognisable and spectral variations correlate with expectations.

4.3. The Hyperspectral Smartphone

Building on the success of hypothesis testing, the very low-cost prototype was converted into a more robust, scientific grade design. The Hyperspectral Smartphone (Figure 4.3) is comprised of an easily attachable 3-D printed spectral housing containing an Edmund Optics transmission diffraction grating (#49-580). The instrument weighs approximately 210 g (including the approximate weight of the attached smartphone) and has dimensions (length x width x height) of 16 cm x 10 cm x 12 cm. It is intended to be versatile, and as such the attachment grip and spectral housing position are adjustable, increasing usability across a variety of smartphone widths and camera configurations. The 3-D printed housing provides a robust structure, increasing the overall reliability of this design. Furthermore, a standard slit is present within the printed design, which can be narrowed to best fit the intended target scene. The diffraction grating is positioned directly in front of the smartphone camera sensor. To minimise potential light leaks at this location, cushioning foam was attached to provide a secure fit between the smartphone and spectrometer components. This new design can be easily and reliably attached to a wide range of smartphone devices allowing for accurate, repeatable data collection in a range of environmental settings. Furthermore, the optics provide substantial improvements to the quality of data capture possible without introducing significant costs. The Hyperspectral Smartphone costs ca. £100, making it a highly accessible, ultra-low-cost hyperspectral instrument when compared to currently available portable hyperspectral imagers in commercial markets. Table 4.1. shows the cost breakdown of the individual components and their justification.

Table 4.1 Cost breakdown and justification for the Hyperspectral Smartphone.

Component	Cost	Justification
Samsung Galaxy A12 Smartphone	£200*	It was decided to use an easily accessible “budget friendly” smartphone to demonstrate that more expensive state-of-the-art smartphone devices are not required to successfully capture hyperspectral datasets.
Edmund Optics Diffraction Grating #49-580	£95.94	A robust and reliable diffraction grating with a wavelength range matching the abilities of a built-in smartphone camera. Gratings are available from a range of different providers, however, this particular grating was chosen because its physical dimensions, combined with the wavelength range were the best fit for the application.
Total Cost	**£95.94**	
*Note, the cost of the Smartphone is not included within the Total Cost for the instrument because the attachment is designed to be versatile, working with a range of smartphones of higher and lower price points. The cost of the particular smartphone used within this research is, however, provided here for transparency.		

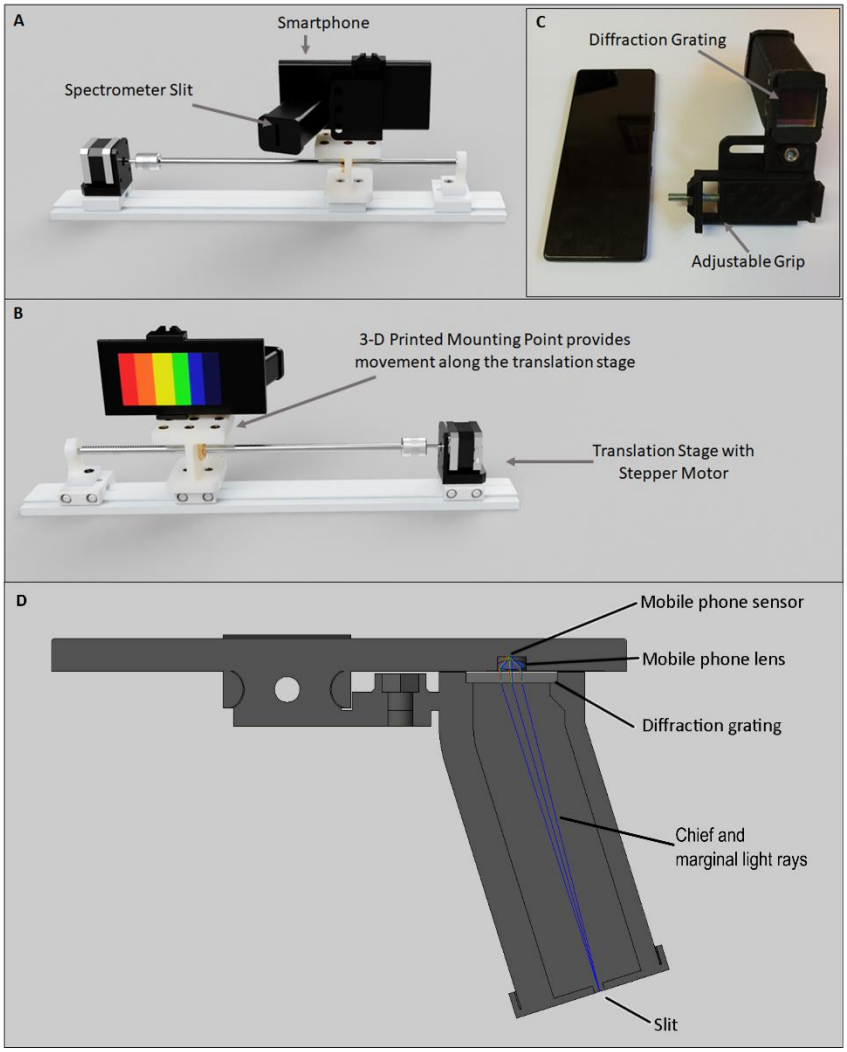

Figure 4.3 Schematic diagram of the Hyperspectral Smartphone mounted to the translation stage. A and B show the front and rear views respectively, C shows the Hyperspectral Smartphone attachment prior to connection with a smartphone, highlighting the location of the spectral optics. D shows a cross section of the smartphone spectrometer system and shows how the marginal and chief rays travel through the system.

4.3.1. Image Capture and Data Processing

The Hyperspectral Smartphone is a push broom style sensor that can be used as either a hand-held or tripod-based instrument; however, it should be noted that, due to operator shake, datasets captured as a hand-held device can be subject to greater distortion, this is discussed in greater detail in Section 4.7. where a MATLAB algorithm is proposed as a means of minimising these distortions to allow for accurate hand-held analysis. At this stage in development, to minimise these effects, the device was mounted on an automated translation stage, where a stepper motor is used to track across the target scene. The slit width of the system is 0.5 mm and the slit-lens distance is 90 mm. The inclusion of the translation stage allows for stable, repeatable scene passes, resulting in clearer datasets. Data collection was completed using the video function of the smartphone camera. For all data collection, the video frame rate was set at 30 fps. Once recording, the device was tracked, left to right, across a scene at 1 mm/sec intervals across the target. When recording scenes within a laboratory setting, the target object is placed within a dark box to minimise the interference of ambient stray light and is illuminated using a 20 Watt LED lamp with a diffuser to minimise bright spots within the scene. Figure 4.4. shows the Hyperspectral Smartphone ready for data collection within a laboratory environment. As mentioned above, the instrument is versatile and can, therefore, be used with a wide range of

smartphones, however, for the purposes of this research, the smartphone used is a Samsung Galaxy A12. The presence of an auto-focus feature within the smartphone camera software is of significant benefit to this instrument, minimising the specialist knowledge required to operate the Hyperspectral Smartphone, and as such, providing a versatile, accessible, user friendly system. A full list of camera specifications for the Galaxy A12 can be found within Table 4.2. The instantaneous field of view (IFOV) [22] for each pixel within the spectrometer image was measured to be approximately 5 mm × 5 mm for a 95% energy enclosure at a working distance of 300 mm. Whilst the total field of view (TFOV) is determined by several factors. At short working distances (on the order of the travel distance) the vertical field of view (VFOV) is determined by the slit height and the distance between the slit and the grating, and the horizontal field of view (HFOV) is determined by the travel distance of the phone. At greater working distances, the acceptance angle of the slit (which is determined by the slit width, height, and distance to the grating) makes a greater contribution to both the HFOV and the VFOV. No additional coupling optics were incorporated before the spectrometer slit.

Table 4.2 Camera specifications for the Samsung Galaxy A12 smartphone.

	Samsung Galaxy A12
Resolution	48 MP (1920 x 1080 for video)
F Number	2.0
Focal Length (mm)	26
Fps	30

Once capture was complete, individual frames were extracted from the video file. Dark and white reference frames were also captured at this stage. To obtain a white reference a piece of matt white card was positioned in place of the target object and illuminated in the same manner. To correct the image frames for illumination and sensor biases whilst preserving the colour data of the output, the following analysis was implemented in MATLAB for each colour region in each frame (Appendix 8.4.).

$$target_{\lambda} = \frac{(target_{raw\ \lambda} - dark_{\lambda})}{(white_{\lambda} - dark_{\lambda})} \cdot \frac{(white_{\lambda_1} - dark_{\lambda_1})}{(target_{raw\ \lambda_1} - dark_{\lambda_1})} \quad (4.1)$$

Where target represents the object to be imaged, and dark and white represent the dark and white references respectively. The subscript raw λ represents an uncorrected spectrum.

In order to calibrate the instrument and to enable samples from different sources to be accurately compared a radiometric assessment of the optical power represented by each pixel within the image was performed by measuring the power reflected by the white reference target. This was performed using a photodiode-based radiometer, as described by Zhu et al. [23], but with its RG850 long-pass filter replaced by a narrow bandpass filter, centred on 550 nm with a full width half maximum of 10 nm (Thorlabs Stock #FB550-10, Ely, UK). By comparing the photocurrent measured by the radiometer with and without the filter in place, the reflected optical power collected by the radiometer could be calculated. Given that the FOV of the radiometer represented an area upon the target of approximately 14 mm in diameter at its 1 m operating distance, the reflected power per unit area, without the filter in place, was calculated from this to be approximately 46.55 µW/m^2. Therefore, the optical power reflected from the white reference target was estimated to be 7.17 nW. For a comparison, the radiometer was sighted at the LED lamp directly, resulting in an optical power measurement of 108.62 nW. These values show that the optical throughput (related to etendue [24]), is approximately 6.6%. Given that each pixel within the image of the spectrometer represents an area of 5 mm × 5 mm, the power collected in total per pixel of the spectrometer is approximately 1.16 nW for the white reference target. In the development of optical instrumentation, a typical 'rule of thumb' is that a good signal to noise ratio can be achieved using a silicon-based detector measuring 1 nW in 1 µm in 1 ms.

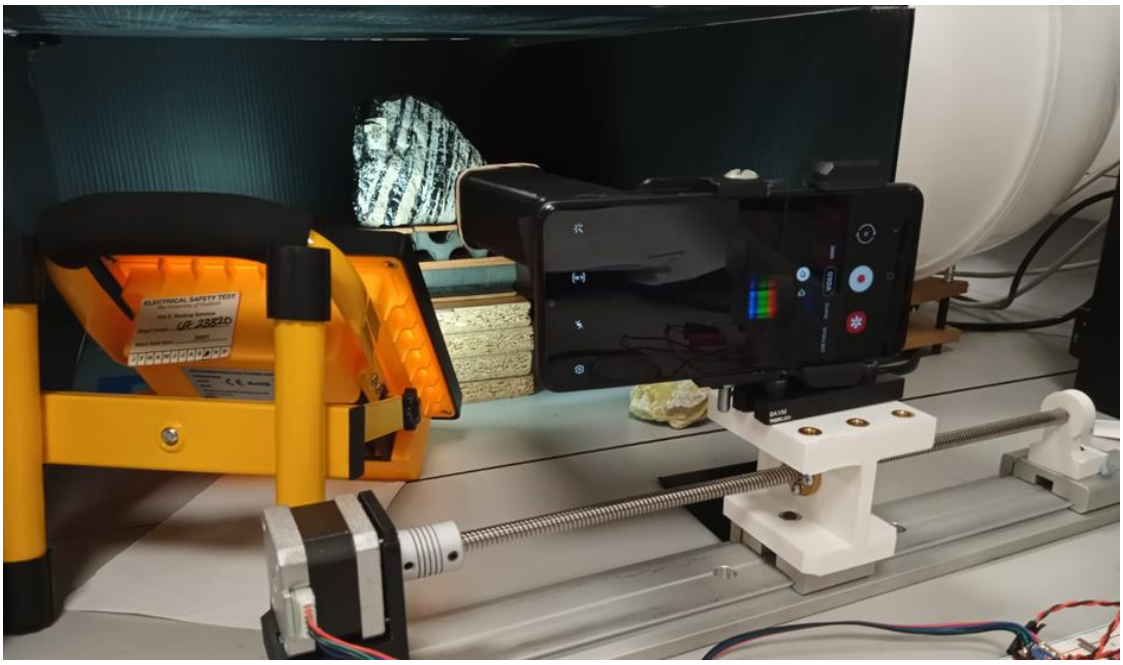

Figure 4.4 The Hyperspectral Smartphone mounted on the translation stage ready to image an obsidian flow banded ash tuff rock within a laboratory setting.

In order to calibrate the instrument spectrally, and to extract a spectral response curve from each corrected image frame the calibration process within the Spectral Workbench software was utilised. This software is also publicly available and accessible from Public Lab [25], further demonstrating the accessible nature of this instrument. To complete the calibration accurately, a separate calibration image needed to be captured, by the instrument, of a fluorescent lamp. Compact fluorescent lamps contain Mercury vapour which, when energised, emits a consistent, characteristic spectrum. Accurate wavelength ranges can then be applied to the image frames by aligning the peaks present at 436 nm and 546 nm, within the software with their respective peaks in the calibration image. The resulting spectral curves were then averaged to provide one comparable spectrum for each target, allowing for direct comparisons to be made between different days and/or different targets. In its current format, the presence of a Bayer colour filter within the smartphone optics will reduce the sensitivity of the

measurements captured with this instrument, however, the following sections demonstrate that this instrument is capable of producing accurate, high quality qualitative datasets. Spatial datasets were created in Origin Pro (2020b) by extracting the pixel values from a specific wavelength/column within each image frame from the chosen scene. These columns were then combined to create a spatial dataset of the target object that displayed the spectral response captured from a specific wavelength. Sections 4.7. and 4.8. discuss improvements to these data processing methods including the introduction of an in-scene calibration reference that can be utilised to obtain quantitative datasets, broadening the applications of this instrument, however, at present I wish to highlight what is possible with this more straightforward approach and, in doing so, demonstrate the substantial potential available in this area of research.

To better understand the spectral capabilities of the Hyperspectral Smartphone the spectral response of a range of block colour targets were measured and compared against a laboratory measured spectrum that was captured using a Thorlabs CCD spectrometer (CCS200). Figure 4.5. shows the spectral response acquired for these targets. Whilst the responses obtained with the Hyperspectral Smartphone are noisier than the laboratory measured responses, the expected trends for each colour remain visible within the dataset, highlighting the potential available for this instrument. However, it is also clear that the presence of a Bayer filter within the smartphone optics has some influence on the output datasets. This is particularly evident in the prominent spectral feature present in all datasets at ca. 575 nm. From this information it can be inferred that the Bayer filter may have some influence on the spectral response in these regions, therefore, potentially impacting the spectral response acquired for different targets. The spectral response of this instrument is improved within Section 4.8.2. where an in-scene reference is developed to mitigate these external influences and improve the spectral outputs of the instrument, however, the data shown in Figure 4.5. is representative of earlier applications of this instrument.

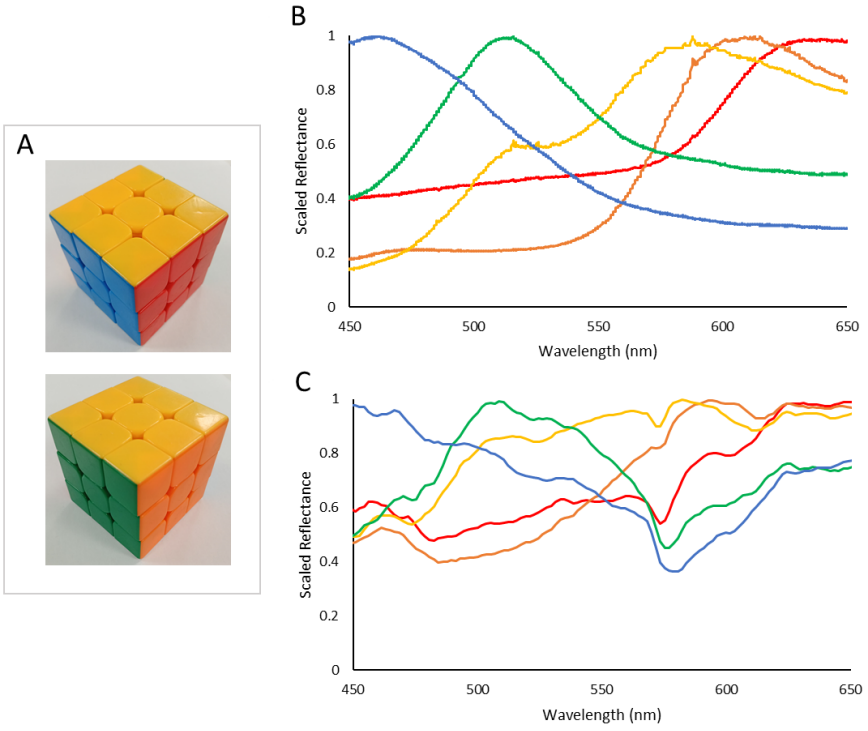

Figure 4.5 Spectral response obtained from colour targets. A shows the colour targets used (red, orange, yellow, green, and blue). B shows the laboratory measured spectrum for these targets, C shows the spectrum acquired using the Hyperspectral Smartphone. The colours of the spectral response curves correspond to their respective colour. Note the similarities present between graphs B and C.

4.4. Early Applications

The laboratory-based environmental applications discussed in Sections 4.4.1. and 4.4.2. below also replicate the experimental work conducted in Chapter 3. It was decided to continue to replicate these experiments with the Hyperspectral Smartphone as their simple implementation and rapid results allow for the capabilities of the instrument to be demonstrated with ease when the resulting datasets are compared to the existing literature. Furthermore, by continuing this narrative it enables the demonstration of the sizeable improvements of the Hyperspectral Smartphone over the very low-cost set-up. Additionally, accurate, low-cost hyperspectral alternatives remain somewhat absent in these contexts at present; therefore, this work aims to provide a foundation for the development of low-cost hyperspectral data collection in these application areas.

4.4.1. Fruit Quality Control and Assessment

Hyperspectral images of a healthy apple fruit were captured every 24 hours over the course of five days in order to observe any potential changes in spectral response associated with the breakdown of pigments during the fruit ripening process [3], [26], [27]. Figure 4.6. shows the observed spectral response curve of the fruit over the five-day measurement period. A clear increase in reflectance over time can be observed which is to be expected during the ripening process [28], [29], emphasising the Hyperspectral Smartphone's capabilities in detecting accurate spectral data. Furthermore, absorption features associated with the pigmentation of the fruit are evident within the dataset; most notably a 'shoulder' starting at ca. 550 nm associated with anthocyanin absorption and a slight 'shoulder' at ca. 650 nm highlighting the absorption of chlorophyll b [26], [30]. The literature also highlights an absorption feature for chlorophyll a, which is represented by a distinct loss in reflectance around ca. 675 nm followed by a rapid increase in reflectance towards the infrared [26], [28]–[30]. Whilst a loss in reflectance is observed in this dataset in this region, the subsequent increase is not present. This is believed to be due to the spectral range of the Hyperspectral Smartphone as this absorption feature is present close to the upper boundary of the instrument's spectral range. It is, therefore, inferred that the reduced sensitivity associated with the edges of the spectral range of the diffraction grating may be resulting in some data loss in this region. Despite these losses, and the potential influence of the Bayer filter within these measurements, this dataset compares favourably with the existing literature, demonstrating a similar spectral response to that shown in [26] showing that the Hyperspectral Smartphone is capable of capturing accurate spectral datasets that are comparable with the existing literature in this field.

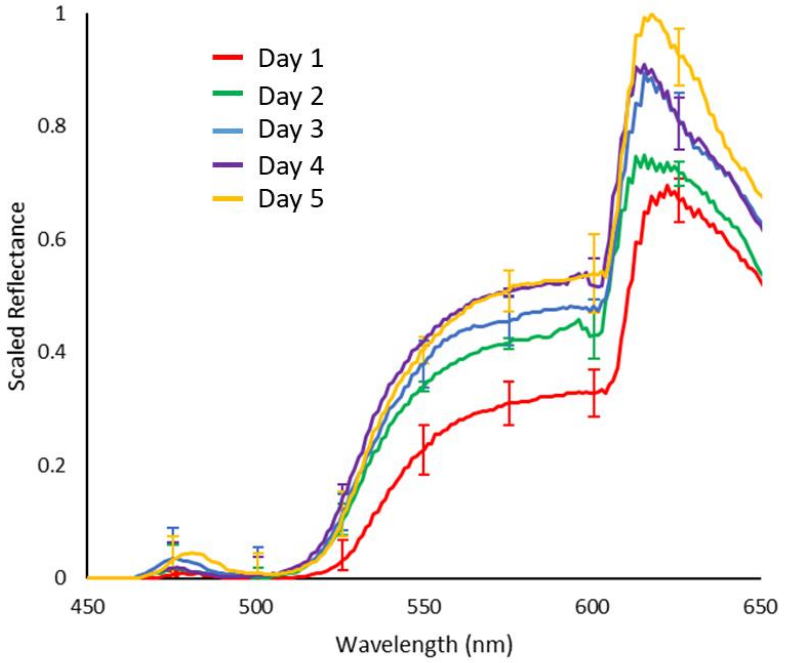

Figure 4.6 Observed spectral response curves of a healthy apple over the five-day measurement period. Note the general increase in reflectance over the measurement period and the absorption features present at ca. 550 nm and 650 nm. Error bars show the standard deviation.

The abilities of the Hyperspectral Smartphone are further illustrated in Figure 4.7. which demonstrates clear spatial data collection which clearly highlights the variations in pigmentation across the apple's surface, and correlates well with the observed spectral response curve. The clarity of the datasets obtained, using the automated translation stage, highlights the significant potential of this device, and indeed smartphone-based hyperspectral devices as a whole. This is particularly relevant given the ultra-low-cost of the instrumentation. The data quality possible with an instrument costing ca. £100, helps to establish that expensive commercial systems, costing upwards of £30,000, are not required for high quality hyperspectral imaging and, as such, the widespread democratisation of these imaging techniques is achievable.

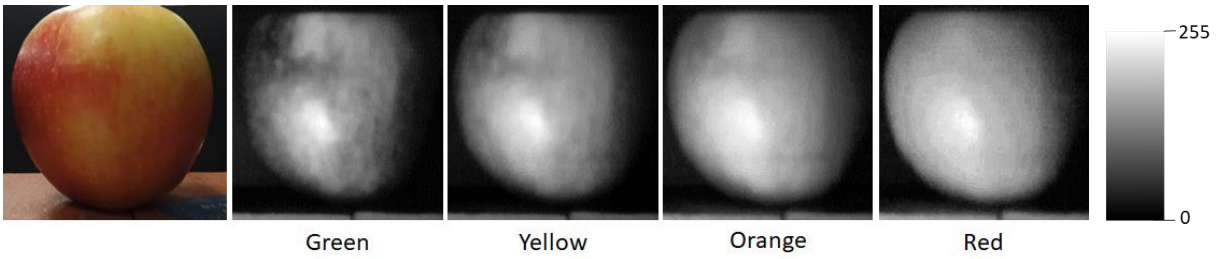

Figure 4.7 Spatial datasets of an apple across different wavelengths. Note the variations in pigments across the spectrum. Displayed wavelengths extracted from the overall data cube. Scale shows pixel intensity.

4.4.2. Volcanic Rock Mineralogy

Volcanic rock images were also captured with the Hyperspectral Smartphone. These images were acquired as a means of demonstrating the device's ability to identify variations and feature changes across a target object's surface. Figure 4.8. shows the hyperspectral data captured of an obsidian flow banded ash tuff. As Figure 4.8**.** shows, this target has clear variations present across its surface. These variations are clearly replicated in the hyperspectral data, adding further support to the capabilities of

this low-cost design. The banding across the rock is easily recognisable within the hyperspectral image, allowing for the straightforward identification of the individual flow bands.

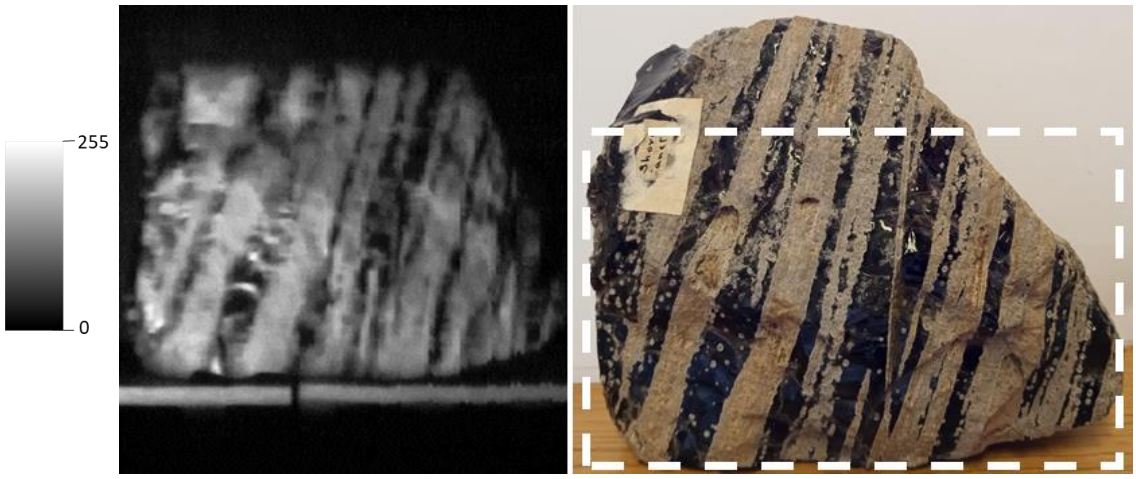

Figure 4.8 Spatial dataset obtained of an obsidian flow banded ash tuff, clearly highlighting the individual flow bands. Hyperspectral dataset taken from ca. 600 nm. Scale shows pixel intensity.

To further demonstrate the spectral capabilities of this instrument a Sulphur rock was imaged. Sulphur was chosen due to its distinctive spectral response where a distinct increase in reflectance is evident from ca. 500 nm [31]. Figure 4.9. shows the spectral response for Sulphur collected by the Hyperspectral Smartphone. This figure clearly shows the expected increase in reflectance from ca. 500 nm emphasising the capabilities of this instrument. The additional variations across the spectrum are likely to be the result of variations present across the surface of the Sulphur target used due to the presence of colour variations across the rock's surface, as highlighted in Figure 4.10. and the potential influence of the Bayer filter within the smartphone optics. However, the key reflectance feature at ca. 500 nm remains prominent within the captured dataset.

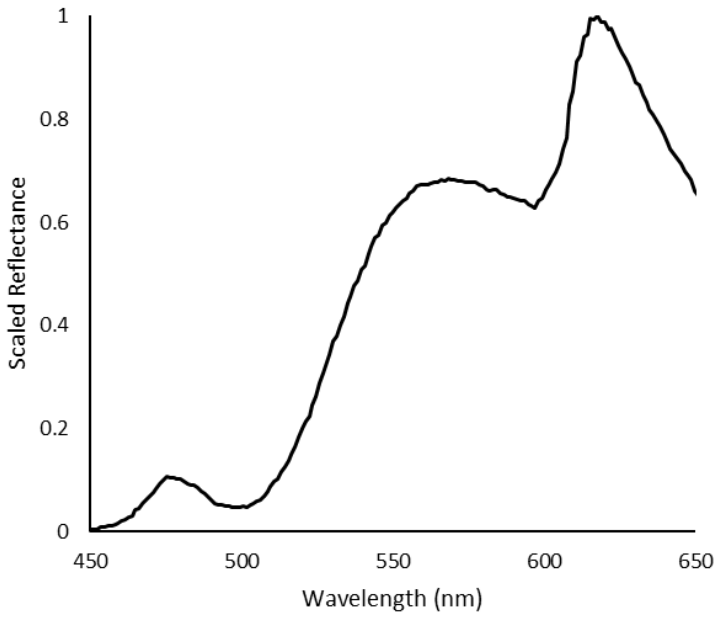

Figure 4.9 Observed spectral curve for a sulphur target. Note the clear increase in reflectance from ca. 500 nm.

.

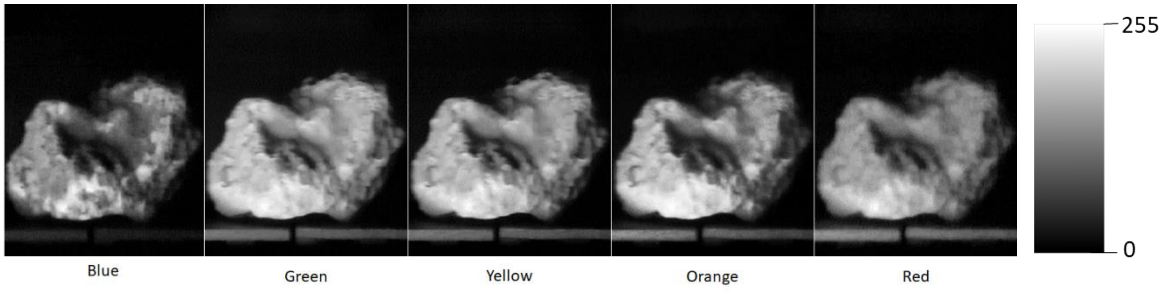

Figure 4.10 Spatial datasets for the sulphur target highlighting the variations in reflectance across the different wavelengths. Scale shows pixel intensity.

4.5. Direct Comparison to the Laboratory-Based Hyperspectral Imager

To further define the quality of the data capture and examine the capabilities of the Hyperspectral Smartphone in more detail at this stage in its development, this instrument was directly compared to the low-cost laboratory-based hyperspectral imager described in Chapter 3. This enables a more extensive understanding of the Hyperspectral Smartphone. By presenting its abilities alongside a pre-existing low-cost instrument it allows it to be determined whether the image capture capabilities, combined with enhanced portability of the Hyperspectral Smartphone provide a more beneficial hyperspectral instrument, enabling high quality data capture in a wider range of application areas.

Table 4.3. provides a direct comparison between the Hyperspectral Smartphone and laboratory-based hyperspectral imager. As Table 4.3. highlights, both instruments represent valuable, low-cost hyperspectral sensors that can be deployed with relative ease, without the need for extensive additional set-up time. Both devices are capable of a range of image capture scenarios and allow the operator to vary the image dimensions to fit the target scene, either through manually editing the dimensions prior to scene capture (Laboratory-Based Hyperspectral Imager), or through the extension of scene capture sweeps (Hyperspectral Smartphone). Whilst the Hyperspectral Smartphone is constrained to the settings available within the built-in smartphone software, it represents a significantly cheaper and, therefore, more accessible hyperspectral imaging sensor, when compared to the laboratory-based imager. Furthermore, the presence of an autofocus feature within the smartphone software allows the Hyperspectral Smartphone to be especially user friendly. However, its spectral range is limited to the visible spectrum, whereas the laboratory-based imager is capable of a broader spectral range and could be converted to cover different regions of the spectrum, such as the infrared, with relative ease [3]. The prominent differences present between both instruments are largely a result of the cost of the components involved and their intended research area. The laboratory-based hyperspectral imager represents a more specialised instrument in this comparison, because it is typically suited to bench-top laboratory analysis, whereas the Hyperspectral Smartphone represents a more accessible design that can be implemented in a range of settings outside the laboratory. As such these differences are clearly represented in the set-up costs associated with each device.

Table 4.3 Direct comparison between the Hyperspectral Smartphone and the laboratory-based hyperspectral imager.

	Hyperspectral Smartphone	**Laboratory-Based Hyperspectral Imager**
Imaging Mode	Push Broom	Whiskbroom
Data Capture Method	System translated by operator	Stationary, mirrors provide movement across scene.
Approximate Cost of Instrument[1]	~£100	<£6,000
Image Capture Dimensions	Variable—can be modified by the operator.	Variable—can be modified by the operator.
Spectral Range (nm)	400 – 700	340 – 850
Spectral Resolution (FWHM nm)	14	12
Operator Input Options	Limited. Exposure settings can only be modified within the constraints of the built-in smartphone software	Variable. Exposure settings and image parameters can be modified by the operator.
Potential Portability	Highly portable. Can be deployed anywhere with sufficient lighting. Capable of both indoor and outdoor data capture.	Limited portability within a laboratory setting.
Additional Equipment Required for Successful Data Capture	Additional illumination required for indoor data collection, e.g., an LED lamp.	Additional LED illumination required. Target object placed in a low-cost integrating sphere during data capture.

[1] These values represent the cost associated with the spectral set-ups and do not include potential additions such as LED lamps. However, these additions are often commonplace within laboratory environments or can be easily purchased for minimal additional cost.

Figure 4.11 provides a side-by-side comparison of apple targets captured by both instruments. As this figure demonstrates, both the Hyperspectral Smartphone and the laboratory-based hyperspectral imager are capable of detecting pigment variations across this type of target. When comparing the two spatial datasets, the Hyperspectral Smartphone appears capable of greater image resolution, however, it should be noted that the optical system present within the laboratory-based instrument represents a basic set-up, as discussed in Chapter 3, and is, therefore, capable of improved image clarity, subject to the inclusion of aberration correcting optics. The Hyperspectral Smartphone benefits from the built-in optical system present within the chosen smartphone, as most smartphones are now capable of high quality image capture and, therefore, aberration correction, it fits that the Hyperspectral Smartphone would be superior in the context of this comparison.

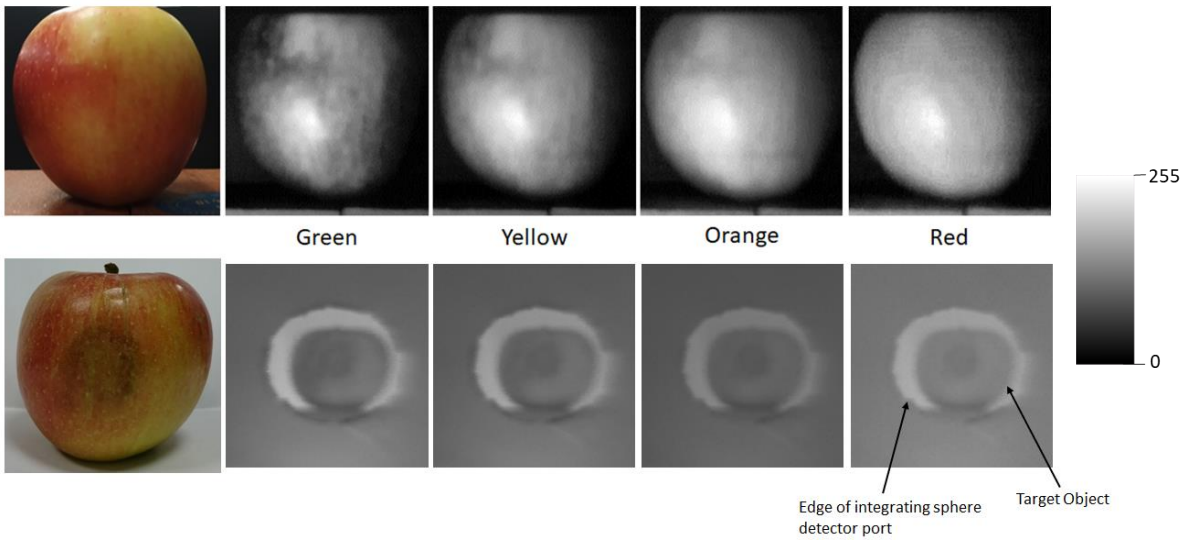

Figure 4.11 Side-by-side comparison of apple targets captured across different wavelengths by both the Hyperspectral Smartphone (top dataset) and the laboratory-based hyperspectral imager (bottom dataset). Note that the apple target is placed within a low-cost integrating sphere during data capture with the laboratory-based instrument. Scale shows pixel intensity.

4.6. A Field Portable Low-Cost Hyperspectral Imager

The above sections have demonstrated the Hyperspectral Smartphone to be a valuable low-cost instrument, capable of high quality, accurate hyperspectral data collection within a laboratory setting. This section will further test its capabilities as a robust, field portable instrument. To do this the Hyperspectral Smartphone, with the translation stage, was mounted to a tripod to allow for stable data capture, and the translation stage converted to battery power. Figure 4.12. shows the Hyperspectral Smartphone in the field, ready for data collection.

Figure 4.12 The Hyperspectral Smartphone ready for data capture within a field setting.

In the field, a variety of targets were imaged in order to determine the Hyperspectral Smartphone's abilities in a field setting at a range of different working distances. For this data collection, measurements were completed within Weston Park, Sheffield. This site was chosen due to the wide range of potential targets available without the need for extended travel, allowing for initial field tests to be completed under COVID-19 travel restrictions. Datasets were captured at both short ca. 1 m and longer ca. 20 m working distances. Figure 4.13. shows the results obtained over a short working distance for a distinct target, in this case a sign within the park. It is clear from this figure that the Hyperspectral Smartphone is capable of clearly defining target object features in this instance, replicating the writing clearly within the spatial data.

Figure 4.13 Spatial dataset captured of a sign within Weston Park over a short working distance.

More intricate targets were also imaged at this working distance, Figure 4.14. shows the spatial and spectral data collected from a section of a flower bed. Whilst some of the details of the target are lost within the spatial datasets, the spectral response variations remain clear, following the expected response from this particular target. These datasets show the Hyperspectral Smartphone to be a valuable short-range field instrument. The spectral response curves compare favourably with the hyperspectral image frames, showing increases in reflectance in predominantly green, yellow and orange regions of the spectrum. Furthermore, the reconstructed RGB image highlights that it is possible to recreate an RGB image that is clearly recognisable as the original target from the hyperspectral image frames, demonstrating the spectral abilities of the instrument at this stage in its development.

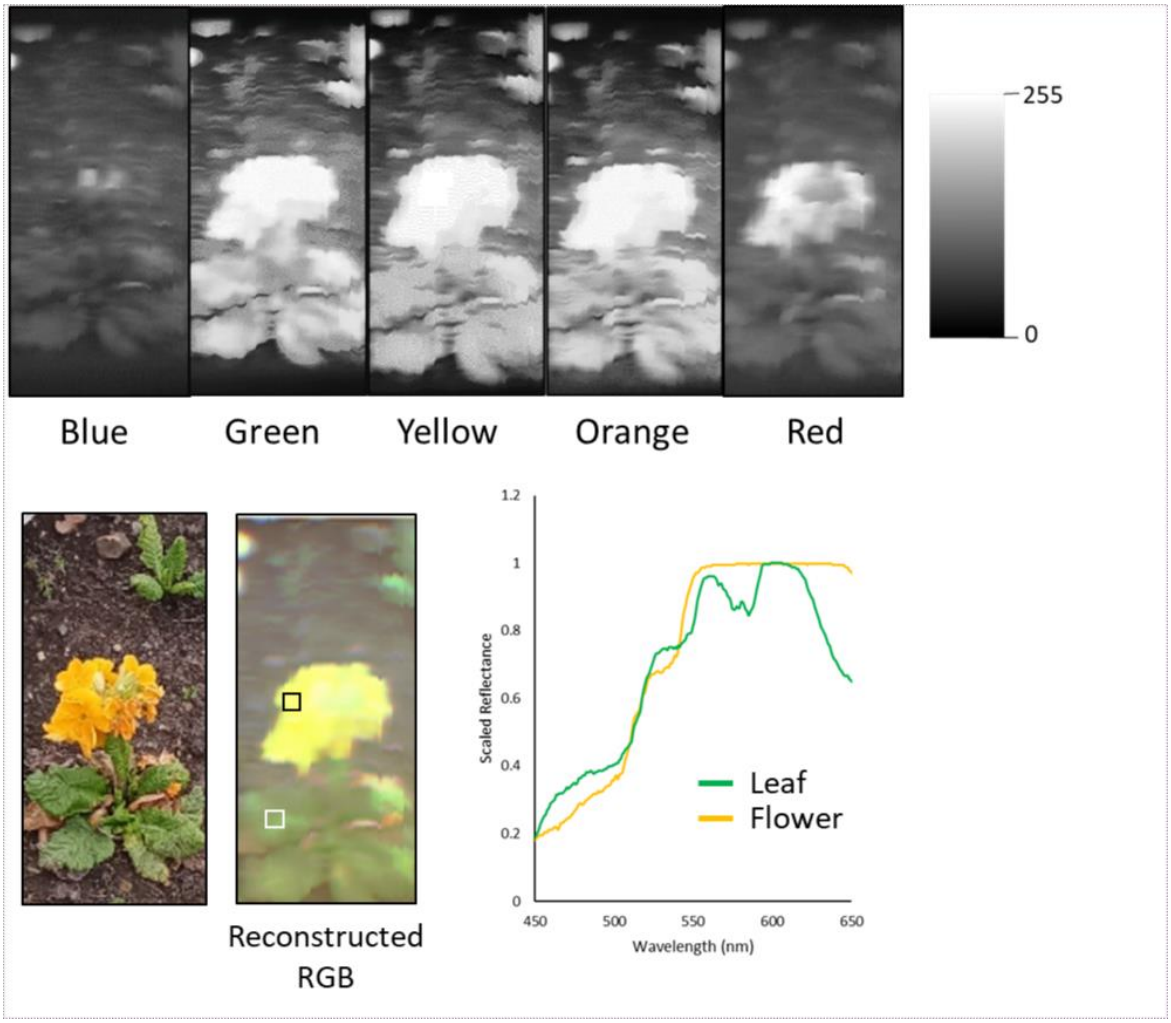

Figure 4.14 Spatial datasets across different wavelengths for a section of flower bed acquired over a short working distance. The reconstructed RGB image is created using red-green-blue equivalent images taken from the hyperspectral data cube. Black and white squares in this frame highlight the approximate location of the pixels utilised for the flower and leaf spectral response curves respectively. Grey scale shows pixel intensity.

Finally, the Hyperspectral Smartphone was used to capture landscape-style datasets over a longer working distance. Figure 4.15. shows a spatial dataset captured over this range. Whilst this dataset is poor in comparison to the other data provided within this section, it is evident that there remains potential for the acquisition of these landscape-style datasets with this style of device. Furthermore, the reconstructed RGB image frame, created using red green and blue equivalent images within the hyperspectral data cube, demonstrates the relative accuracy of the spectral datasets over this longer working distance, suggesting potential remains for accurate spectral data acquisition over this longer working distance in future. From these datasets it is clear that, in its current format, the Hyperspectral Smartphone is more suited to shorter range data capture, however, the preliminary data captured over longer distances shows promise, suggesting that with some minor modifications to the existing instrument landscape scenes may prove possible to accurately capture with this style of low-cost hyperspectral system.

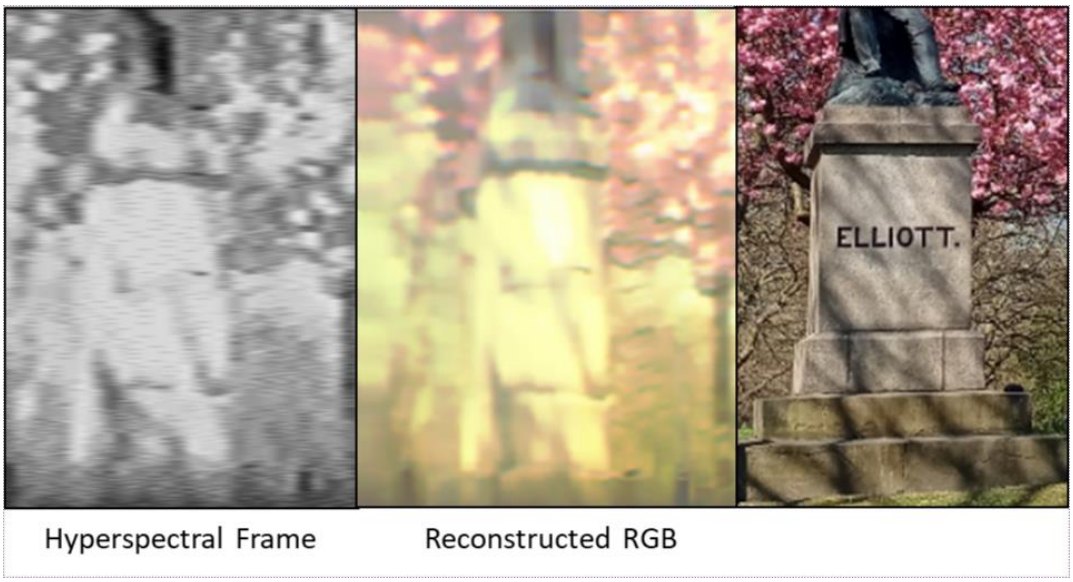

Figure 4.15 Spatial dataset captured of a statue over a longer working distance (ca. 20 m). Whilst this dataset is of poorer quality than others captured with this instrument, the target object can be identified highlighting the potential for the capture of landscape-style scenes in the future. The reconstructed RGB image is created using red-green-blue equivalent images taken from the hyperspectral data cube.

4.7. Improvements for Hand-Held Applications

Despite the successes in laboratory and field deployments discussed above, the Hyperspectral Smartphone still suffers from limitations associated with the chosen image capture method. Namely, image distortions caused by variations from the single translatory direction, and non-linear scanning speeds, resulting in further distortions related to the spatial compression or expansion of the chosen scene. This was solved above with the inclusion of a translation stage, allowing for stable, steady movement across the image scene, however, this detracts from the overall portability of the instrumentation by providing additional components that are required to achieve usable results. This section will, therefore, detail the development of an algorithm coded in MATLAB that, when combined with an in-scene reference card, enables the collection of spatially accurate hand-held datasets with this low-cost hyperspectral instrument.

4.7.1. Image Acquisition with the Hand-Held Hyperspectral Smartphone

Image acquisition with the hand-held set-up is comparable to the description in Section 4.3.1., however, it has been streamlined to provide a fully automated data processing workflow, further reducing the time restraints associated with data processing and analysis. The target object is placed within the “target object location” section of the in-scene reference card shown in Figure 4.16, and the smartphone translated across the scene (left to right) by the operator**.** Vertical correction is provided by the straight line at the bottom of the reference card that runs parallel to the scan direction. This is used to determine the amount of distortion within a captured scene as the line will deviate in the output images proportionally to the amount the scan deviated from the ideal path. A correction algorithm, written in MATLAB is then used to carry out the correction.

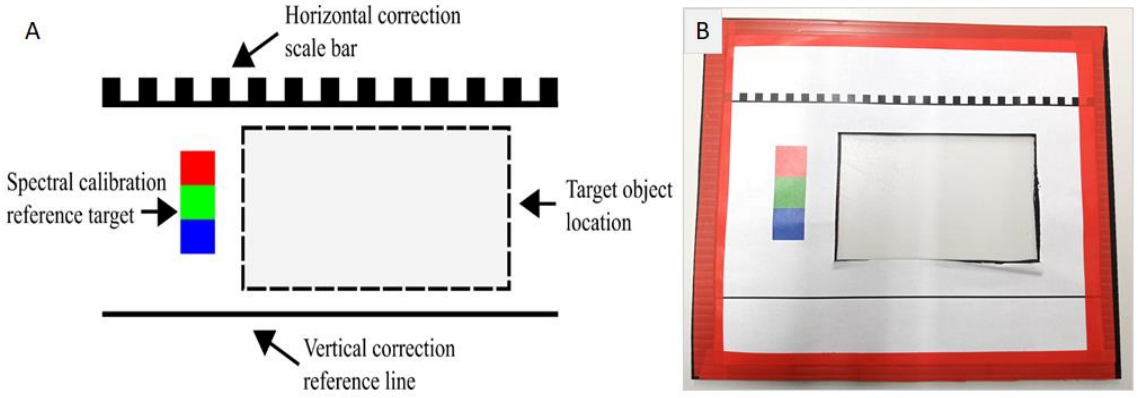

Figure 4.16 The in-scene reference card. A details the components of the card, B shows an example card used for hyperspectral measurements. The object or area to be imaged is placed within/aligned with the Target Object Location window. The Horizontal and Vertical Correction Bars are used to spatially correct the dataset, whereas the Spectral Calibration Reference Target is used to spectrally calibrate the dataset.

A mask is created by thresholding the bottom section of the captured image according to the minimum brightness value of each column. This allows for the amount of vertical deviation (y-deviation) to be measured as distance in pixels corresponding to how much the vertical correction line had deviated from straight, for each x-value of the line mask. Each column of pixels is then shifted down by the calculated corresponding y-deviation value. Figure 4.17. provides a visual example of this correction procedure.

Horizontal corrections, to account for acceleration and/or deceleration during the scene scan, are completed using the horizontal correction scale bar located at the top of the in-scene reference card. This scale bar is comprised of alternating black and white squares. As the operator translates the instrument across the target the size of these squares within the output image appear compressed or stretched depending on the scan speed. To correct this, the top section of the output images is thresholded to produce a mask which allows the widths of the squares to be measured for each square present within the scene. The threshold value is half the height of the top hat function produced by taking a line profile of the horizontal correction scale bar and is expressed in Equation 4.2;

$$\text{Threshold} = \text{mask}_{\text{min}} + \frac{\text{mask}_{\text{max}} - \text{mask}_{\text{min}}}{2} \tag{4.2}$$

Where $mask_{min}$ and $mask_{max}$ are the minimum and maximum values of the selected region respectively. The width of the images corresponding to the position and width of each square were then resized to the height of the square, correcting the horizontal distortions. This is shown visually within Figure 4.18.

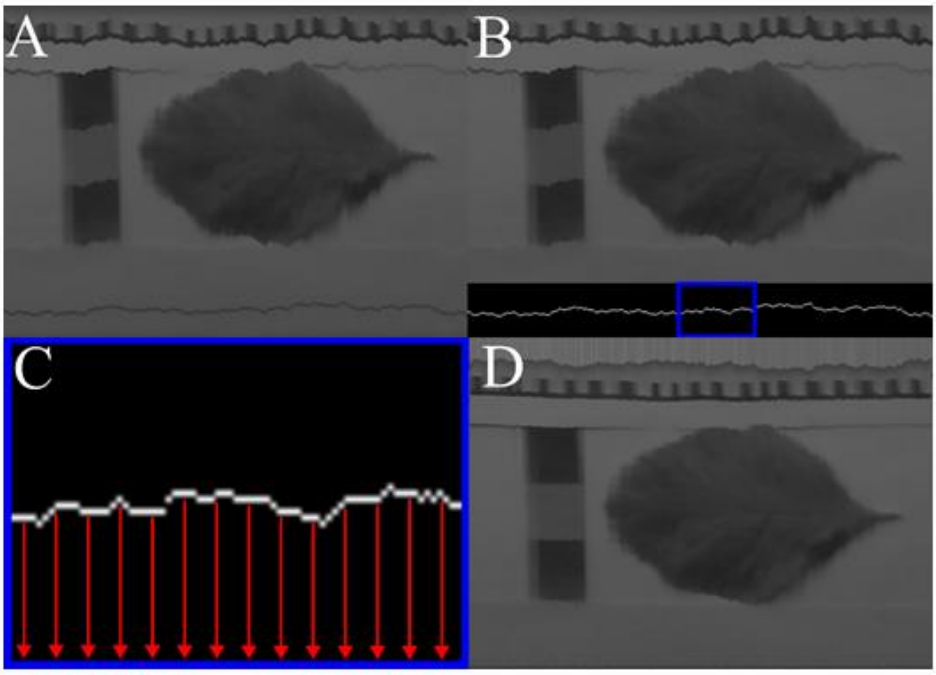

Figure 4.17 The stages of the vertical spatial correction. A shows the raw output from the data cube, B shows the masked area of the vertical correction reference line, the area highlighted in blue is enlarged in C. In C the arrows demonstrate the motion of the pixel columns to complete the correction. D shows the vertically corrected image with the top of the image uncropped to emphasise the effect of the column shifts.

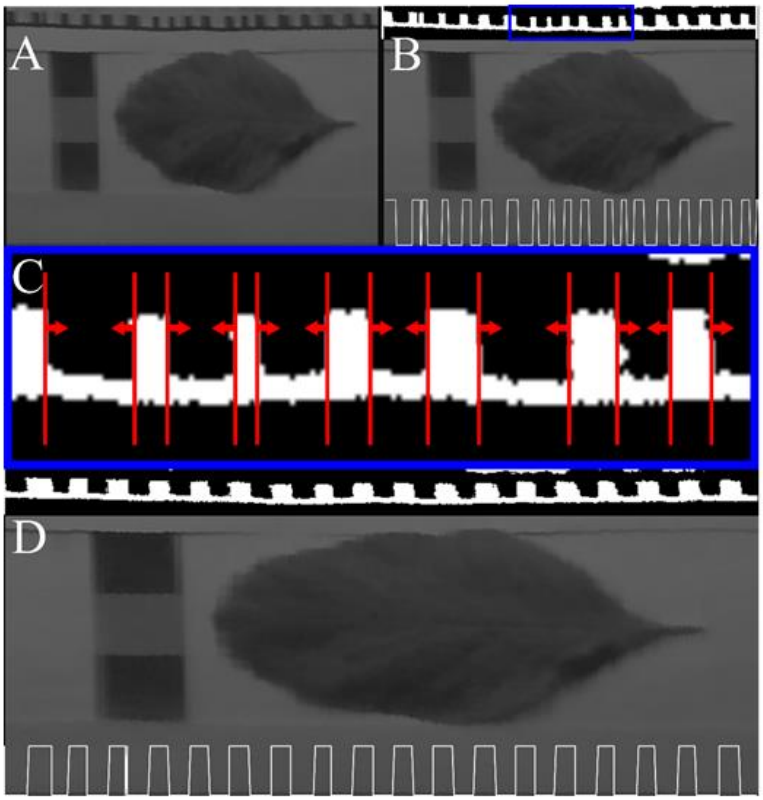

Figure 4.18 Stages of the horizontal spatial correction. A shows the output image from the vertical correction in Figure 4.17, B shows the masked area of the Horizontal Correction Scale Bar, with a line profile of the masked area shown within the bottom of this image to emphasise the lack of uniformity. The area highlighted in blue is shown in C where the arrows indicate the scaling required of each vertical slice to complete the horizontal correction. D shows the horizontally corrected output with a corrected line profile to demonstrate the greater uniformity of the corrected image.

4.7.2. Spatial Correction Results

The introduction of this spatial correction algorithm allows the Hyperspectral Smartphone to be utilised as a fully hand-held portable hyperspectral instrument. The removal and mitigation of distortions resulting from operator shake and non-linear scanning speeds provides the user with valuable output datasets that can be easily visualised to pinpoint areas of spectral variation. Figure 4.19. demonstrates the effectiveness of these corrections. When the original and corrected images are compared it demonstrates how effective these corrections can be even when supplied with a heavily distorted dataset. This is of significant benefit to a variety of imaging applications, however, it can be particularly useful when implemented in more extreme environmental settings, where the challenging nature of these environments can work to exacerbate the distortions observed. The corrected image is much clearer to the observer and provides significantly better context for the spectral information. By correcting these datasets to provide accurate spatial outputs it further improves the usability of this instrument. The outputs obtained from this instrument can easily be viewed, and understood without the need for extensive training. Furthermore, by correcting the spatial distortion, it means that spectral variations across the target object or scene can easily be pinpointed for further, more detailed analysis.

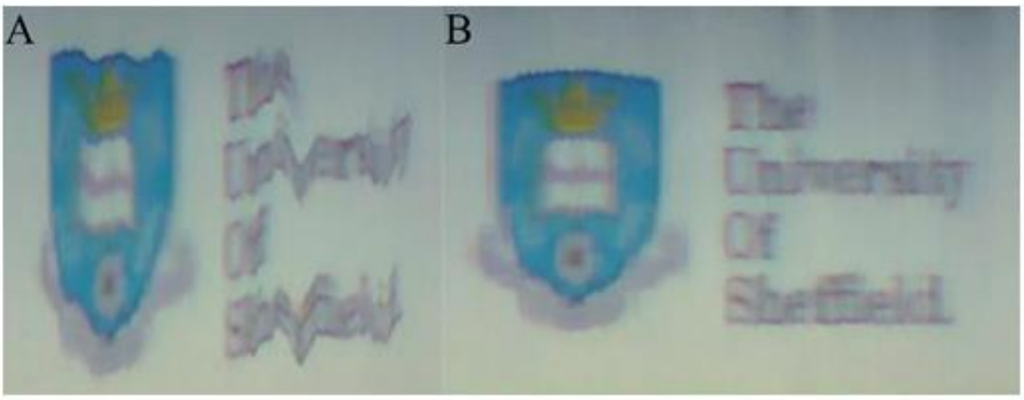

Figure 4.19 An example spatial correction. A shows an RGB reconstruction of the non-spatially corrected data. B shows the same image but after spatial correction has taken place.

4.8. In-Scene Spectral Calibration

In order to further develop the Hyperspectral Smartphone into a robust and accurate hyperspectral imaging instrument that can be utilised reliably for quantitative data analysis across a variety of applications and under a range of different conditions, potential problems relating to calibration drift needed to be resolved. Section 4.3.1. discussed the calibration process for the Hyperspectral Smartphone. This method, where a spectral source with known peaks is utilised to identify features in the instrument's output, is a common calibration technique for spectral sensing instruments[32], [33]. However, despite its widespread use, this method of calibration does have its drawbacks, for example, with the push broom imaging method, as utilised by the Hyperspectral Smartphone, any change in alignment between the slit, diffraction grating and the imaging optics of the instrument causes the spectral calibration to drift. This is because the spectrum of the scene is no longer being projected onto the same region of the sensor array. Whilst this is avoided in many instruments through fixed component locations, this is not possible with the Hyperspectral Smartphone due to the adjustable connection between the spectral and imaging optics. Furthermore, these changes in alignment could cause particular issues when the instrument is deployed for long periods of field-based data collection where conditions are not always favourable and instrumentation is often transported between multiple measurement sites. In-situ calibration helps to mitigate the chances of drift, however, this is

not always feasible due to the extra equipment required and the subsequent impacts of extended measurement periods and post-processing.

To overcome these problems with the Hyperspectral Smartphone a pre-calibrated reference was included in the in-scene reference card shown in Figure 4.16. This reference is imaged simultaneously with the target, providing a known spectral response which could be used to determine and remove illumination biases, as well as allowing spectral locations to be determined within the chosen scene. Thus, providing a more streamlined method of instrument calibration and image correction, providing significant time benefits during measurement periods. Additionally, this approach remains accurate under a range of lighting conditions, providing the illumination source broadly covers the visible spectrum.

4.8.1. Bias Correction Improvements

In order to spectrally calibrate the dataset, the images first needed to be corrected for sensor and illumination biases, as discussed in Section 4.3.1. These corrections and calibrations were coded in MATLAB and combined with the calibration calculations, providing an improvement on the existing correction process. The dark noise was subtracted from each colour channel to correct for sensor bias. This then allowed other influences, such as illumination bias from the light source, and the spectral transmission of the Bayer filter within the smartphone optics to be focused on. To enable accurate quantitative datasets to be obtained these biases needed to be accounted for. To achieve this, a ratio of the measured signal at each point in the image to the signal at a point in the scene, a white point on the in-scene reference card, was taken;

$$\mathrm{S_{calibrated}}(\lambda, \mathrm{x}, \mathrm{y}) = \frac{\mathrm{S_{image}}(\lambda,\mathrm{x},\mathrm{y})}{\mathrm{S_{paper}}(\lambda,\mathrm{x},\mathrm{y})} \times \mathrm{R_{paper}}(\lambda) \tag{4.3}$$

Where $S_{calibrated}$ is the calibrated spectral dataset, S_{image} is the measured signal, S_{paper} is the measured signal of the paper reference card, and R_{paper} is the true spectral response of the paper of the reference card. Note that in this equation the ratio is multiplied by R_{paper} because its inverse was introduced when the ratio was taken. In the MATLAB code this is completed after the spectral calibration (Section 4.8.2.), however, it has been included here as it represents the final stage of the bias correction process. In this process all other terms cancel as they are present and equal in both measured signals, leaving only the spectral response of the target object at a given point (x,y) within the image.

4.8.2. Spectral Calibration

The spectral calibration reference shown within the in-scene reference card in Figure 4.16. is used to calibrate the images after spatial and bias corrections have been completed. The spectral response of the reference was measured using a Thorlabs CCD spectrometer (CCS200). Illumination was provided by a broad spectrum white LED. The spectral response of the red, green, and blue sections of the reference were then measured. The illumination bias was removed from these measurements by measuring the emission spectrum of the LED then completing a light source correction;

$$\lambda_{\mathrm{corr}} = \frac{\lambda_{\mathrm{RGB}}}{\lambda_{\mathrm{LED}}} \tag{4.4}$$

Where λ_{corr} is the true spectral response of the spectral calibration reference, λ_{RGB} is the measured response of the spectral calibration reference, and λ_{LED} is the emission spectrum of the illumination source. λ_{corr} is then normalised to unity for each colour channel of the spectral calibration reference. After the data cube has been assembled, the normalised intensity of the spectral calibration reference can be compared to the calibrated spectra of the reference. The cross-over points between blue and green, and green and red were recorded in the calibrated response as 495 nm and 596 nm respectively.

These features can also be identified in the uncalibrated spectra (Figure 4.20.) and provide known points to interpolate between and extrapolate from to provide quantitative wavelength values for each image in a data cube. The light source correction could not be fully applied until the spectral calibration was complete, as highlighted in Section 4.8.1., as the paper's reflectance spectrum could not be multiplied by the data until there was a 1:1 wavelength correspondence. The ratio of S_{image} and S_{paper} was still taken and the spectral response of the paper introduced to both the laboratory measured reflectance spectrum and the spectral calibration reference. Both the laboratory and smartphone-measured spectral response of the spectral calibration reference had the influence of the inverse reflectance spectrum of the paper. Figure 4.20. shows a comparison between the S_{image} and S_{paper} ratio signal and the laboratory measured spectral response of the calibration reference. The widths of Δλ' and Δλ were used to calculate the wavelength increment between each image in a data cube in nanometres by taking the ratio of Δλ to Δλ'. This increment was then applied to each image from the known point at 495 nm, providing an assigned wavelength value to each image in a data cube, and, therefore, spectrally calibrating the dataset.

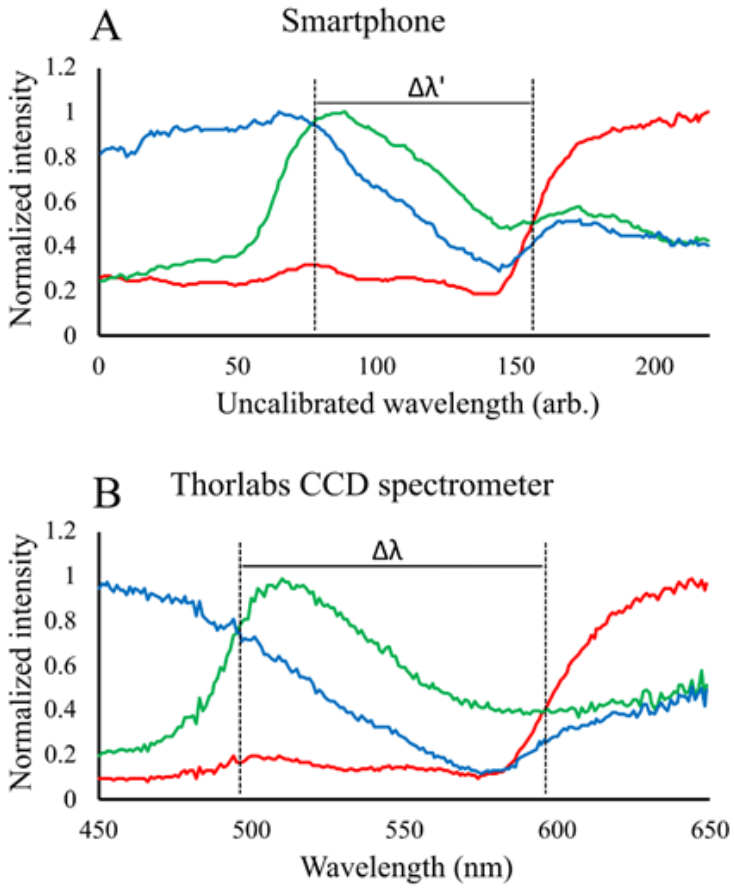

Figure 4.20 Spectral response of the calibrated reference target. A shows the wavelength plot from the uncalibrated data cube for three x-y points corresponding to the red, green, and blue parts of the reference target. B shows the calibrated reflectance spectrum for each colour of the reference target measured using the Thorlabs CCD spectrometer. The similarity between these plots enabled the selection of known wavelength calibration points. These points are highlighted by the vertical dashed lines in each plot.

4.8.3. Spectral Calibration Testing

To test the abilities of this in-situ calibration and to demonstrate its independence from the chosen illumination source a sample of lapis lazuli (a deep blue coloured semi-precious stone) was imaged with the Hyperspectral Smartphone under three different lighting conditions, and compared to a laboratory measurement undertaken with the Thorlabs CCD spectrometer, to determine how much the spectral response of the illumination source influenced the calibrated output of the sample. Lapis lazuli was chosen as its distinct blue colouring provides a clear spectral response that can be easily identified, making variations in this response easier to distinguish. Figure 4.21. shows the results of these measurements.

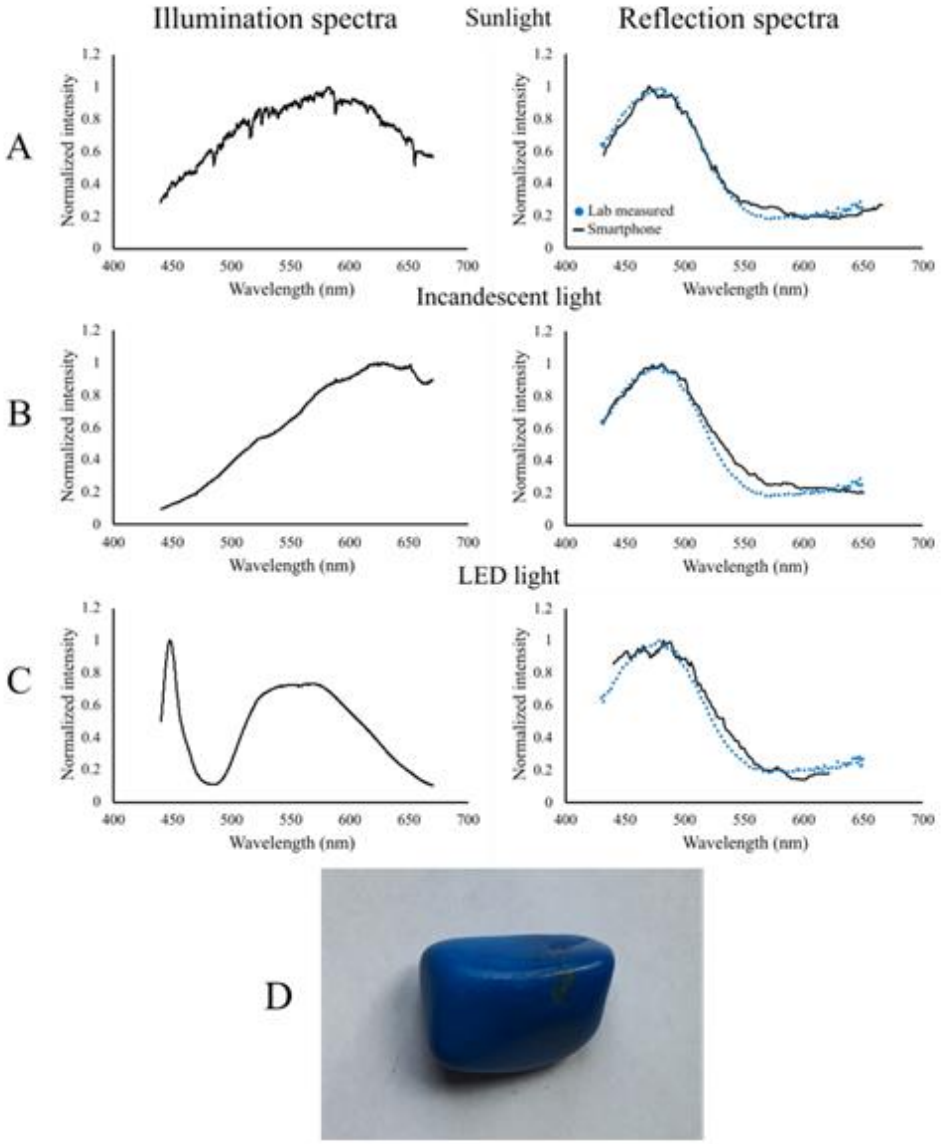

Figure 4.21 Spectral calibration testing using lapis lazuli. A is natural sunlight, B incandescent light, and C LED light. The graph on the left displays the spectral response of the particular light source, and the graph on the right shows the measured spectral response of the lapis lazuli in comparison to the laboratory measured spectrum (overlaid in blue) for each example. D shows the lapis lazuli sample.

It is clear in this figure that the Hyperspectral Smartphone is capable of light source independent spectral calibrations. All three measured spectra demonstrate a peak in the blue at 485 nm which then tails off towards the red before indicating an increase towards the near infrared. The measurement undertaken with natural illumination shows the closest resemblance to the laboratory measured spectrum, however, this is to be expected due to the nature of the light source. Natural lighting provides more intense illumination across all wavelengths, without the influence of distinct illumination peaks. This makes it considerably easier to remove from a dataset than a narrower wavelength source as its influence is more evenly spread across the spectrum. Both the incandescent and LED illumination measurements also provide a close resemblance to the laboratory measured spectrum, however, the LED example in particular shows the presence of noise which is indicative of low signal. This is to be expected as, looking at the illumination spectrum for the LED there are clear regions with lower levels of illumination across the spectrum which are more prevalent here than within the natural and incandescent examples. Furthermore, the LED spectrum also contains a localised peak at 450 nm, however, this presents minimally in the lapis lazuli spectrum with only a slight increase which remains within the range of variation caused by noise within the dataset, indicating the resilience of this calibration method. This demonstrates that the Hyperspectral Smartphone is capable of working effectively in a range of different illumination settings, allowing for accurate spectral calibration to be achieved in both indoor and outdoor settings. Furthermore, this evidences the instruments utility as a whole, showing it to be a fully portable, hand-held low-cost hyperspectral instrument capable of accurate and robust hyperspectral analysis.

4.9. Environmental Monitoring Applications

The improvements discussed above mean that the Hyperspectral Smartphone is now capable of both qualitative and quantitative hyperspectral measurements, increasing its potential application options to a considerable range of subject areas. As such, the instrumentation is now being incorporated into a range of real-world environmental monitoring measurement applications. One such application is the non-invasive monitoring of the health of peatlands using plant species spectral response as a proxy for below ground conditions. Peatland habitats are of significant importance due to their carbon storage and sequestration potential, making them key factors in a number of climate warming mitigation plans [34]–[36], therefore, the continued monitoring and preservation of these habitats is of considerable importance. Hyperspectral imaging techniques can be utilised for this purpose, providing a non-invasive means of estimating below ground conditions through the spectral responses of above ground vegetation communities [37]–[39]. This particular application is discussed in greater detail in Chapter 6, however, it remains a relevant addition at this stage due to the incorporation of the Hyperspectral Smartphone in the data collection process.

The hand-held Hyperspectral Smartphone was utilised in this measurement application providing valuable datasets for a range of plant samples under varying degrees of water stress. Figure 4.22. shows a plant sample ready for data capture utilising the in-scene reference card. With the Hyperspectral Smartphone the spectral response for a range of plant samples could be easily ascertained and accurate differentiations could be made between samples affected by drought stress and those kept at saturation through variations in their spectral response. An example of this is shown in Figure 4.23. Further details of this testing are discussed in Chapter 6, however, the datasets obtained with the Hyperspectral Smartphone show it to be a robust and promising hyperspectral measurement tool.

Figure 4.22 A sample of Sphagnum moss ready for image capture using the hand-held Hyperspectral Smartphone and the in-scene reference card. Illumination is provided by two 20 W LED lamps.

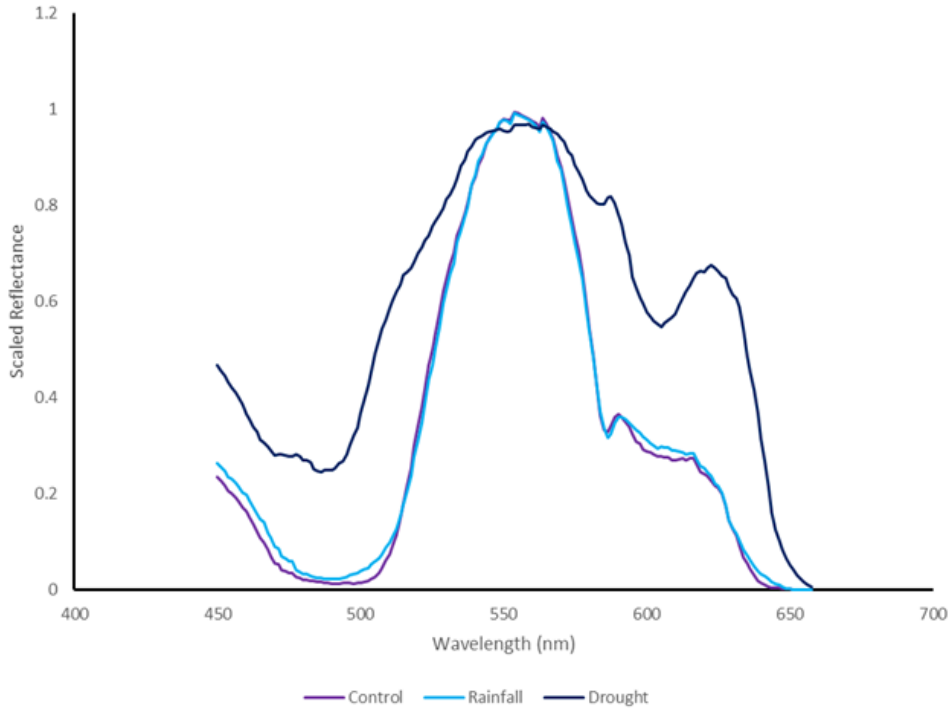

Figure 4.23 Example dataset obtained of three Sphagnum groups under varying degrees of water stress. Control and Rainfall represent healthy plant conditions; Drought represents unfavourable conditions. The Hyperspectral Smartphone can clearly differentiate between these different groups, highlighting significant areas of absorption and reflectance.

4.10. Chapter Summary

This chapter has documented the development of the Hyperspectral Smartphone from initial prototype testing to a fully portable, hand-held low-cost hyperspectral imaging instrument that is capable of deployment in a wide range of application areas and environmental conditions. This is the first smartphone-based hyperspectral imaging instrument of its kind and, as such, it represents a significant addition to the field of hyperspectral imaging analysis and a step towards the democratisation of hyperspectral imaging techniques. Its abilities have been tested in a wide range of imaging scenarios and set-up configurations, demonstrating it to be a versatile instrument capable of robust and accurate hyperspectral data collection. Device metrology and a thorough comparison against the laboratory-based hyperspectral imager and the existing literature have been provided. The results obtained with the Hyperspectral Smartphone demonstrate the significant potential within the field of smartphone-based hyperspectral imaging, providing a solid foundation for future development and improvements in this area of research. The Hyperspectral Smartphone has demonstrated that high performance hyperspectral imaging instrumentation capable of accurate and robust spatial and spectral data capture, can be developed without the need for expensive components. The following chapter will use the skills and knowledge gained here to further improve on the data quality outputs possible with low-cost hyperspectral imaging technologies with the aim of providing further accurate low-cost alternatives to currently available systems capable of competing with currently available commercial instrumentation.

4.11. References

[1] M. B. Stuart *et al.*, "Low-cost hyperspectral imaging with a smartphone," *J. Imaging*, vol. 7, no. 8, pp. 1–13, 2021.

[2] M. Davies, M. B. Stuart, M. Hobbs, A. McGonigle, and J. R. Willmott, "Image correction and in-situ spectral calibration for low-cost, smartphone hyperspectral imaging," *Remote Sens.*, vol. 14, p. 1152, 2022.

[3] M. B. Stuart *et al.*, "Low-cost hyperspectral imaging system: Design and testing for laboratory-based environmental applications," *Sensors (Switzerland)*, vol. 20, no. 11, pp. 1–13, 2020.

[4] F. Sigernes, M. Syrjäsuo, R. Storvold, J. Fortuna, M. E. Grøtte, and T. A. Johansen, "Do it yourself hyperspectral imager for handheld to airborne operations," *Opt. Express*, vol. 26, no. 5, p. 6021, 2018.

[5] A. J. S. McGonigle *et al.*, "Smartphone spectrometers," *Sensors (Switzerland)*, vol. 18, no. 1, pp. 1–15, 2018.

[6] Y. Ju, "Fabrication of a low-cost and high-resolution papercraft smartphone spectrometer," pp. 1–21.

[7] T. C. Wilkes, A. J. S. McGonigle, J. R. Willmott, T. D. Pering, and J. M. Cook, "Low-cost 3D printed 1 nm resolution smartphone sensor-based spectrometer: instrument design and application in ultraviolet spectroscopy," *Opt. Lett.*, vol. 42, no. 21, p. 4323, 2017.

[8] S. Kim *et al.*, "Smartphone-based multispectral imaging and machine-learning based analysis for discrimination between seborrheic dermatitis and psoriasis on the scalp," *Biomed. Opt. Express*, vol. 10, no. 2, p. 879, 2019.

[9] H. Ding, C. Chen, H. Zhao, Y. Yue, and C. Han, "Smartphone based multispectral imager and its potential for point-of-care testing," *Analyst*, vol. 144, no. 14, pp. 4380–4385, 2019.

[10] W. G. C. Bandara *et al.*, "A multispectral imaging system to assess meat quality," *IEEE Reg. 10 Humanit. Technol. Conf. R10-HTC*, vol. 2018-Decem, pp. 1–6, 2019.

[11] L. Wang *et al.*, "LeafSpec: An accurate and portable hyperspectral corn leaf imager," *Comput. Electron. Agric.*, vol. 169, no. January, 2020.

[12] A. N. Hegyi and J. Martini, "Compact hyperspectral image sensor based on a novel hyperspectral encoder," *Next-Generation Spectrosc. Technol. VIII*, vol. 9482, no. June 2015, p. 948214, 2015.

[13] J. Lin, J. Pfefer, P. Ghassemi, and Y. Chen, "Hyperspectral imaging with near-infrared-enabled mobile phones for tissue oximetry," no. February 2018, p. 11, 2018.

[14] C. C. Wilcox, M. Montes, M. Yetzbacher, J. Edelberg, and J. Schlupf, "An ultra-compact hyperspectral imaging system for use with an unmanned aerial vehicle with smartphone-sensor technology," *Proc. SPIE - Int. Soc. Opt. Eng.*, vol. 10639, no. May, 2018.

[15] Q. He and R. Wang, "Hyperspectral imaging enabled by an unmodified smartphone for analyzing skin morphological features and monitoring hemodynamics," *Biomed. Opt. Express*, vol. 11, no. 2, p. 895, 2020.

[16] S. M. Park *et al.*, "mHealth spectroscopy of blood hemoglobin with spectral super-resolution," *Optica*, vol. 7, no. 6, p. 563, 2020.

[17] M. B. Stuart, A. J. S. McGonigle, and J. R. Willmott, "Hyperspectral imaging in environmental

monitoring: A review of recent developments and technological advances in compact field deployable systems," *Sensors (Switzerland)*, vol. 19, no. 14, 2019.

[18] "Public Lab: Papercraft Spectrometer Intro Kit." [Online]. Available: https://publiclab.org/wiki/papercraft-spectrometer. [Accessed: 06-Aug-2021].

[19] L. J. Wang *et al.*, "Smartphone Optosensing Platform Using a DVD Grating to Detect Neurotoxins," *ACS Sensors*, vol. 1, no. 4, pp. 366–373, 2016.

[20] F. Stanculescu and A. Stanculescu, "Polycarbonate-Based Blends for Optical Non-linear Applications," *Nanoscale Res. Lett.*, vol. 11, no. 1, pp. 1–13, 2016.

[21] Y. S. Lee, W. J. Chen, J. S. Huang, and S. C. Wu, "Effects of composition on optical and electrical properties of amorphous In-Ga-Zn-O films deposited using radio-frequency sputtering with varying O 2 gas flows," *Thin Solid Films*, vol. 520, no. 23, pp. 6942–6946, 2012.

[22] I. S. O. (ISO), *Non-Destructive Testing-Infrared Thermography-Vocabulary*. Geneva, Switzerland: International Standards Organisation, 2013.

[23] C. Zhu, M. J. Hobbs, R. C. Masters, C. Rodenburg, and J. R. Willmott, "An accurate device for apparent emissivity characterization in controlled atmospheric conditions up to 1423 K," *IEEE Trans. Instrum. Meas.*, vol. 69, no. 7, pp. 4210–4221, 2020.

[24] W. Wolfe, *Introduction to Radiometry*. Bellingham, DC, USA: SPIE Press, 1998.

[25] "SpectralWorkbench." [Online]. Available: https://spectralworkbench.org/. [Accessed: 06-Aug-2021].

[26] M. A. Hossain, J. Canning, K. Cook, and A. Jamalipour, "Optical fiber smartphone spectrometer," *Opt. Lett.*, vol. 41, no. 10, p. 2237, 2016.

[27] A. J. Das, A. Wahi, I. Kothari, and R. Raskar, "Ultra-portable, wireless smartphone spectrometer for rapid, non-destructive testing of fruit ripeness," *Sci. Rep.*, vol. 6, no. April, pp. 1–8, 2016.

[28] A. Solovchenko, O. Chivkunova, A. Gitelson, and M. Merzlyak, "Non-Destructive Estimation Pigment Content, Ripening, Quality and Damage in Apple Fruit with Spectral Reflectance in the Visible Range," *Fresh Prod.*, vol. 4, no. 1, pp. 91–102, 2010.

[29] O. B. Chivkunova, A. E. Solovchenko, S. G. Sokolova, M. N. Merzlyak, I. V. Reshetnikova, and A. A. Gitelson, "Reflectance Spectral Features and Detection of Superficial Scald – induced Browning in Storing Apple Fruit," *J. Russ. Phytopathol. Soc.*, vol. 2, no. June, pp. 73–77, 2001.

[30] M. N. Merzlyak, A. E. Solovchenko, and A. A. Gitelson, "Reflectance spectral features and non-destructive estimation of chlorophyll, carotenoid and anthocyanin content in apple fruit," *Postharvest Biol. Technol.*, vol. 27, no. 2, pp. 197–211, 2003.

[31] T. H. Burbine, T. J. McCoy, and E. . Cloutis, "Reflectance spectra of Aubrites, Sulfides, and E Asteroids: Possible implications for Mercury," in *Mercury: Space Environment, Surface, and Interior*, 2001.

[32] X. Yu, Y. Sun, A. Fang, W. Qi, and C. Liu, "Laboratory spectral calibration and radiometric calibration of hyper-spectral imaging spectrometer," *2014 2nd Int. Conf. Syst. Informatics, ICSAI 2014*, no. Icsai, pp. 871–875, 2015.

[33] G. Polder and G. W. van der Heijden, "Calibration and characterization of spectral imaging systems," *Multispectral Hyperspectral Image Acquis. Process.*, vol. 4548, no. September 2001, p. 10, 2001.

[34] D. Carless, D. J. Luscombe, N. Gatis, K. Anderson, and R. E. Brazier, “Mapping landscape-scale peatland degradation using airborne lidar and multispectral data,” *Landsc. Ecol.*, vol. 34, no. 6, pp. 1329–1345, 2019.

[35] E. Grand-Clement *et al.*, “Evaluating ecosystem goods and services after restoration of marginal upland peatlands in South-West England,” *J. Appl. Ecol.*, vol. 50, no. 2, pp. 324–334, 2013.

[36] UK Government, “England Peat Action Plan,” no. May, 2021.

[37] K. J. Lees *et al.*, “Using spectral indices to estimate water content and GPP in sphagnum moss and other peatland vegetation,” *IEEE Trans. Geosci. Remote Sens.*, vol. 58, no. 7, pp. 4547–4557, 2020.

[38] T. Lendzioch, J. Langhammer, L. Vlček, and R. Minařík, “Mapping the groundwater level and soil moisture of a montane peat bog using uav monitoring and machine learning,” *Remote Sens.*, vol. 13, no. 5, pp. 1–30, 2021.

[39] M. Kalacska, M. Lalonde, and T. R. Moore, “Estimation of foliar chlorophyll and nitrogen content in an ombrotrophic bog from hyperspectral data: Scaling from leaf to image,” *Remote Sens. Environ.*, vol. 169, pp. 270–279, 2015.

Chapter 5

Development of a Low-Cost High-Resolution Hyperspectral Imaging Instrument and Its Application Within Environmental Monitoring Scenarios

This chapter is associated with the work presented in Stuart et al., [1]. It introduces a semi-portable low-cost hyperspectral imaging instrument that is capable of high spatial and spectral resolution hyperspectral image capture allowing for the detection of mm-scale targets. This builds on the instrumentation from chapters 3 and 4, combining the skills learnt from their design to produce an instrument that is both semi-portable and capable of high quality intricate data capture. Instrument design and testing are discussed before the abilities of the instrumentation are demonstrated through its application to a mineralogy-based environmental monitoring study, showcasing it as a valuable asset to the field of low-cost high-resolution hyperspectral imaging.

5.1. Introduction

High spatial and spectral resolution hyperspectral imaging is becoming increasingly important for a wide range of industries. It has reached a reasonable level of maturity in agriculture. It promises to be a beneficial measurement modality that can provide datasets capable of resolving intricate details and variations across a broad range of targets. Continued uptake of the technology will require a reduction in cost of hardware along with an increased knowledge of the meaning behind the spectra for any particular application. Despite the benefits, high spatial resolution hyperspectral imaging can be difficult to achieve due to the associated trade-offs between spatial resolution, spectral resolution, and signal to noise ratio [2], [3]. These factors represent key performance parameters within instrumentation design, having a significant impact on the overall abilities of the final configuration [4]–[6]. The instrumentation design process, therefore, often becomes a balancing act, finding the best possible combination of these three factors that allows the highest quality data to be captured from the chosen application. Whilst these trade-offs affect hyperspectral imaging applications as a whole, many low-cost designs are typically more adversely affected as a result of their use of lower cost components. This results in many low-cost hyperspectral instruments foregoing high spatial resolution in order to achieve effective spectral outputs, and, in turn, limits high spatial resolution hyperspectral imaging to more costly commercial instrumentation [7], [8]. These limitations have further repercussions; by placing these high-resolution datasets ‘out-of-reach’ for many less well-resourced research teams and organisations, it hinders the continued democratisation of hyperspectral imaging techniques and, in so doing, limits a wide range of data collection applications. Low-cost high-resolution hyperspectral imaging, therefore, represents a critical area for continued development. By developing instrumentation that is capable of accurate spectral identification of small-scale spatial targets it enables a broad range of more detailed spectral measurements that can provide key knowledge and understanding in a variety of application areas. Low-cost hyperspectral imaging will

not only open up the technology to a wider range of applications, it will also enable an increase in knowledge of the correlations/causations between spectra and the parameters that can be used to improve e.g. manufacturing processes by hugely expanding the user base.

In environmental monitoring applications high spatial resolution hyperspectral imaging can enable the capture of intricate features that would often be overlooked by traditional monitoring methods. This approach is, therefore, employed across a wide variety of applications, from spatially complex environments such as swamps [9], or dense forest canopies [2], to the accurate identification of volcanic gases [4], [10]. Many existing applications focus on natural and agricultural vegetation monitoring [11]–[15], however, there has also been a recent increase in interest in high-resolution analyses for mining operations [16]–[18], geological exploration [19]–[21], mineralogy [22]–[26] and petrology [24], [27]–[30]. Hyperspectral imaging provides a rapid, non-destructive, and information rich means of data collection [16], [24], [31], enabling both an increase in our understanding of the structure and composition of key environmental settings whilst also providing valuable planetary analogues for continued solar system exploration [31]–[36]. The application of high spatial resolution hyperspectral imagers within these scenarios is, therefore, of considerable benefit.

To date, whilst high spatial resolution instrumentation has become more common place within these applications, there remains a considerable gap in the existing literature surrounding the application of low-cost instrumentation within these domains. Whilst many existing low-cost alternatives are capable of accurate and detailed data capture, making them valuable additions to the research field, very intricate targets, ca. < 1 mm, are often not easily resolved by these approaches. This chapter, therefore, introduces a Low-Cost High-Resolution hyperspectral imager as an accessible alternative to existing measurement and monitoring approaches. The term “high-resolution” is used to refer to data capture quality required to be associated with high definition (HD) video, however, given the final processed output datasets are not a video format, HD is not used more broadly within the text. Furthermore, “high-resolution” can also be attributed to the spectral resolution of this instrument. With a spectral resolution of 0.29 nm, this instrument compares favourably with a broad range of existing instrumentation [7]. Additionally, the term “low-cost” is used to refer to instrumentation that is significantly cheaper than the typical cost of commercially available systems. Commercial hyperspectral imaging instrumentation often cost more than £30,000, with some systems costing up to £150,000 [8]. In comparison, this instrument costs ca. £11,000 to develop, with the majority of these costs associated with the chosen camera sensor. This single-instrument cost would fall significantly if the design were to be supplied commercially due to the inverse relationship between sales volume and price. The instrument is semi-portable and capable of mm-scale spatial data acquisitions. It weighs approximately 9 kg including a 6 kg optical breadboard and has dimensions (Length x Width x Height) of 60 cm x 30 cm x 18 cm. This chapter presents a thorough analysis of, and introduction to, the Low-Cost High-Resolution hyperspectral imager providing insights that demonstrate its significant potential. Instrument design and metrology are presented before its application within a mineralogy based study with the aim of demonstrating the instrument’s efficacy and potential within environmental monitoring contexts. In so doing, highlighting the significant potential offered by this Low-Cost High-Resolution instrument, demonstrating it to be a valuable addition to the research field and an additional step towards the wide-spread democratisation of hyperspectral imaging techniques.

5.2. Instrumental Design

The Low-Cost High-Resolution hyperspectral imager (Figure 5.1), is a semi-portable instrument, capable of capturing spectral information from mm-scale spatial targets, focus can be adjusted to best fit the intended target. This is demonstrated within Figure 5.2 which shows an example of the data quality capture possible with this set-up using two different focal lengths**.** The instrument is composed of commercially available components, as listed in Table 5.1. A key benefit of the Low-Cost High-Resolution instrument is its inherent modularity. This enables key components and their configuration to be altered to best fit the intended application without compromising the overall abilities of the imager. The components listed in Table 5.1. were selected to best fit the intended applications discussed within this chapter, however, many of them can be altered or exchanged, enabling a wider range of applications with the additional benefit of potential cost reduction if required. For example, the width of the slit can be adjusted without disturbing the existing set-up, enabling the capture of a greater range of target scenes under variable illumination conditions. Furthermore, for targets with key spectral features outside of the existing range of this instrument, the diffraction grating can be replaced with an alternative with relative ease. Finally, the Hamamatsu C13440 camera makes up a considerable portion of the development costs for this particular design. It could be replaced with a lower cost alternative, for example, a Thorlabs Quantalux CS2100M-USB. Of course, replacing the camera with a considerably lower cost alternative, will influence the data capture quality. However, the operator can look to determine the acceptable limitations and trade-offs between data quality and cost reduction within the specifics of their intended application. The ease of these alterations highlight the versatility of this approach to instrument design, demonstrating the significant potential for versatile, low-cost, high-resolution hyperspectral instrument development for a range of applications and research fields, including potential adaptations for the capture of longer wavelengths within the infrared, however, these alterations would likely result in a significant increase in development costs.

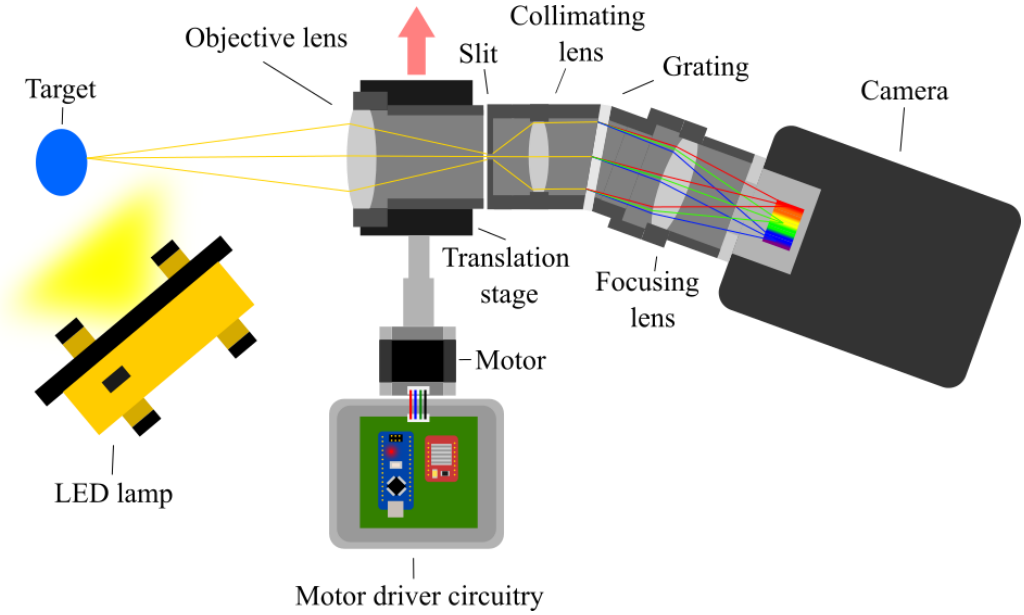

Figure 5.1. Schematic diagram of the Low-Cost High-Resolution hyperspectral imager showing how axial and marginal rays pass through the optical system. Not to scale.

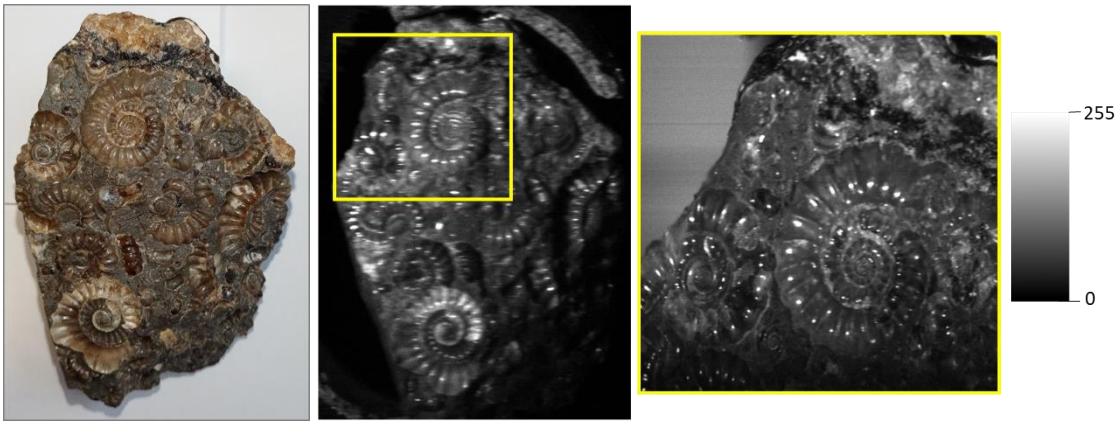

Figure 5.2. Example frames of an ammonite fossil taken from a hyperspectral data cube demonstrating the spatial resolution possible with this instrument. The first panel shows a standard colour image of the target for reference. The additional panels show hyperspectral frames captured at focal lengths of 18 mm and 55 mm respectively. Scale shows pixel intensity.

Table 5.1. Components and cost breakdown for the Low-Cost High-Resolution instrument

Component	Part Used	Cost
Objective Lens	Canon EF-S 18 – 55 mm	£179.99
Slit	Thorlabs VA100C (set at 300 µm).	£221.28
Collimating Lens	Thorlabs MVL75M1 75 mm telephoto c mount	£379.34
Transmission Diffraction Grating	Edmund Optics #49-580	£95.94
Focusing Lens	Thorlabs MVL50M23 50 mm telephoto c mount	£163.05
Camera Sensor	Hamamatsu C13440	£10,000
Total Cost		**£11,039.60**

In its current form (Figure 5.3.), the instrument is capable of detecting spectral information across the visible spectrum (450 – 650 nm), however, given its inherent modularity this wavelength range can be altered with relative ease allowing spectral coverage across the visible and near infrared (400 – 1000 nm). The wavelength range of the instrument is limited by the focusing lens which produced mild vignetting. The sensor was, therefore, partially cropped, sacrificing some of the spectral range. This could be avoided by replacing the focusing lens or selecting a diffraction grating with a lower groove density. However, it should be noted that whilst replacing the diffraction grating would enable a greater spectral range to be captured it would result in a trade-off, reducing the spectral resolution. The instrument is semi-portable and can be operated using a laptop, removing its reliance on a static computer terminal. This enables it to be utilised in a wider range of data collection scenarios, increasing its range of potential applications.

To obtain a hyperspectral image with this instrument, the objective lens is translated across the scene using a compact translation stage travelling at a rate of 0.2 mm/sec providing stable and reliable scene capture that is unaffected by factors such as operator shake. Using this method, a full hyperspectral scene could be captured in 1 minute. The scanning range is determined by the fore optics, and, as such, can be altered/replaced to better fit a range of larger and smaller targets e.g. using scanning mirrors or microscope coupling respectively. Illumination under laboratory conditions is provided by a 20 W

LED lamp. The instrument is controlled using HC Image Live (4.3.1.30) software. The software can be used to tailor the camera settings to the specifics of the chosen application; factors such as exposure time, and image dimensions can be altered by the operator. Similarly, the focal length, and working distance can be altered to best fit the chosen scene. The settings utilised for the data capture discussed within this chapter are shown in Table 5.2. After data capture was completed the hyperspectral data cube was built within MATLAB (Appendix 8.5.) to create a visual representation of the acquired dataset. Spectral datasets were also corrected for sensor and illumination biases within this software allowing the true spectral response curves of each target scene to be extracted for further examination and analysis (Appendix 8.6.). To do this, white and dark references were obtained during the image capture phase. Note the white reference utilised was a piece of matt white card illuminated in the same manner as the target scene. Figure 5.4. shows the workflow required to capture a hyperspectral image, highlighting the sequence of steps as they were implemented.

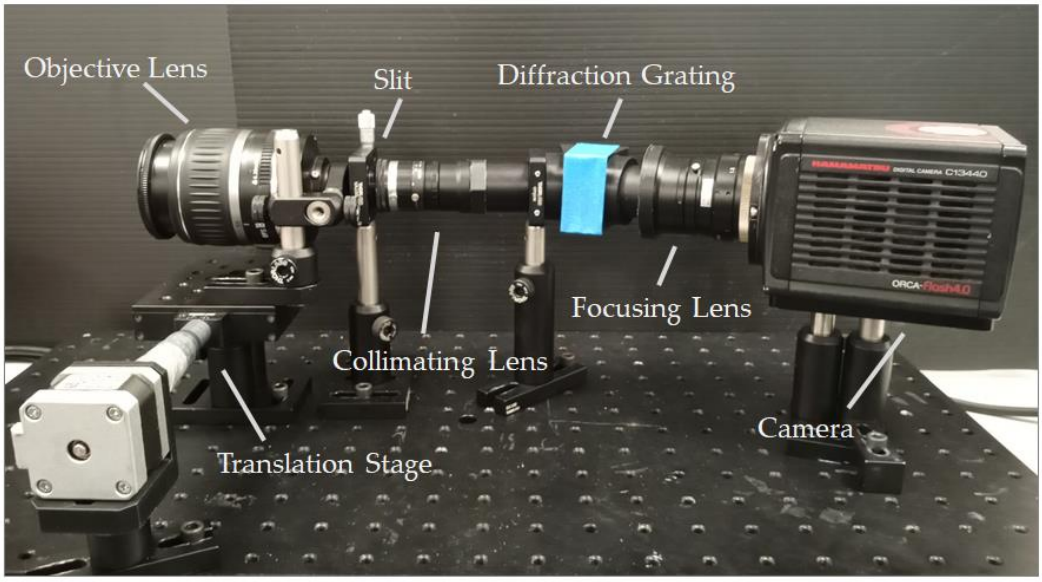

Figure 5.3. The Low-Cost High-Resolution hyperspectral imager within a laboratory setting.

Table 5.2 Data capture settings used for the high-resolution hyperspectral imager.

High-Resolution Instrument	**Setting**
Exposure Time (ms)	60
Wavelength Range (nm)	450 – 650 (Adjustable within the boundaries of 400 – 1000)
Spectral Resolution (nm)	0.29
Spatial Resolution (pixels)	1000 x 1000
Focal Lengths (mm)	18 and 55

Spectral calibration was completed using a Mercury Argon lamp that produced a series of intense narrow peaks at known wavelengths. This research utilised the peaks present at 546.074 nm and 576.960 nm, as shown in Figure 5.5. These two known points were used to calculate the wavelength range and the increment present between each value. The full width at half maximum (FWHM) was calculated using the 546.074 nm peak and was found to be two pixels.

The Instantaneous Field of View (IFOV) for each pixel within the spectrometer image was measured to be approximately 2 mm x 2 mm (18 mm focal length) and 300 µm x 300 µm (55 mm focal length) for a

95% energy enclosure at a working distance of 300 mm. The Total Field of View (TFOV) is determined by the slit height relative to the image circle of the objective lens and the travel distance of the translation stage. To calibrate the instrument allowing samples from different sources to be accurately compared, a radiometric assessment of the optical power represented by each pixel within the image was performed by measuring the power reflected by the white reference target. This was performed using a photodiode-based radiometer, described by Zhu et al. [37]. The RG850 long-pass filter was replaced by a Thorlabs narrow bandpass filter (#FB550-10), centred on 550 nm with a FWHM of 10 nm. The reflected optical power collected by the radiometer was calculated by comparing the photocurrent measured by the radiometer with and without the filter in the optical path. Given that the FOV of the radiometer represented an area upon the target of approximately 14 mm in diameter at its 1 m operating distance, the reflected power per unit area, without the filter in place, was calculated from this to be approximately 250.26 $\mu W/m^2$. The optical power reflected from the illumination reference target was, therefore, estimated to be 38.51 nW.

Acquisition	1. Set parameters and scan scene
Post Processing	2. Dark frame subtraction 3. Bias correction 4. Data cube formation 5. Spectral calibration

Figure 5.4. Work flow used to capture a hyperspectral image with the Low-Cost High-Resolution instrument detailing image acquisition and post processing stages.

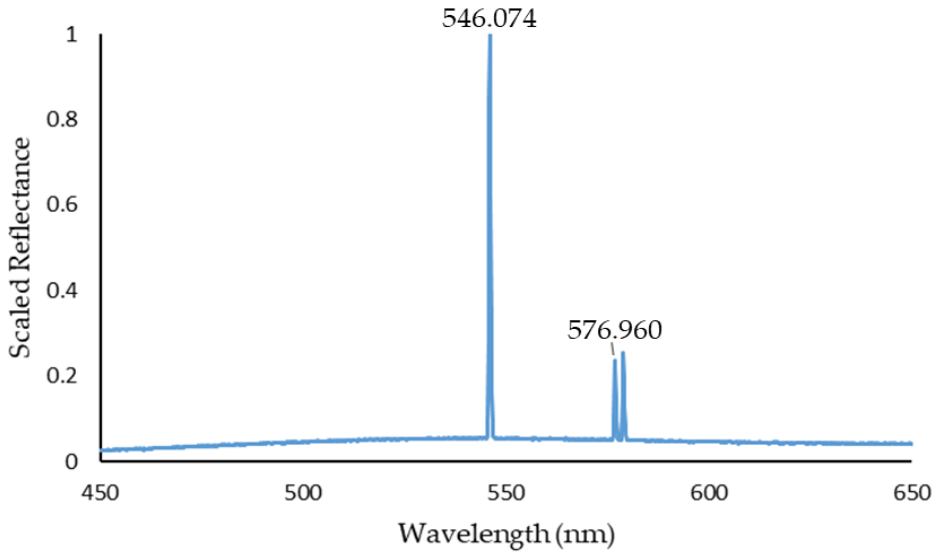

Figure 5.5. Spectrum captured from a Mercury Argon lamp using the Low-Cost High-Resolution instrument highlighting the peaks present at 546.074 nm and 576.960 nm that were used to spectrally calibrate the instrument.

5.3. Optical Characterisation

To provide a quantifiable measure of the optical abilities of the instrument, the Contrast Transfer Function (CTF) was calculated for both focal lengths used within this chapter. The modulation depth was measured with a Thorlabs R2L2S1N resolution target. Images were captured of the target and the modulation depth for a number of line pair widths was calculated (Figure 5.6). The modulation depth was different for horizontally and vertically orientated CTF targets. This is due to the scanning nature of the system. The optical resolution was measured from the horizontal CTF targets (as shown in Figure 5.6) because the vertical CTF targets were influenced by small variations in scan speed, minor perturbations in the translation stage, and the finite slit width. A knife-edge measurement provides a simple method of determining the point-spread-function of an optical system [38]. The point-spread-function quantifies the extent to which an optical system can resolve a point source of light. A knife-edge was, therefore, used to assess the influence of these sources of error on the resolution. The width in pixels between 5% and 95% of the measured signal normal to the knife-edge was measured vertically (parallel to the slit) and horizontally (normal to the slit). Figure 5.7. shows the horizontal and vertical knife-edge measurements for both focal lengths. In this figure it is clear that the vertical knife-edge measurements are better than the horizontal measurements, as expected. However, given the discrepancy of one pixel for the 18 mm focal length, and two pixels for the 55 mm focal length, this difference does not appear to be great enough to significantly influence the quality of output datasets acquired with this instrument.

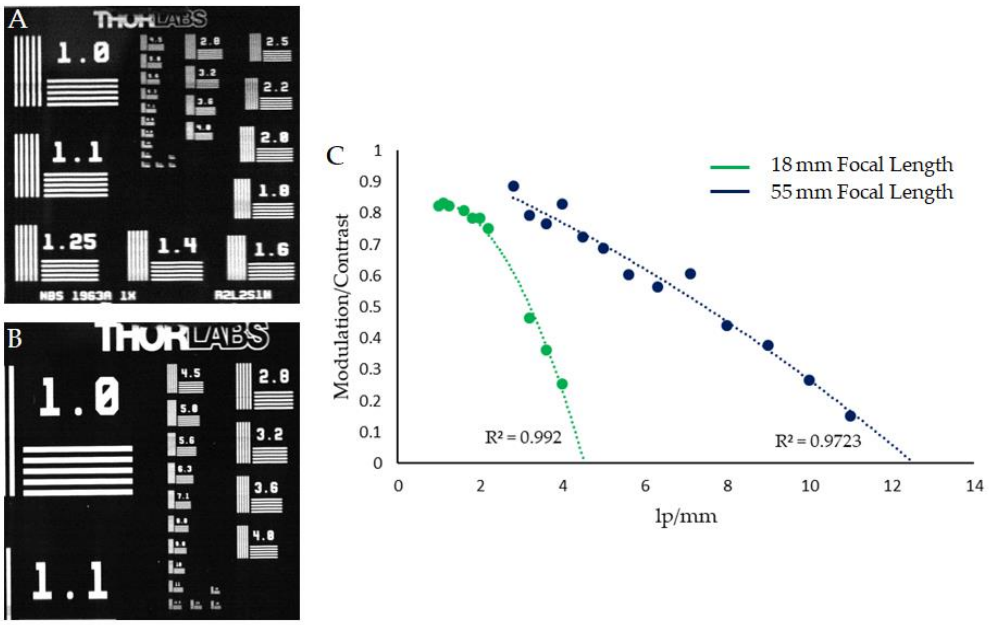

Figure 5.6. CTF analysis for both focal lengths. A and B show an image frame of the resolution target captured at an 18 mm focal length and a 55 mm focal length respectively, C shows the resulting CTF values for horizontal line pairs.

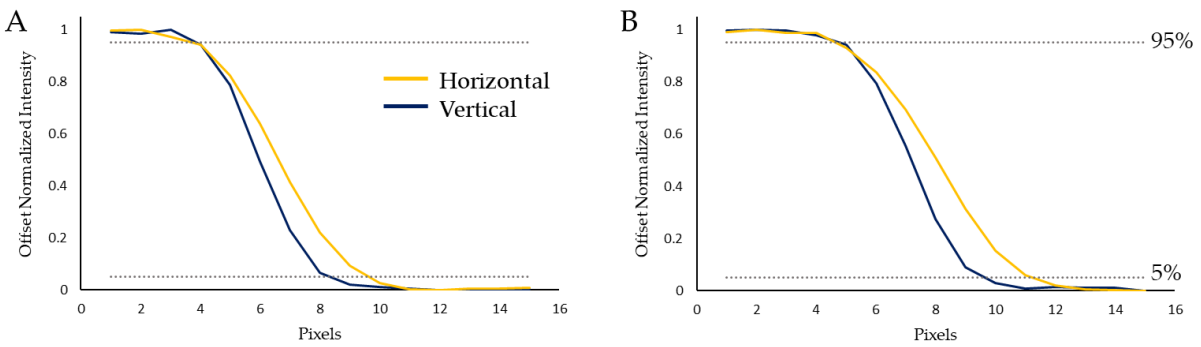

Figure 5.7. Knife-edge measurements for each focal length. A shows the results for the 18 mm focal length demonstrating a one-pixel discrepancy between orientations. B shows results for the 55 mm focal length demonstrating a two-pixel discrepancy between orientations.

5.4. Initial Testing

To visually demonstrate the spatial and spectral abilities of this instrument a range of targets featuring intricate structures were imaged. These targets were chosen as they each contained intricate small-scale features that are often difficult to resolve using low-cost hyperspectral sensors. By demonstrating the instrument's abilities with these initial targets it helps to highlight the variety of targets that can be resolved with this instrument, emphasising the significant potential available in the continued democratisation of high-resolution hyperspectral sensing. Figure 5.8. shows a spatial dataset captured using the high-resolution instrument of a section of a printed circuit board (PCB). This image was captured in a laboratory setting at a working distance of 30 cm using diffuse illumination from a 20 W LED lamp. This figure demonstrates the clarity of images that this instrument is capable of resolving. The writing and features present across the PCB are easily discernible within the image, highlighting the high spatial resolution possible with this instrument.

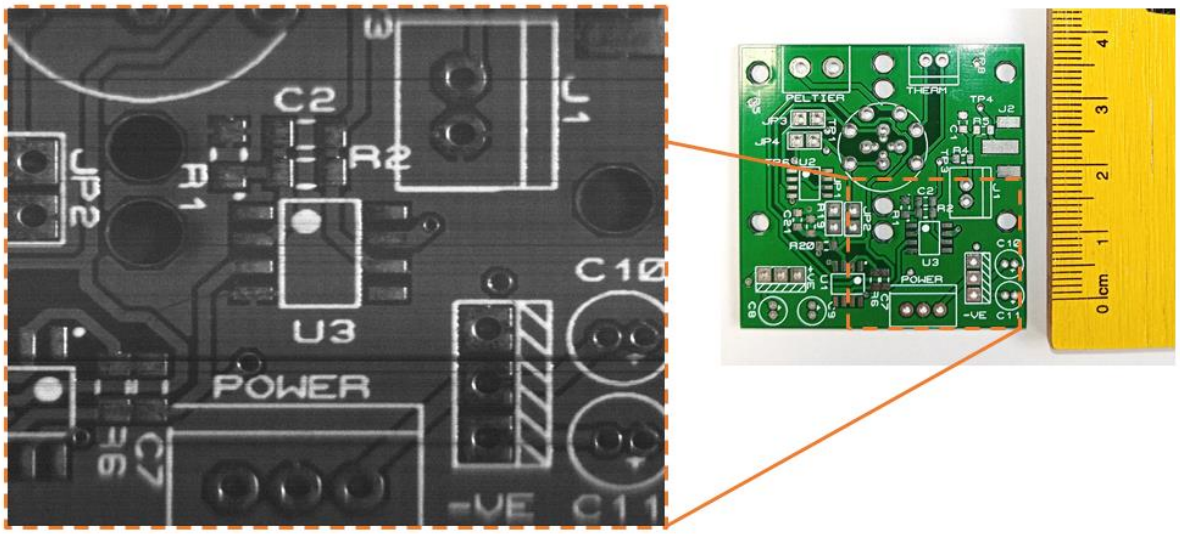

Figure 5.8 Spatial dataset captured of a PCB, highlighting the quality of spatial data collection possible with the high-resolution instrument.

In order to further test the spectral abilities of the high-resolution instrument a red/green Gala apple, with impact bruising that was not yet visible with the naked eye was imaged using this set-up. To minimise illumination variations across this target, it was placed within the low-cost integrating sphere analogue discussed in Chapter 3. However, it should be noted that the integrating sphere analogue is

not an integral component for reliable data capture with this instrument, as will be demonstrated within the example applications of this chapter. In this instance, the integrating sphere analogue was used in lieu of a diffuser to reduce the impact of illumination bright spots across the chosen target. This decision was made based on my experience from previous experiments, discussed within earlier chapters, that had shown these features to be prevalent across fruit targets without the inclusion of a sufficiently diffuse illumination source. Figure 5.9. shows the instrument set-up for data collection with the apple target within the low-cost integrating sphere. Given the significantly improved resolution available with this instrument it should be able to detect both the bruised area and the boundaries of different pigments within the healthy tissues. Figure 5.10. shows the spectral response observed across the visible spectrum for the apple target. It is clear in this figure that the instrument is capable of accurately detecting the bruise location, with the greatest visibility showing within the red region of the spectrum. This correlates well with expectations and the existing literature, because due to the predominantly red colouring of the apple, this region of the spectrum has the greatest contrast between the healthy and damaged tissues of the fruit. Conversely, the bruising is not visible within blue regions of the spectrum because the apple pigmentation is not particularly reflective in this region, resulting in minimal contrast between the healthy and damaged tissues. Additionally, this figure also demonstrates the spatial resolution of this instrument. The data cube accurately replicates the target object including smaller features, such as the stalk, which are often not clearly resolved by lower cost instrumentation. The pigment variations across the fruit are also easily discernible in these datasets further emphasising the clarity of data capture capable with this set-up.

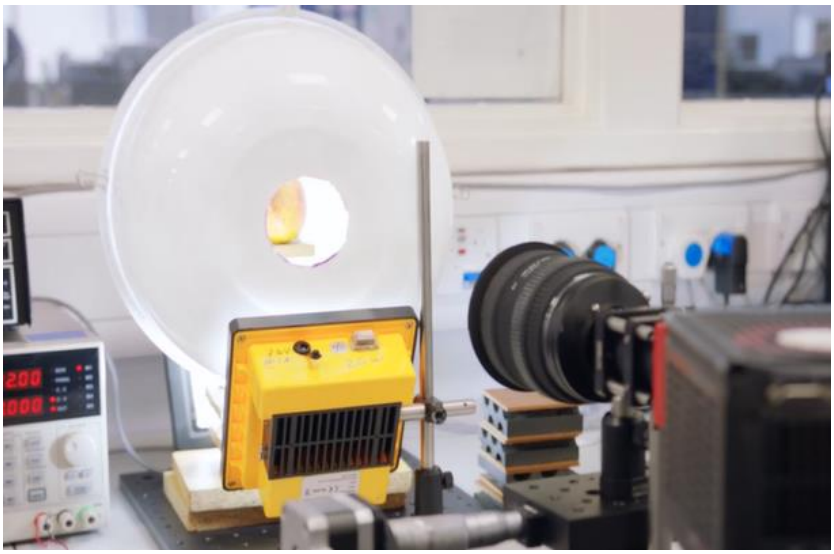

Figure 5.9 The high-resolution hyperspectral imager ready to image an apple target placed within the low-cost integrating sphere analogue.

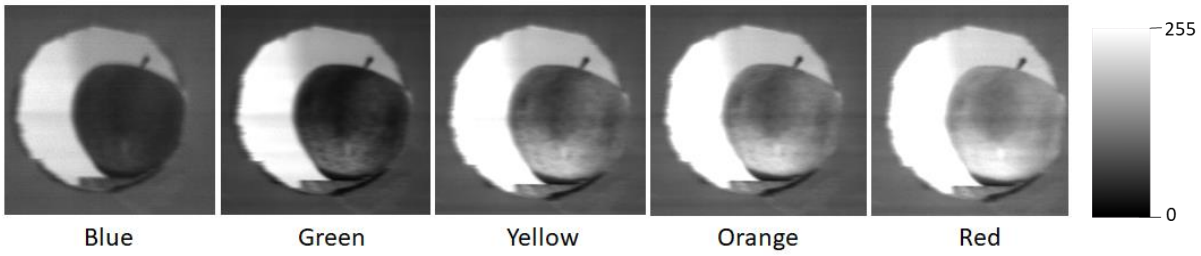

Figure 5.10 Spatial and spectral datasets acquired of an apple target with bruising that remains invisible to the naked eye. Note the variations in clarity across different wavelengths. Scale shows pixel intensity.

5.5 Example Application

To demonstrate both the spectral and spatial abilities of the Low-Cost High-Resolution hyperspectral imager within an environmental monitoring-based application, I chose to focus within the field of mineralogy. Section 5.1. highlighted the importance of resolving highly detailed spectral and spatial datasets within this discipline, therefore, the following measurements aim to highlight the efficacy of the instrumentation within this important area of research. Furthermore, the existing literature highlights the general absence of low-cost hyperspectral imaging applications within this domain, therefore, this aims to provide a foundation for further developments in low-cost hyperspectral imaging techniques within this field.

A variety of rock samples exhibiting intricate crystal structures and surface variations were imaged to demonstrate the clarity of datasets the instrumentation was capable of capturing. Figure 5.11. shows a gneiss sample with characteristic banding. Looking at the hyperspectral frames of this sample, the quality of the spatial data resolution is clearly demonstrated. The sample can be clearly identified within the hyperspectral data, and exact locations can be determined for further, more detailed analysis if required. This is of significant benefit within the field of mineralogy, enabling the precise spectral response of specific sample locations to be observed and monitored effectively.

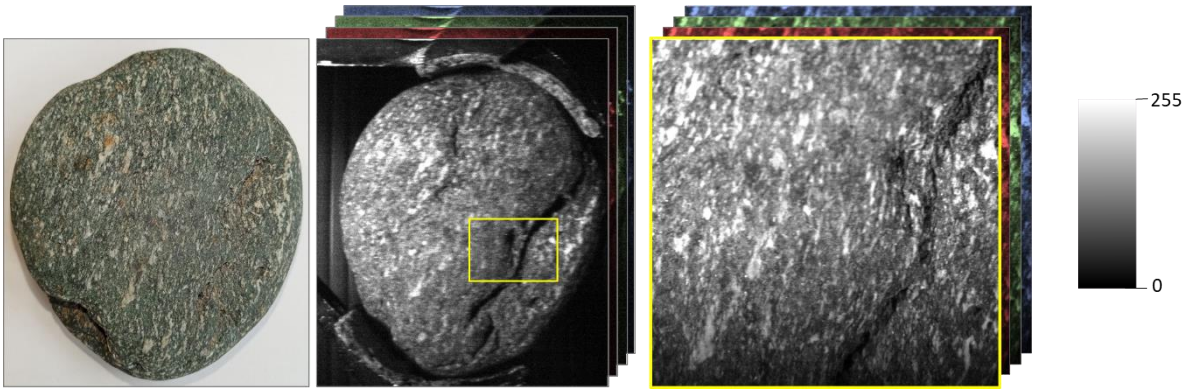

Figure 5.11. Hyperspectral image frames of a gneiss sample demonstrating the spatial resolution of this instrument. Characteristic banding and surface features are clearly visible within the hyperspectral data and can be easily related to their specific location on the original target. The image on the left is a standard colour image of the sample and the hyperspectral images are on the right hand side of the figure. The hyperspectral images are just one slice through the data cube that contains 689 discrete wavelength values. Scale shows pixel intensity for hyperspectral frames.

Similarly, when presented with a more complex target, the instrument was shown to perform well. Figure 5.12. demonstrates this using a basalt sample with plagioclase feldspars. The figure highlights this sample has a greater surface complexity with irregular surface variations, and bubble structures present alongside the feldspar features. This provides a much greater challenge for effective hyperspectral image collection, however, this figure demonstrates that the Low-Cost High-Resolution instrument is capable of accurately detecting these irregular features, clearly identifying individual mm-scale targets.

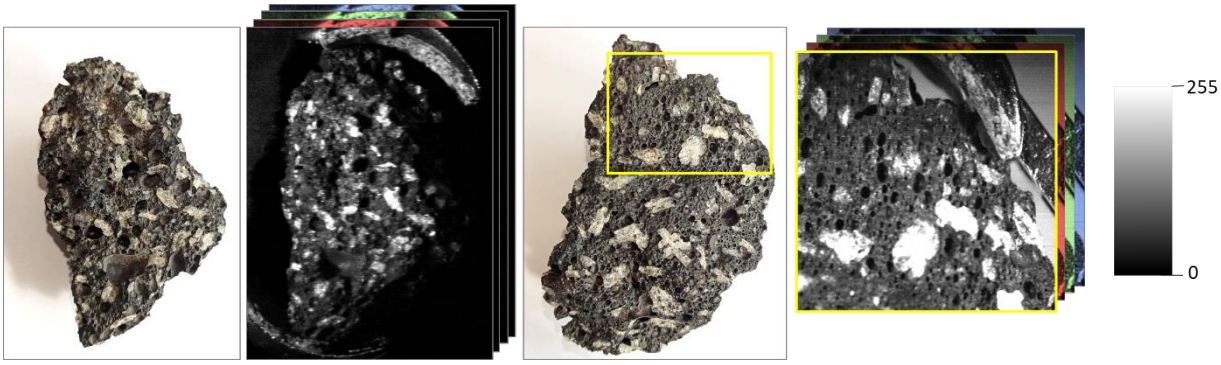

Figure 5.12. Two hyperspectral image frames of a basalt sample compared to standard colour images. Note the clarity of the surface features within the hyperspectral frames allowing clear differentiation between feldspar and surface features. The hyperspectral images are just one slice through the data cube that contains 689 discrete wavelength values. Scale shows pixel intensity for hyperspectral frames.

It should be noted that the hyperspectral image frames shown within the figures of this chapter only represent single slices of a data cube spanning 689 discrete wavelength values. This means that for each imaged scene the instrument builds a 689 Mega Pixel (MP) image (1000 x 1000 x 689). Each image frame, therefore, represents a small piece of the total data available. This is demonstrated in Figure 5.13. which shows the spectral graphs that demonstrate the wealth of underlying data. Subtle changes in spectral response can be accurately attributed to specific locations by effectively visualizing these small-scale features within the hyperspectral images. Figure 5.13 shows a sample of glacial debris with clear variations across its surface. These variations can be clearly identified within the graphed spectral responses. Furthermore, the spectral response recorded across this target correlates well with expectation; areas of the rock surface display a generally brighter response across the visible spectrum, whilst areas with orange pigmentation display more limited reflectance across shorter wavelengths.

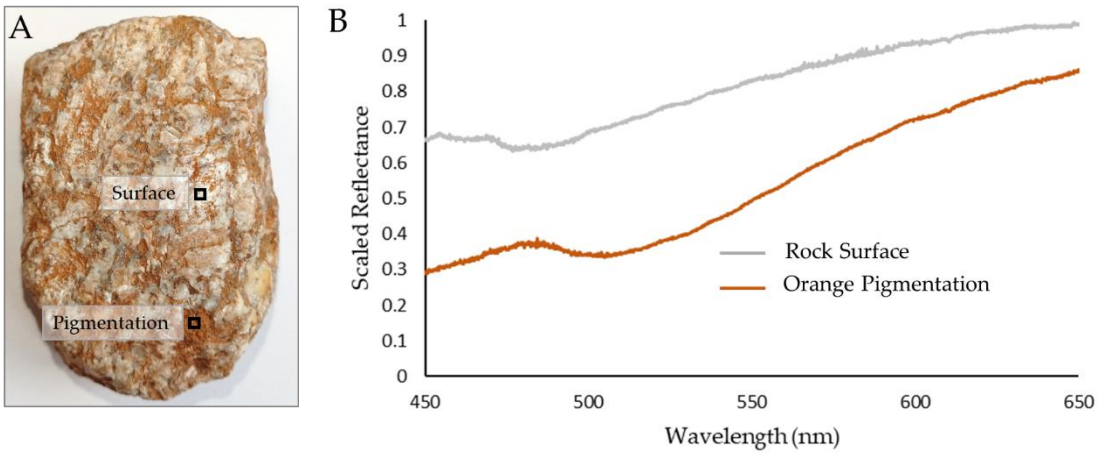

Figure 5.13. Spectral data for a piece of supraglacial debris with orange pigmentation. A shows a standard colour image of the rock sample highlighting the approximate locations that correspond to the spectral curves shown in B.

This is further demonstrated in Figure 5.14., which shows the spectral and spatial information captured for a sample of lapis lazuli. The hyperspectral data clearly shows a distinct peak in reflectance across blue wavelengths followed by a steady decline in reflectance towards red wavelengths, with areas of lighter, near-white, surface pigment becoming more obvious, across these generally darker wavelengths. This response is to be expected given the distinct visual colouring of the sample, and correlates well with the spectral response graph (Figure 5.15.), which, in turn, matches with the known spectral response of this target [39].

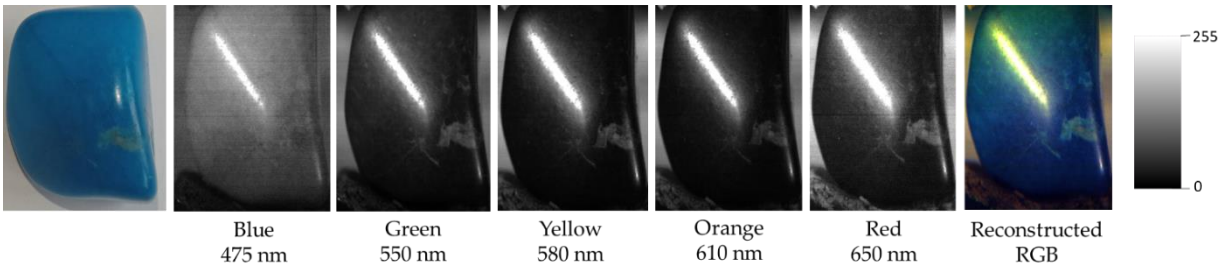

Figure 5.14. Spectral and spatial information obtained for a sample of lapis lazuli. Note the expected increase in reflectance across blue wavelengths followed by a steady reduction in reflectance towards longer wavelengths. The hyperspectral images represent single slices through the data cube that contains 689 discrete wavelength values. The reconstructed RGB image is created using red-green-blue equivalent images taken from the hyperspectral data cube. Scale shows pixel intensity for grey scale image frames.

The data discussed above clearly demonstrates the high spatial and spectral resolution achievable with the Low-Cost High-Resolution hyperspectral imager. The accurate identification of specific areas of spectral change is of significant benefit to a broad range of environmental monitoring applications and beyond. By clearly highlighting areas of specific spectral change it can enable targeted analysis and further investigation. This, in turn, enables the thorough analysis of intended targets with minimal, disruption and/or invasive analysis. Within the field of mineralogy these benefits can be particularly pertinent, increasing the accuracy of target studies whilst also minimizing the need for invasive investigation. Furthermore, these benefits remain in high demand across a broad range of applications, particularly within a low-cost, more accessible alternative. There is, therefore, significant potential to expand the use of low-cost high-resolution hyperspectral instrumentation across a variety of fields and disciplines. The datasets discussed within this chapter have shown the Low-Cost High-Resolution instrument to be capable of highly detailed data capture and analysis, demonstrating it to be a valuable addition to the research field.

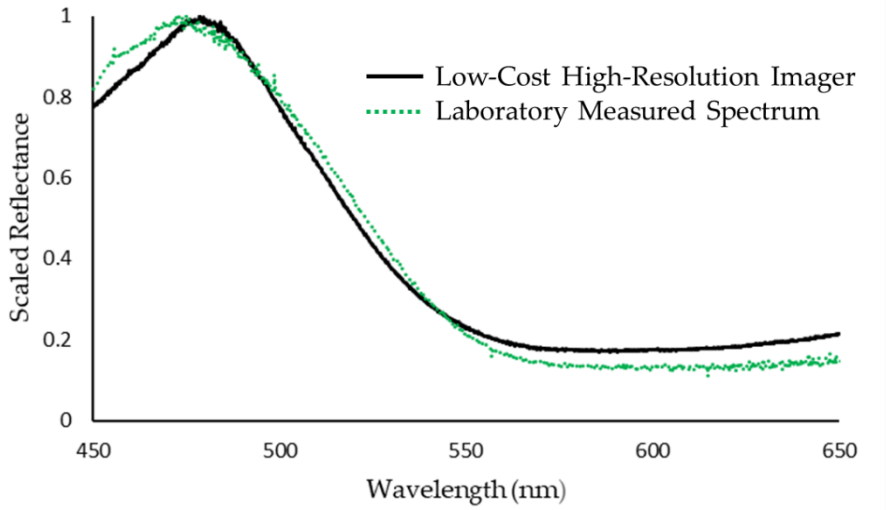

Figure 5.15. Spectral data obtained from a sample of lapis lazuli. Deviations from the laboratory measured spectrum are associated with regions of low signal within the illumination spectrum. Note the correlation between the spectral response curve and the spectral-spatial data shown in Figure 5.14.

The ability to capture high-resolution hyperspectral datasets using low-cost components outside of a laboratory setting is highly sought-after, enabling non-invasive in situ analyses, and removing the need for sample collection and preparation. This would be of significant benefit to a broad range of applications, particularly where vulnerable and/or fragile environmental settings are the focus of the intended study. The Low-Cost High-Resolution hyperspectral imager provides an opportunity to continue to improve the availability, and accessibility of hyperspectral imaging techniques, adding to a range of low-cost alternative devices suitable for a wide variety of situations and application areas. By demonstrating the abilities of the Low-Cost High-Resolution hyperspectral imager we have provided a further step towards this realisation, demonstrating the significant potential within the continued development of low-cost hyperspectral imaging alternatives.

5.6. Chapter Summary

This chapter has introduced a low-cost, high-resolution hyperspectral instrument that is capable of resolving mm-scale targets, providing a level of detail not typically available in low-cost hyperspectral imaging technologies. The instrument is semi-portable and has been demonstrated within a range of settings. It has been shown to be capable of high-resolution hyperspectral imaging using a portable laptop computer to enable data collection at different measurement locations, removing its reliance on a static computer terminal. The instrument can produce a 689 MP image of a chosen scene, with a 50% modulation of 3 lp/mm and 7.1 lp/mm for focal lengths of 18 mm and 55 mm respectively. The efficacy of this imager was demonstrated within the field of mineralogy, clearly emphasising its spectral and spatial abilities, as well as demonstrating its proficiency within, and value to, the field of low-cost hyperspectral imaging in environmental monitoring. The instrument was shown to be capable of resolving a range of mm-scale targets across a variety of samples with different surface features and complexities. The accurate identification of these features within the hyperspectral data provides substantial benefits, significantly increasing the quality and accuracy of the acquired hyperspectral datasets without the expected costs. Its efficacy across a broad range of hyperspectral imaging

applications has been validated, emphasising its potential as a valuable addition to the field of low-cost hyperspectral imaging.

5.7. References

[1] M. B. Stuart, M. M. J. Davies, M. J. Hobbs, T. D. Pering, A. J. S. McGonigle, and J. R. Willmott, "High-Resolution Hyperspectral Imaging Using Low-Cost Components: Application Within Environmental Monitoring Scenarios," *Sensors*. 2022.

[2] J. Jia *et al.*, "Tradeoffs in the Spatial and Spectral Resolution of Airborne Hyperspectral Imaging Systems: A Crop Identification Case Study," *IEEE Trans. Geosci. Remote Sens.*, pp. 1–18, 2021.

[3] J. Jia, Y. Wang, J. Chen, R. Guo, R. Shu, and J. Wang, "Status and application of advanced airborne hyperspectral imaging technology: A review," *Infrared Phys. Technol.*, vol. 104, no. October 2019, p. 103115, 2020.

[4] Q. Yang, "Design study of a compact ultra-wide-angle high-spatial-resolution high-spectral-resolution snapshot imaging spectrometer," *Opt. Express*, vol. 29, no. 2, p. 2893, 2021.

[5] D. J. Brady, *Optical Imaging and Spectroscopy*. 2009.

[6] A. Barducci, D. Guzzi, C. Lastri, V. Nardino, P. Marcoionni, and I. Pippi, "Radiometric and signal-to-noise ratio properties of multiplex dispersive spectrometry," *Appl. Opt.*, vol. 49, no. 28, pp. 5366–5373, 2010.

[7] M. B. Stuart, A. J. S. McGonigle, and J. R. Willmott, "Hyperspectral imaging in environmental monitoring: A review of recent developments and technological advances in compact field deployable systems," *Sensors (Switzerland)*, vol. 19, no. 14, 2019.

[8] M. B. Stuart *et al.*, "Low-cost hyperspectral imaging system: Design and testing for laboratory-based environmental applications," *Sensors (Switzerland)*, vol. 20, no. 11, pp. 1–13, 2020.

[9] B. P. Banerjee, S. Raval, and P. J. Cullen, "UAV-hyperspectral imaging of spectrally complex environments," *Int. J. Remote Sens.*, vol. 41, no. 11, pp. 4136–4159, 2020.

[10] T. C. Wilkes, T. D. Pering, A. J. S. McGonigle, G. Tamburello, and J. R. Willmott, "A low-cost smartphone sensor-based UV camera for volcanic SO2emission measurements," *Remote Sens.*, vol. 9, no. 1, pp. 1–11, 2017.

[11] E. Adam, O. Mutanga, and D. Rugege, "Multispectral and hyperspectral remote sensing for identification and mapping of wetland vegetation: A review," *Wetl. Ecol. Manag.*, vol. 18, no. 3, pp. 281–296, 2010.

[12] J. Zhang, B. Rivard, A. Sánchez-Azofeifa, and K. Castro-Esau, "Intra- and inter-class spectral variability of tropical tree species at La Selva, Costa Rica: Implications for species identification using HYDICE imagery," *Remote Sens. Environ.*, vol. 105, no. 2, pp. 129–141, 2006.

[13] A. Galieni, N. Nicastro, A. Pentangelo, C. Platani, T. Cardi, and C. Pane, "Surveying soil-borne disease development on wild rocket salad crop by proximal sensing based on high-resolution hyperspectral features," *Sci. Rep.*, vol. 12, no. 1, pp. 1–15, 2022.

[14] G. Yang, K. Huang, W. Sun, X. Meng, D. Mao, and Y. Ge, "ISPRS Journal of Photogrammetry and Remote Sensing Enhanced mangrove vegetation index based on hyperspectral images for mapping mangrove," *ISPRS J. Photogramm. Remote Sens.*, vol. 189, no. January, pp. 236–254, 2022.

[15] Y. Ma *et al.*, "Estimation of cotton leaf area index (LAI) based on spectral transformation and vegetation index," *Remote Sens.*, vol. 14, no. 1, 2022.

[16] I. F. Barton, M. J. Gabriel, J. Lyons-Baral, M. D. Barton, L. Duplessis, and C. Roberts, “Extending geometallurgy to the mine scale with hyperspectral imaging: a pilot study using drone- and ground-based scanning,” *Mining, Metall. Explor.*, vol. 38, no. 2, pp. 799–818, 2021.

[17] A. Parbhaker-Fox, B. Lottermoser, and D. J. Bradshaw, “Cost-Effective Means for Identifying Acid Rock Drainage Risks – Integration of the Geochemistry- Mineralogy-Texture Approach and Geometallurgical Techniques,” *Proc. Second AusIMM Int. Geometallurgy Conf.*, no. June, pp. 143–154, 2013.

[18] E. A. Gallie, S. McArdle, B. Rivard, and H. Francis, “Estimating sulphide ore grade in broken rock using visible/infrared hyperspectral reflectance spectra,” *Int. J. Remote Sens.*, vol. 23, no. 11, pp. 2229–2246, 2002.

[19] R. F. Kokaly *et al.*, “Spectral Geology and Remote Sensing Paper 84 Multiscale Hyperspectral Imaging of the Orange Hill Porphyry Copper Deposit, Alaska, USA, with Laboratory-, Field-, and Aircraft-based Imaging Spectrometers,” *Proc. Explor.*, vol. 17, no. October, pp. 923–943, 2017.

[20] F. D. van der Meer *et al.*, “Multi- and hyperspectral geologic remote sensing: A review,” *Int. J. Appl. Earth Obs. Geoinf.*, vol. 14, no. 1, pp. 112–128, 2012.

[21] F. F. Sabins, “Remote sensing for mineral exploration,” *Ore Geol. Rev.*, vol. 14, no. 3–4, pp. 157–183, 1999.

[22] G. A. Swayze *et al.*, “Using imaging spectroscopy to map acidic mine waste,” *Environ. Sci. Technol.*, vol. 34, no. 1, pp. 47–54, 2000.

[23] J. Shang, B. Morris, P. Howarth, J. Lévesque, K. Staenz, and B. Neville, “Mapping mine tailing surface mineralogy using hyperspectral remote sensing,” *Can. J. Remote Sens.*, vol. 35, pp. S126–S141, 2009.

[24] W. Nikonow, D. Rammlmair, J. A. Meima, and M. C. Schodlok, “Advanced mineral characterization and petrographic analysis by µ-EDXRF, LIBS, HSI and hyperspectral data merging,” *Mineral. Petrol.*, pp. 417–431, 2019.

[25] S. Roy, S. Bhattacharya, and S. N. Omkar, “Automated Large-Scale Mapping of the Jahazpur Mineralised Belt by a MapReduce Model with an Integrated ELM Method,” *PFG - J. Photogramm. Remote Sens. Geoinf. Sci.*, vol. 90, no. 2, pp. 191–209, 2022.

[26] M. A. Iqbal, R. Rezaee, C. Laukamp, B. Pejcic, and G. Smith, “Integrated sedimentary and high-resolution mineralogical characterisation of Ordovician shale from Canning Basin, Western Australia: Implications for facies heterogeneity evaluation,” *J. Pet. Sci. Eng.*, vol. 208, no. PA, p. 109347, 2022.

[27] E. Lombi, M. D. De Jonge, E. Donner, C. G. Ryan, and D. Paterson, “Trends in hard X-ray fluorescence mapping: Environmental applications in the age of fast detectors,” *Anal. Bioanal. Chem.*, vol. 400, no. 6, pp. 1637–1644, 2011.

[28] R. Belissont, M. Muñoz, M. C. Boiron, B. Luais, and O. Mathon, “Distribution and oxidation state of Ge, Cu and Fe in sphalerite by µ-XRF and K-edge µ-XANES: Insights into Ge incorporation, partitioning and isotopic fractionation,” *Geochim. Cosmochim. Acta*, vol. 177, pp. 298–314, 2016.

[29] S. Flude and M. Storey, “40Ar/39Ar age of the Rotoiti Breccia and Rotoehu Ash, Okataina Volcanic Complex, New Zealand, and identification of heterogeneously distributed excess 40Ar in supercooled crystals,” *Quat. Geochronol.*, vol. 33, pp. 13–23, 2016.

[30] F. Melcher, T. Oberthür, and D. Rammlmair, “Geochemical and mineralogical distribution of

germanium in the Khusib Springs Cu-Zn-Pb-Ag sulfide deposit, Otavi Mountain Land, Namibia," *Ore Geol. Rev.*, vol. 28, no. 1, pp. 32–56, 2006.

[31] D. M. Bower *et al.*, "Spectroscopic characterization of samples from different environments in a Volcano-Glacial region in Iceland: Implications for in situ planetary exploration," *Spectrochim. Acta - Part A Mol. Biomol. Spectrosc.*, vol. 263, p. 120205, 2021.

[32] S. Amici, A. Piscini, and M. Neri, "Reflectance Spectra Measurements of Mt. Etna: A Comparison with Multispectral/Hyperspectral Satellite," *Adv. Remote Sens.*, vol. 03, no. 04, pp. 235–245, 2014.

[33] F. Capaccioni *et al.*, "Mars-IRMA: In-situ infrared microscope analysis of Martian soil and rock samples," *Adv. Sp. Res.*, vol. 28, no. 8, pp. 1219–1224, 2001.

[34] M. Sgavetti *et al.*, "Two geologic systems providing terrestrial analogues for the exploration of sulfate deposits on Mars: Initial spectral characterization," *Planet. Space Sci.*, vol. 57, no. 5–6, pp. 614–627, 2009.

[35] S. Amici, A. Piscini, M. F. Buongiorno, and D. Pieri, "Geological classification of Volcano Teide by hyperspectral and multispectral satellite data," *Int. J. Remote Sens.*, vol. 34, no. 9–10, pp. 3356–3375, May 2013.

[36] G. M. Gadd, "Metals, minerals and microbes: Geomicrobiology and bioremediation," *Microbiology*, vol. 156, no. 3, pp. 609–643, 2010.

[37] C. Zhu, M. J. Hobbs, R. C. Masters, C. Rodenburg, and J. R. Willmott, "An accurate device for apparent emissivity characterization in controlled atmospheric conditions up to 1423 K," *IEEE Trans. Instrum. Meas.*, vol. 69, no. 7, pp. 4210–4221, 2020.

[38] L. Stanger *et al.*, "Reconstruction of microscopic thermal fields from oversampled infrared images in laser-based powder bed fusion," *Sensors*, vol. 21, no. 14, 2021.

[39] M. Davies, M. B. Stuart, M. Hobbs, A. McGonigle, and J. R. Willmott, "Image correction and in-situ spectral calibration for low-cost, smartphone hyperspectral imaging," *Remote Sens.*, vol. 14, p. 1152, 2022.

Chapter 6

Using Peatland Plant Spectral Response as a Proxy for Peat Health, Analysis Using Low-Cost Hyperspectral Imaging Techniques

This chapter is associated with the work presented in Stuart et al., [1]. It demonstrates the successful application of the Hyperspectral Smartphone and the Low-Cost High-Resolution instrument within a real-world systematic study where they are utilised to monitor the influence of drought stress on Sphagnum moss samples. Both instruments are shown to perform well, detecting key absorption and reflectance features and variations in spectral response associated with changing water content conditions up to three weeks before the onset of distinct visual changes. This represents a novel application of low-cost instrumentation, demonstrating that expensive commercial instrumentation are not necessarily required for accurate and robust environmental monitoring.

6.1. Introduction

To expand on the promising results demonstrated within their individual chapters the Hyperspectral Smartphone and the Low-Cost High-Resolution instrument were applied within a real world systematic study. This study focuses on a non-invasive method of determining the health of peatland below ground conditions, utilising these low-cost devices to monitor variations in spectral response in peatland vegetation communities, providing rapid, high quality hyperspectral datasets without the typically associated costs. This is an important area of research that will benefit significantly from the introduction of more low-cost, non-invasive monitoring techniques, therefore, this study aimed to provide a foundation for further developments and innovation within this field.

The continued monitoring and preservation of peatland environments is of significant importance to people, wildlife, and the planet [2]–[4]. Peatlands represent important terrestrial carbon stores [5]–[8], and provide habitats for a variety of rare plant and animal species [5], [7], [9], as well as being natural providers of water regulation and valuable records of our past [2], [3]. They play a key role in the global carbon cycle, storing ca. 30% of soil organic carbon, despite only representing ca. 3% of global land surface coverage [8]–[11], highlighting their importance for carbon storage and sequestration in a warming world. However, despite these key benefits, many peatland environments are subject to severe levels of erosion and degradation [10], [12], [13], resulting in a substantial reduction in the quality of the ecosystem services they are capable of providing. This, in turn, can result in these vast carbon stores reverting to carbon sources, releasing carbon back to the atmosphere, and can ultimately lead to the loss of peatland areas [8], [12], [14]–[16]. Monitoring the overall health of these environments, and the natural processes taking place within them, is, therefore, of significant importance, allowing us to gain a better understanding of these environments and the factors influencing the progression of degradation and erosion in these locations.

Spectral information acquired from above ground vegetation communities has been shown to be an effective means of estimating a variety of factors relating to the health of underlying peat deposits, providing valuable insights, from moisture content [11], [15], [17]–[19], to below ground carbon stock [14], [20], and nitrogen content estimations [21]. These approaches have been shown to provide a non-invasive alternative to conventional fieldwork techniques [15], allowing for larger study locations to be analysed over considerably shorter time scales [19]. Sphagnum moss is a key peatland genus that has been used extensively in this manner due to its specific characteristics that can affect its spectral response and, as such, can be used to estimate below ground peat conditions without the need for coring or other invasive peat sampling methods [17], [22]–[25]. Generally, the presence of Sphagnum mosses across a peatland area are an indication of good below ground conditions [17], [26]. These mosses thrive in the waterlogged environments of healthy peatland areas but, have been shown to decrease photosynthesis activity and perform more poorly in areas where the below ground water content is reduced [27]–[32]. These changes to photosynthesis activity result in changes in the spectral response of these mosses, with bleaching occurring as they start to dry out [30], [33], [34]. By monitoring these variations, it allows for estimates relating to below ground water table conditions and general peat health to be inferred, in turn, providing a means of long-term, non-destructive monitoring. In this chapter, the high-resolution hyperspectral imager, and the Hyperspectral Smartphone are applied to the field of peatland monitoring with the aim of highlighting the potential data collection opportunities available in this area of research utilising low-cost hyperspectral imaging techniques. Sphagnum samples under varying degrees of water stress are analysed under laboratory conditions with the aim of developing a spectral library that can be used to inform non-destructive, in-situ analyses of peatland environments, providing an early warning monitoring system for the onset of poorer conditions in these indispensable natural environments.

6.2. Sample Preparation and Simulated Environmental Conditions

To prevent undue disturbance to peatland areas the Sphagnum plants utilised in this study were obtained as samples, cultivated off-site within a micropropogation facility, rather than removing cuttings directly from the moorland. The moorlands at the focus of this research project, located within the Peak District National Park, have been subject to high levels of erosion and degradation, generally characterised by large expanses of bare peat and networks of erosion gullies [35]. These features have been exacerbated by a variety of factors including drainage, controlled burning, livestock grazing, and pollution from nearby urban areas, resulting in these moorlands being amongst the most degraded within the United Kingdom [36], [37]. However, more recently, restoration projects have been undertaken in this area with the aim of halting the losses associated with peatland erosion and returning the blanket peat to its natural, non-eroded state [36]–[39]. Many of these restoration projects involve the reintroduction of cultivated Sphagnum plants to areas of bare peat. These cultivated plants and those obtained for this research project have been obtained from the same source and are representative of the Sphagnum plants found across the moorland. A total of 30 Sphagnum samples of ca. 6 cm diameter were used. The Sphagnum species distribution within the samples is shown in Table 6.1.

Table 6.1. Sphagnum species distribution per sample.

Sphagnum Species	Approximate Percentage of Sample
Magellanicum	33
Palustre	33
Subnitens	33

The Sphagnum samples were split into three separate groups; a control group that was kept at saturation for the duration of the measurement period, a drought group that received no water inputs, and a rainfall group that received simulated rainfall events based on rainfall datasets obtained from a monitoring station situated on Kinder Scout, a moorland plateau within the Peak District National Park**.** Table 6.2. shows the individual groups and their inputs for the duration of the measurement period.

Table 6.2. Water inputs for each sample group.

Group	Observing	Water Inputs
Control	Maintained saturation	Steady-state maintenance determined by weight
Rainfall	Average rainfall experienced by in-situ plants	7 mm simulated rainfall every 3 - 4 days
Drought	Simulated drought	None

Each sample was housed within an individual container (Figure 6.1.). For the duration of the experiment the samples were kept within a controlled environment chamber (Argus Conviron controlled reach-in chamber) to imitate conditions experienced across the Kinder Scout plateau. The environmental data used here was obtained from the Kinder Scout Community Science Monitoring Station maintained by the Moors for the Future Partnership. Within these datasets records captured from April to September across a 4-year monitoring period, (2016 – 2019) for temperature and relative humidity; (2014 – 2017) for rainfall datasets were utilised. The months of April to September were selected to provide environmental conditions representative of the months where Sphagnum plants are most active, removing datasets from winter months where plant growth and productivity is significantly reduced. Within the controlled environment chamber the samples were kept within a 24-hour day cycle with 12 hours of daylight and 12 hours of darkness. During hours of daylight the chamber cycled through a gradual increase in light intensity towards midday, reaching a maximum of 400 umol m^{-2} s^{-1}, before steadily decreasing towards dusk. Temperature conditions followed a 24-hour cycle based on the average hourly temperature experienced at the environmental monitoring site (Table 6.3), representing a gradual increase in temperature towards midday, followed by a steady decrease towards dusk. The average relative humidity for the Kinder Scout location was 90.8%. This was replicated within the controlled environment chamber. Rainfall datasets were used to establish the typical rainfall volume and frequency experienced by in-situ Sphagnum plants. The average monthly rainfall was 104 mm occurring over 15 rain days. This equates to approximately 7 mm rainfall every 3 – 4 days. This approximation was used to simulate rainfall events for Sphagnum plants within the rainfall group for the duration of the study period. Figure 6.1. shows the samples within the controlled environment chamber.

Figure 6.1 Sphagnum samples within the controlled environment chamber. Each group was kept within a separate tray with samples rotated regularly during the measurement period.

Table 6.3. Temperature dataset used within the controlled environment chamber.

Time	Temperature (°C)
00:00	8.3
01:00	8.1
02:00	7.9
03:00	7.8
04:00	7.7
05:00	7.8
06:00	8.4
07:00	9.4
08:00	10.6
09:00	11.8
10:00	12.9
11:00	13.7
12:00	14.3
13:00	14.6
14:00	14.6
15:00	14.4
16:00	13.7
17:00	12.9
18:00	11.8
19:00	10.7
20:00	9.7
21:00	9.1
22:00	8.8
23:00	8.5

6.3. Data Collection

For the duration of the study, measurements were taken every three days using both the Hyperspectral Smartphone from Chapter 4, and the low-cost high-resolution hyperspectral imager from Chapter 5.

Smartphone datasets were captured at a nadir angle, where the samples were placed directly below the observing instrument. The high-resolution instrument utilised a flat mirror to achieve an approximate nadir angle without tilting the instrument. Samples were also weighed, and photographed with a standard RGB camera before being returned to the controlled environment chamber. Care was taken to ensure that each sample spent a minimal amount of time outside of the chamber, with samples being returned to the chamber promptly after their measurements had been completed. Additionally, to reduce any potential influences of edge effects, sample positions within the chamber were rotated randomly after each measurement phase.

6.3.1. Hyperspectral Smartphone

Hyperspectral datasets were captured with the Hyperspectral Smartphone utilising the hand-held method discussed in Chapter 4. Each Sphagnum sample was placed within the in-scene reference card and illuminated using two 20 W LED lamps situated at either side of the test card to minimise the influence of shading/bright spots across the spectral dataset. The working distance utilised for these measurements was a short working distance of ca. 1 m. Calibration was completed using the RGB panel of the reference card, allowing for datasets to be easily and accurately compared without the need for additional data collection. These datasets were processed in MATLAB then averaged to provide a single dataset that was representative of each group (Control, Rainfall, and Drought) for each measurement day, enabling datasets to be compared to accurately monitor any changes in spectral response between these groups across the measurement period.

6.3.2. High-Resolution Instrument

To capture hyperspectral datasets with the high-resolution instrument, each sample was positioned, in turn, below the external flat mirror to enable the easy collection of nadir datasets with this instrument, resulting in a working distance of ca. 30 cm. A wavelength range of 565 nm – 740 nm was used for these measurements. This particular range was selected because it enabled the capture of datasets across the visible-infrared boundary whilst also providing additional data across the green-red region of the visible spectrum, including the region where the Hyperspectral Smartphone has been shown to have reduced sensitivity. By focusing within these wavelengths it enabled the capture of a broad spectrum of data using two low-cost portable systems, which, in turn, provides a greater spectral range for analysis. Figure 6.2. shows the set-up used for this period of data collection. Illumination was provided by a 30 watt Halogen lamp situated above the sample to minimise shading across the scene. This thermal illumination system was used because its spectral response better fitted the wavelength range of this instrument, reducing the potential for noise associated with low signal across longer wavelengths, compared to LED illumination. The compact translation stage was utilised to traverse the scene. Once captured, these datasets were processed within the MATLAB code discussed in Chapter 5, to remove sensor and illumination biases, and spectrally calibrate the dataset. The spectral datasets obtained for each sample within a group were then averaged to provide a single comparable, representative response for each group for each measurement day.

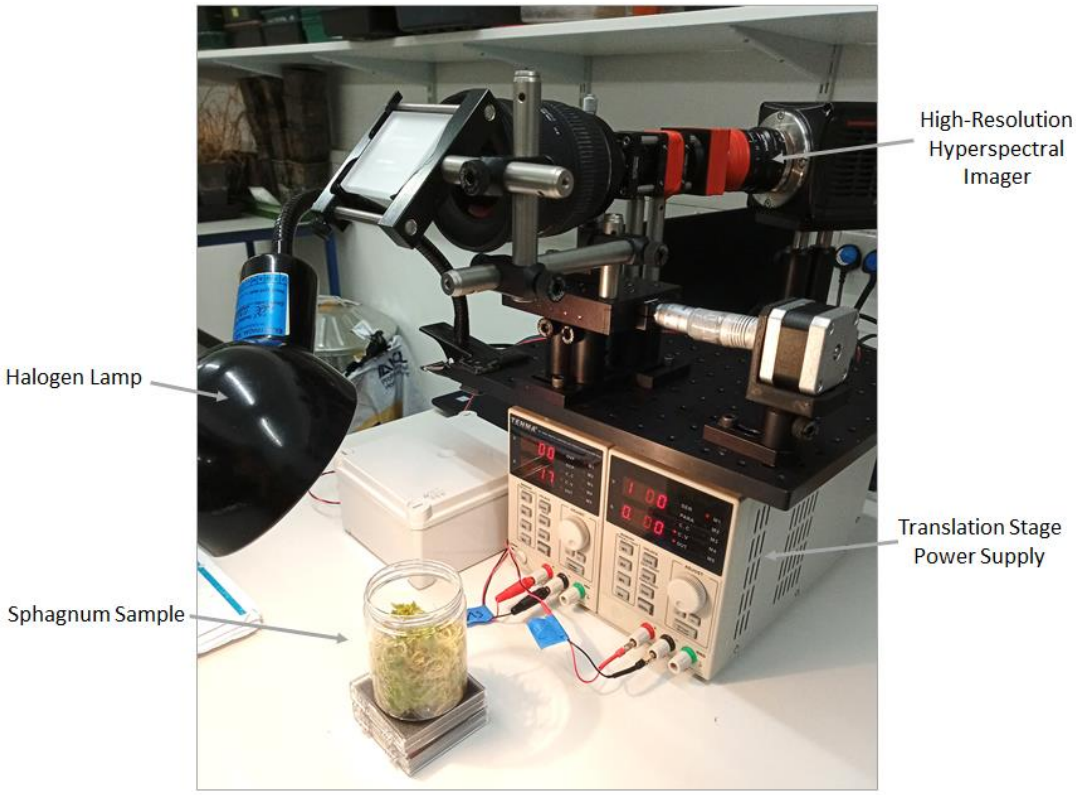

Figure 6.2 High-resolution hyperspectral imager set-up for Sphagnum sample analysis.

After all datasets had been collected the resulting spectral response graphs from both the Hyperspectral Smartphone and the low-cost high-resolution hyperspectral imager were combined to produce a single, continuous spectrum for each measurement day. This code can be found in Appendix 8.7.

6.4. Sphagnum Sample Change Over Time

6.4.1. Spatial Target Identification

Figure 6.3. shows a spatial and spectral dataset acquired of a Sphagnum sample using the high-resolution instrument. It is clear from this dataset the quality of spatial resolution achievable with this set-up from the detail observed across the Sphagnum sample. The individual capitula of the Sphagnum plant are clearly recognisable within the images allowing for the spectral response of specific regions of the sample to be determined with significant accuracy. Typically, low-cost hyperspectral imaging instruments are unable to accurately resolve these more intricate features within a more complex target, such as the Sphagnum sample. This is demonstrated in Figure 6.4. where the spatial datasets of the high-resolution instrument and the Hyperspectral Smartphone are directly compared. Whilst these instruments have significantly different price points, making them infeasible for a true direct comparison they illustrate the significant difference in spatial clarity of the collected data between two low-cost hyperspectral imaging instruments. This highlights the different applications each instrument is most suited for. For example, the ultra-low-cost Hyperspectral Smartphone provides a rapid and easy detection method enabling datasets to be acquired over numerous locations without the need for extensive operator training. Conversely, the low-cost high-resolution hyperspectral imager does require a basic level of expertise and generally represents a more complex instrument. The high-

resolution instrument is, therefore, better suited to targeted data collection activities allowing more intricate datasets to be acquired for areas that need further investigation.

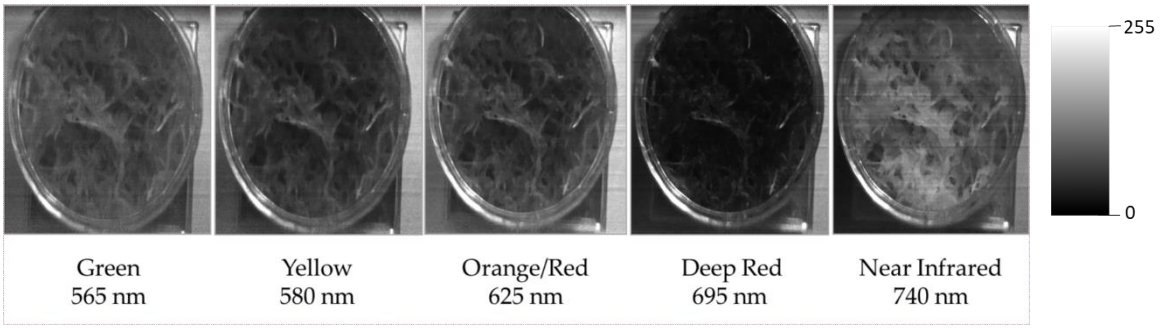

Figure 6.3 Spatial and spectral datasets acquired of a healthy Sphagnum sample using the high-resolution hyperspectral imager. Note the distinct reduction in reflectance in the deep red related to chlorophyll absorption. Scale shows pixel intensity.

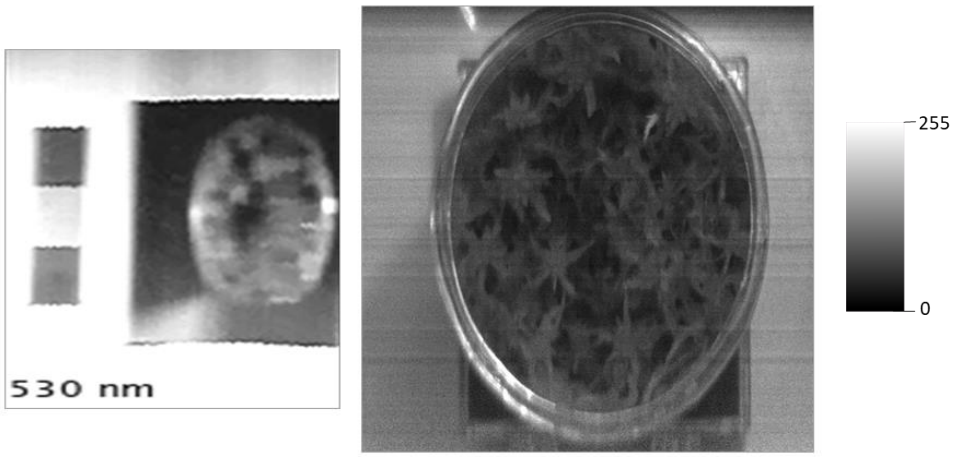

Figure 6.4 Spatial dataset comparison between the Hyperspectral Smartphone and the high-resolution hyperspectral imager. Hyperspectral Smartphone dataset (left) taken from 530 nm, Low-Cost High-Resolution dataset taken from 565 nm. Scale shows pixel intensity.

6.4.2. Change Over Time Observations

Hyperspectral imaging datasets were acquired for each Sphagnum plant within each group to determine how the individual samples reacted to their associated water conditions. The results obtained by each instrument were then averaged to provide a single representative response for each set of conditions for each measurement day to enable comparisons to be drawn between different groups and/or different days. Figure 6.5. shows the averaged spectral change over time observed for each measurement group. In this figure the datasets captured by both instruments have been combined to produce an extended dataset that covers the range of 400 nm to 740 nm, providing a comprehensive dataset in which to analyse any spectral changes occurring within the sample groups.

The spectral change over time for each group is clearly visible within this data. All groups can be seen to undergo a period of initial change, however, within the Control and Rainfall groups these changes quickly reduce. Conversely, the Drought group can be seen to continuously increase in reflectance, resulting in a brighter, and flatter spectral response. This is indicative of the bleaching process observed in Sphagnum species undergoing drought and water stress conditions. In the data the brightness of the Drought group's response can be seen to increase gradually for the duration of the measurement period, however, there are also more subtle changes occurring within this time frame.

Focusing on the Control and Rainfall groups, a number of reflectance peaks and absorption features can be identified across their spectral response indicating the presence of a number of pigments within their tissues. The distinct peak present at ca. 550 nm is a key reflectance feature of Sphagnum species [28], [40], [41], indicative of healthy conditions. Furthermore, absorption features can also be identified within these spectral curves with a shoulder at ca. 630 nm indicating chlorophyll b absorption and a distinct loss of reflectance at ca. 680 nm highlighting the presence of chlorophyll a [28], [40]. These features remain evident within the Control and Rainfall groups for the duration of the measurements, indicating continued healthy conditions in these groups. However, whilst these features are initially clear within the Drought group, they quickly become less easily discernible as the plants reduce in water content. Looking at Figure 6.5. subtle differences in the Drought group's spectral response can be observed as early as week two of measurements, with definite differences observed from week three onwards, highlighting rapid changes in spectral response. When these changes are compared with the visual response of the groups, shown in Figure 6.6. the benefits of hyperspectral imaging techniques become clear.

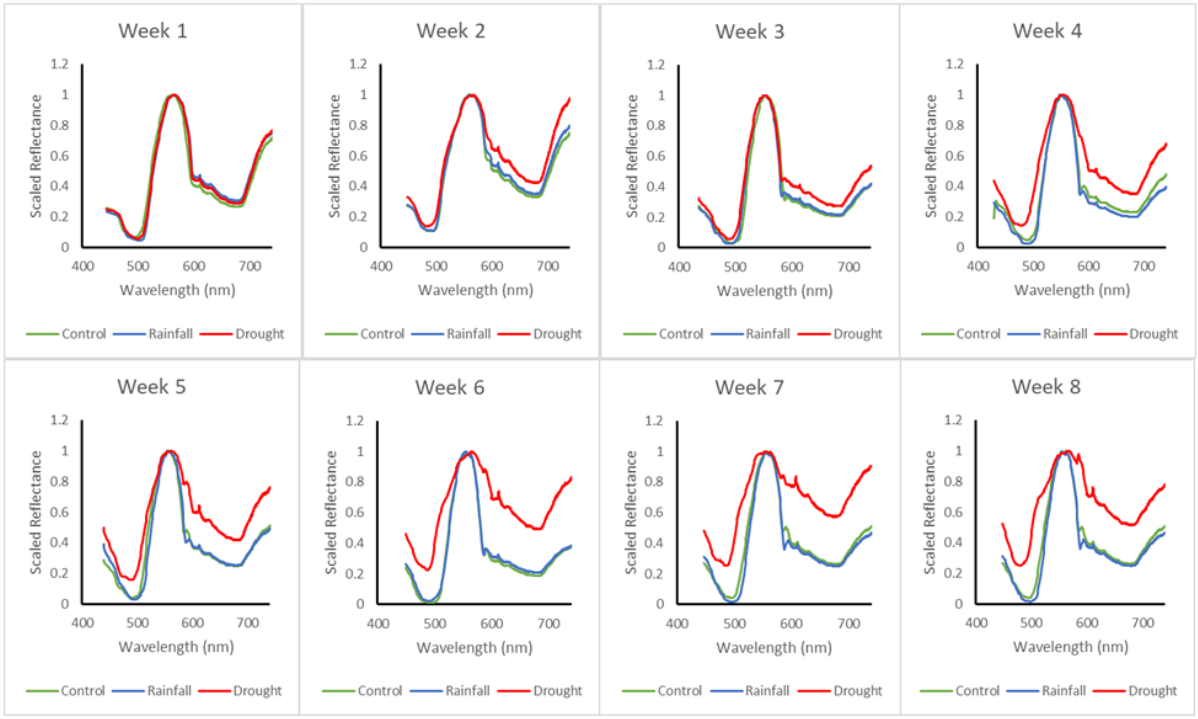

Figure 6.5 Sphagnum spectral change over time observed within each group. Datasets from the Hyperspectral Smartphone and the high-resolution hyperspectral imager are combined to provide reliable spectral information for the full range of measurements. Note the shift in spectral response of the Drought group over the measurement period.

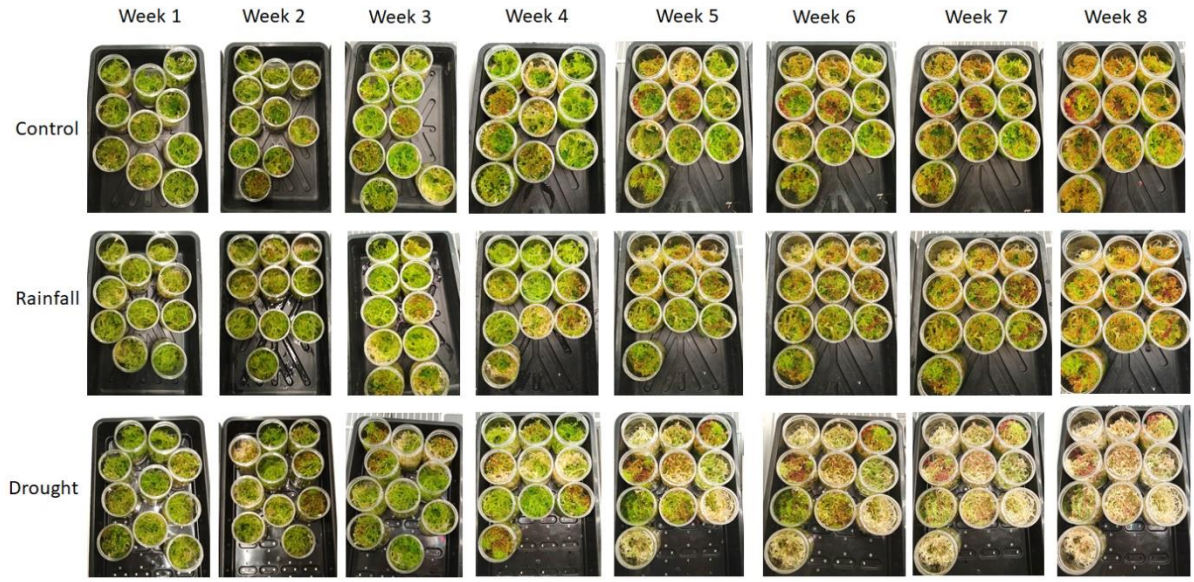

Figure 6.6 Visual change over time for each group. Note the later onset of visual change in the Drought group compared to spectral changes in Figure 6.5.

Whilst clear differences in the spectral response are observable from week three, visual changes in the Drought group only begin to show definitive differences from the Control and Rainfall groups at week five, after which point the Drought plants undergo a sudden increase in bleaching. This emphasises the early warning provided by hyperspectral imaging techniques, providing valuable time for the implementation of mitigation strategies. Furthermore, given the sudden increase in bleaching visually observed in the Drought plants it can be inferred that at the point where the Sphagnum plants show these definitive visual signs of water stress the damage may already have taken place. Relying on visual indicators alone, therefore, increases the chances of the plants being lost. This is a serious issue for peatland environments as areas of exposed peat are significantly more likely to be adversely affected by erosion and degradation processes. However, with the early indications observed within the spectral response graphs, there is a much greater opportunity to reduce the impact of poorer below ground conditions, providing a greater opportunity to revive the affected plants and maintain vegetation coverage.

The differences between the spectral responses of these groups is further illustrated in Figure 6.7. which shows the averaged spectral change observed at 680 nm for each group. This particular wavelength was selected due to its presence within the region of chlorophyll absorption, providing a more detailed look at spectral change within this region. In this figure it is clear that all groups underwent a period of initial change. The Control and Rainfall groups can be seen to undergo a period of increasing reflectance in this region before levelling off. From this information it can be inferred that these initial changes were a result of the samples acclimatising to their new environment. The conditions within the controlled environment chamber were colder than those experienced previously by the Sphagnum samples. The samples, as mentioned above, were obtained from a micropropogation green house with inherently warmer temperature conditions than those experienced by in-situ plants on moorland plateaus. Whilst the samples were given a period of two weeks to acclimatise within the controlled environment prior to the onset of measurements, it is clear that further changes were observed within the first few weeks of measurements. Sphagnum plants situated in colder conditions typically appear more red in colour. This was observed visually within the Sphagnum samples as shown in Figure 6.8. These initial changes within each Sphagnum group would, therefore, be expected, with

initial increases at 680 nm associated with the increase in red pigmentation across the Sphagnum samples

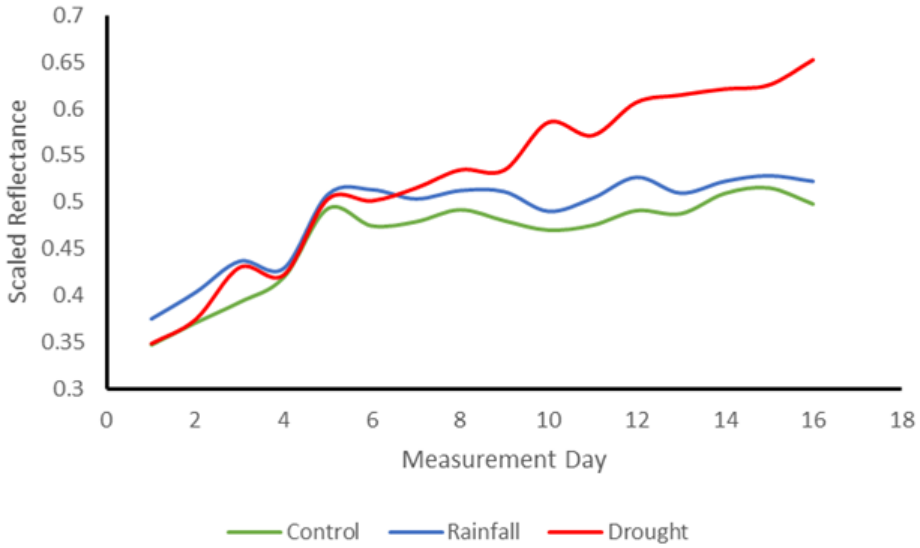

Figure 6.7 Spectral change observed at 680 nm for each group. Note the continued increase observed in the Drought group for the duration of the study.

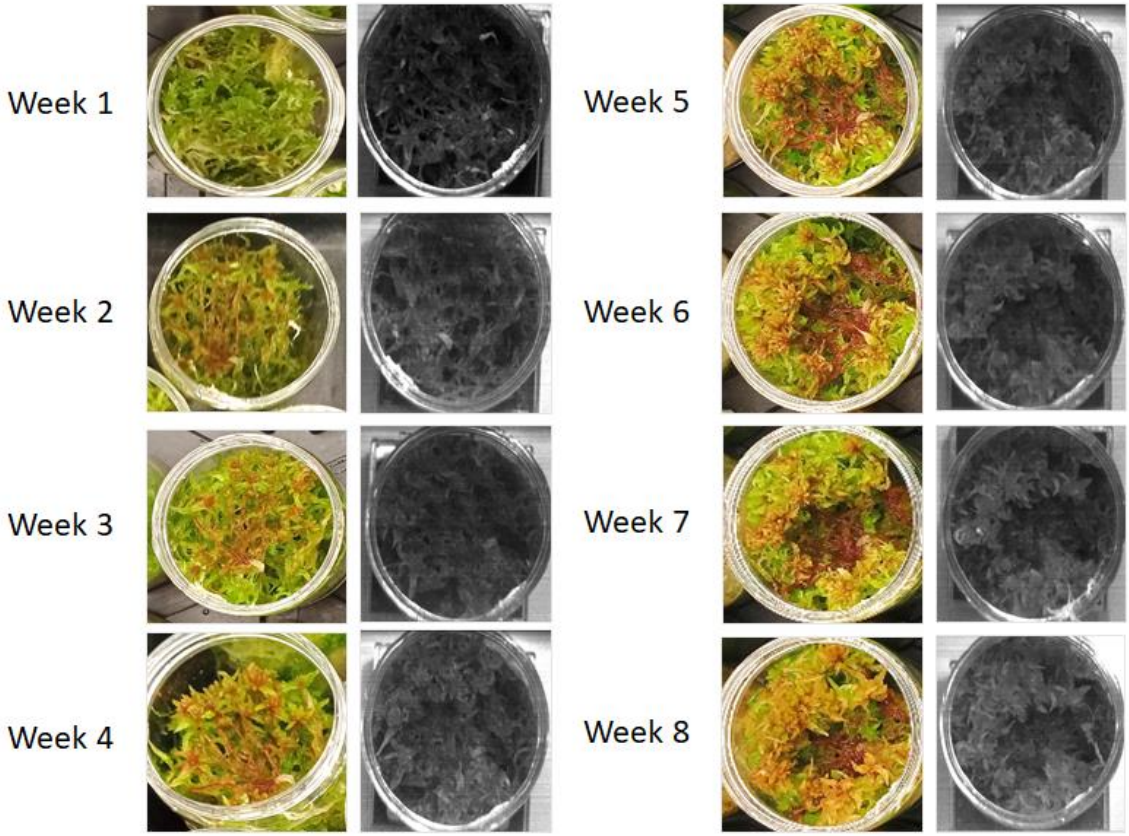

Figure 6.8 Visual change to redder pigments observed in all groups as a result of a change to colder conditions shown alongside spatial data obtained from the red region of the hyperspectral dataset, demonstrating the clear change observed in the spectral data. Example taken from a Control group sample.

Conversely, the Drought group can be seen to show a steady increase in reflectance at this wavelength for the duration of the study period. This highlights the reduction in chlorophyll pigmentation within these samples and further highlights the response of these samples to steadily increasing drought conditions. This correlates well with the recorded weights of the samples within each group which demonstrates relatively steady weights for Control and Rainfall groups and a consistent and sustained decline in weight for the Drought group (Figure 6.9.), highlighting the consistent reduction in water content.

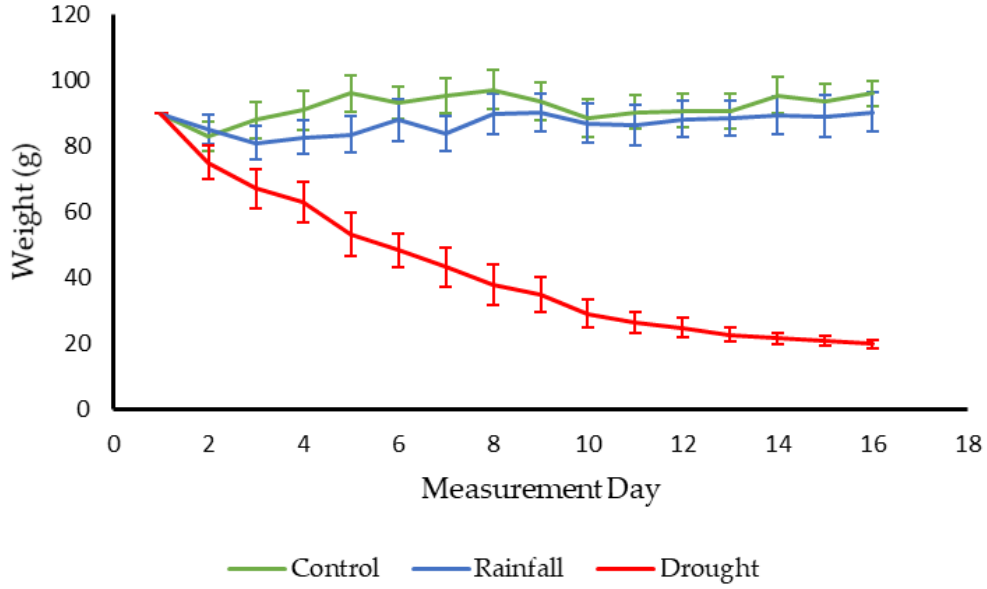

Figure 6.9 Weight variations across the measurement period highlighting the steady decline in weight within the Drought group suggesting a continuous reduction in water content. Error bars show range.

The spectral variations between groups are further emphasised in Figure 6.10. which demonstrates the ratio between two wavelengths for each group. The chosen wavelengths were 630 nm and 550 nm. These particular wavelengths were selected because, within healthy plants, the ratio of 630:550 should produce a relatively low value. This is because 550 nm represents a distinct peak in reflectance, whereas 630 nm produces a comparatively low response. Increases in the spectral response of the Drought group should, therefore result in an increasingly higher value as the spectral response at 630 nm increases over time. This trend is clear within the figure demonstrating the increase in reflectance within the Drought group compared to the lower values of Control and Rainfall plants. Whilst the dataset is noisy in places, this is indicative of the influence of plant shape variations on the spectral response. During the measurement period the Sphagnum samples will have continued to grow, causing the spatial shape of the plants to change in a way that will result in minor variations in spectral response. Despite these variations, the distinct trend in reflectance remains clear within the dataset.

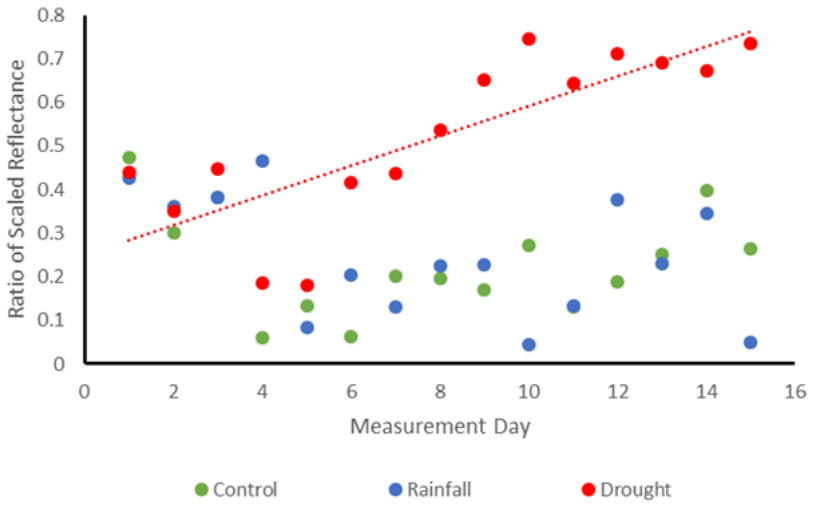

Figure 6.10 Change in ratio values for two key wavelengths (630 nm: 550 nm) for each group further highlighting the distinct changes within the Drought group. Trend line based on the Drought dataset.

6.4.3. Individual Variations, Key Examples

Whilst Section 6.4.2. focused on the responses observed across the groups as a whole, this section will focus on a key example obtained from each of the three groups to provide a greater insight into how individual plants responded to their associated environmental conditions. These specific samples have been selected because they each demonstrated interesting spectral changes across the measurement period, providing valuable datasets for further analysis. The ratio of spectral change over time between 630 nm and 550 nm for samples C9, R5, and D3 are shown in Figure 6.11**.** This figure is similar to Figure 6.10., however, instead of the averaged group data, Figure 6.11. provides the individual responses observed from selected examples. This figure, therefore, demonstrates that the main trends of the groups more generally can be replicated by individual plants, adding further support to the findings of this research. The control group samples, including C9 (shown in Figure 6.12) were kept saturated for the duration of the measurement period. Due to high levels of water content within this group, the spectral response of this sample would be expected to remain reasonably unchanged for the measurement duration, with the key reflectance and absorption features remaining easily identifiable within the data. This is clearly shown within Figure 6.11., with the greatest observable change occurring within the initial weeks of data collection. These changes can be inferred to be a result of the continued acclimatisation of these plants during the measurement period as discussed in Section 6.4.2**.** above. The maintained health of this sample for the duration of the measurement period suggests that its environmental conditions were favourable. This is to be expected as Sphagnum species are known to be capable of existing within semi-aquatic conditions which can be found in a number of locations across blanket bogs.

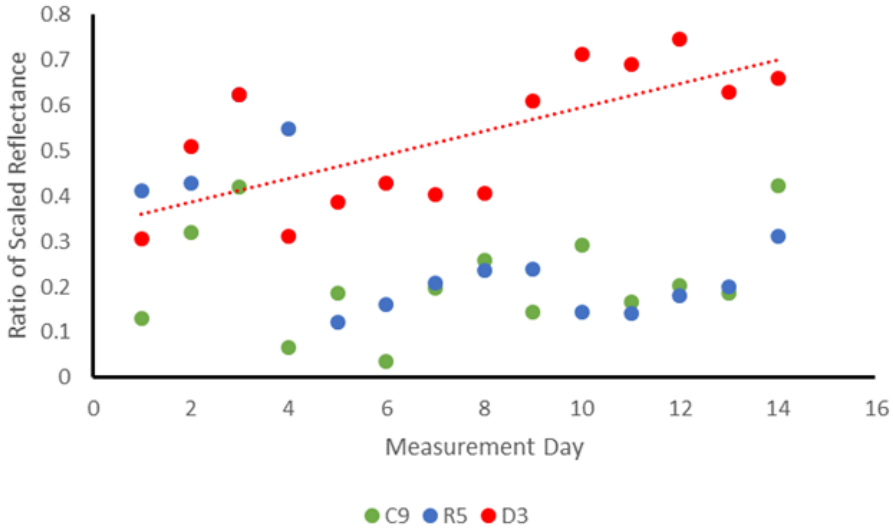

Figure 6.11 Change in ratio values for two key wavelengths (630 nm : 550 nm) for individual samples obtained from each of the three groups. Demonstrating that despite the additional noise within this dataset, the Drought sample still shows a substantial increase in reflectance compared to Control and Rainfall samples, demonstrating that key findings can be replicated between individual plants. Trend line based on the Drought dataset.

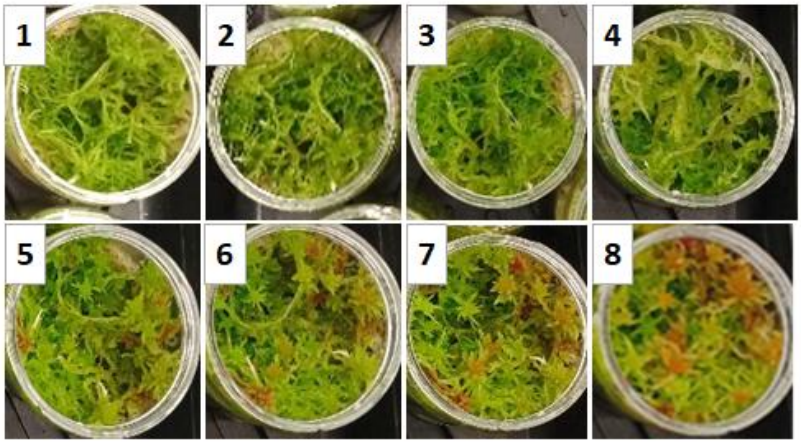

Figure 6.12 Visual change observed for sample C9 for each week of measurements highlighting the minimal changes occurring through the measurement period.

Similarly, sample R5 of the Rainfall group, shown in Figure 6.13., appears to have undergone similar changes to C9. The Rainfall group received simulated rainfall events similar to those experienced by in-situ moorland plants for the duration of the study. This resulted in these plants receiving water inputs but not maintaining saturation. It is clear within Figure 6.11. that this sample is also representative of a healthy plant, with reflectance and absorption features remaining evident for the duration of the measurement period, as highlighted through the low ratio between 630 nm and 550 nm. Whilst there are variations in the onset of an increase of red pigmentation between these Control and Rainfall samples, which is also evident within the ratio data of Figure 6.11. both responses remain indicative of healthy conditions demonstrating the importance of water content within Sphagnum plant communities. Furthermore, the results obtained for the rainfall group allow us to infer that the environmental conditions experienced by in-situ plants within the Peak District are typically conducive

to healthy Sphagnum growth. This provides a valuable insight into moorland conditions, suggesting that the continued reintroduction of Sphagnum plants to eroded peatlands within this area will be largely successful.

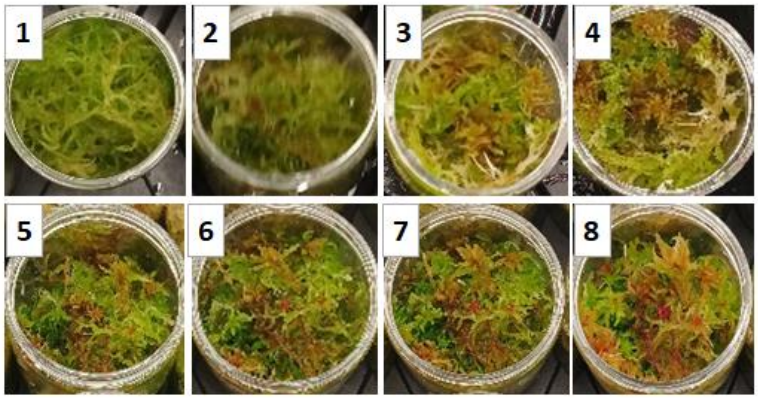

Figure 6.13 Visual changes observed from sample R5 for each week of measurements highlighting initial changes in pigmentation followed by stabilisation, indicating a healthy sample.

When the above samples are compared to sample D3 of the Drought group, clear differences can be observed. The Drought group received no water inputs for the measurement period, therefore, these samples experienced a steady reduction in water content causing them to undergo changes associated with the onset of prolonged water stress conditions. Figure 6.11**.** clearly shows this steady increase in spectral response for the duration of the measurement period, highlighting the regular reduction in the presence of key reflectance and absorption features as the sample undergoes bleaching associated with critical water losses. Furthermore, when this is compared to the visual changes in sample D3 (Figure 6.14), it also highlights the earlier onset of spectral indicators of drought stress over the presence of visual indicators, adding further emphasis on the importance, and significant benefits, of hyperspectral measurement and monitoring techniques. By observing these changes in spectral response, it enables the instigation of proactive mitigation approaches, providing a better opportunity to prevent the onset of further unfavourable conditions, and, therefore, increasing the chances of stabilising the underlying peat.

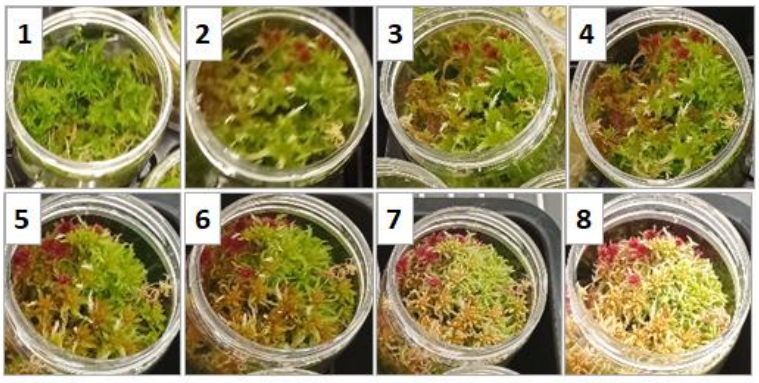

Figure 6.14 Visual change observed for sample D3 for each week of measurements further highlighting the benefits of spectral datasets over visual analysis due to the delayed visual response to unfavourable conditions.

6.5. Discussion

The above sections have highlighted how low-cost hyperspectral imaging instrumentation can be successfully implemented as non-invasive measurement and monitoring tools to the field of peatland health monitoring. It is clear that low-cost hyperspectral imaging alternatives represent a valuable addition to this field, enabling rapid and effective monitoring and decision making without the need to disrupt the underlying peat. The high-resolution hyperspectral imager provides mm-scale resolution enabling accurate and in-depth analysis of individual plants. This is particularly beneficial because, due to the quality of the output datasets it is possible to accurately pinpoint areas of concern that may require the implementation of mitigation measures. Whilst the current instrumental set-up is semi-portable, there remains considerable scope to make this instrument fully portable. This would require a more robust housing for the instrumental architecture and the conversion of the components to battery power. Both of these tasks can be completed with relative ease highlighting the considerable future potential available with this instrumentation.

Equally, the Hyperspectral Smartphone represents an ultra-low-cost user friendly method of obtaining rapid and accurate hyperspectral images both under laboratory and field conditions. Whilst the datasets resolved with this instrument are lower in quality than those of the high-resolution hyperspectral imager, it provides an accessible and low-cost method of undertaking initial non-invasive data collection, that can be undertaken by individuals without the need for extensive training. This enables hyperspectral images to be captured across a site of interest by individuals that are not necessarily familiar with the complexities of hyperspectral imaging analysis, such as peatland restoration volunteers. By providing volunteers with these low-cost devices it enables hyperspectral datasets to be acquired across a vast range of locations that can then be processed centrally by persons with more extensive knowledge and/or training, thus providing an accurate, non-invasive method of determining the health of peatland areas on a large-scale without incurring significant costs or requiring large-scale research trips. The widespread implementation of these ultra-low-cost methods can also be used as a means of highlighting areas that require further in-depth analysis e.g. utilising the high-resolution instrument. This enables measurement and monitoring methods to be applied specifically where they are required, significantly reducing the costs of these activities by reducing the need for vast high detailed surveys, therefore, enabling more timely and cost-effective analyses.

These low-cost hyperspectral imaging technologies have been successfully deployed within a real-world systematic study, demonstrating their proficiency and considerable potential for further deployment within a variety of environmental monitoring application areas. Whilst the Hyperspectral Smartphone and the high-resolution hyperspectral imager represent significantly different price points and, subsequently, data quality capabilities, when used within a combined approach they benefit each other significantly, enabling wide-scale coverage which can be followed up with more intricate analysis if required for a fraction of the cost of traditional monitoring methods. Equally, both instruments have also been demonstrated to be valuable stand-alone additions to hyperspectral imaging applications, providing an indispensable step towards the democratisation of hyperspectral imaging measurement modalities.

6.6. Chapter Summary

This chapter has successfully demonstrated the application of the Hyperspectral Smartphone and the Low-Cost High-Resolution imager to a real-world systematic study. Combined, these two instruments have been shown to be capable of accurately and effectively identifying changes in spectral response related to drought stress, highlighting subtle changes in spectral response that occur within the

datasets prior to the onset of confirmed visual changes. This emphasises the substantial benefits offered by these instruments, demonstrating that expensive commercial instrumentation is not required for robust and reliable hyperspectral imaging. They provide an early warning to the onset of potential unfavourable conditions without the need for invasive analysis in these fragile, yet essential environmental settings. This demonstrates their potential within the field of peatland health monitoring but also highlights their substantial potential as early warning monitoring systems within a broad range of environmental settings.

6.7. References

[1] M. B. Stuart, M. Davies, M. J. Hobbs, A. J. S. McGonigle, and J. R. Willmott, "Peatland Plant Spectral Response as a Proxy for Peat Health, Analysis Using Low-Cost Hyperspectral Imaging Techniques," *Remote Sens.* In Press.

[2] UK Government, "England Peat Action Plan," no. May, 2021.

[3] D. Carless, D. J. Luscombe, N. Gatis, K. Anderson, and R. E. Brazier, "Mapping landscape-scale peatland degradation using airborne lidar and multispectral data," *Landsc. Ecol.*, vol. 34, no. 6, pp. 1329–1345, 2019.

[4] E. Grand-Clement *et al.*, "Evaluating ecosystem goods and services after restoration of marginal upland peatlands in South-West England," *J. Appl. Ecol.*, vol. 50, no. 2, pp. 324–334, 2013.

[5] B. Cole, J. McMorrow, and M. Evans, "Spectral monitoring of moorland plant phenology to identify a temporal window for hyperspectral remote sensing of peatland," *ISPRS J. Photogramm. Remote Sens.*, vol. 90, pp. 49–58, 2014.

[6] K. M. Meingast *et al.*, "Spectral detection of near-surface moisture content and water-table position in northern peatland ecosystems," *Remote Sens. Environ.*, vol. 152, pp. 536–546, 2014.

[7] T. Erudel, S. Fabre, X. Briottet, and T. Houet, "CLASSIFICATION OF PEATLAND VEGETATION TYPES USING IN SITU HYPERSPECTRAL MEASUREMENTS," pp. 5713–5716, 2017.

[8] A. Rastogi, M. Stróżecki, H. M. Kalaji, D. Łuców, M. Lamentowicz, and R. Juszczak, "Impact of warming and reduced precipitation on photosynthetic and remote sensing properties of peatland vegetation," *Environ. Exp. Bot.*, vol. 160, no. October 2018, pp. 71–80, 2019.

[9] F. Beyer, G. Jurasinski, J. Couwenberg, and G. Grenzdörffer, "Multisensor data to derive peatland vegetation communities using a fixed-wing unmanned aerial vehicle," *Int. J. Remote Sens.*, vol. 40, no. 24, pp. 9103–9125, 2019.

[10] K. Medcalf, M. Jarman, and S. Keyworth, "ASSESSING THE EXTENT AND SEVERITY OF EROSION ON THE UPLAND ORGANIC SOILS OF SCOTLAND USING EARTH OBSERVATION AND OBJECT ORIENTATED CLASSIFICATION METHODS," *Int. Arch. Photogramm. Remote Sens. Spat. Inf. Sci.*, p. 2002, 2014.

[11] A. Banskota *et al.*, "Continuous Wavelet Analysis for Spectroscopic Determination of Subsurface Moisture and Water-Table Height in Northern Peatland Ecosystems," *IEEE Trans. Geosci. Remote Sens.*, vol. 55, no. 3, pp. 1526–1536, 2017.

[12] K. Albertson, J. Aylen, G. Cavan, and J. McMorrow, "Climate change and the future occurrence of moorland wildfires in the Peak District of the UK," *Clim. Res.*, vol. 45, no. 1, pp. 105–118, 2010.

[13] M. Evans and J. Lindsay, "High resolution quantification of gully erosion in upland peatlands at the landscape scale," *Earth Surf. Process. Landforms*, vol. 35, no. 8, pp. 876–886, 2010.

[14] J. Lopatin, T. Kattenborn, M. Galleguillos, J. F. Perez-Quezada, and S. Schmidtlein, "Using aboveground vegetation attributes as proxies for mapping peatland belowground carbon stocks," *Remote Sens. Environ.*, vol. 231, no. June, p. 111217, 2019.

[15] T. Lendzioch, J. Langhammer, L. Vlček, and R. Minařík, "Mapping the groundwater level and soil moisture of a montane peat bog using uav monitoring and machine learning," *Remote Sens.*, vol. 13, no. 5, pp. 1–30, 2021.

[16] N. Gatis *et al.*, “Drain blocking has limited short-term effects on greenhouse gas fluxes in a Molinia caerulea dominated shallow peatland,” *Ecol. Eng.*, vol. 158, no. September, p. 106079, 2020.

[17] K. J. Lees *et al.*, “Using spectral indices to estimate water content and GPP in sphagnum moss and other peatland vegetation,” *IEEE Trans. Geosci. Remote Sens.*, vol. 58, no. 7, pp. 4547–4557, 2020.

[18] E. Honkavaara *et al.*, “Remote Sensing of 3-D Geometry and Surface Moisture of a Peat Production Area Using Hyperspectral Frame Cameras in Visible to Short-Wave Infrared Spectral Ranges Onboard a Small Unmanned Airborne Vehicle (UAV),” *IEEE Trans. Geosci. Remote Sens.*, vol. 54, no. 9, pp. 5440–5454, 2016.

[19] A. A. Mustaffa, A. N. Mukhtar, A. W. Rasib, H. F. Suhandri, and S. M. Bukari, “Mapping of Peat Soil Physical Properties by Using Drone- Based Multispectral Vegetation Imagery,” *IOP Conf. Ser. Earth Environ. Sci.*, vol. 498, no. 1, 2020.

[20] J. P. Arroyo-Mora *et al.*, “Airborne hyperspectral evaluation of maximum gross photosynthesis, gravimetricwater content, and CO2 uptake efficiency of the Mer Bleue ombrotrophic peatland,” *Remote Sens.*, vol. 10, no. 4, pp. 1–20, 2018.

[21] M. Kalacska, M. Lalonde, and T. R. Moore, “Estimation of foliar chlorophyll and nitrogen content in an ombrotrophic bog from hyperspectral data: Scaling from leaf to image,” *Remote Sens. Environ.*, vol. 169, pp. 270–279, 2015.

[22] E. Milton *et al.*, “Remote sensing of bog surfaces,” *JNCC Rep.*, no. 366, p. 99, 2005.

[23] A. Harris, R. G. Bryant, and A. J. Baird, “Mapping the effects of water stress on Sphagnum: Preliminary observations using airborne remote sensing,” *Remote Sens. Environ.*, vol. 100, no. 3, pp. 363–378, 2006.

[24] A. Harris, R. G. Bryant, and A. J. Baird, “Detecting near-surface moisture stress in Sphagnum spp.,” *Remote Sens. Environ.*, vol. 97, no. 3, pp. 371–381, 2005.

[25] R. G. Bryant and A. J. Baird, “The spectral behaviour of Sphagnum canopies under varying hydrological conditions,” *Geophys. Res. Lett.*, vol. 30, no. 3, pp. 3–6, 2003.

[26] S. Bonnet, S. Ross, C. Linstead, and E. Maltby, *A review of techniques for monitoring the success of peatland restoration*. York UK: Natural England, 2009.

[27] A. Harris, R. Charnock, and R. M. Lucas, “Hyperspectral remote sensing of peatland floristic gradients,” *Remote Sens. Environ.*, vol. 162, pp. 99–111, 2015.

[28] K. E. Van Gaalen, L. B. Flanagan, and D. R. Peddle, “Photosynthesis, chlorophyll fluorescence and spectral reflectance in Sphagnum moss at varying water contents,” *Oecologia*, vol. 153, no. 1, pp. 19–28, 2007.

[29] M. Strack and J. Price, “Ecohydrology Bearing - Invited Commentary Transformation ecosystem change and ecohydrology: ushering in a new era for watershed management,” *Ecohydrology*, vol. 130, no. February, pp. 126–130, 2010.

[30] K. J. Lees, J. M. Clark, T. Quaife, M. Khomik, and R. R. E. Artz, “Changes in carbon flux and spectral reflectance of Sphagnum mosses as a result of simulated drought,” *Ecohydrology*, vol. 12, no. 6, 2019.

[31] P. McNeil and J. M. Waddington, “Moisture controls on Sphagnum growth and CO2 exchange on a cutover bog,” *J. Appl. Ecol.*, vol. 40, no. 2, pp. 354–367, 2003.

[32] B. J. M. Robroek, M. G. C. Schouten, J. Limpens, F. Berendse, and H. Poorter, “Interactive effects of water table and precipitation on net CO2 assimilation of three co-occurring Sphagnum mosses differing in distribution above the water table,” *Glob. Chang. Biol.*, vol. 15, no. 3, pp. 680–691, 2009.

[33] E. Bortoluzzi, D. Epron, A. Siegenthaler, D. Gilbert, and A. Buttler, “Carbon balance of a European mountain bog at contrasting stages of regeneration,” *New Phytol.*, vol. 172, no. 4, pp. 708–718, 2006.

[34] L. Bragazza, “A climatic threshold triggers the die-off of peat mosses during an extreme heat wave,” *Glob. Chang. Biol.*, vol. 14, no. 11, pp. 2688–2695, 2008.

[35] S. Goudarzi *et al.*, “Blanket Peat Restoration: Numerical Study of the Underlying Processes Delivering Natural Flood Management Benefits,” *Water Resour. Res.*, vol. 57, no. 4, 2021.

[36] M. Pilkington, J. Walker, R. Maskill, T. Allott, and M. Evans, “Restoration of Blanket bogs; flood risk reduction and other ecosystem benefits Final report of the Making Space for Water project Prepared for By Moors for the Future Partnership, 2015,” 2015.

[37] K. J. Lees *et al.*, “Using remote sensing to assess peatland resilience by estimating soil surface moisture and drought recovery,” *Sci. Total Environ.*, vol. 761, p. 143312, 2021.

[38] D. M. Alderson *et al.*, “Trajectories of ecosystem change in restored blanket peatlands,” *Sci. Total Environ.*, vol. 665, pp. 785–796, 2019.

[39] J. Benson, T. Crouch, D. Chandler, and W. J, “Harvesting Sphagnum from donor sites Pilot study report,” 2019.

[40] Y. Pang, Y. Huang, Y. Zhou, J. Xu, and Y. Wu, “Identifying spectral features of characteristics of sphagnum to assess the remote sensing potential of peatlands: A case study in China,” *Mires Peat*, vol. 26, pp. 1–19, 2020.

[41] J. E. Vogelmann and D. M. Moss, “Spectral reflectance measurements in the genus Sphagnum,” *Remote Sens. Environ.*, vol. 45, no. 3, pp. 273–279, 1993.

Chapter7

Discussion and Concluding Remarks

This chapter brings together the work discussed within this thesis, and highlights areas of work and applications that can be completed in the future either using the discussed instrumentation directly or as a foundation for further innovation.

7.1. Discussion

This thesis has presented the development and application of three low-cost hyperspectral imaging instruments primarily designed for environmental monitoring applications. These are: a low-cost laboratory-based hyperspectral instrument, a fully portable ultra-low-cost, smartphone-based instrument (Hyperspectral Smartphone), and a low-cost high-resolution hyperspectral instrument. Tests of each instrument within a range of environmental monitoring applications have shown them to perform well despite being, in some cases, over an order of magnitude cheaper than currently available commercial instrumentation. The value of their addition to the field of low-cost hyperspectral sensing has been demonstrated showing them to provide a significant step towards the democratisation of hyperspectral imaging techniques.

Chapter 3 first demonstrated the 'proof of concept' through the development of a low-cost, laboratory-based hyperspectral imager that was semi-portable within a laboratory environment. This instrument was designed using low-cost commercially available components, demonstrating that accurate, high quality hyperspectral datasets can be obtained from low-cost instrumentation. Instrumental metrology was shown through a radiometric calibration of the optical power, allowing the instrument's abilities to be quantifiably compared to different instrumentation. Initial testing was shown, which highlighted the significant influence of directional illumination on the quality of target outputs. These influences were minimised through the design and subsequent integration of a low-cost integrating sphere analogue. After these modifications were made to the imaging configuration, the efficacy of the instrument was highlighted through its application to a variety of environmental monitoring scenarios emphasising its compatibility with a broad range of applications.

Chapter 4 used the knowledge gained from the construction of the laboratory-based instrument in Chapter 3 to develop the Hyperspectral Smartphone, an ultra-low-cost smartphone-based hyperspectral instrument. This chapter started with initial measurements taken using a cardboard prototype to determine whether a smartphone was capable of constructing a spectral image. After successful testing, a more robust 3-D printed version was designed to enable accurate and reliable data capture. This instrument was demonstrated to be a portable hyperspectral sensor capable of accurate and repeatable data capture through its application to a range of environmental monitoring applications. This initial design relied on the inclusion of a basic translation stage to ensure steady and stable movement across the intended image scene. Further improvements were then highlighted, where an algorithm, coded in MATLAB, was demonstrated as an effective means of completing in-situ spectral calibrations, and enabling accurate, hand-held data collection. These improvements made the Hyperspectral Smartphone a fully portable system, removing the need to include the translation stage, and further optimising its associated accessibility. In its hand-held format the Hyperspectral

Smartphone is almost universally accessible, providing a significant step in the democratisation of hyperspectral imaging techniques.

Chapter 5 demonstrated the development of a low-cost high-resolution hyperspectral instrument, capable of identifying targets on the mm-scale. This instrument combined the skills learnt within Chapters 3 and 4 to produce an instrument that is semi-portable and capable of high quality, intricate data capture. Initial tests within a range of laboratory-based environmental applications demonstrated the proficiency of this instrument, before it was applied within a mineralogy-based study. The instrument was shown to be capable of resolving a range of mm-scale targets across a variety of samples with different surface complexities, emphasising its value to the research field.

Chapter 6 demonstrated the application of these devices within a real-world scenario. The high-resolution instrument from Chapter 5 and the Hyperspectral Smartphone from Chapter 4 were applied to a systematic study investigating the influence of drought conditions on the spectral response of Sphagnum moss, as a means of providing a non-invasive method of estimating peatland health. Both instruments were shown to work proficiently within this scenario for their respective price points enabling the collection of high quality datasets that are comparable to the existing literature. The hyperspectral analysis demonstrated that the Sphagnum spectral response provided an early warning for the onset of unfavourable conditions, providing valuable extra time for the implementation of mitigation measures that could benefit the peatland significantly. This, in turn, demonstrated the potential of these instruments for further applications within a broad range of real-world measurement and monitoring scenarios.

Overall, this body of work has presented three novel, low-cost instruments that have demonstrated utility within environmental monitoring applications and could potentially be more broadly applied, for example, within industrial applications. Each of these instruments, compared in Table 7.1., is optimised to fill a separate research niche. The Laboratory-Based Hyperspectral Imager of Chapter 3 provides a basic laboratory-based imager, demonstrating that hyperspectral imaging does not require expensive commercial instrumentation. The Hyperspectral Smartphone from Chapter 4 is the most accessible and practical of the developed instruments. Its user friendly hand-held design makes it the easiest to transport to, and deploy within more challenging environmental settings, providing researchers with a robust, inexpensive means of in-field hyperspectral data collection. Finally, the Low-Cost High-Resolution instrument from Chapter 5 represents the most accurate of the instrumentation discussed within this thesis. With a demonstrated spectral resolution of 0.29 nm, this instrument compares favourably with a broad range of commercial instrumentation, without incurring the associated costs. Whilst this instrument is the most expensive of the devices discussed within this thesis, it remains significantly cheaper than typical instruments available within commercial markets.

Table 7.1. Direct comparison between the three instruments discussed within this thesis.

	Laboratory-Based Instrument	**Hyperspectral Smartphone**	**Low-Cost High Resolution Instrument**
Cost	£5,980	£95.94	£11,039.60
Approximate Weight (g)	100	210*[1]	3,000
Weight Inc. Optical Breadboard (g)	3,100		9,000
Dimensions (L x W x H) (cm)	35 x 20 x 13	16 x 10 x 12	60 x 30 x 18
Portability	Semi-Portable	Portable	Semi-Portable
Imaging Mode	Whiskbroom (static*[2])	Push Broom	Push Broom (static*[2])
Spectral Range (nm)	340 – 850	400 – 700	400 – 1000
Spectral Resolution (nm)	12	14	0.29
*[1]Weight and dimensions include incorporated smartphone (Samsung Galaxy A12) and, therefore, are subject to minor variations depending on the particular smartphone used.			
*[2]Static refers to the use of components such as mirrors or translation stages to provide the spatial data capture. These instruments can, therefore, produce the spatial dataset without the operator having to physically move or translate the instrument.			

The low-cost nature of these instruments helps to promote the continued democratisation of hyperspectral imaging measurement modalities and could promote the widespread proliferation of low-cost, accessible measurement and monitoring instrumentation across the globe. This is particularly pertinent within environmental monitoring applications since the current lack of low-cost, portable hyperspectral instrumentation is resulting in significant limitations to the datasets that can be captured, resulting in much of our knowledge of a broad range of application areas being limited to a few more easily accessible locations that have been measured by a comparatively small number of better resourced research teams and organisations. In general, these more easily accessed sites are not representative of the, much larger, whole, resulting in substantial limitations to our knowledge, and therefore understanding of a broad range of important environmental settings. From glaciers and volcanos in Iceland, to blanket bogs within the Peak District of the UK, increasing the availability and accessibility of measurement and monitoring instrumentation for these locations is of paramount importance, enabling a significant increase in the availability of datasets for these regions and, subsequently increasing our understanding of how these environments will be affected by the impacts of climate change.

7.2. Future Work

Whilst the instruments developed and discussed within this thesis have been shown to perform well within a range of environmental applications, as with any emerging technology, there is still room for further improvements within these designs. The following sections, therefore, discuss possible next steps for these instruments, in an attempt to identify where future work could be focused.

7.2.1. Laboratory-Based Hyperspectral Imager

To reduce aberrations present within the datasets produced by the laboratory-based hyperspectral imager, the optical system may be improved. This was briefly discussed within Chapter 3 which

highlighted the additional costs associated with these improvements. Given the intention to maintain the low-cost aspect of this instrumentation the benefits of these improvements need to be contrasted with the expected increase in costs (within the region of a few hundred pounds), to determine their overall feasibility and benefit. If implemented, these improvements would likely involve the inclusion or development of a multiple lens system specifically designed to reduce the presence of spherical aberrations within more simple optics. This system would use a combination of concave and convex lenses to effectively cancel the aberrations resulting from each component. These alterations would provide significant improvements to the data quality capture abilities of this instrumentation, however, with the primary advantage of the laboratory-based hyperspectral imager being its low price point whether the expected increase in performance outweighed the additional costs would need to be carefully considered.

7.2.2. Hyperspectral Smartphone

Chapter 4 demonstrated the unique abilities of the Hyperspectral Smartphone, providing an ultra-low-cost means of rapid and accurate hyperspectral data capture. It is, therefore, an instrument with significant potential for further application across the environmental sciences and beyond. However, there remain areas where improvements to the hyperspectral datasets could be made. The current image capture method is a push broom design requiring the operator to translate the instrument across a target scene. Whilst this approach is sufficient, as has been demonstrated within this body of work, there is significant potential for the development of a snapshot style Hyperspectral Smartphone.

Snapshot hyperspectral imaging enables the collection of a complete hyperspectral dataset within a single exposure. Currently available commercial set-ups present a prohibitive cost for many would-be users, therefore, a low-cost smartphone-based alterative provides significant potential for substantial democratisation within this area. To develop the current Hyperspectral Smartphone design into a snapshot hyperspectral imager would be a considerable, but highly beneficial undertaking. It would enable the collection of a complete hyperspectral dataset within a single photograph, instead of extracting the data from a series of video frames. This, in turn, would provide the operator with increased flexibility within the image capture parameters because, typically, smartphone camera settings offer more adjustability within single image capture applications over video applications.

Initial steps in this process would focus on the instrumental hardware, converting the current single slit design into a multi-slit system. This approach to snapshot hyperspectral imaging has been used extensively in the past with the implementation of pinhole arrays to distribute the spectral response of each pixel [1], [2]. In this system the spatial resolution of the instrument would be directly proportional to the number of slits and, therefore, in initial iterations would likely be considerably reduced. However, the intention is that each of these slits would provide the spectral data for a single pixel within a scene, allowing the full extent of the smartphone sensor to be used, rather than limiting it as is the case with the current system. This avenue of research requires significant investigation to determine the true feasibility of the idea and, if feasible, the optimised configuration of the required hardware. Software developments would also be required to convert the new data format into the hyperspectral data cube. Although these initial ideas are limited, they highlight a tangible route to the realisation of smartphone-based snapshot hyperspectral imaging.

7.2.3. Low-Cost High-Resolution Instrument

A significant limitation of the low-cost high-resolution hyperspectral instrument is its limited portability. Whilst in its current format it is capable of deployment within a range of different locations, it is not, as yet, ready for full field deployment. This limits the instruments current applicability,

however, further developments to enable field-based data capture with this high-resolution instrument would provide significant benefits to a number of applications, including the peatland health monitoring application discussed within Chapter 6. To complete these improvements, the instrumentation would need to be housed within a robust, weatherproof casing capable of maintaining the precise optical configurations required. Care would need to be taken to appropriately incorporate the translation stage within this set-up. An initial portable set-up could, therefore, be completed relatively simply with the inclusion of a robust casing and the conversion of electronic components to battery power. This would enable high-resolution hyperspectral datasets to be acquired with this instrument across an array of field locations. Whilst it would remain bulky by comparison to the Hyperspectral Smartphone, it represents a different style of data capture, for example, the Hyperspectral Smartphone is designed for rapid, accurate hyperspectral data collection enabling a wide area to be imaged with relative ease, the high-resolution instrument, however, provides much more detailed analysis and, therefore, is best deployed only within areas where initial data collection suggests more detailed analysis is required. By further developing this system to enable field-based data collection it will provide substantial benefits to a number of environmental monitoring applications, providing a low-cost means of capturing intricate hyperspectral datasets without disrupting the subject environment.

7.3. Extended Applications

The instruments developed and presented in this thesis have the potential for numerous applications additional to the ones discussed in previous chapters. Here, a few such examples are briefly presented.

7.3.1. In-situ Imaging of Speleothems with The Hyperspectral Smartphone

Speleothems are a key feature in palaeoclimatic reconstructions, providing valuable proxy records and environmental archives in their growth rate, internal structure and chemical composition [3], [4], providing a precise and reliable record of environmental change. The seasonal resolution afforded by this technique allows for the production of records spanning hundreds of years [4], [5]. Speleothem formation is led by water transport through a cave system, either through the influx of flood waters, or drip action through the cave canopy, resulting in mineral deposition [6]. Variations in environmental conditions during their formation can affect their mineral composition, producing concentric layers and banding which, in turn, can be used to inform palaeoclimatic studies [7]. Traditionally, these features have been analysed optically using visual observations obtained by flatbed scanners or standard RGB cameras [3]. Whilst these methods provide valuable datasets highlighting visual changes in speleothem composition, they lack the spectral resolution to resolve a complete spectral dataset, resulting in the potential loss of important spectral features, that are not visible to the naked eye, within the data. Furthermore, due to the typical restrictions experienced in these environments, regarding accessibility and illumination [8], many of these optical sensing methods require the destructive collection of samples for detailed, laboratory-based analyses.

Hyperspectral imaging has seen a considerable uptake in field deployable applications across a wide range of environmental settings, providing new avenues for more detailed data collection and analysis. Furthermore, the introduction of miniaturised, low-cost components has enabled the collection of hyperspectral datasets in a variety of less accessible locations, where hyperspectral data collection with existing commercial set-ups remains infeasible due to physical limitations such as the weight and size of the instrumentation. This is a factor that has had a particular impact on cave surveys and analyses as the complexity of these environments limits the use of a wide range of instruments [8]. Indeed, the complex spatial patterns present in cave environments have influenced numerous

analytical applications [7]–[9]. Hyperspectral imaging analysis utilising these innovative miniaturised instruments, therefore, represents a viable, non-destructive alternative to traditional analysis approaches in these restrictive and more extreme environmental settings. To date, whilst hyperspectral imaging techniques have been used in speleothem analysis in previous studies, e.g. [3], [7], they have often required the collection of samples, resulting in the destruction of these cave features which can cause significant alterations to the structural environment.

The Hyperspectral Smartphone, therefore, provides a promising, low-cost non-invasive means of data collection within these more challenging environments. The implementation of this ultra-low-cost alternative will allow for the collection of in-situ speleothem datasets within the confines of more difficult to access cave locations. This information can then be used as a means of mapping cave features without requiring the collection of samples and/or as a method of pinpointing locations for further, more detailed investigation. The Hyperspectral Smartphone has already been demonstrated as a proficient field instrument. To test its capabilities within this new environmental setting, it will be deployed within a cave system within the Peak District, UK. In this environment the Hyperspectral Smartphone will be used to capture datasets of a number of speleothem structures using a range of illumination techniques. The resulting datasets will be analysed and compared to the existing literature to determine the abilities of the Hyperspectral Smartphone under these circumstances and to analyse the best method of illumination for future measurements.

After these initial investigations, if successful, the Hyperspectral Smartphone will then be redeployed within more difficult to access systems within the Peak District to provide new datasets for these more challenging locations. The user friendly nature of the Hyperspectral Smartphone provides key benefits to this application, allowing datasets to be obtained by individuals without the need for extensive training or knowledge of hyperspectral imaging techniques. This enables the collection of datasets with the Hyperspectral Smartphone to be undertaken by experienced cavers, reducing the training requirements for any proposed research. By demonstrating this instrument within these more extreme settings it provides a unique opportunity for the collection of datasets under environmental conditions that were infeasible hitherto. This, in turn, enables the development of new knowledge across these locations, providing significant benefits to the research field.

7.3.2. Monitoring Vegetation Stress Response

Chapter 6 demonstrated the successful application of the Hyperspectral Smartphone and the high-resolution hyperspectral imager to the monitoring of Sphagnum spectral response as a proxy to help determine below ground conditions. The field of vegetation health monitoring, therefore, provides a significant range of application opportunities, with the implementation of these low-cost instruments providing significant potential benefits. The monitoring of vegetation health with hyperspectral imaging techniques provides beneficial early warning of the onset of unfavourable conditions such as, water stress and disease development. The effects of these conditions can be devastating within both natural and agricultural settings, therefore, there is significant need to provide low-cost hyperspectral monitoring approaches within these settings.

The low-cost instrumentation presented within this thesis could easily be applied to a greater range of vegetation monitoring scenarios providing a rapid and reliable means of hyperspectral data collection. For example, monitoring water stress within rice crops, or identifying disease spots on tomato vines. Each of these crops is of significant importance within agriculture and food production and, therefore, benefit from hyperspectral imaging applications that can monitor conditions to help maximise yield and product quality. The low-cost instrumentation developed within this thesis could provide a rapid

means of in-situ monitoring without the need for the collection of samples. To implement these technologies within these applications initial measurements would be completed within controlled environment facilities before transitioning to the measurement of in-situ plants. By determining a robust and accurate spectral library, documenting indications of varying stress responses within the spectral response of these vegetation types, it would enable rapid measurement and monitoring approaches and, in turn, help to prevent significant losses due to disease or drought in key vegetation species.

7.3.3. Differentiation of Supraglacial Debris Types using a Low-Cost Field Deployable Hyperspectral Imager

The monitoring of melt-inducing impurities present across glacial and ice sheet locations is of paramount importance to ongoing efforts to minimise the effects of climate change in these areas. Whilst the impact of debris layers on ice melt rates are already well documented, it remains important to be able to differentiate between the types of impurities present. Impurities that affect these regions typically fit within three distinct groups: mineral dust, black carbon, and algal blooms. The accurate differentiation of these impurities is important, particularly because quantities of black carbon are predominantly driven by anthropogenic activities. Quantifying their presence, therefore, provides valuable information for pollution and emissions research.

Previous research has identified that these impurities can be accurately differentiated by their spectral responses, however, this remains difficult with currently available technologies within these applications, which are typically limited to multispectral and/or satellite-based instrumentation [10]–[12]. These limitations have a significant effect of the data quality currently available for these applications, limiting the spectral and spatial information of the output datasets [13], [14]. The introduction of lightweight, low-cost hyperspectral instruments to these environments would, therefore, be of significant benefit.

To introduce the low-cost instrumentation presented in this thesis to this field, initial measurements of known impurities would be conducted within a laboratory setting. This will enable the development of a robust spectral library for each impurity type, providing an accurate means of identification for field derived datasets. In-situ monitoring would then be implemented within a glacial setting, such as the Greenland Ice Sheet. The Russell and Leverett glaciers situated near Kangerlussuaq, Greenland provide an ideal location for testing in-situ measurements. Significant deposits of a range of ice impurities are present within this area, enabling widespread instrument testing. Furthermore, this location is an ice marginal site and, therefore, allows for easy site access without the need for the significant support of more central studies. If successful, these instruments will enable rapid in-situ ice impurity identification and analysis using low-cost, accessible hardware, significantly progressing data collection techniques within this field.

7.4. Concluding Remarks

This thesis has presented the development of a variety of low-cost hyperspectral imaging instruments and their application to a broad range of environmental monitoring scenarios. These instruments have been demonstrated to be valuable additions to the field of low-cost hyperspectral imaging, and have significant potential beyond the applications highlighted within this thesis. Specifically, this thesis has outlined the design and testing of: a laboratory-based hyperspectral imager, capable of low-cost hyperspectral data capture within a laboratory setting; the Hyperspectral Smartphone, an ultra-low-cost fully portable smartphone-based hyperspectral imager; and a low-cost, high-resolution hyperspectral imager, capable of capturing mm-scale spatial targets within hyperspectral datasets.

Each of these instruments is designed to fit a different style of monitoring application, enabling the collection of accurate and robust hyperspectral datasets within a broad range of environmental settings and applications.

Each instrument has been shown to perform well within a range of measurement applications, providing results that are comparable with the existing literature despite, in some cases being over an order of magnitude cheaper than currently available commercial systems. Additionally, in the case of the Hyperspectral Smartphone and the high-resolution hyperspectral imager, their application within a real-world systematic study has further highlighted the considerable potential for new knowledge and greater understanding with their continued application to key environmental monitoring studies. For each of these designs future work on both hardware and software could improve the instruments and their utility to researchers across a range of fields. However, at present these instruments have proven utility across the field of environmental monitoring, and provide a key step towards the continued democratisation of hyperspectral imaging measurement modalities.

7.5. References

[1] C. Kern *et al.*, "Mobile snapshot hyperspectral imaging device for skin evaluation using diffractive optical elements," *Ski. Res. Technol.*, vol. 27, no. 4, pp. 589–598, 2021.

[2] A. Bodkin, A. Sheinis, A. Norton, J. Daly, S. Beaven, and J. Weinheimer, "Snapshot hyperspectral imaging: the hyperpixel array camera," *Algorithms Technol. Multispectral, Hyperspectral, Ultraspectral Imag. XV*, vol. 7334, no. April 2009, p. 73340H, 2009.

[3] C. Jex, E. Claridge, A. Baker, and C. Smith, "Hyperspectral imaging of speleothems," *Quat. Int.*, vol. 187, no. 1, pp. 5–14, 2008.

[4] A. R. Pearson, A. Hartland, S. Frisia, and B. R. S. Fox, "Formation of calcite in the presence of dissolved organic matter: Partitioning, fabrics and fluorescence," *Chem. Geol.*, vol. 539, no. October 2019, 2020.

[5] A. Borsato, S. Frisia, I. J. Fairchild, A. Somogyi, and J. Susini, "Trace element distribution in annual stalagmite laminae mapped by micrometer-resolution X-ray fluorescence: Implications for incorporation of environmentally significant species," *Geochim. Cosmochim. Acta*, vol. 71, no. 6, pp. 1494–1512, 2007.

[6] N. Fukuyo, H. Oda, Y. Yokoyama, G. Clark, and Y. Yamamoto, "High spatial resolution magnetic mapping using ultra-high sensitivity scanning SQUID microscopy on a speleothem from the Kingdom of Tonga, southern Pacific," *Earth, Planets Sp.*, vol. 73, no. 1, 2021.

[7] E. Garcia-Anton *et al.*, "Mineral-variations study of Canelobre cave phosphate stalactites by Raman and luminescence methods," *Spectrosc. Lett.*, vol. 44, no. 7–8, pp. 539–542, 2011.

[8] D. Giordan, D. Godone, M. Baldo, M. Piras, N. Grasso, and R. Zerbetto, "Survey solutions for 3d acquisition and representation of artificial and natural caves," *Appl. Sci.*, vol. 11, no. 14, 2021.

[9] V. Bayarri, E. Castillo, S. Ripoll, and M. Sebastian, "Improved application of hyperspectral analysis to rock Art," *Appl. Sci.*, 2021.

[10] A. Dal Farra, S. Kaspari, J. Beach, T. D. Bucheli, M. Schaepman, and M. Schwikowski, "Spectral signatures of submicron scale light-absorbing impurities in snow and ice using hyperspectral microscopy," *J. Glaciol.*, vol. 64, no. 245, pp. 377–386, 2018.

[11] R. Garzonio *et al.*, "A novel hyperspectral system for high resolution imaging of ice cores: Application to light-absorbing impurities and ice structure," *Cold Reg. Sci. Technol.*, vol. 155, no. June, pp. 47–57, 2018.

[12] B. Di Mauro *et al.*, "Impact of impurities and cryoconite on the optical properties of the Morteratsch Glacier (Swiss Alps)," *Cryosphere*, vol. 11, no. 6, pp. 2393–2409, 2017.

[13] J. M. Cook *et al.*, "Quantifying bioalbedo: A new physically-based model and critique of empirical methods for characterizing biological influence on ice and snow albedo," *Cryosph. Discuss.*, no. 1875, pp. 1–29, 2017.

[14] C. J. Williamson, K. A. Cameron, J. M. Cook, J. D. Zarsky, M. Stibal, and A. Edwards, "Glacier algae: A dark past and a darker future," *Front. Microbiol.*, vol. 10, no. APR, 2019.

Appendices

The following pages contain further information and code relevant to the instrumentation discussed within this thesis.

8.1. Ray trace model developed for the laboratory-based hyperspectral imager

Below are the simulation results for the ray trace modelling of the laboratory-based hyperspectral imager. The model assumes a focal length of 60 mm for the singlet lens, a working distance of 500 mm, and a detector size of 0.5 mm x 0.05 mm. Rays are traced from spectrometer entrance pupil to target object (left to right in image).

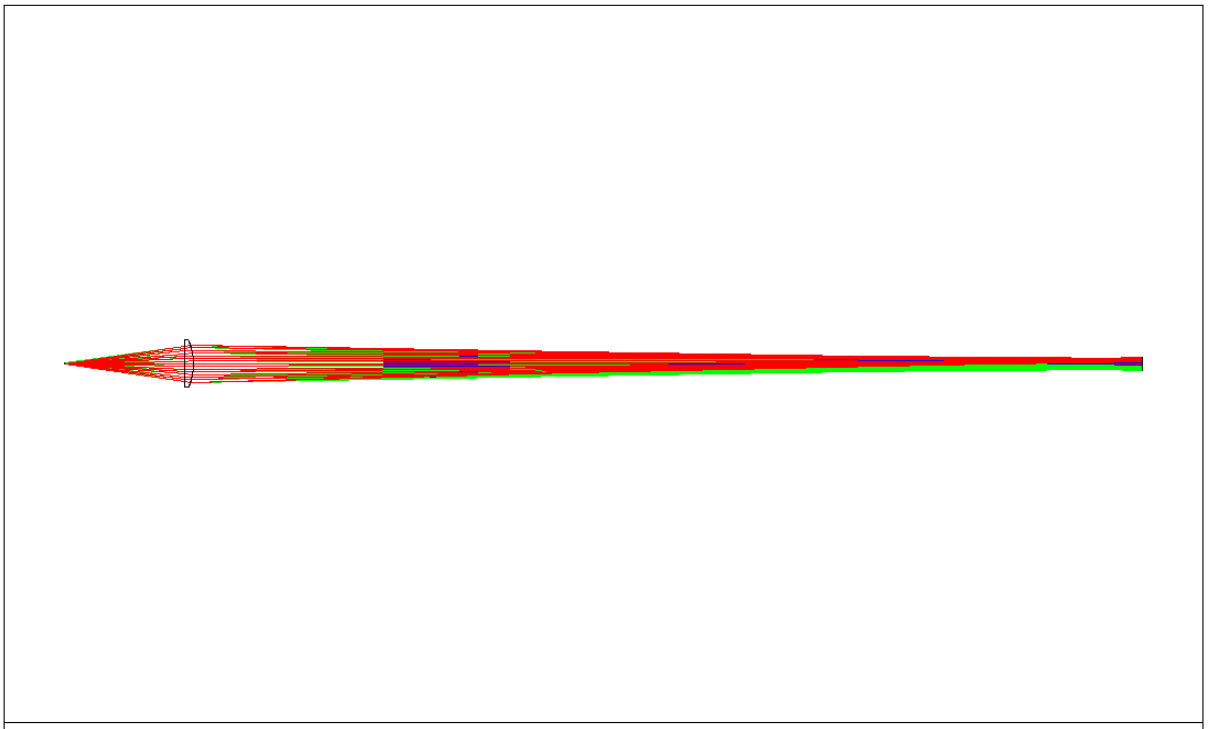

Layout	
26/05/2020 Total Axial Length: 567.87414 mm	Mary-spectrometer-V1.0.zmx Configuration 1 of 1

0.5 mm Detector

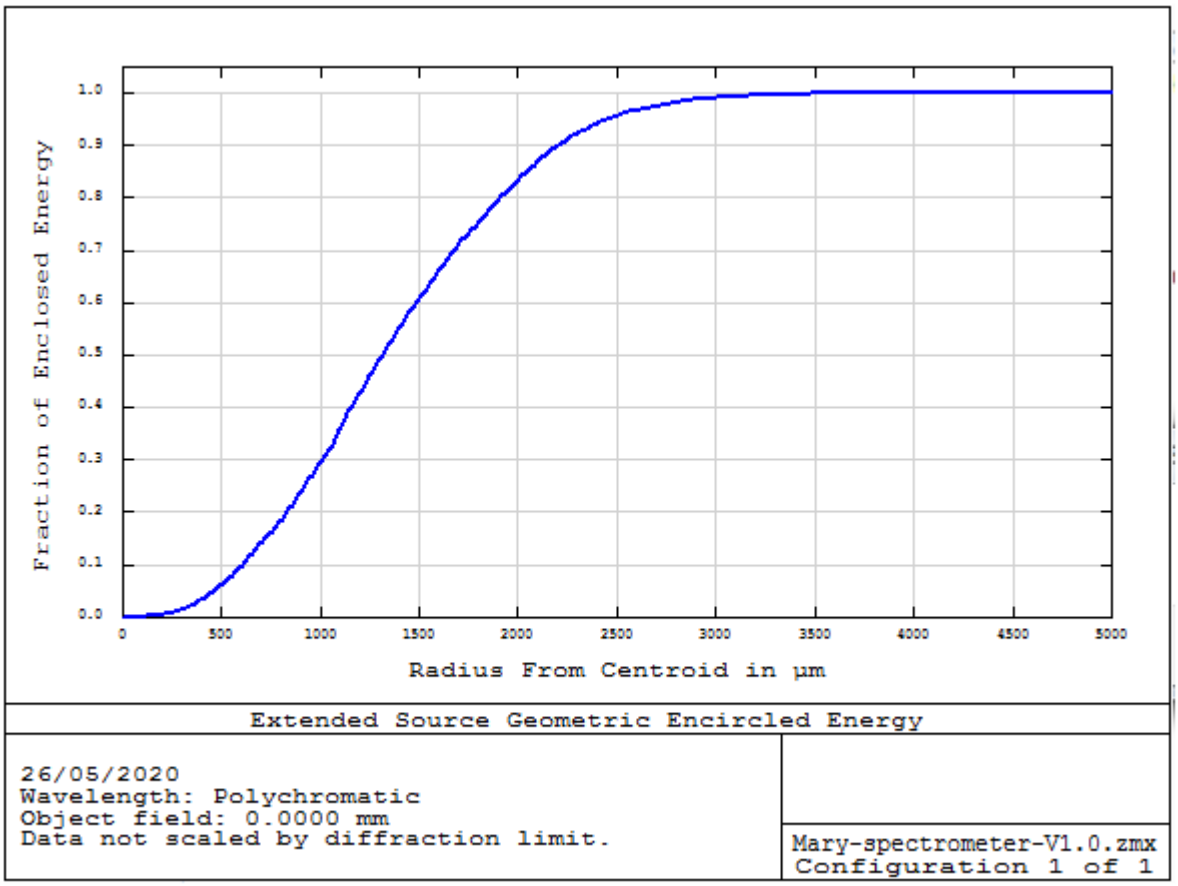

Extended Source Geometric Encircled Energy

Surface: Image

Wavelength: Polychromatic

Object field: 0.0000 mm

Reference: Centroid

Reference coordinate units are Millimetres

Distance units are µm.

Field: 0.0000 mm
Reference Coordinates: 4.662E-001 -4.463E-001

Radial distance	Fraction
0.000	0.000000
100.000	0.000567
200.000	0.004474
300.000	0.013957
400.000	0.033419
500.000	0.063269
600.000	0.096572

700.000	0.142417
800.000	0.183882
900.000	0.238602
1000.000	0.294350
1100.000	0.359860
1200.000	0.426106
1300.000	0.490647
1400.000	0.553561
1500.000	0.606766
1600.000	0.660456
1700.000	0.711682
1800.000	0.752034
1900.000	0.796411
2000.000	0.834510
2100.000	0.870957
2200.000	0.900394
2300.000	0.924049
2400.000	0.943709
2500.000	0.957751
2600.000	0.967807
2700.000	0.974890
2800.000	0.982647
2900.000	0.988093
3000.000	0.991107
3100.000	0.993984
3200.000	0.995461
3300.000	0.997338
3400.000	0.998104
3500.000	0.998687
3600.000	0.999057
3700.000	0.999417
3800.000	0.999417
3900.000	0.999656
4000.000	0.999796
4100.000	0.999796
4200.000	1.000000
4300.000	1.000000
4400.000	1.000000
4500.000	1.000000
4600.000	1.000000
4700.000	1.000000
4800.000	1.000000
4900.000	1.000000
5000.000	1.000000

0.05 mm Detector

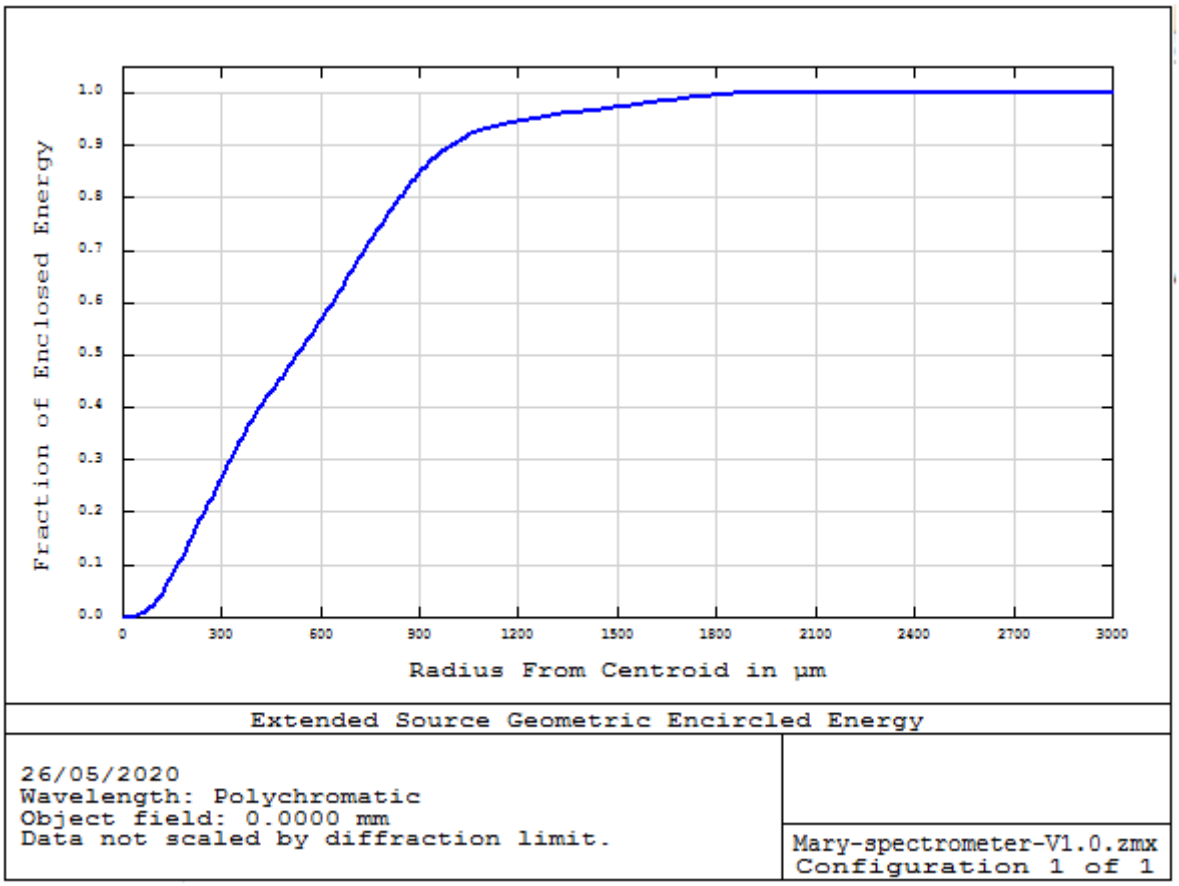

Extended Source Geometric Encircled Energy

Surface: Image

Wavelength: Polychromatic

Object field: 0.0000 mm

Reference: Centroid

Reference coordinate units are Millimetres

Distance units are µm.

Field: 0.0000 mm
Reference Coordinates: 4.651E-002 -2.701E-002

Radial distance	Fraction
0.000	0.000000
50.000	0.003912
100.000	0.026795
150.000	0.079941
200.000	0.138224
250.000	0.202532
300.000	0.264934
350.000	0.326727

400.000	0.385077
450.000	0.430576
500.000	0.472236
550.000	0.519789
600.000	0.565360
650.000	0.613543
700.000	0.668837
750.000	0.717094
800.000	0.765305
850.000	0.808478
900.000	0.847124
950.000	0.879873
1000.000	0.901038
1050.000	0.921253
1100.000	0.932263
1150.000	0.940332
1200.000	0.946215
1250.000	0.951029
1300.000	0.957279
1350.000	0.961942
1400.000	0.964923
1450.000	0.968835
1500.000	0.972193
1550.000	0.977543
1600.000	0.982147
1650.000	0.985794
1700.000	0.989937
1750.000	0.992696
1800.000	0.996232
1850.000	0.998652
1900.000	0.999498
1950.000	0.999878
2000.000	1.000000
2050.000	1.000000
2100.000	1.000000
2150.000	1.000000
2200.000	1.000000
2250.000	1.000000
2300.000	1.000000
2350.000	1.000000
2400.000	1.000000
2450.000	1.000000
2500.000	1.000000
2550.000	1.000000
2600.000	1.000000
2650.000	1.000000
2700.000	1.000000

2750.000	1.000000
2800.000	1.000000
2850.000	1.000000
2900.000	1.000000
2950.000	1.000000
3000.000	1.000000

8.2. Laboratory-based hyperspectral imager instrument control and data cube construction LabVIEW code

The following sections provide the LabVIEW front panel and block diagram layouts used to control the laboratory-based hyperspectral imager and to construct the resulting data cubes.

Front Panel Tab One

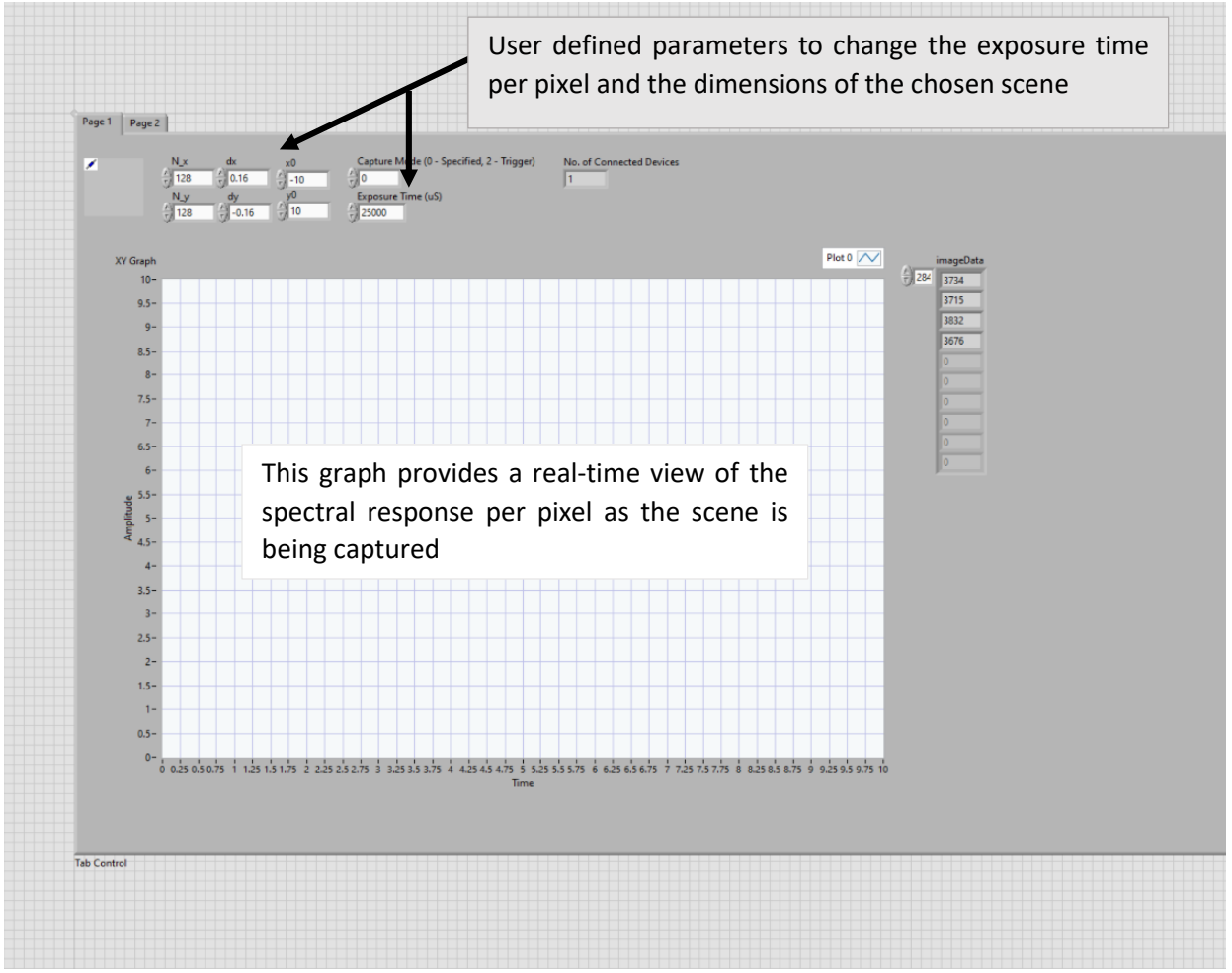

Front Panel Tab Two

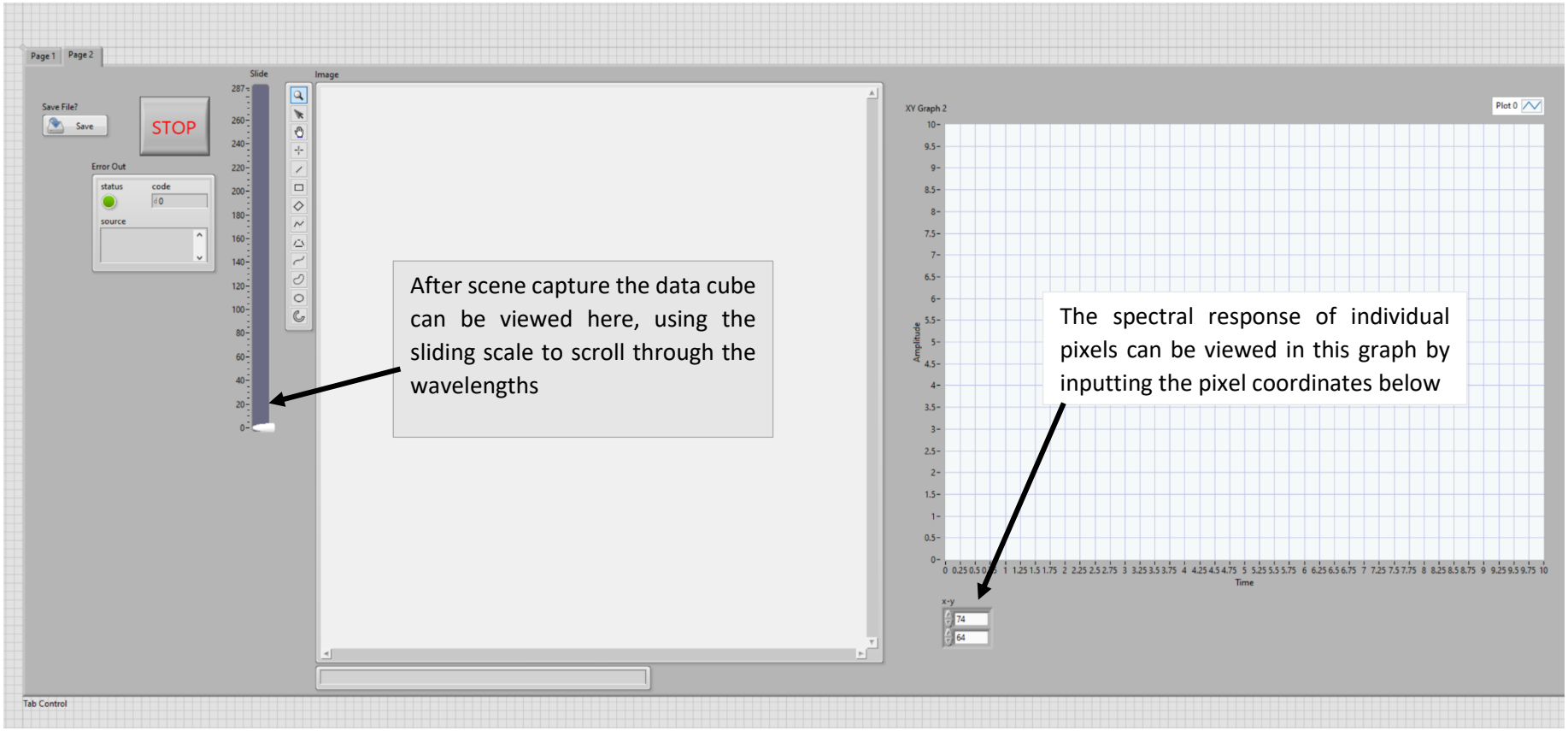

Block Diagram Part One

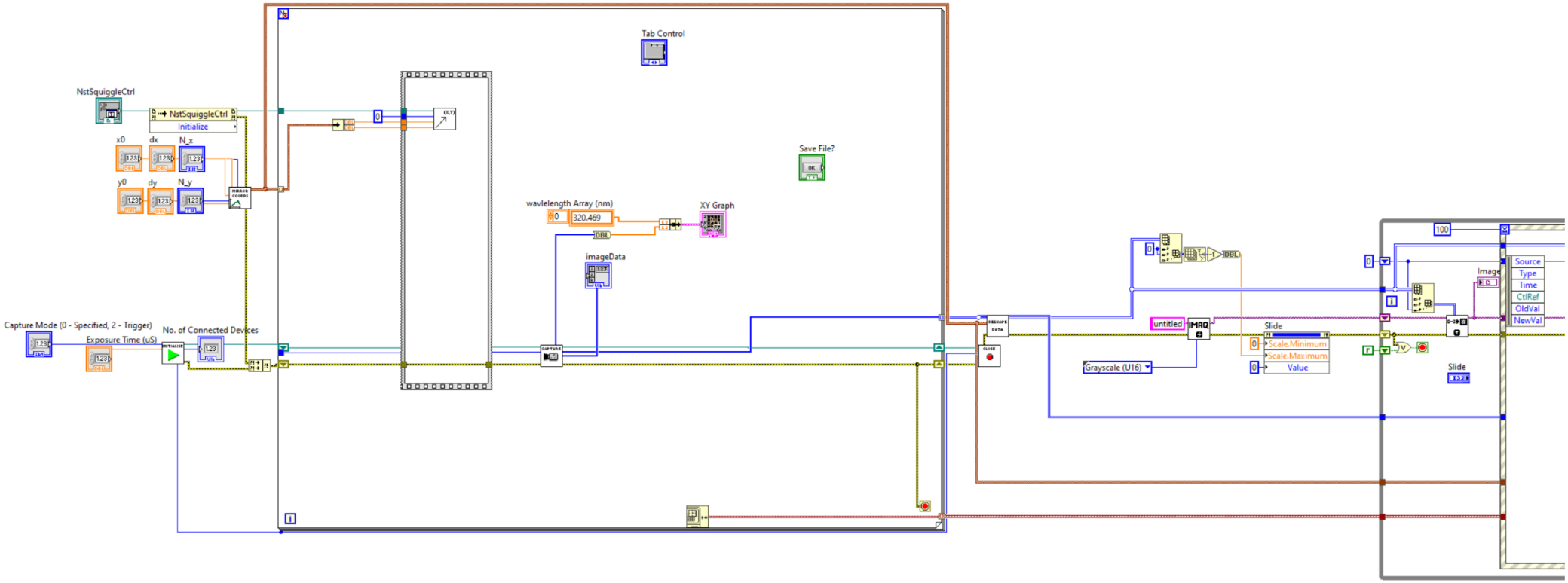

Block Diagram Part Two

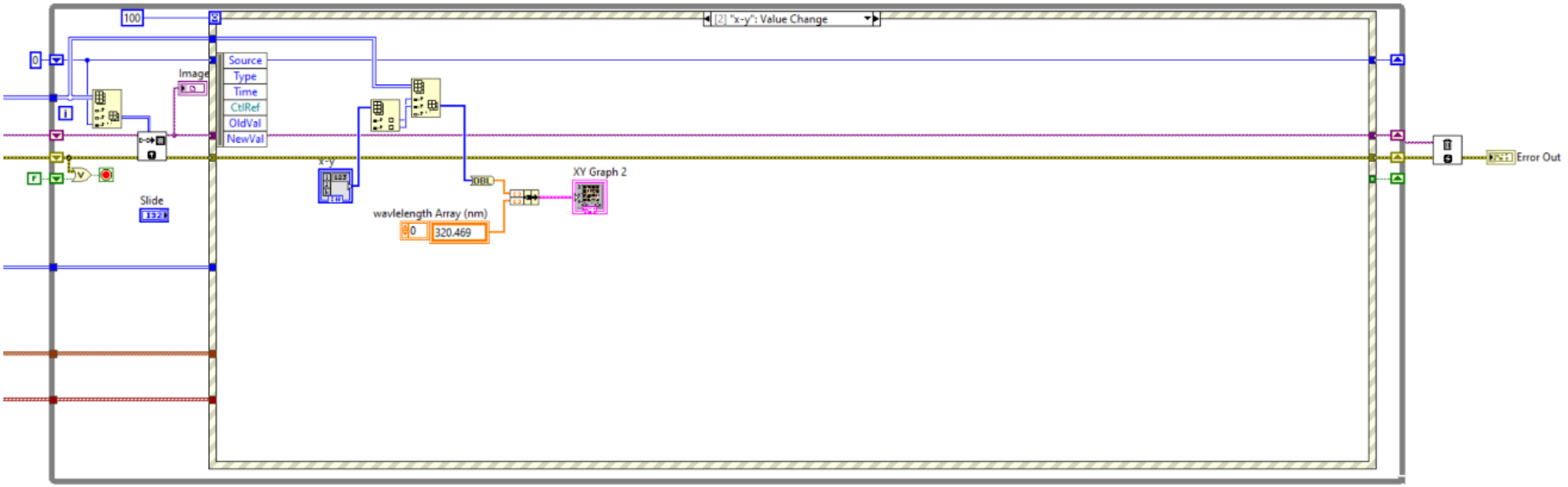

8.3. Laboratory-Based Hyperspectral Imager Dataset Bias Correction Code

The following sections provide the LabVIEW front panel and block diagram layouts used to bias correct the datasets obtained using the laboratory-based hyperspectral imager.

Front Panel Tab One

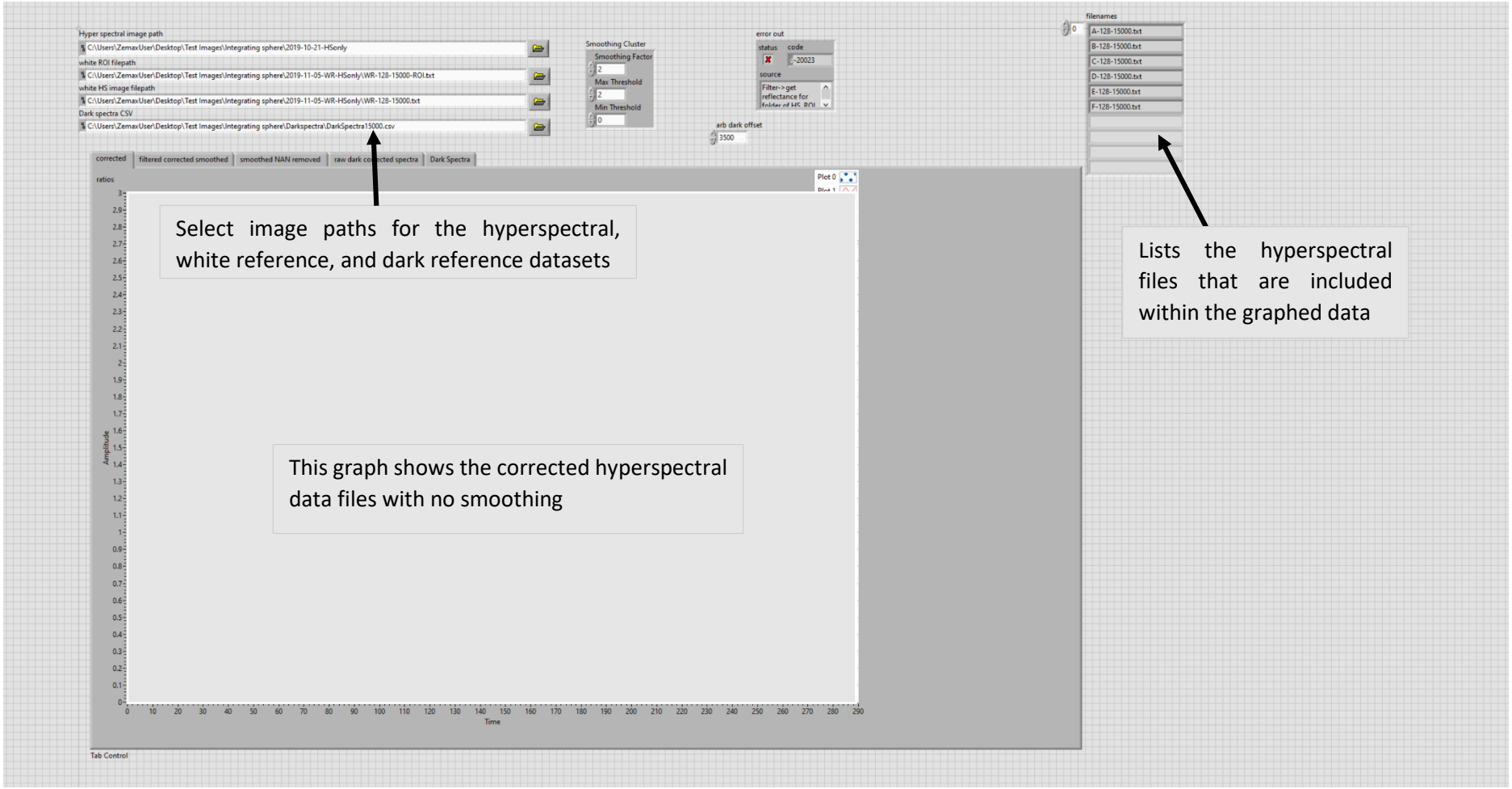

Front Panel Tab Two

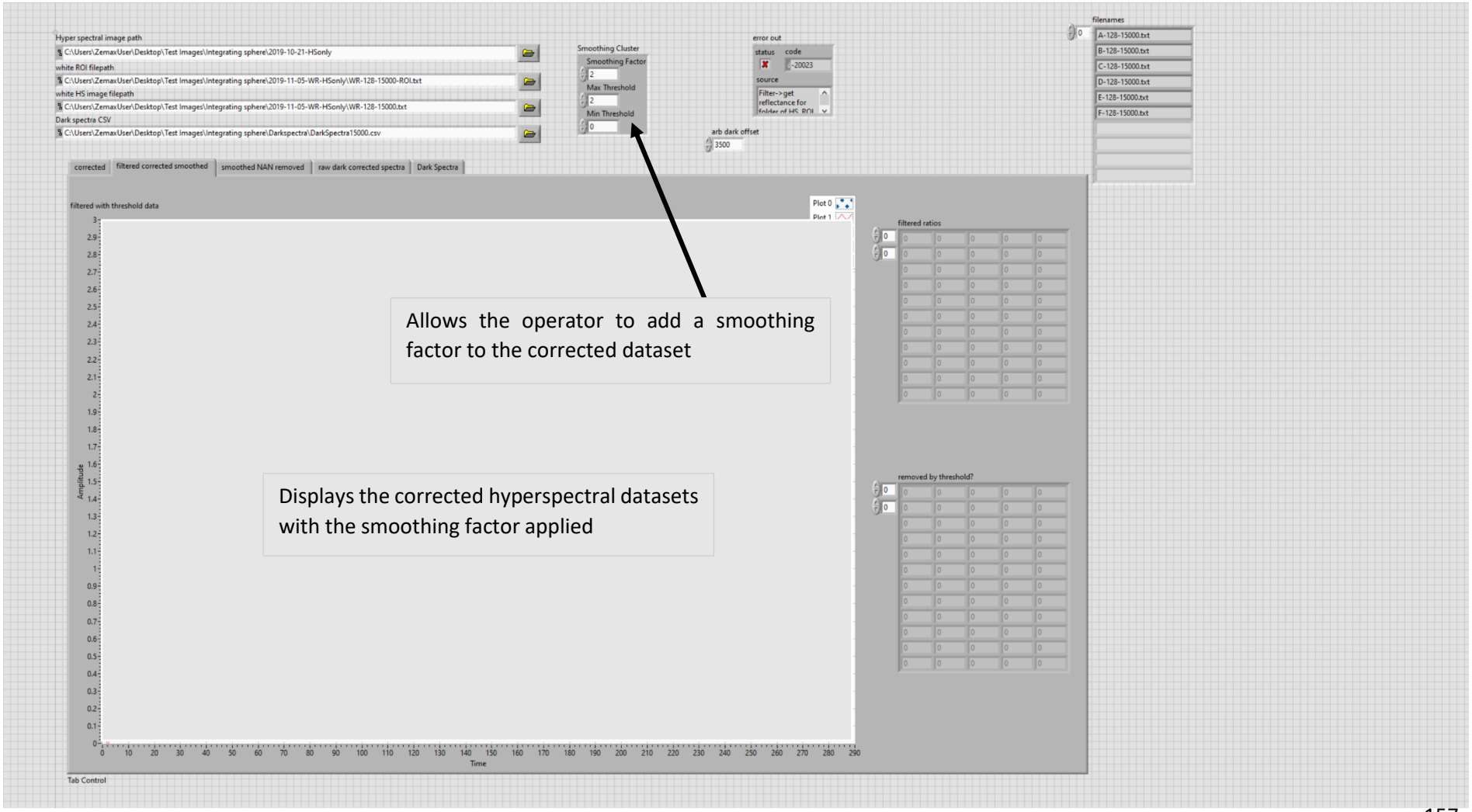

Front Panel Tab Three

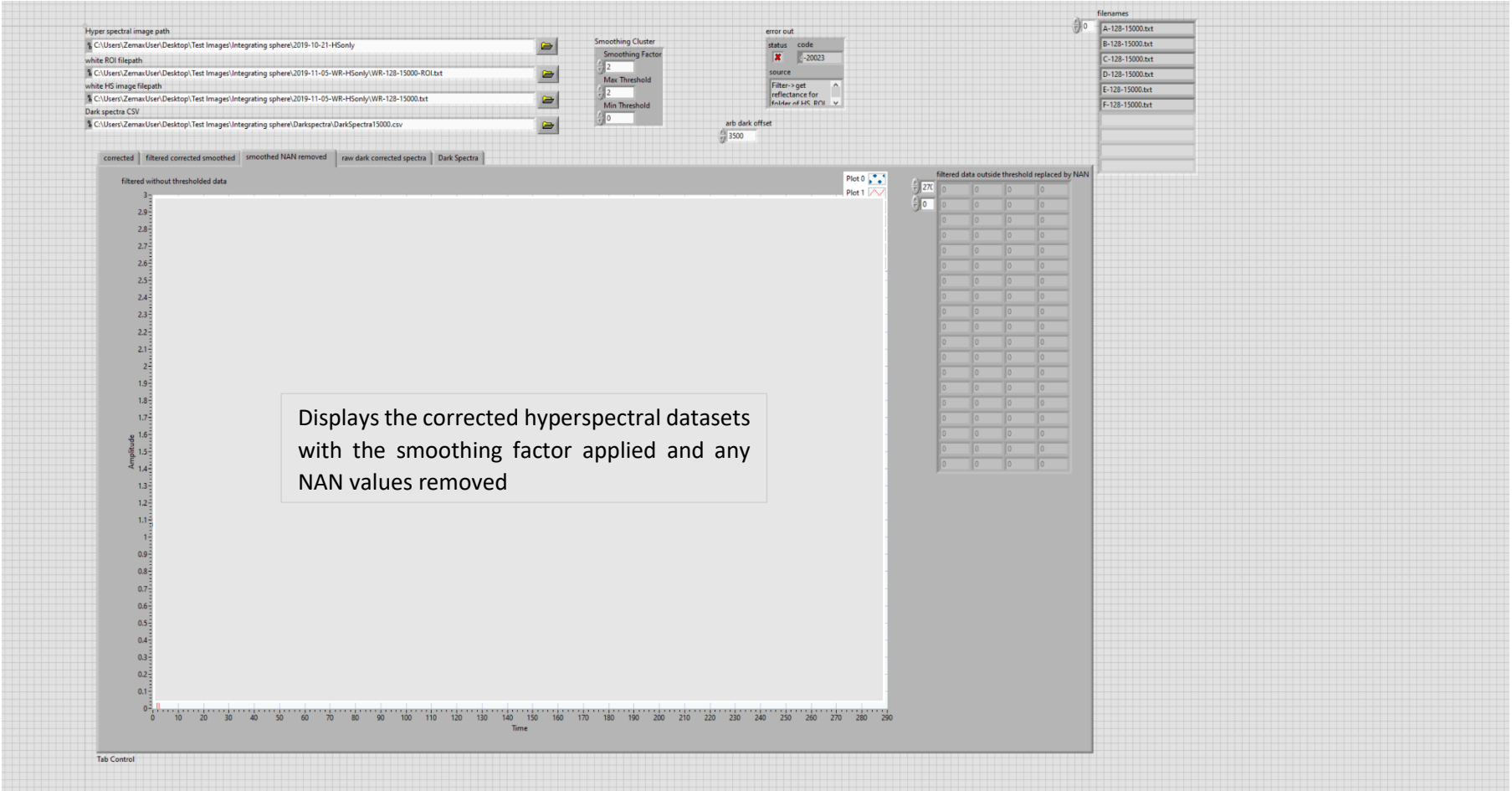

Front Panel Tab Four

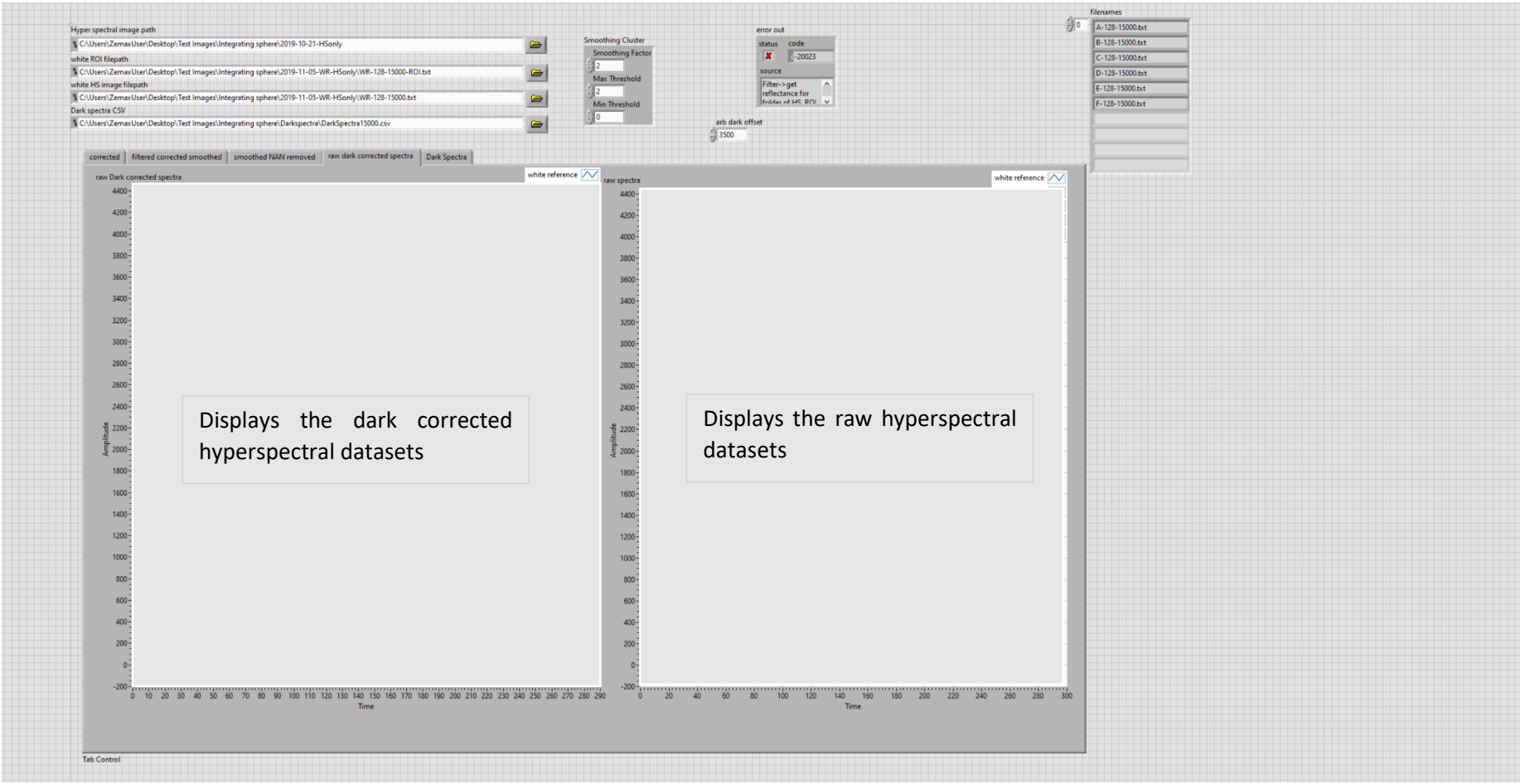

Front Panel Tab Five

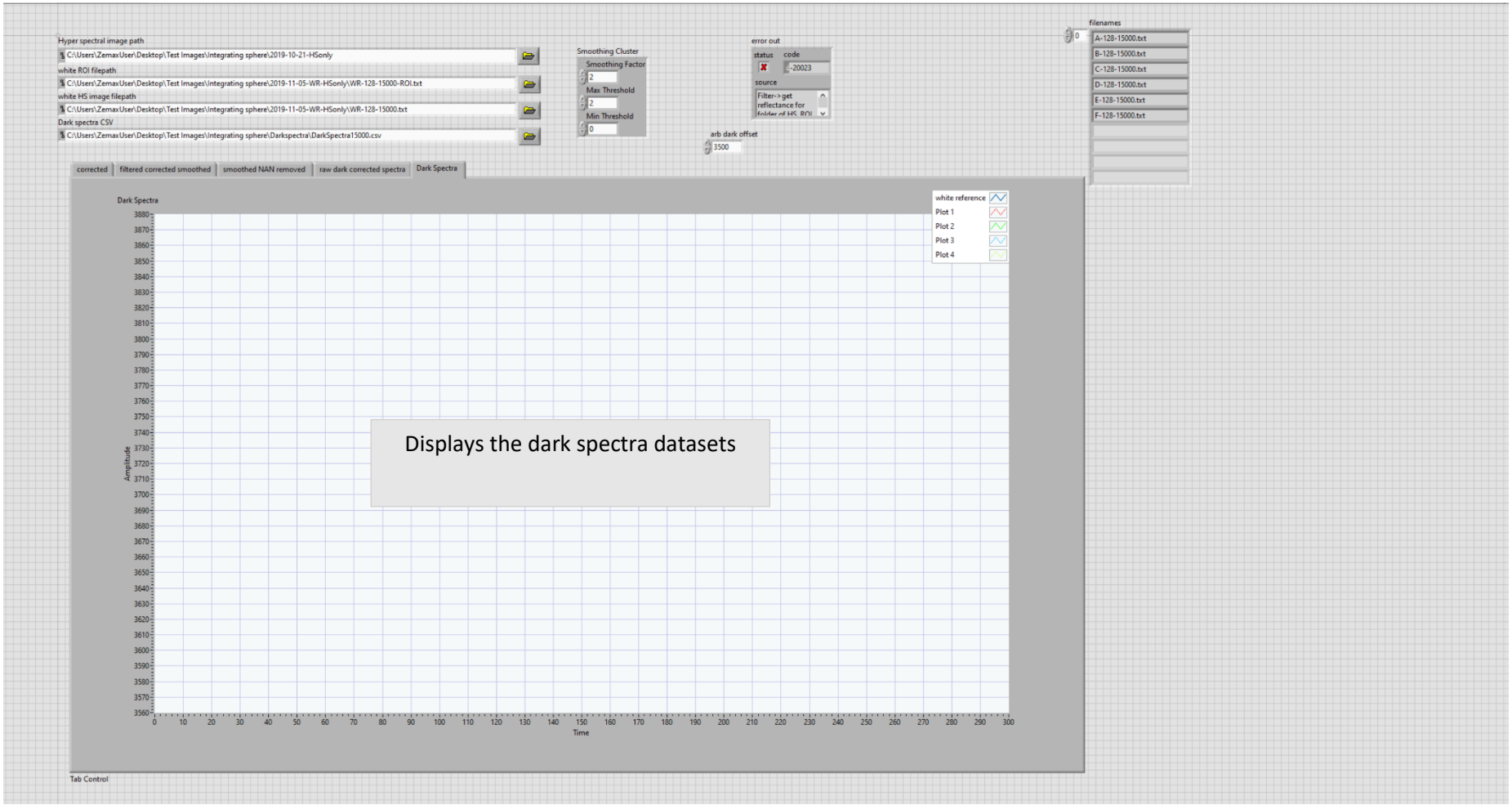

Block Diagram Part One

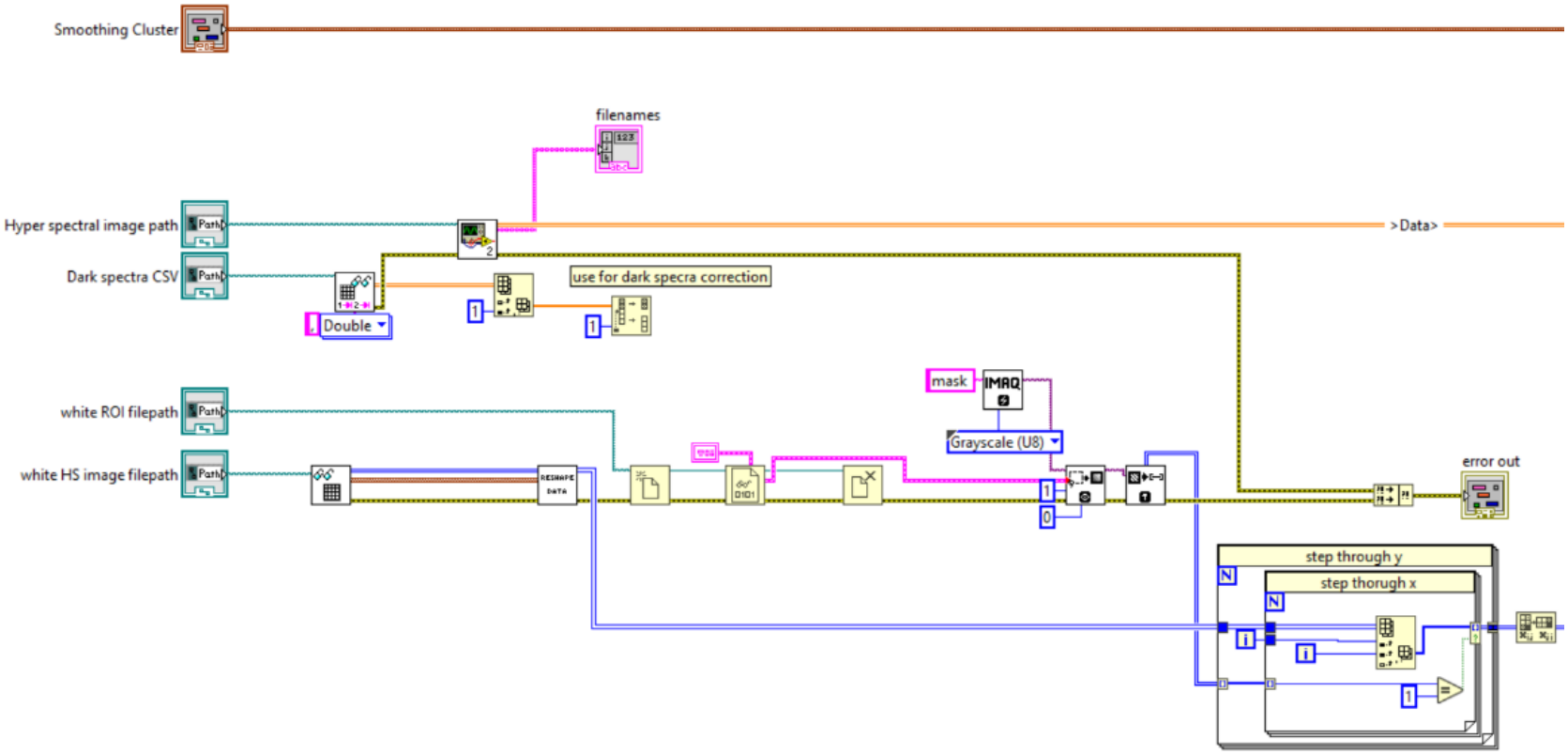

Block Diagram Part Two

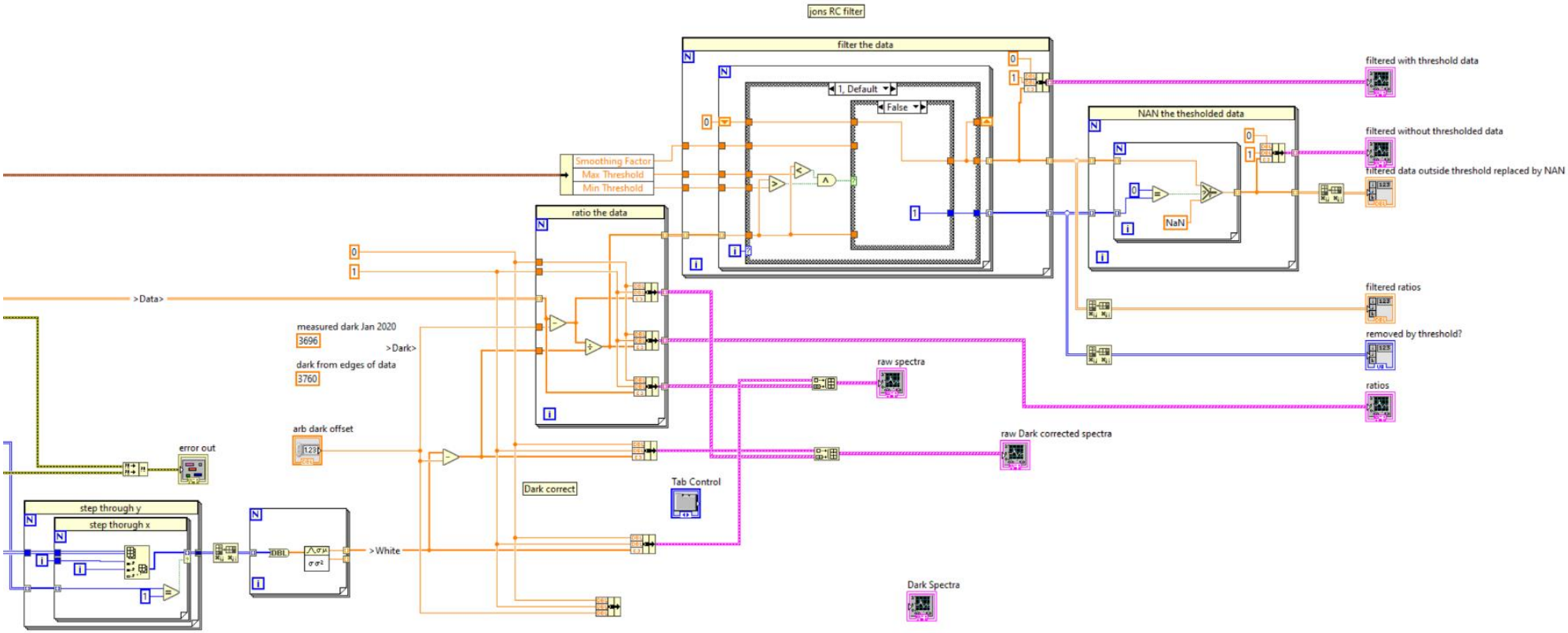

8.4. Hyperspectral Smartphone Initial Bias Correction

Below is the MATLAB script used for bias correction in early iterations of the Hyperspectral Smartphone.

```
%% Setup the script using these variables
imgDir = 'C:\Users\maryb\OneDrive\Desktop\for-correction';
imgPrefix = 'scene00129';
imgRange = 1;
imgRangePadding = 0;
imgExtension = '.png';

whiteImgPath = 'C:\Users\maryb\OneDrive\Desktop\for-correction\white.png';
darkImgPath = 'C:\Users\maryb\OneDrive\Desktop\for-correction\dark.png';

%% Script start

whiteImg = imread(whiteImgPath);
darkImg = imread(darkImgPath);
darkImgDbl = double(darkImg) / 255;

paddingStr = ['%0' num2str(imgRangePadding) 'd'];

correctionImg = whiteImg - darkImg;
correctionImgDbl = double(correctionImg) / 255;

correctionImgZero = ones(size(denom)) .* (correctionImg == 0);
useImg = ~logical(correctionImgZero);

outDir = [imgDir 'Output ' date ' ' datestr(now,'HH.MM.SS') '\'];
mkdir(outDir);

for i = imgRange
    rawImg = imread([imgDir imgPrefix num2str(i, paddingStr)
imgExtension]);

    normalisedR = ((double(rawImg) / 255) - darkImgDbl) ./
correctionImgDbl;

    normalisedR(isnan(normalisedR)) = 0;

    normalisedRNonZero = normalisedR .* useImg;

    imwrite(normalisedRNonZero, [outDir 'out_' num2str(i, paddingStr)
'.tiff']);
end
```

8.5. Data Cube Construction Code for the High-Resolution Hyperspectral Imager

Below is the MATLAB script used to construct the data cube for the high-resolution hyperspectral imager.

```
clear all

dark = imread('AVG_darks.tif');
cal = dlmread('cal_1.txt');
cal = cal(525:1324);
cal = cal/max(cal);
flat = double(imread('flat.tif'));
flat = flat/max(max(flat));

cd 2022-01-03-data
cd C9

frame_count = 1000;
frame_width = 1000;

data_cube = zeros(200, frame_width, frame_count);

x = 1;

for frame_index = 1:frame_count
    frame = imread(['Image3_', num2str(frame_index), '.tif']);
    frame = frame - dark;
    frame = uint16(frame);
%     ['data cube construction ' num2str(100*(frame_index/frame_count)) '%
complete']
    for index = 1:200
        data_cube(index,:,frame_index) = frame(:,index*4);
    end
end

cd ../
cd ../

cd data

scale = (65000*min(min(flat)))/(max(max(max(data_cube))));

index = 1;

length(cal(:,1))

while index < length(data_cube(:,1,1))
    image = squeeze(data_cube(index,:,:));
    image = image./flat;
    image = scale*(double(image)/cal(index));
    image = uint16(image);
    imwrite(image, [num2str(index) '.tif']);
    index = index + 1;
end
 cd ../
```

8.6. High-Resolution Instrument Spectral Data Correction and Extraction Code

Below is the MATLAB script used to extract the spectral datasets from the captured data.

```
base_dir = 'D:\moss_imaging\';
sub_dir = '2022-01-17-data\';
type = 'C';

cal = dlmread('cal.txt');
cal = cal/max(cal);

wavelength = zeros(800,1);

for index = 1:800
    wavelength(index,1) = index*0.22;
end

wavelength = wavelength + 611.6-(0.22*212);

spectra = zeros(800,11);
spectra(:,1) = wavelength(:,1);

for folder = 1:10

    spectrum = zeros(200,800);

    for index = 1:200
        image = imread([base_dir, sub_dir, type, num2str(folder),'\',
'Image3_', num2str(1+300),'.tif']);
        spectrum(index,:) = mean(image(index+400:index+600,:));
    end

    spectrum = mean(spectrum)';
    spectrum = spectrum./cal;
%     self
%             spectrum = spectrum/max(spectrum(:,1));

    spectra(:,folder+1) = spectrum(:,1);

end

% batch
       spectra(:,2:end) = spectra(:,2:end)/max(max(spectra(:,2:end)));
```

8.7. Spectral Data Combination Code

Below is the MATLAB script used to combine the spectral outputs of the Hyperspectral Smartphone and the High-Resolution Hyperspectral Imager.

```
wavelengths_phone_round = round(phone(:,1),0);
wavelengths_hires_round = round(hires(:,1),0);
a = 600;
pos_phone = find(wavelengths_phone_round==a);
pos_hires = find(wavelengths_hires_round==a);

if isempty(pos_phone)==1
    pos_phone = find(wavelengths_phone_round==a+1);
end

ratio_C = phone(pos_phone(1),2)/hires(pos_hires(1),2);
ratio_R = phone(pos_phone(1),3)/hires(pos_hires(1),3);
ratio_D = phone(pos_phone(1),4)/hires(pos_hires(1),4);

phone_scaled_C = (1/ratio_C)*(phone(:,2));
phone_scaled_R = (1/ratio_R)*(phone(:,3));
phone_scaled_D = (1/ratio_D)*(phone(:,4));

data =
zeros(pos_phone+length(wavelengths_hires_round(pos_hires(1):end,1)),4);

data(1:pos_phone,1) = phone(1:pos_phone,1);
data(1:pos_phone,2) = phone_scaled_C(1:pos_phone,1);
data(1:pos_phone,3) = phone_scaled_R(1:pos_phone,1);
data(1:pos_phone,4) = phone_scaled_D(1:pos_phone,1);

data(pos_phone+1:end,:) = hires(pos_hires:end,:);

data(:,2) = data(:,2)/max(data(:,2));
data(:,3) = data(:,3)/max(data(:,3));
data(:,4) = data(:,4)/max(data(:,4));

plot(data(:,1),data(:,2))
hold
plot(data(:,1),data(:,3))
plot(data(:,1),data(:,4))
hold
```